2020

Hydrogeology of salt flats:
the Salar de Atacama example

Miguel Ángel Marazuela Calvo

3 *Li*

PhD thesis 2020

Hydrogeology of salt flats: the Salar de Atacama example

Miguel Ángel Marazuela Calvo

Hydrogeology of salt flats:
the Salar de Atacama example

Miguel Ángel Marazuela Calvo

PhD thesis

Hydrogeology of salt flats:
the Salar de Atacama example

Miguel Ángel Marazuela Calvo

PhD thesis

Hydrogeology of salt flats:

the Salar de Atacama example

Thesis presented by

Miguel Ángel Marazuela Calvo

Barcelona, February 2020

(Publicly defence on March 27th 2020)

Work conducted at:

Institute of Environmental Assessment and Water Research (IDAEA, CSIC)

Department of Civil and Environmental Engineering, Polytechnic University of Catalonia (UPC)

Associated Unit: Hydrogeology Group (UPC-CSIC)

Advisors:

Enric Vázquez Suñé

Sebastià Olivella Pastalle

A mis padres,

Miguel Ángel y María José

Agradecimientos

Esta tesis supone el final de una etapa irrepetible que me ha aportado mucho a nivel científico, pero sobre todo a nivel personal. A lo largo de este tiempo me he enfrentado a retos que me han hecho crecer y obtener nuevas herramientas para afrontar el futuro. Sin embargo, lo que más valoro son todas las personas increíbles que he conocido, que me han acompañado dentro y fuera del trabajo y que han hecho de esta etapa una experiencia maravillosa. ¡Estas líneas van por vosotros!

A **Enric** y **Sebas** por darme la oportunidad de realizar la tesis doctoral en un entorno tan apasionante como es el Salar de Atacama, y por facilitarme el acceso al Grupo de Hidrología Subterránea (GHS) de Barcelona.

Especial agradecimiento a **Carlos Ayora**, no solo por haber ejercido como si fuese mi director, sino por la forma en la que lo ha hecho. Tus consejos y ayuda siempre desinteresada, sin esperar nada a cambio, de la que escasea en este mundo, han sido imprescindibles para que esta tesis saliese adelante. Solo puedo decirte ¡MUCHAS GRACIAS! por todo lo que me has aportado durante la tesis y, sobre todo, por mostrarme el camino que quiero seguir en el futuro.

A **Alex García** por ser la persona que hizo posible que toda esta aventura comenzase. Aun no sé muy bien cómo acabé aquí, pero sé que te lo tengo que agradecer a ti. Espero que en el futuro podamos seguir colaborando como hasta

ahora para que sigas transmitiéndome tu entusiasmo por la ciencia y ganas de aprender.

También, quiero agradecer a **Emilio Custodio** toda la ayuda y experiencia que me ofreció cuando comencé a trabajar en salares. Sin duda, sus sabios consejos, siempre humildes y llenos de contenido, supusieron un fuerte impulso para afrontar los primeros retos. Además, quiero agradecer a **Juan Hidalgo** todos los consejos y discusiones que me ha ofrecido siempre que lo he necesitado.

Pero sin duda, esta etapa no habría tenido sentido sin todos los **amigos** y **compañeros** que me han acompañado por este largo camino y que, seguro, lo harán en el futuro. En primer lugar, gracias a Berta, Sheila y Laura Scheiber, por todas las risas, cotilleos, conversaciones interminables y momentos surrealistas (tranquilas, no los voy a contar aquí... jeje) que hemos compartido dentro y fuera del despacho. Sin duda, muchos de los mejores recuerdos que me llevo han sido gracias a vosotras ¡MIL GRACIAS! También a Silvia, Tomás, Yoar, Tybaud, Alba, Rotman, Laura Martínez, Carol "La Pati", Tere, Alec,… por todos los cafés, cervezas y cenas que hemos compartido en el Tritón/Versalles/Concordia, congresos, viajes y muchos otros sitios inolvidables. A Diego Sampietro, Helena, Gonzalo y Laura Paricio (y ¿S.M.? jeje) por poner el acento maño a esta etapa en la que cualquier excusa ha sido buena para improvisar una celebración, y por todas las aventuras que hemos vivido juntos en Barcelona, Zaragoza y Chile (excepto cuando Laura perdió las llaves del coche en mitad del desierto, jeje). A los compañeros del CIHS y del Master en Hidrología Subterránea con los que tan buenos momentos compartí cuando llegué a Barcelona (la pizzería "Divina Pedralbes" siempre quedará en el recuerdo).

Además, quiero aprovechar estas últimas líneas para agradecer al Departamento de Ciencias de la Tierra de la Universidad de Zaragoza donde me formé como Geólogo, a mis amigos de la carrera y, en especial, a **Antonio Pérez** por introducirme en el mundo de la investigación y guiarme en mis primeros retos científicos.

Por último, pero no menos importante, a mi familia y amigos de Zaragoza. En especial a **mis padres**, Miguel Ángel y María José, a quienes va dedicada esta tesis, por apoyarme siempre en todas las decisiones que he tomado y creer en mí ¡MUCHAS GRACIAS!

Contents

Abstract

This thesis aims to advance the knowledge of the hydrogeological functioning of salt flats in order to achieve a sustainable management of their mineral resources and ecosystems. Salt flats are saline endorheic systems associated to arid and hyperarid climates where the water table is located a few centimetres below the ground due to the strong evaporation. Salt flats are a major source of Li, B, I, K, Mg and NaCl, and they host some of the most outstanding ecosystems on earth. Around 25 % of Li world reserves are located in the Salar de Atacama (Northeast of Chile). The exploitation of this raw material, highly valued in the technological and pharmaceutical industries, is carried out by brine pumping. Brine pumping can affect the natural hydrogeological regime of salt flats and, in many cases, the possible impact on their ecosystems is unknown. This threat, together with the lack of knowledge about its complex hydrodynamics, hinders its sustainable management.

This thesis contributes to (1) explain the geometry and groundwater flow of the mixing zone (saline interface) located around salt flats, (2) define the water balance and hydrodynamics of the Salar de Atacama under the natural regime, (3) analyse and quantify the impacts caused by brine pumping, (4) improve the design of the brine exploitations in salt flats and (5) question the traditional ideas on the origin of the Li-enrichment in the Salar de Atacama.

The groundwater recharged in the mountains is forced to flow upward when it reaches the mixing zone around the salt flat due to its lower density, feeding the lake and wetland ecosystems. A 3D mapping of a salt flat mixing zone has been carried out for the first time in the Salar de Atacama and it has shown a slope of the mixing zone much lower than previous assumptions. The 2D modelling of the mixing zone demonstrated as the permeability of the upper aquifer increases, the slope of the mixing zone decreases, resulting in a shallower mixing zone. Thus, the permeability of the upper aquifer, mostly constituted of very permeable karstified evaporites and alluvial deposits, is critical to the geometry of the mixing zone. In addition, a methodology to consider the effect of the mixing zone in groundwater flow management models has been proposed.

The hydrogeological conceptual model of the Salar de Atacama, prior to brine pumping (natural regime), has been defined and validated using a 3D steady-state groundwater flow model. The recharge occurs mainly in the eastern side of the basin due to its higher topographic level. The discharge takes place from the free water surface of the lakes or from the shallow water table of the mixing zone, and minority the nucleus, as phreatic evaporation. This results in a water table whose minimum hydraulic head is located in the easternmost nucleus, close to the eastern mixing zone.

The 3D transient-state modelling of the Salar de Atacama basin from 1986 to 2018 has allowed to explain the hydrodynamics and water balance impacts caused by brine exploitation. From 1986 to 1994, under the natural regime, the gradual drawdown of the water table resulting from the negative water balance was counteracted by the sharp rises caused by rainfall events occurred directly on the salt flat. From 1994 to 2015, under the mining regime, the brine pumping caused an additional drawdown of the water table that triggered a decrease of the phreatic evaporation. This effect has been defined as "damping capacity" and it allows to counteract the disturbances occasioned by natural or anthropogenic events on the water table and balance of salt flat basins.

A methodology based on field data and spatio-temporal analysis has been proposed and applied to the Salar de Atacama to quantify the impacts caused by brine pumping on the water table and evaporation discharge of salt flats. Evaporation pans and lysimeters allowed to measure the potential evaporation rate

and to define the exponential decrease of the evaporation with respect to the water table depth. The decrease of the evaporation discharge from 1986 to 2018 has been quantified in 15 %. The damping capacity compensated, at least in part, the decrease of the evaporation discharge, but nowadays it is already amortized in the nucleus and the mixing zone begins to be impacted.

The 3D modelling of a hypothetical salt flat under brine exploitation has contributed to optimize the spatial distribution of the pumping wells in terms of impact on the water balance. The damping capacity can reach to compensate the total pumped brine if the previous evaporation discharge is higher than the pumped brine. Brine exploitations should consider to distribute the pumping outflow in the greatest extent possible to take full advantage of the damping capacity.

The results of the hydro-thermo-haline modelling of an East-West vertical cross section of the Salar de Atacama basin has suggested the Salar Fault System (SFS), which is located in the central zone of the nucleus, as the main contributor for the extreme Li-enrichment, either through the rise of Li-rich brines from a deep hydrothermal reservoir or remobilization of ancient layers of Li-enriched salts and/or clays by non-evaporated recharge waters coming from the West. The present minimum hydraulic head located in the eastern side of the nucleus prevents to consider advanced evaporation as a present day mechanism of reaching the high Li-content of the brines located on the SFS. Moreover, the persistence of the mixing zones in depth also dismissed previous ideas of (1) leaking of brines from the present salt flats of the Altiplano-Puna and (2) leaching of hypothetical salt flats buried by volcanic eruptions in the Altiplano-Puna as sources for the extreme Li-enrichment of the Salar de Atacama brines.

Resumen

Esta tesis contribuye a avanzar en el conocimiento del funcionamiento hidrogeológico de los salares con el fin de mejorar la gestión de sus recursos minerales y ecosistemas. Los salares son sistemas endorreicos salinos asociados a climas áridos e hiperáridos donde la superficie freática se localiza unos centímetros por debajo del suelo como consecuencia de la fuerte evaporación. Los salares son una fuente principal de Li, B, I, K, Mg y NaCl, y albergan algunos de los ecosistemas más excepcionales de la tierra. Alrededor del 25 % de las reservas mundiales de Li se localizan en el Salar de Atacama (Noreste de Chile). La explotación de esta materia prima, altamente valorada en las industrias tecnológica y farmacéutica, se realiza mediante bombeo de salmuera. El bombeo de salmuera puede afectar al régimen hídrico natural de los salares y, en muchos casos, se desconoce el posible impacto sobre sus ecosistemas. Esta amenaza, junto con la falta de conocimiento sobre su compleja hidrodinámica, dificulta una gestión sostenible de estos sistemas.

Esta tesis ayuda a (1) explicar la geometría y el flujo subterráneo de la zona de mezcla (interfaz salina) ubicada alrededor de los salares, (2) definir el balance hídrico y la hidrodinámica del Salar de Atacama en su régimen natural, (3) analizar y cuantificar los impactos causados por el bombeo de salmuera, (4) mejorar el diseño de las explotaciones de salmuera en salares y (5) cuestionar las ideas tradicionales que explican el origen del enriquecimiento en Li del Salar de Atacama.

El agua subterránea recargada en las montañas es forzada a fluir hacia la superficie cuando alcanza la zona de mezcla que rodea al salar debido a su menor densidad, alimentando los ecosistemas lagunares y humedales. La primera cartografía 3D de la zona de mezcla de un salar se ha llevado a cabo en el Salar de Atacama, evidenciando una pendiente de la zona de mezcla mucho menor que las predicciones anteriores. El modelado 2D de la zona de mezcla ha demostrado que cuanto mayor es la permeabilidad del acuífero superior, más baja es la pendiente y más superficial se vuelve la zona de mezcla. Por lo tanto, la permeabilidad del acuífero superior, principalmente constituido por evaporitas karstificadas y depósitos aluviales muy permeables, es crítica para la geometría de la zona de mezcla. Además, se ha propuesto una metodología para considerar el efecto de la zona de mezcla en los modelos de gestión.

El modelo hidrogeológico conceptual del Salar de Atacama, previo al bombeo de salmuera (régimen natural), se ha definido y validado utilizando un modelo estacionario 3D del flujo subterráneo. La recarga se produce, principalmente, en el lado oriental de la cuenca debido a su mayor elevación topográfica. La descarga de la cuenca tiene lugar desde la superficie de agua libre de las lagunas o desde la superficie freática de la zona de mezcla, y en menor medida del núcleo, mediante evaporación freática. Esto da como resultado una superficie freática cuyo mínimo nivel hidráulico se localiza en el sector más oriental del núcleo, cerca de la zona de mezcla oriental.

El modelado transitorio 3D de la cuenca del Salar de Atacama desde 1986 hasta 2018 ha permitido explicar los impactos causados por la explotación de salmuera sobre la hidrodinámica y el balance hídrico. Desde 1986 hasta 1994, bajo el régimen natural, la disminución gradual de la superficie freática resultante de un balance hídrico negativo fue contrarrestada por los ascensos bruscos desencadenados por los eventos de lluvia ocurridos directamente sobre el salar. Desde 1994 hasta 2015, bajo el régimen de explotación minera, el bombeo de salmuera causó una profundización adicional de la superficie freática que desencadenó una disminución de la evaporación freática. Este efecto ha sido definido como la "capacidad de autorregulación" y permite a los salares contrarrestar las perturbaciones ocasionadas por eventos naturales o antropogénicos sobre la superficie freática y el balance hídrico.

Se ha propuesto y aplicado al Salar de Atacama una metodología basada en datos de campo y análisis espacio-temporal de los mismos para cuantificar los impactos causados por el bombeo de salmuera sobre la superficie freática y la descarga por evaporación de los salares. Las bandejas de evaporación y los lisímetros permitieron medir la tasa de evaporación potencial y definir la disminución exponencial de la evaporación con respecto a la profundidad de la superficie freática. La disminución de la descarga por evaporación desde 1986 hasta 2018 ha sido cuantificada en un 15 %. La capacidad de autorregulación compensó, al menos en parte, la disminución de la descarga por evaporación, pero hoy en día ya está amortizada en el núcleo y la zona de mezcla comienza a verse afectada.

El modelado 3D de un hipotético salar bajo explotación de salmuera ha contribuido a optimizar la distribución espacial de los pozos de bombeo en términos de impacto sobre el balance hídrico. La capacidad de autorregulación puede llegar a compensar la salmuera bombeada si la descarga por evaporación previa es mayor que la salmuera bombeada. Para aprovechar al máximo la capacidad de autorregulación, las explotaciones de salmuera deben considerar distribuir el caudal bombeado en la mayor área posible.

Los resultados del modelado hidro-termo-halino de una sección vertical Este-Oeste de la cuenca del Salar de Atacama han señalado al Sistema de Fallas Salar (SFS), localizado en el sector central del núcleo, como el principal contribuyente para explicar el enriquecimiento extremo en Li, ya sea por el ascenso de salmueras ricas en Li desde un reservorio hidrotermal profundo o por removilización de antiguas capas de sales y/o arcillas ricas en Li por aguas de recarga no evaporadas provenientes del Oeste. La localización del mínimo nivel hidráulico regional en el lado oriental del núcleo descarta considerar la evaporación avanzada como un mecanismo actual para alcanzar el alto contenido de Li de las salmueras ubicadas sobre el SFS. Además, la persistencia de las zonas de mezcla en profundidad también permite descartar las hipótesis previas de 1) infiltración de salmueras desde los salares actuales del Altiplano-Puna y 2) lixiviado de hipotéticos salares enterrados por erupciones volcánicas en el Altiplano-Puna como origen del enriquecimiento excepcional en Li de las salmueras de Salar de Atacama.

List of figures

List of tables

Chapter 1

Introduction

1.1. Motivation and objective

Salt flats (*salars*) are saline endorheic systems associated to arid and hyperarid climates, in which the water table is several centimetres or decimetres below the ground due to the strong evaporation. The largest salt flats in the world are located in the Altiplano-Puna plateau of the Central Andean Range, which includes northwestern Argentina, southwestern Bolivia and northeastern Chile (Risacher et al., 2003; Warren, 2010). Salt flats are a major source of Li, B, I, K, Mg and NaCl, at the same time that they host some of the most outstanding ecosystems on earth (Evans, 1978; Kesler et al., 2012; Munk et al., 2016).

The brines of salt flats account the 80 % of the world's reserves of Li used for the development of mobile phones and electric car batteries, as well as in the pharmacology industry (USGS, 2019). Its demand has notably increased in the last decade, and this trend will probably continue in the future (Vikström et al., 2013), as large quantities may be needed to develop nuclear fusion reactors using tritium generated from lithium. This fact is evidenced by the large number of countries that are just now commissioning studies to determine the mineral potential of their salt

flats or to increase the amounts of resources that could be exploited during current mining activities (e.g., Salar de Atacama in Chile; Salar de Uyuni and Salar de Coipasa in Bolivia; Salar de Hombre Muerto and Salar de Cauchary-Olaroz in Argentina). In salt flats, the exploitation of Li and other raw materials is executed by brine pumping. The brine is pumped and then transported to evaporation pools where is progressively concentrated until the salts of interest precipitate (Flexer et al., 2018). However, the hydrogeological functioning of the salt flat basins and the mechanisms of the extreme Li-enrichment of its brines is still surrounded by unknowns what hinder the sustainable management of its mining resources and ecosystems.

Around 25 % of the Li world reserves are located in the Salar de Atacama (NE Chile) (Liu et al., 2019). The Salar de Atacama (SdA) is the third largest salt flat on earth after the Salar de Uyuni (Bolivia) and Salinas Grandes (Argentina) and its brine reaches extreme Li-concentration (up to 5,000 mg/L), making it the main Li-reserve worldwide. In addition, exceptional lake and wetland ecosystems, encompassed within the Reserva Nacional de los Flamencos (Ramsar site), are located around the Salar de Atacama. However, these ecosystems are threatened by the brine exploitation that has been carried out since the 1980s. Paradoxically, the strong investment made for its mining exploitation has resulted in an outstanding monitoring network which has made the Salar de Atacama a reference for scientific community.

The origin of the Salar de Atacama dates to the Oligocene-Miocene boundary, synchronous with the increase in volcanic activity and the Altiplano-Puna uplift (Arriagada et al., 2006). The uplift of the Altiplano-Puna marked the paleoclimatology history as a consequence of the strong topographic gradient reached, giving rise to a more humid Altiplano-Puna than the hyperarid salt flat (Rech et al., 2006). Thus, the main recharge occurs by infiltration of rainfall in the eastern volcanic arc (western edge of the Altiplano-Puna) and the discharge takes place by evaporation in the marginal zone and nucleus of the salt flat. The discharge occurs from the free water surface of the lakes and the phreatic evaporation that takes place from the shallow water table as a function of the water table depth (Philip, 1957). However, the water balance of the Salar de Atacama basin and the possible contribution of groundwater flow coming from the Altiplano-Puna (outside of the basin) is still unknown. In addition, the increase in thickness of the unsaturated zone

caused by brine pumping suggests that the natural regime of the Salar de Atacama basin may be threatened and the ecosystems comprised.

The marginal zone surrounding the salt flat nucleus, where the lake and wetland ecosystems are located, matches the mixing zone (saline interface) resulting from the density contrast between the freshwater recharged in the mountains and the evaporated brine of the nucleus. When the groundwater recharged in the mountains arrives at the marginal zone, it is forced to flow upward by its lower density, feeding the lakes and wetlands. Therefore, the need to assess the detailed characteristics, geometry and hydrodynamics of the mixing zone occurs immediately when managing both mineral resources and their associated ecosystems.

The origin of solutes in salt flats has been intensively debated in the recent decades. Although whatever the origin of solutes a strong evaporation is needed for water to acquire Li concentrations higher than 5,000 mg/L, it seems unlikely that such exceptional concentration are achieved from the evaporation of the freshwater inflows (<5 mg/L) coming from the recharge zone in the Altiplano-Puna. Several hypothesis has been proposed to explain the extreme Li-enrichment in the Salar de Atacama: (1) leaking of brines from the present salt flats of the Altiplano-Puna (Risacher et al 2003; Risacher and Fritz 2009), (2) leaching of hypothetical salt flats buried by volcanic eruptions in the Altiplano-Puna (Risacher and Fritz 2009; Risacher et al., 2011) and (3) rising of hydrothermal brines from deep reservoirs through faults (Lowenstein and Risacher 2009). However, all the previous hypotheses have been based on geological or hydrochemical conceptual models and any of them has been validated by groundwater flow numerical models that take into account the complex hydro-thermo-haline circulation of these systems. The hydro-thermo-haline circulation that results from the strong coupling of flow, mass and heat transport and its density and viscosity dependency is essential at basin-scale modelling and could contribute to explain the complex hydrogeochemistry and the extreme Li-enrichment of salt flats (Driesner and Heinrich, 2007; Klyukin et al., 2016; Li et al 2016; Magri et al 2015; Hardie 1990; Hardie 1991).

This background shows that several critical questions must be explained to achieve a sustainable management of the mineral resources and ecosystems of salt flats:

3

- How is the geometry and the groundwater flow of the mixing zone (saline interface) of salt flats?
- How is the hydrogeological functioning of the Salar de Atacama under natural conditions?
- What impact does the brine pumping on the hydrodynamics and the water balance of salt flats?
- Can the impacts caused by brine extraction be spatio-temporally quantified? Is it possible to improve the design of mining operations to reduce environmental impacts?
- What is the origin of the extreme Li-enrichment in the Salar de Atacama?

Considering the high economic and ecological impact of these issues that remain unknown, the general objective of this thesis is to establish and validate through numerical models the hydrogeological functioning of the salt flats under natural and anthropogenic regimes. This approach is needed in order to evaluate the impacts of mining exploitation on the natural hydrodynamics of the basin and to increase our understanding on the processes leading to the extreme Li-enrichment of their brines.

1.2. Thesis outline

The general objective of this thesis is broken down into specific objectives that are addressed in a total of seven chapters. After the introduction chapter, the following five chapters are written as independent journal publications addressing the specific goals of each one. Each of them corresponds to an article already published in a journal of the first quartile (Q1) (Chapter 2, 3, 4 and 5) or in preparation (Chapter 6). The last chapter includes the synthesis and conclusions drawn from this thesis.

Chapter 2, based on the paper Marazuela et al. (2018), focuses on the geometry, hydrodynamics and groundwater flow modelling of the mixing zone (saline interface) of the Salar de Atacama. This study allows to explain why the saline interface of salt flats is shallower than previous predictions. In addition, it proposes a new methodology to incorporate the complex groundwater flow associated to the mixing zone into 3D hydrogeological models of low computational cost.

Chapter 3, based on the paper Marazuela et al. (2019a), establishes and validates the hydrogeological model of the Salar de Atacama basin in its natural regime, prior to the intensive brine pumping. To reach this goal, the quantification of the recharge

and evaporation is performed and the water balance of the basin is discussed and justified against the previous estimations. The methodology proposed in the Chapter 2 to incorporate the effect of the mixing zone in density-constant groundwater flow models is used.

Chapter 4, based on the paper Marazuela et al. (2019b), addresses the impacts induced by brine pumping on the natural regime of the salt flats. The steady-state groundwater flow model of Chapter 3 is enhanced to perform a 3D transient-state model that reproduces the natural (evaporation and recharge) and anthropogenic (brine pumping and reinjections) time series to quantify the impacts caused by brine exploitation on the natural hydrodynamics of the basin. The "damping capacity" of salt flats to cushion the volume of brine pumped by reduction of phreatic evaporation is defined.

Chapter 5, based on the paper Marazuela et al. (2020), proposes a methodology to quantify the evaporation discharge in salt flats and to evaluate the impacts caused by brine exploitation on the water table and water balance. This is used as basis to improve the design of the brine exploitation in terms of hydroecological impact. Evaporation pans and lysimeters are used to measure the free water surface and phreatic evaporation respectively. The spatio-temporal quantification of the evaporation discharge and the water table depth, prior to brine pumping and after brine pumping, allowed to quantify in detail the impacts and to define their spatial distribution. Additionally, a 3D groundwater flow model of a hypothetical salt flat under exploitation is used to propose the optimum distribution of pumping wells in brine exploitations.

Chapter 6, that constitutes the basis of an article in preparation, discusses the validity of the traditional ideas on the extreme Li-enrichment in the Salar de Atacama under the filter of the hydro-thermo-haline groundwater flow modelling of the basin. The hydro-thermo-haline circulation allows to discard some of the most accepted previous hypotheses, as well as to highlight the role played by faults in the extreme Li-enrichment.

Chapter 7 summarizes the main scientific contributions of this thesis.

1.3. Scientific and technical production

Several scientific and technical contributions have been performed in the framework of this PhD thesis. The Appendix A comprises the scientific articles directly related with the PhD thesis, other scientific articles in which the author has been committed and involved actively during this period, chapters in books, proceedings in congresses and scientific and technology transfer projects. In addition, the cover of the scientific articles already published can be consulted in Appendix B.

Chapter 2

3D mapping, hydrodynamics and modelling of the freshwater-brine mixing zone in salt flats similar to the Salar de Atacama (Chile)

2.1. Introduction

Salt flats (*salars*) are an important source of minerals. They account for half of the world´s lithium production and contain the main economic reserves of this element (USGS, 2017). In addition, boron and potash are economically mined from salt flats. Lithium is a strategic commodity; its uses vary from light batteries to cancer treatment. Its demand has notably increased in the last decade, and this trend will probably continue in the future (Vikström et al., 2013), as large quantities may be needed to develop nuclear fusion reactors using tritium generated from lithium. This fact is evidenced by the large number of countries that are just now commissioning studies to determine the mineral potential of their salt flats (e.g., Salar de Uyuni in Bolivia or Salar del Hombre Muerto in Argentina) as well as to increase the amounts of resources that could be exploited during current mining activities (e.g., Salar de Atacama in Chile). This explains the current worldwide interest in salt flat hydrogeology, which is also due to the existence of peripheral brine and saline water lagoons that have high ecological, human and tourist value, in addition to their scientific value.

Salt flats are endorheic lagoon systems associated with arid or hyperarid climates, where the rate of evaporation is very high; in many cases, this causes the surface water to disappear and the water table to lie just below the land surface (Yechieli and Wood, 2002). This characteristic is what triggers the important precipitation or accumulation of high-value industrial minerals (Corenthal et al., 2016; Kesler et al., 2012; Munk et al., 2016; Risacher et al., 2003). In these endorheic basins, it is common for evaporation to be higher than local recharge (Hardie, 1991); thus, some other contribution, which is often groundwater, may compensate for this difference. In the simplest case, ignoring hypothetical deep contributions or inflows from other basins, the only water input to the salt flat system is lateral inflow and direct rainfall (which is minor due to the aridity of the climate), and the only output from the system is evaporation. These factors are all strongly related to climate variability and could potentially be affected by global climate change (Rosen, 1994).

The most accepted hydrogeological model assumes that dense brines produced from surface evaporation overturn and sink in the central area of the salt flat, setting up large-scale convection cells in its nucleus (i.e., the core of the salt flat, which is dominated by halite). These cells return to the surface at the margins of the salt flat,

where the brines mix with incoming fresh groundwater in a complex process (Fan et al., 1997; Hamann et al., 2015; Nield et al., 2008; Wood and Sanford, 1990; Wooding et al., 1997). For this reason, the discharge of groundwater essentially occurs at the resulting freshwater-brine mixing zone areas, where lagoons may appear (Duffy and Al-Hassan, 1988; Tejeda et al., 2003). As a result, wetlands are commonly present in the margins of salt flats and are the bases for complex and sensitive ecological habitats surrounded by barren lands.

The contact between two miscible fluids of different densities is characterized by a mixing zone, which is also called a saline interface. This interface results from the dynamic equilibrium of moving fresh- and saltwater (Custodio and Bruggeman, 1987; Custodio and Llamas, 1976; Dentz et al., 2006), where the relationship between the concentrations of both fluids is stoichiometric.

In coastal aquifers, the position and characteristics of the mixing zone are well known, and its upper part coincides with the coastline in water table aquifers (Bear, 1972; Glover, 1959; Werner et al., 2013). In salt flats, where the density contrasts are much greater than those in coastal aquifers, the mixing zone develops as a result of point pressure equilibrium between recharge and evaporated water, but its position and geometry are more difficult to predict. This is because the brine in the salt flats is generated in situ as a result of evaporation (Acosta and Custodio, 2008), and recharge and evaporation are strongly subject to climatic oscillations (Tyler et al., 2006). Brine mining can affect the dynamics of the mixing zone in a short period of time, similar to freshwater extraction in coastal aquifers (Oude-Essink, 2001). In the natural state, evaporation occurs in both the salt flat nucleus and the marginal zone, regardless of whether it is a sheet of open water (marginal lagoons) or a shallow water table, which commonly have very irregular spatial distributions.

The need to assess the detailed characteristics of the mixing zone occurs immediately when managing both mineral resources and their associated ecosystems. The best management tool are the numerical models in which the effects of variable density are taken into account. These models are expensive to run in two-dimensional (2D) cases and are currently very difficult to run in three-dimensional (3D) cases at the regional scale (Oude-Essink and Boekelman, 1996). Nevertheless, 3D regional scale models are needed for the management of any hydrogeological system. In the case of coastal systems, this problem is solved in two ways: (1)

neglecting the effects of variable density by assuming some simplifications or (2) converting the pressures of marine and variable-density waters into equivalent pressures of freshwater (Lu et al., 2015; Maas and Emke, 1989). The last solution, despite providing only an approximation of the actual situation (Post et al., 2007), is the one that has been chosen to model many coastal systems. However, to date, there is no evidence that any similar methodology has been proposed for the study and management of salt flats. Furthermore, the simplifications that are frequently assumed in coastal aquifers, such as neglecting density variations when advection is dominant over convection (Iribar et al., 1997; Vázquez-Suñé et al., 2006), are not acceptable in salt flats.

To obtain solutions for the above problem, the Salar de Atacama (NE Chile) was chosen as a case study. The choice was based on three characteristics: (1) it is the third largest salt lake on Earth, with a surface area of 3000 km^2, (2) it contains exceptional water ecosystems and bird nesting areas in the surficial mixing zone area, which require scientific solutions for their preservation and sustainability and (3) there is a unique monitoring network that is regularly operated and well instrumented (Tyler et al., 2006) thanks to the exploitation of brine resources carried out in the southwestern area of the salt flat nucleus.

The main objective of this work is to obtain the first 3D map of the salt flat mixing zone, using the Salar de Atacama as a case study. This 3D map, together with an idealized 2D numerical model, allows us to understand the dynamics of the mixing zone and the effects of heterogeneity on its large-scale geometry. We also propose the use of the 3D map to apply simplified rules for constant-density 3D models that include mixing zones.

The structure of this chapter follows the order described below. First, the 3D mapping of the mixing zone is addressed. Second, the usefulness of 3D mapping in the salt flats to correct the hydraulic heads by density differences and to facilitate their modelling at a constant density is shown. Third, the idealized 2D numerical model of the regional mixing zone is performed. Fourth, the sensitivity analysis of the hydraulic conductivity of the upper aquifer is carried out to determine its influence on the geometry of the mixing zone on a regional scale.

2.2. Materials and methods

2.2.1. Geographic setting

The Salar de Atacama (hereinafter SdA) is located in northern Chile between 23° and 24° South latitudes and 68° and 69° West longitudes; it is located in Region II (Antofagasta) and within the limits of the community (municipality) of San Pedro de Atacama (Fig. 2.1). The basin where the salt flat is located has an oval shape, with the long axis in the N-S direction and an extent of approximately 20,000 km². It is bordered to the west by the Cordillera de la Sal (Salt Range), which stretches from NNE to SSW at the slopes of the Domeyko Range, and to the East by the western Cordillera de los Andes (Andean Range), whose high peaks are crowned by the current volcanic arc (> 5500 m a.s.l., metres above sea level). The northern part of the basin is bounded by the merging of the Domeyko Range and the Andean Range, while the southern part is bounded by the Lila Mountains.

Because the Andean Range acts as a geographic barrier to atmospheric movement, the SdA is characterized by a hyperarid climate, resulting in a very low rainfall rate (Bookhagen and Strecker, 2008; Garreaud et al., 2010; Hartley and Chong, 2002). On average, the salt flat receives less than 20 mm/yr of precipitation. The major water source is groundwater coming from the Andean Range. In the mountains, the average precipitation reaches 160 mm/yr (IDAEA-CSIC, 2017). The output is water table evaporation produced in the nucleus and marginal zone, where the mean surficial water evaporation rate is 4.3 mm/d. Evaporation decreases as the depth of the water table increases, and it depends on the soil composition (Kampf et al., 2005; Kampf and Tyler, 2006; Muñoz-Pardo and Ortiz-Astete, 2004).

The two main river courses contributing to the salt flat, as shown in Fig. 2.1, are the San Pedro River, which has an average flow of 1 m³/s and torrential events of up to 25 m³/s, and the Vilama River, which has an average flow of 0.2 m³/s. These rivers flow from North to South (Salas et al., 2010). The San Pedro River ends in a delta with the same name, while the Vilama River disappears in the upper half of its basin. There are also some intermittent streams that descend from the mountains and infiltrate into the extensive alluvial fans on the eastern side of the salt flat. In many cases, these streams are controlled by structural features.
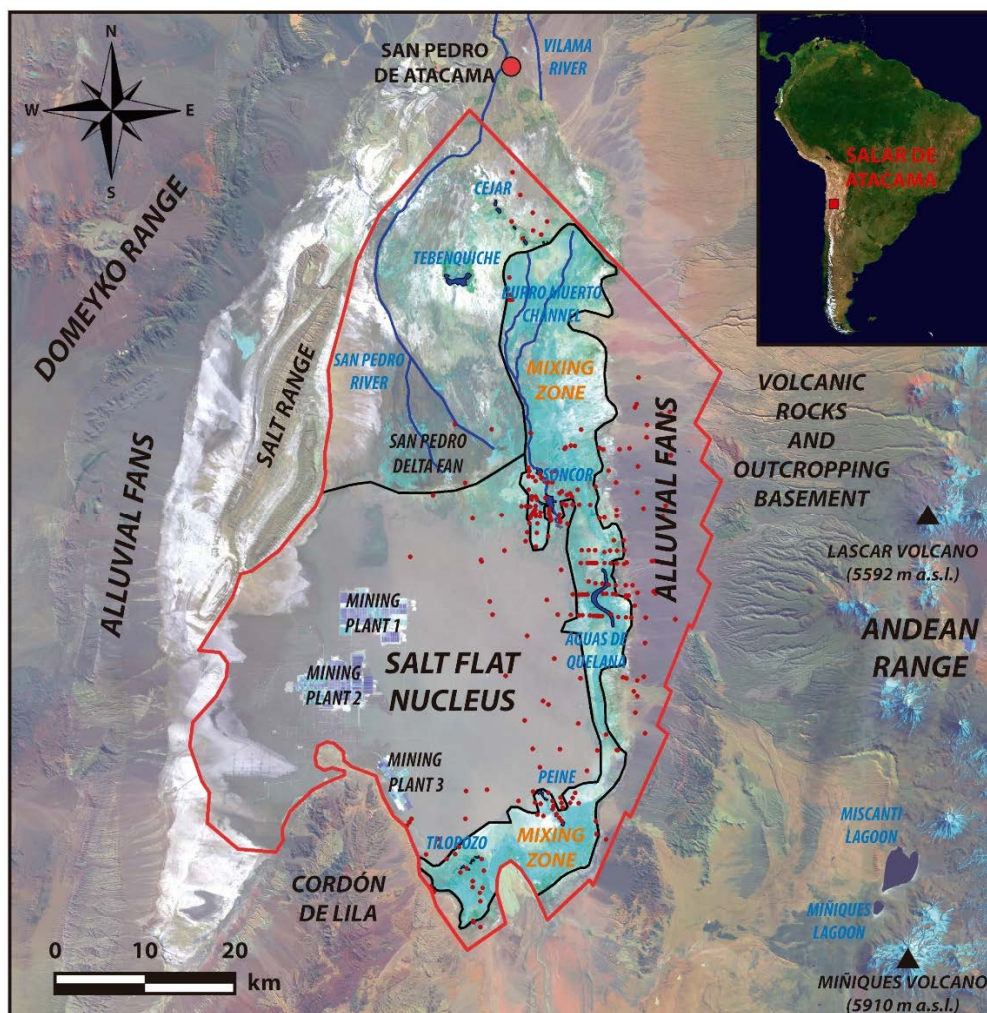
Figure 2.1. *Location of the SdA (LANDSAT 8, 27 September 2016). The main geological and geographical domains are shown in black lettering; rivers, channels and water systems are shown in blue lettering. The saline interface or mixing zone are shown as black lines and orange lettering. Red points are the observation points used for the 3D mapping of the mixing zone.*

In addition, in the eastern margin (surficial mixing zone) of the SdA, there are many lagoons and wetlands; in some cases, these have been defined as Ramsar sites. This area has been recognized by the international community as an environment with significant value for humanity. Some lagoons reach surface areas of several hectares, although most are smaller. The lagoons are grouped into four systems (Fig. 2.1): Soncor (Chaxa, Barros Negros and Puilar lagoons), which is connected by the

Burro Muerto channel; Aguas de Quelana; Peine (Salada, Saladita and Interna lagoons); and Tilopozo (La Punta and La Brava lagoons). These lagoons are the habitats for several migratory or endemic species, mainly birds, among which there are three species of high Andean flamingos, xerophytic and halophytic shrubs or grass, and some mammals, microcrustaceans, microalgae and bacteria.

Flamingos mainly feed on microcrustaceans (e.g., Artemia), whose range of vital salinity has more or less defined thresholds. Outside these limits, the population of this biota is reduced due to its inability to reproduce and survive if the salt concentration increases or to compete with new predators if the concentration of dissolved salts decreases (Gajardo and Beardmore, 2012).

2.2.2. Hydrogeological framework

The SdA is currently located in a compressive tectonic basin, which is framed by inverse faults which affect from the Palaeozoic basement to present deposits (Arriagada et al., 2006; Jordan et al., 2007; Mpodozis et al., 2005). Based on its geomorphological, geological and hydrogeological characteristics, four large domains can be distinguished from the watershed line to the basin depocenter (Figs. 2.1 and 2.2): 1) the basement and the volcanic deposits of the mountain range, 2) the alluvial fans descending therefrom, 3) the marginal zone (2300 to 2320 m a.s.l.) and 4) the SdA nucleus (2300 m a.s.l.).

In the actual basin depocenter (i.e. the halite nucleus), a series of clastic and evaporitic sediments are known to have been deposited from the Upper Miocene to the present, with a thickness that exceeds 1400 m in some areas (Jordan et al., 2007; Mpodozis et al., 2005; Pananont et al., 2004). The evaporite deposits in the nucleus and marginal zone show a well-defined asymmetric zonation that follows a sequence of classic evaporite precipitation, with a gradual evolution from carbonates and sulphates in the marginal zone to halite in the salt flat nucleus (Vásquez et al., 2013), where solutes of mining interest are concentrated in the remnant final brines.

Alluvial deposits and some layers of the salt flat nucleus have medium to high hydraulic conductivities (IDAEA-CSIC, 2017; Muñoz-Pardo and Ortiz-Astete, 2004; Rockwood Lithium, 2015). In the alluvial deposits, this is due to their primary lithological properties; in the salt flat nucleus, this is the result of intense karstification processes. In the salt flat, the main aquifer is the upper layer of halite

(60 to 300 m/d). There is also a deeper second halite aquifer (0.1 to 20 m/d), which is confined by a layer of low-permeability gypsum acting as an intermediate aquitard (0.01 to 5 m/d). This same aquifer-aquitard-aquifer sequence applies to the alluvial fans as a regional simplification, where the upper (80 to 300 m/d) and lower (20 m/d) high-permeability detrital deposits are separated from the lower ones by some relatively poorly permeable layers (0.01 to 5 m/d).
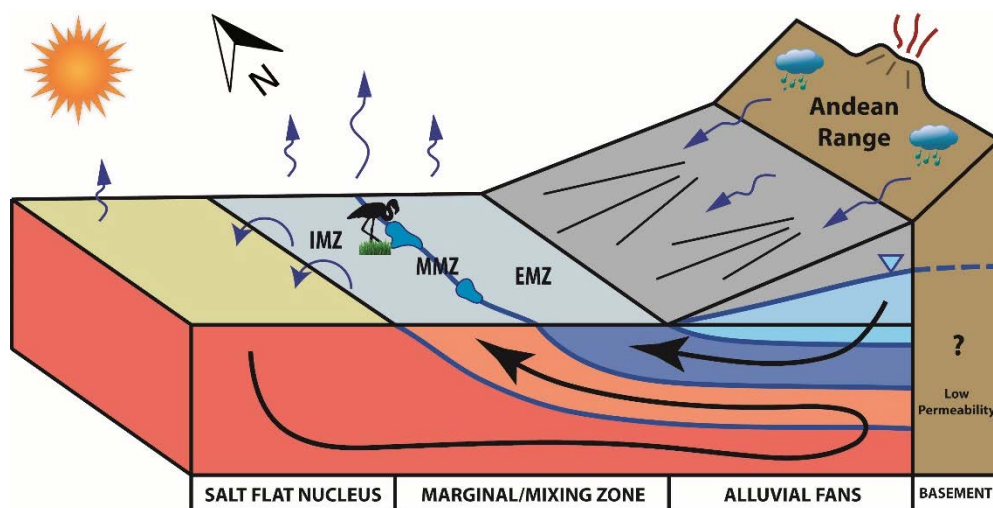
Figure 2.2. *Conceptual model of the mixing zone in the Salar de Atacama. Black lines represent the flow paths. IMZ - Internal mixing zone; MMZ - Middle mixing zone; EMZ - External mixing zone.*

The regional potentiometric surface shows a concentric flow that extends from the highest areas to the depocenter of the basin. Due to the low recharge and topography, the water head gradients are very small (<0.001 m/m), especially in the nucleus and marginal zones, where these gradients are almost zero. In the marginal zone (mixing zone), groundwater crops out, thus indicating the freshwater-brine interface zone (Fig. 2.2).

2.2.3. Hydraulic role of the mixing zone in the lagoons and wetlands of the Salar de Atacama

Three hydraulic domains have been distinguished in the mixing zone, from the eastern boundary of the salt flat nucleus to the lateral alluvial fans. These are the internal (IMZ), middle (MMZ) and external (EMZ) mixing zones (Fig. 2.2).

Freshwater recharge is mainly produced on the eastern mountain side. The marginal lagoons, wetlands and springs are located in the MMZ (Fig. 2.2). The resulting flow discharges into this zone and ascends to the surface, resulting in the Quelana, Peine and Tilopozo lagoons. The Soncor lagoon system is a special case, as it is located in the IMZ and not in the MMZ; its origin is not the direct groundwater overflow of the MMZ (Ortiz et al., 2014). Along the final flow path, the total dissolved solids (TDS) of the groundwater gradually increase as a consequence of mixing and evaporation, as it is very shallow. Some of the water returns to the IMZ and the salt flat nucleus as concentrated brine (Fig. 2.2). This dynamic behaviour is strongly variable due to the seasonality of recharge and evaporation (Salas et al., 2010).

2.2.4. Hydrogeological data

The analysis of satellite images (LANDSAT 8) allows us to map the surface hydrological features and the mixing-zone geometry near the land surface.

Water heads and physico-chemical parameters (e.g., electrical conductivity) were measured in the field. The same physico-chemical parameters and solute concentrations were measured in the laboratory following standard procedures. Some vertical electrical conductivity (EC) profiles were obtained in boreholes. Data are available from a total of 310 observation points (wells, piezometers, trenches and surface water courses) distributed throughout the area (Fig. 2.1), with records dating back to 1984. Most of the data used for this research project were provided by the SQM Company. These data have been complemented with other difficult-to-access sources of information (Rio Chilex S.A, 1997; Rockwood Lithium, 2015). The main information of the wells with physico-chemical data (coordinates and average values of EC, density and salinity) is compiled in Appendix C.

The monitoring network consists of well-levelled points with which to measure the water head and collect water samples. These monitoring points are most often boreholes, but they often designed as wells and piezometers. Some boreholes are point wells, which are open or screened in a short interval at a given depth, but they often have long open and screened sections. The cased section of the piezometer may contain water of a different density and salinity than that in the open part (Rushton, 1980). This affects the measured water head. This effect can be corrected by obtaining an electrical conductivity (EC) log to calculate vertical density changes and introduce

the needed corrections; it can also be corrected by substituting the water inside the borehole before measuring the level for water in the open section by repeated bailing or low-flow pumping from near the water surface. Nevertheless, in low-permeability layers, this measurement may be distorted by residual water level drawdown. In most cases, the depth to the water level is measured without considering the salinity in the uncased section. This may introduce some errors in marginal areas with great vertical salinity gradients and where shallow water may enter the borehole. Water samples are often collected using a bailer or a thief sampler that opens at the desired depth. Some mixing may thus occur with other water in the borehole or pit. The best water samples are obtained with a low-flow pump with the inflow inside the section to be sampled. Measuring and sampling protocols are applied.
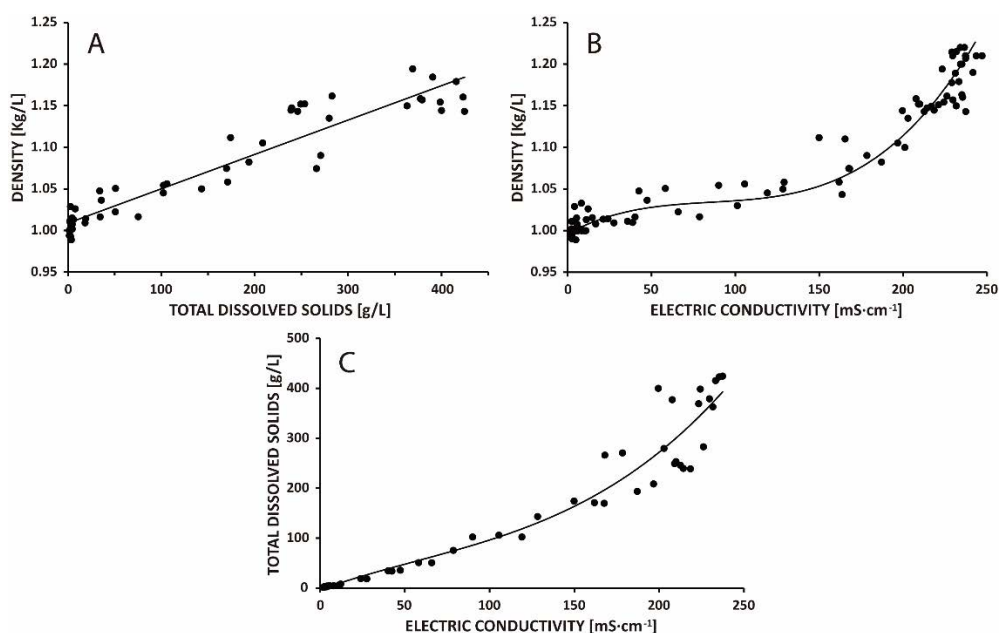
Figure 2.3. *A) Correlation between total dissolved solids (TDS) and density; B) correlation between electrical conductivity (EC) and density; and C) correlation between electrical conductivity and TDS. The black line shows the best-fit curve for both correlations.*

To increase the number of available data points, correlations between density, EC and TDS were obtained (Fig. 2.3). Their magnitudes show a clear mutual correlation (Kohfahl et al., 2015) and provide a practical technique with which to map the interface. For EC measurements, it is necessary to apply a correction for temperature (T) (Hayashi, 2004) of approximately 2%/°C, if it is not automatically done when EC

and T are measured. The EC correction and probe calibration errors may also explain part of the dispersion. The correlation between density and EC is not linear and follows a more complex polynomial line. The correlation between TDS and EC shows linear behaviour up to 100 mS·cm⁻¹, similar to other brines (Jellison et al., 1999); however, for higher EC values, the correlation is nonlinear, which will increase dispersion if a polynomial relationship is not applied.

2.2.5. Darcy´s law, head and pressure formulation in variable-density flow

Calculating flow directions and flow rates is the basic goal of almost all hydrogeological studies. These values can be obtained using Darcy's law. In the case of variable density, the Darcy's law in terms of water pressure is (Bear, 1972):

$$\mathbf{q} = -\frac{\mathbf{k}}{\mu}(\nabla P + \rho g \nabla z) \tag{2.1}$$

Where $\mathbf{k}$ is the intrinsic permeability tensor, μ is the fluid viscosity, P is the pressure, ρ is the fluid density and g is the gravitational acceleration and ∇z denotes the vertical upward direction. The spatial components of $\mathbf{q}$ are:

$$\mathbf{q_x} = -\frac{k}{\mu}\frac{\partial P}{\partial x} \tag{2.2}$$

$$\mathbf{q_y} = -\frac{k}{\mu}\frac{\partial P}{\partial y} \tag{2.3}$$

$$\mathbf{q_z} = -\frac{k}{\mu}\left(\frac{\partial P}{\partial z} + \rho g\right) \tag{2.4}$$

The horizontal flow components, $\mathbf{q_x}$ and $\mathbf{q_y}$, can be calculated based on the corresponding horizontal components of the pressure gradients or from the head gradients referring to the same water density.

For vertical flow, $\mathbf{q_z}$, there is a buoyant term associated with the gravity vector, which does not appear in the horizontal directions.

2.2.6. Numerical approach

A variable-density flow pattern is the result of strongly coupled flow and mass transport differential equations. Flow in porous media can be described using the following water mass conservation differential equation:

$$S_s \frac{\partial h}{\partial t} + \nabla \cdot \mathbf{q} = 0 \qquad (2.5)$$

Where S_s is the specific storage, and t is the time.

Neglecting all density dependencies in the balance terms except for the buoyancy term (the Oberbeck-Boussinesq approximation), $\mathbf{q}$ is given by the following expression in terms of water heads:

$$\mathbf{q} = -\frac{\mathbf{k}\rho_0 g}{\mu} \frac{\mu_0}{\mu} \left(\nabla h + \frac{\rho - \rho_0}{\rho_0} \nabla z \right) \qquad (2.6)$$

Note that ∇z is multiplied by the density ratio in which ρ_0 is the reference water density. The viscosity relation function, where μ_0 is the reference fluid viscosity, may be neglected in viscosity constant models.

Salt transport can be described using the differential equation:

$$\phi \frac{\partial C}{\partial t} + \mathbf{q} \cdot \nabla C + \nabla \cdot (-\mathbf{D}\nabla C) = 0 \qquad (2.7)$$

Where porosity is ϕ, solute concentration is C, and the hydrodynamic dispersion tensor is $\mathbf{D}$.

The code FEFLOW was used to solve this set of coupled governing equations. More information about the formulation and performance of this code can be found in Diersch (2014).

2.3. Results

2.3.1. 3D mapping of the freshwater-brine mixing zone

The central axis of the mixing zone at the surface was identified through the use of satellite images (Fig. 2.4). This axis coincides with wetlands and small, easily recognizable seasonal lagoons (Tejeda et al., 2003).

The three-dimensional mapping of the main mixing zone was performed by identifying the position of its central surface (EC = 150 mS·cm⁻¹), upper surface (EC = 100 mS·cm⁻¹) and lower surface (EC = 200 mS·cm⁻¹). These surfaces are used to delineate the main mixing zone, which is the region in which the salinity gradient changes most rapidly. The given limits do not represent the extreme EC values corresponding to brine and freshwater. Values between 200 and 240 mS·cm⁻¹ are only

reached in the central area of the nucleus, and values of less than a few mS·cm⁻¹ are reached in the recharge areas.
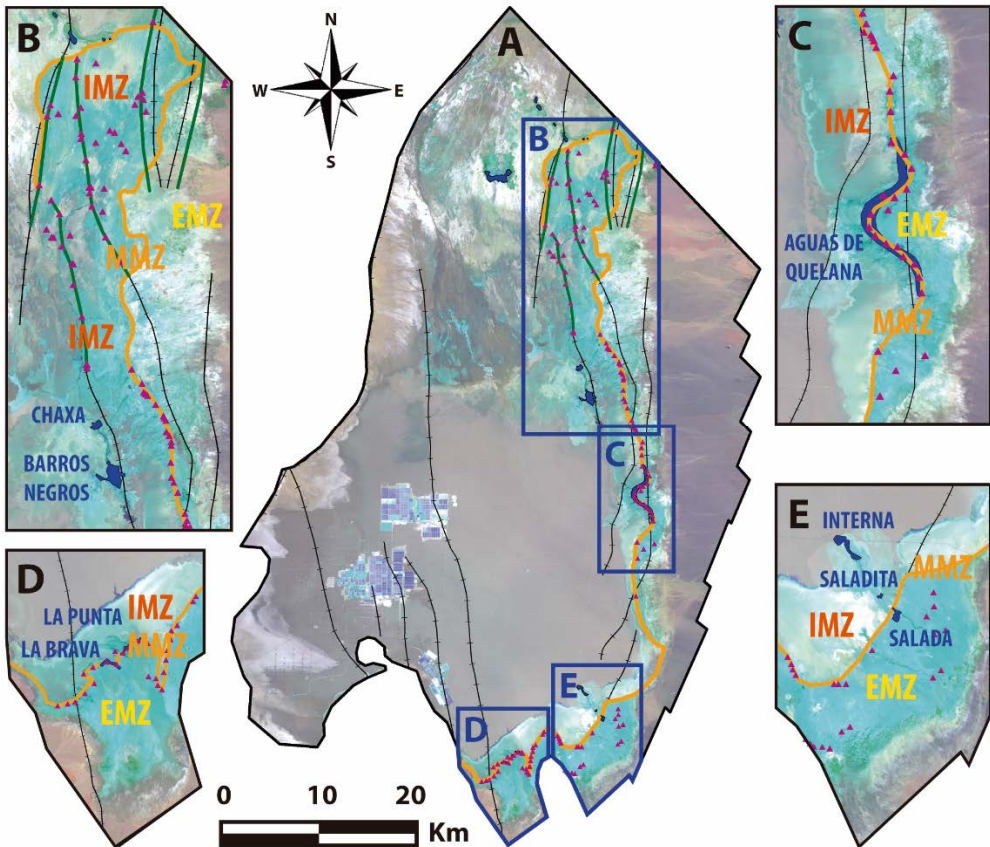
Figure 2.4. *Surficial mixing zone mapping of the SdA. A) General mixing zone framework. The orange line is the middle mixing zone (MMZ); the purple triangles are springs; the black lines with small cross lines are the faults described by Universidad de Chile (2016), and the green lines are the proposed extensions of these faults, which coincide with numerous springs in the IMZ. The dark blue rectangles show the positions of figures B, C, D and E. B) Mixing zone of the north and Soncor lagoon systems; it highlights the structural controls (faults and fractures) on the springs; words in red, orange and yellow indicate the internal (IMZ), middle (MMZ) and external (EMZ) mixing zones, respectively. C) Eastern area of the surficial mixing zone, with the Aguas de Quelana lagoon system. D) Mixing zone of the southeast area of Peine (Salada, Saladita and Interna lagoons). E) Mixing zone of the southwestern area of Tilopozo (La Brava and La Punta lagoons).*

The position of the mixing zone was deduced based on the density data measured or calculated in each piezometer. Using nests of wells, where each one is open at a different depth, allows the more faithful characterization of the geometry of the

19

mixing zone. Nevertheless, considering the particular characteristics of each monitoring point, the majority of these sites could be used to produce valuable information.

The SdA mixing zone mainly extends throughout the Northeast, East and Southeast salt flat margins (Figs. 2.5 and 2.6). The full range of densities present in the mixing zone can be observed on the land surface. The surficial densities closest to 1.23 kg/L were measured in the salt flat nucleus, while the densities closest to 1 kg/L were measured in the external mixing zone and the recharge zone. The mixing zone shows a moderate slope in the IMZ (internal mixing zone), strong deepening in the MMZ (middle mixing zone) and a gradual slope reduction in the EMZ (external mixing zone) and recharge areas. The external limits have been defined as far away as possible, as monitoring wells are very scarce. It is expected that the interface will extend beyond these limits but that it will have a low slope.
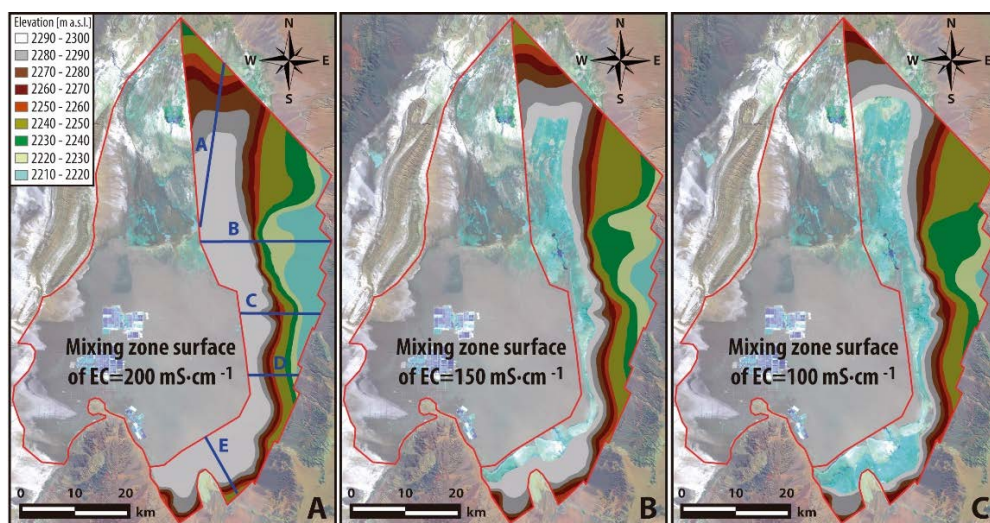
Figure 2.5. Three-dimensional mapping of the mixing-zone control surfaces. A) Surface of 200 mS·cm^{-1}. B) Surface of 150 mS·cm^{-1}. C) Surface of 100 mS·cm^{-1}. The blue lines show the locations of the cross-sections in Fig. 2.6.
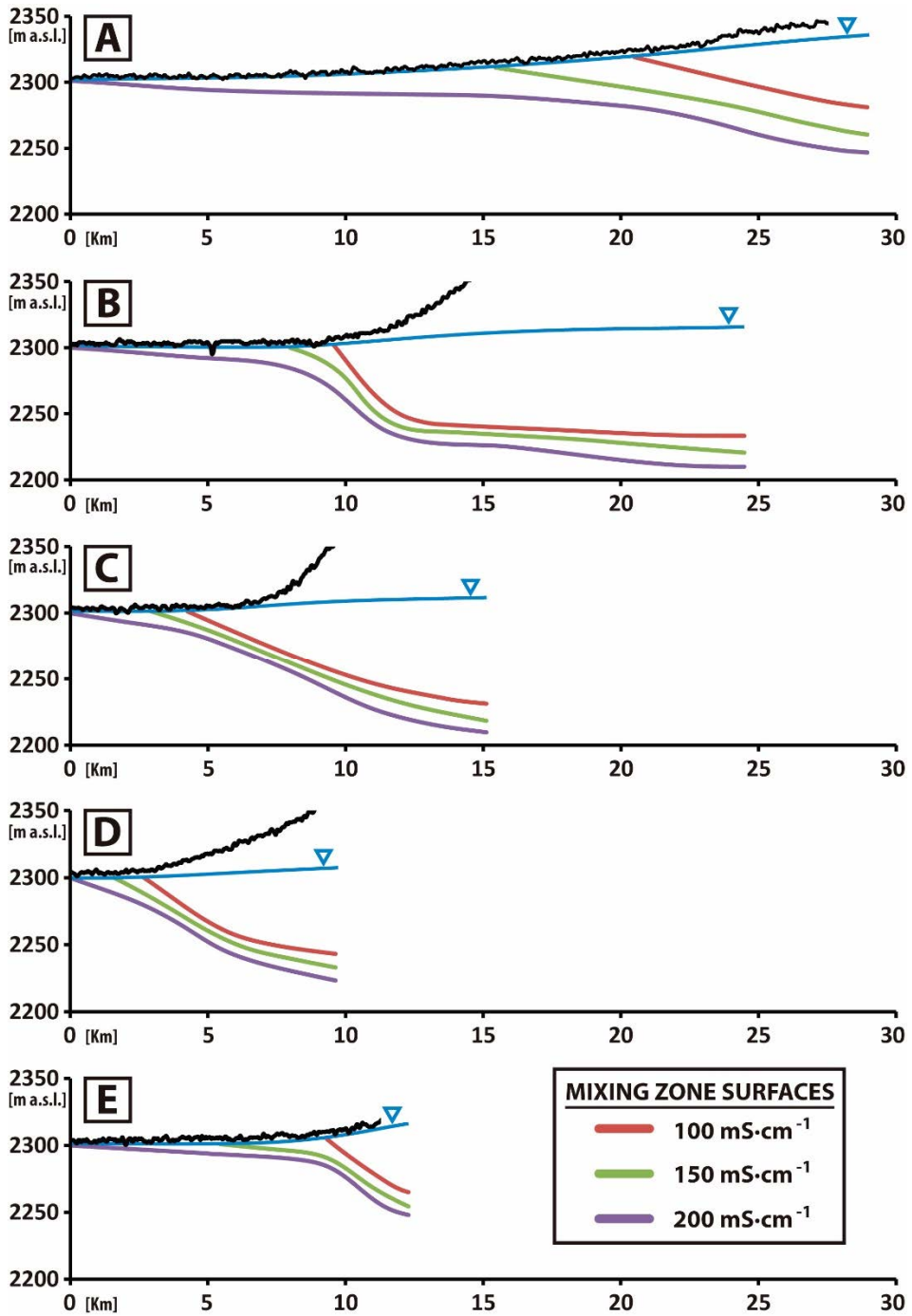
Figure 2.6. *Cross-sections of the mixing zone. In figures B, C and D the upper vertical scale has been limited to 2350 m a.s.l. for enhanced clarity. The locations of the profiles are shown in Fig. 2.5. The black line corresponds to the topography, and the blue line corresponds to the water table.*

2.3.2. 2D numerical model of the Salar de Atacama mixing zone

An idealized vertical profile 2D numerical model was carried out to use it as a tool to understand the geometry of the mixing zone. Although great local heterogeneity has been described in the Salar de Atacama (Muñoz-Pardo and Ortiz-Astete, 2004; Ortiz et al., 2014; Salas et al., 2010), only three simplified layers have been considered for the idealized regional model (Fig. 2.7). These layers attempt to represent the regional aquifer-aquitard-aquifer sequence that has often been identified in both the salt flat nucleus and the alluvial fans. As shown in the pumping tests done in the region, the hydraulic contrast between these three units (aquifer A, aquitard AB and aquifer B) is conspicuous and spatially continuous, but the hydraulic conductivity values may vary due to heterogeneities and karstification (IDAEA-CSIC, 2017).
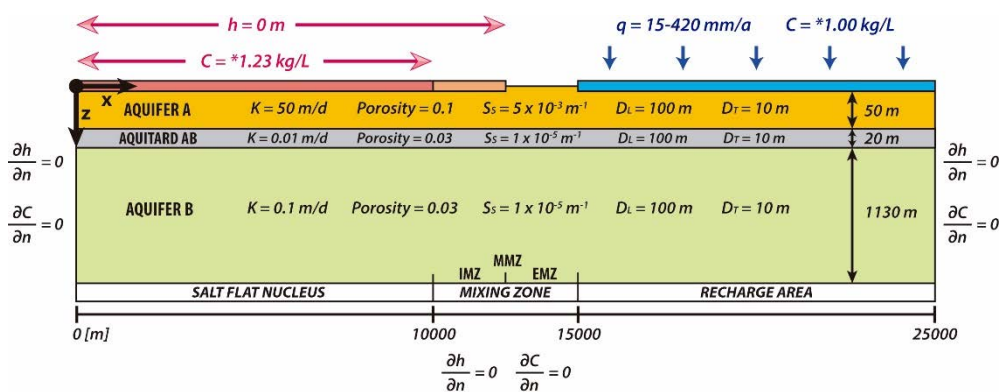
Figure 2.7. *Geometry, boundary conditions and hydraulic properties used in the two-dimensional numerical model. The boundary conditions are shown in blue for the recharge area and in red and orange for the evaporation area. DL and DT are the longitudinal and transversal dispersivities, respectively. The hydraulic conductivity (K) of the aquifer A was modified during the sensitivity analysis described in the text. The concentration values (*) were normalized to the density value.*

The model domain represents an idealized vertical cross-section that is 25,000 m long and 1,200 m high (Fig. 2.7). The length is the characteristic of any section of the eastern mixing zone, including 10,000 m of nucleus, 5,000 m of mixing zone and 10,000 m of alluvial fans. The thickness chosen corresponds to the thickness of the nucleus (Vilama Formation) in the eastern area (Jordan et al., 2007). The right boundary is the contact between the basement rocks and alluvial fans that may be considered impermeable in a simplification because the water that falls in the

mountains (volcanic rocks and basement of low permeability) reaches the alluvial fans largely superficially, where it infiltrates due to their greater permeability; the left boundary is located inside the salt flat, similar to other models (Duffy and Al-Hassan, 1988; Fan et al., 1997; Hamann et al., 2015); the lower boundary is located at the bottom of the geological unit B; and the upper boundary is the water table. Aquifers are modelled as confined aquifers (with constant transmissivity) because the water table variations are very small compared to the aquifer thickness due to the very low hydraulic gradients. The model mesh has approximately 153,000 triangular elements.

To model the salt flats, two main methodologies are used, depending on the objective for which the model is constructed. To study the geochemistry or detailed evaporation processes of the salt flat, reactive transport models can be carried out that include evaporation and dissolution using well-established saturation indices (Hamann et al., 2015; Vásquez et al., 2013). However, this coupling requires extremely high calculation times even for idealized problems (Hamann et al., 2015); thus, techniques are often used that simplify the problem numerically without altering the geometry of the resulting mixing zone (Duffy and Al-Hassan, 1988; Fan et al., 1997). In this way, it is possible to limit the maximum density without needing to precipitate salts based on saturation indices.

Following these guidelines, the left, lower and right boundaries are treated as no-flow zones for water and mass (i.e., Neumann-type boundary conditions).

At the top, different boundary conditions are selected for each spatial stretch with the purpose of representing the evaporation and recharge processes. The reference values of recharge were taken from IDAEA-CSIC (2017). The recharge, considering the total length (36.25 km) from the distal alluvial fans to the watershed line, ranges from 20 to 140 mm/yr, respectively. If a detention of 25 % is considered, then the net recharge rate ranges from 15 to 105 mm/yr. But in our simplified model we only considered 10 km of the total recharge length. By this motive, a fluid inflow (Neumann-type boundary condition) was fixed on the recharge surface, with a minimum value of 15 mm/yr in the contact between the mixing zone and the alluvial fans and a maximum value of 420 mm/yr (an unrealistic recharge rate that allows the model to enter the total recharge volume) in the contact between the alluvial fans and the basement. As in previous models (Duffy and Al-Hassan, 1988; Fan et al., 1997)

the recharge was applied on the top to not condition the mixing zone in the right boundary. This takes advantage of a large part of the water recharged in the mountains infiltrates the alluvial fans. A water head (Dirichlet) was fixed in the halite nucleus and the internal mixing zone.

For mass transport, fixed solute concentration of 1.23 kg/L for the salt flat nucleus and 1.00 kg/L for the freshwater recharge area were implemented. Concentrations were normalized to the densities of freshwater and brine as end members.

The upwinding option for the numerical treatment has been used to smoothen out steep concentration changes, although this causes some additional numerical dispersivity.

A stationary simulation was carried out to obtain the initial water heads. For the initial mass condition, a concentration of 1.00 kg/L was assigned, corresponding to a hypothetical initial scenario where all groundwater is fresh. The model was run for several thousands of years, with a semiautomatic time-step control, to reach a quasi-stationary state. The hydraulic parameters deduced from pumping tests, or in some cases from the literature (IDAEA-CSIC, 2017), are given in Fig. 2.7.
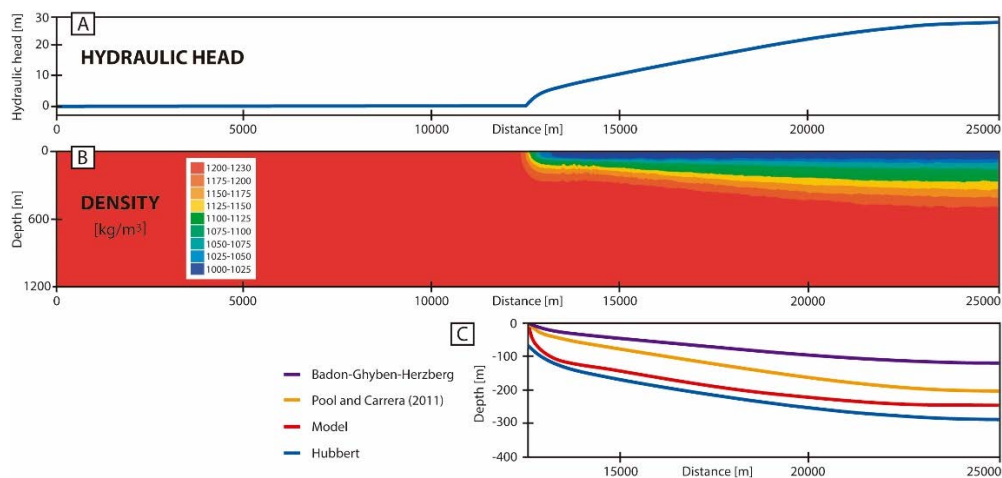
Figure 2.8. Results of the idealized 2D numerical model. A) Computed hydraulic heads of the top boundary, relative to the mean altitude of the nucleus. B) Resulting densities. C) Comparison between the modelled mixing zone and the three main analytical solutions for the mixing zone in homogeneous coastal aquifers: Badon-Ghyben-Herzberg (BGH), Hubbert, and Pool and Carrera (2011). The vertical scale was exaggerated by a factor of three.

The results are shown in Fig. 2.8. The geometry of the mixing zone in accordance with the 2D numerical model and the 3D mapping presents a very small slope which allows it to penetrate through all of the alluvial fans. Only in the first section (between the nucleus and the alluvial fans) is the interface slope greater. This type of mixing zone corresponds to arid and high-permeability salt flats, in accordance with the case 4 described by Duffy and Al-Hassan (1988).

2.3.2.1. Comparison with analytic solutions for the sharp interface in coastal aquifers

A comparison of the results of the model with the most commonly used analytical solutions in coastal aquifers is made below.

In the case of a sharp interface, the freshwater and saltwater pressures must be equal at the interface. The Badon-Ghyben-Herzberg (BGH) principle (Custodio and Bruggeman, 1987; Custodio and Llamas, 1976) establishes that in a homogeneous coastal aquifer, the depth of the interface below sea level ξ is given as $\xi = \alpha h_f$, in which h_f is the freshwater head and α is the inverse of the relative density difference: $\alpha = \rho_f/(\rho_s - \rho_f)$ where ρ_s and ρ_f are the densities of saline water and freshwater, respectively. It is assumed that the freshwater flow is horizontal and that the saline water flow is steady and equal to that of the saline water body. For coastal aquifers, the most frequent value of α is 40. For the Salar de Atacama brine, the value of α is 4.35. As vertical flows and the true brine head are not taken into account in the BGH principle, the predicted depth is generally too shallow, and it does not occur inside the actual mixing zone. Therefore, in most cases, the BGH formula is not a good predictor of the mixing zone depth.

If the actual head of salt water is considered, the Hubbert (Hubbert, 1940) formula is used:

$$\xi = \alpha h_f - (1 + \alpha)h_s \tag{2.8}$$

where h_f and h_s are theoretically measured on the interface. In practice, they are assumed to be equal to the freshwater and saline water heads measured in the point monitoring wells on the vertical axis of the site considered or near it. Thus, vertical components are ignored, which introduces an error. The closer the well screens are

25

to the mixing zone, the more the predicted position generally falls inside or closer to the position of the mixing zone.

Pool and Carrera (2011) proposed an empirical improvement of the BGH principle for coastal aquifers in which $\epsilon = 1/\alpha = (\rho_s - \rho_f)/\rho_f$ is changed to $\epsilon^* = \epsilon[1 - (\alpha_T/b')^{1/6}]$, in which α_T = transversal dispersivity and, b' = depth below sea level of the aquifer bottom, which is assumed to be horizontal. They rewrote the BGH approximation to the interface depth as $\xi = h_f/\epsilon^*$.

None of these predictions take into account the effect of layering, which is very important in the case described here.

In the case study, the sharp BGH interface is always situated well above the mean mixing zone surface (1.115 kg/L) (Fig. 2.8). The sharp interface resulting from the Pool and Carrera (2011) approximation shows a better fit of the mixing zone. The Hubert interface best fits the results of the numerical model, although it requires a greater number of hydraulic head data for its calculation, which hinders its practical applicability.

2.4. Discussion

2.4.1. Water head corrections by contrast densities in salt flats

In the case of SdA, only a few potentiometric surface mappings were completed in previous studies. Moreover, only some simplified three-dimensional numerical modelling has been performed, none of which was at the regional scale and they often neglected the effects of density. Muñoz-Pardo and Ortiz-Astete (2004) performed a 3D numerical model of the nucleus and marginal zone of the SdA by neglecting density effects, although they recognized a range of densities between 0.99 and 1.22 kg/L. Ortiz et al. (2014) also showed a potentiometric surface mapping of the Soncor lagoons system without taking density effects into account. Salas et al. (2010) were the only authors to consider the effects of density although they did not explain the followed methodology. In that study, the flow path lines did not describe the expected behaviour of a natural freshwater-brine mixing zone because at the time of that study the brine pumps had already depressed the water table in the nucleus.

Establishing the direction and sense of the water flow directly from the water head data measured in piezometers and wells with waters of different salinities is often erroneous. This error may be very important if the contrast in densities is as important as it is in the SdA. Thus, all water head measurements have been transformed to the same reference density, and these were subsequently used following the rules of considering consider buoyancy effects.

In the case of salt flats, especially in the nucleus, marginal zone and its surroundings areas, the dominant flow component is vertical, unlike that in coastal aquifers. Therefore, it is essential to apply a correction allowing for the most faithful reproduction possible of the vertical flow near the mixing zone. If the density dependence of the flow is neglected, the predicted flow path lines have their origin in the mountains and end in the salt flat nucleus (Fig. 2.9A). This contrasts with a general observation in which groundwater discharge and wetlands occur at the margins of the salt flats (Fig. 2.9B). However, taking into account the effects of density on flow in three-dimensional complex numerical modelling is almost impossible because of the high degree of computational power that is required.

An interesting solution would be to apply a density-correction methodology similar to that applied to coastal aquifers (Lusczynski, 1961) to transform saltwater heads into freshwater heads. The results obtained using this methodology indicate that the lagoons are in the regional minimum water head and that they represent the main discharge area, similar to the actual case (Fig. 2.9C). Nevertheless, in contrast to coastal aquifers, the focus of interest and the highest numbers of observation points in salt flats are in the nucleus and the mixing zone but not in the freshwater zone (recharge area). For this reason, it is much more useful to develop a solution that allows for the correction of the water heads by transforming freshwater heads into brine heads.

The following procedure is adopted for the water head correction depending on the characteristics and available information obtained from piezometers or wells. Four study cases have been established: point wells with an EC profile, long-screened wells with an EC profile, point wells without an EC profile, and long-screened wells without an EC profile.
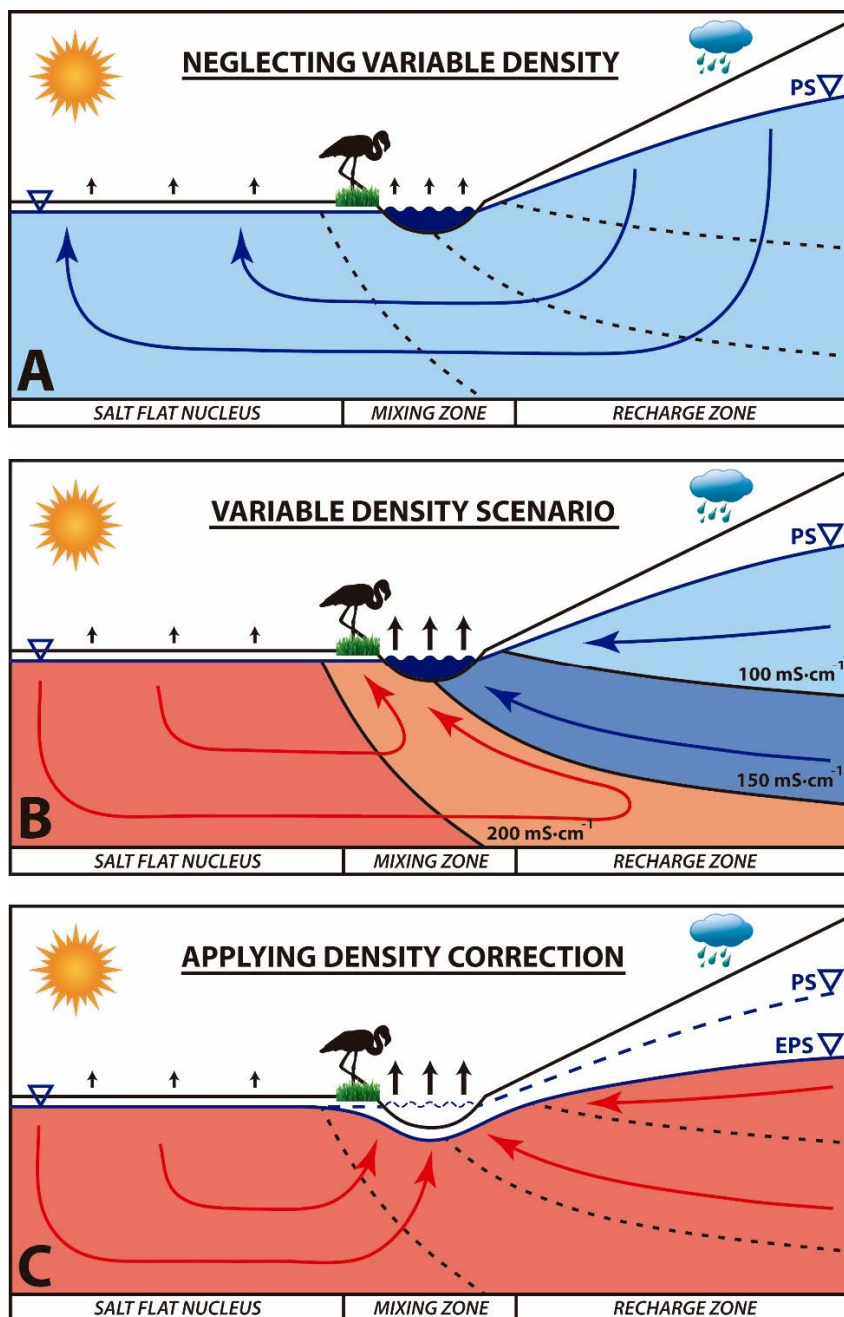
Figure 2.9. *A) Flow dynamics if density variations in groundwater are totally neglected. B) Actual situation of the surficial mixing zone, with freshwater (light blue), brine (dark orange) and intermediate water (dark blue and light orange colours). C) Flow dynamics if density corrections to the potentiometric surface are applied. The mixing zone lagoons at the minimum regional water head clearly stand out. PS is the potentiometric surface and EPS is the corrected potentiometric surface.*

The point wells, slotted only in a very short stretch, in which an EC profile was available have been corrected by taking the vertical density distribution into account using the equation:

$$h_c = h_i + \int_{z_0}^{z_2} z \frac{\rho - \rho_0}{\rho_0} dz \qquad (2.9)$$

where h_c is the corrected water head, h_i is the measured water head, z is the saturated well thickness, z_0 is the origin of the water depths of the well, z_2 is the depth corresponding to an EC of 200 mS·cm⁻¹, ρ is the density measured at each point and ρ_0 is the reference density. In the case of SdA, the reference density is 1.23 kg/L.

The long-screened wells with an EC profile were corrected using the same criteria. A unitary correction for each stretch of the vertical profile may be performed by obtaining the vertical distribution of the water heads.

The point wells in which an EC profile was not available were corrected assuming that the slotted density was homogeneous throughout the entire well. In this case, the previous equation is simplified to:

$$h_c = h_i + z \frac{\rho - \rho_0}{\rho_0} \qquad (2.10)$$

The long-screened wells without an EC profile were corrected by assuming the density distribution of the reference EC/density surfaces obtained in the regional mixing zone mapping (Fig. 2.10). To apply the correction in each piezometer, three stretches are considered inside these monitoring wells: 1) the thickness of the water layer below the surface of 200 mS·cm⁻¹, 2) the thickness between the surfaces of 200 mS·cm⁻¹ and 100 mS·cm⁻¹, with a reference surface of 150 mS·cm⁻¹, and 3) the thickness between the surface of 100 mS·cm⁻¹; and the water table. The first stretch is not corrected because it is considered to be practically brine. The correction of the second stretch is performed based on the thickness of the mixing zone between the surfaces of 200 mS·cm⁻¹ and 100 mS·cm⁻¹ and their average density. Finally, the correction in the third stretch is made by taking into account a linear gradient between the existing density in the surface of 100 mS·cm⁻¹ and the density measured in the upper water of that observation point:

$$h_c = h_i + (z_1 - z_0) \frac{\rho_{01} - \rho_0}{\rho_0} + (z_2 - z_1) \frac{\rho_{12} - \rho_0}{\rho_0} \qquad (2.11)$$

Where z_1 is the depth corresponding to the 100 mS·cm^{-1} surface, ρ_{01} is the average density between z_0 and z_1, and ρ_{12} is the average density between z_1 and z_2. In the monitoring wells where the third stretch does not exist (when the internal mixing zone is close to the land surface), the correction is made by applying the density value measured at the surface to the entire freshwater column.
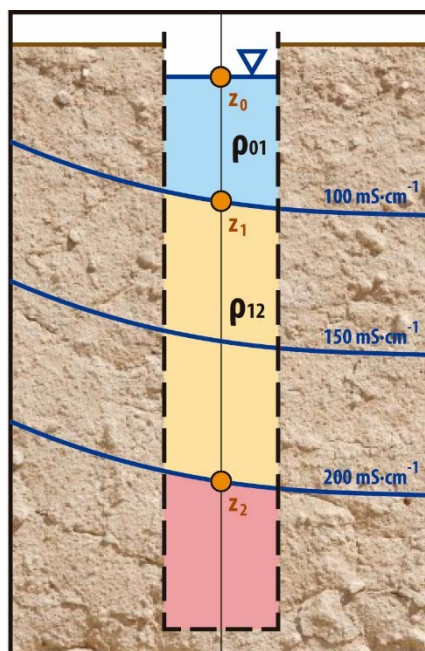
Figure 2.10. *Schematic of a long-screened well in which the reference surfaces utilized to carry out the correction by density contrast are shown. In the case of point wells, the situation would be similar, but the internal density surfaces would not agree with the surfaces of the mixing-zone regional mapping.*

In this case, the corrected water head may be slightly underestimated by not correcting from 200 mS·cm^{-1} to 240 mS·cm^{-1}. However, it is very difficult to map the surface of 240 mS·cm^{-1} (with a density of 1.23 kg/L), as it is only attained in some areas of the salt flat nucleus. The mixing zone stretch in which the density/EC values change faster is between 100 and 200 mS·cm^{-1}. Farther from these surfaces, these changes are slow, diffuse and too complex to be identified.

2.4.2. Mixing zone hydrodynamics

In the quasi-stationary stage (Fig. 2.8), the effects of variable density allow us to differentiate five sectors with very different hydraulic behaviours, namely, the

nucleus, internal mixing zone (IMZ), middle mixing zone (MMZ), external mixing zone (EMZ), and recharge zone. The hydrodynamics in the nucleus are controlled by convection cells that are continuously evolving. Triggered by the evaporation of brine in the surface, these convection cells become denser, collapse, and cause the upward movement of less-dense brine. The presence of low permeability layers, such as the intermediate aquitard AB, produce a vertical break in the convection cells. The lateral convection cell, which is closest to the mixing zone, is the engine of the upward flow in the IMZ, where a mixture with freshwater is produced causing the eastern part of the nucleus to have densities slightly lower than the western and middle zone (Fig. 2.2). In contrast, the recharge zone is primarily characterized by a downward flow of freshwater that gradually rotates and points towards the nucleus until the mixing zone is reached, where the flow ascends parallel to the principal mixing-zone surface. Finally, this groundwater ascends with a relatively high velocity to the land surface in the EMZ and especially in the MMZ. In this way, the MMZ is the zone that clearly presents the highest flow rates because the MMZ is where the flows coming from the nucleus and the recharge water merge (Fig. 2.2). The MMZ thus constitutes the main outflow of the domain, returning part of this water to the more surficial zone of the IMZ.

It is expected that the saline mixing zone, at least in the upper aquifer, is in equilibrium with climatic oscillations, even those of relatively short cycles (e.g., ENSO). In contrast, at depth, these zones do not show visible direct responses to short-term oscillations, as they only reflect the effects of large time-scale cycles. Additionally, stormy events may cause local to regional disturbances in the upper mixing zone, especially in the internal mixing zone.

These hydrological dynamics are consistent with the hydrogeochemical differences observed by Boutt et al. (2016) between the samples collected in the IMZ and EMZ. They are also consistent with the hydraulic response to short-term and long-term variations in precipitation and recharge regimes in both zones, as observed in the abovementioned manuscript. In the IMZ, where the flow is slow and sometimes has short path lines, precipitation events give rise to a more evident water table response than in the EMZ, where the flow is higher and a precipitation event induces a very small or inappreciable effect.

Finally, a special case of mixing zone occurs in the northeastern marginal zone, just to the North of the Soncor lagoon system, where numerous springs have been mapped (Fig. 2.4). The waters that come out of these springs drain to the Burro Muerto channel and finally to the Soncor lagoon system. If the mixing zone geometry of this zone (Figs. 2.4 and 2.5) is compared with those of the previously described southeastern and central-eastern areas, a large plateau can be seen, with its long axis approximately oriented in the N-S direction. Unlike the rest of the marginal zone, where the lagoons tend to be located along the central axis of the middle mixing zone (MMZ), in the Soncor system the mapped springs are not only located along this axis but also located in the internal mixing zone (IMZ). Furthermore, it should be noted that the mixing zone is always located around the salt flat nucleus, except in this area where the mixing zone moves northward and becomes much more gradual. The arrangement of these springs coincides with some of the structural planes described by Universidad de Chile (2016) or their extensions (Fig. 2.4B). There is a lowering of the hydraulic head along the permeable fault planes and an uprising of somewhat deeper freshwater flows that partially feed the springs. This could explain the very low water head gradients, the shallow water table and some of the hydro-chemical anomalies described by other authors (Ortiz et al., 2014).

2.4.3. Influence of heterogeneity on mixing zone geometry

Through the 3D mapping of the mixing zone, important variations in the depth of the mixing zone have been observed along the entire eastern margin of the salt flat. Although different sensitivity analyses have been carried out, both for recharge and for hydraulic conductivity, the hydraulic conductivity of the upper aquifer is the one that shows the greatest sensitivity to the regional geometry of the saline interface. If the recharge varies within a coherent range (for example, by doubling or reducing it by half), the changes produced are very small. In this section we analyse the effects that the high-permeability layers in the top and the aquitards have on the geometry of the mixing zone.

To study the effect of a high-permeability layer on the upper part of the system, the regional 2D vertical model is used as a basis. The hydraulic conductivity values of the AB aquitard and the B aquifer were both set at 0.1 m/d to prevent further factors from coming into play. The hydraulic conductivity of the upper aquifer varied: 0.1 m/d (homogeneous case), 1 m/d, 10 m/d, and 100 m/d. These values are

commonly found in the upper aquifer of the mixing zone and in the alluvial fans of the Salar de Atacama.

The results of the sensitivity analysis show that the higher the permeability of the upper aquifer is, the lower the slope is and the shallower the mixing zone becomes (Fig. 2.11). This occurs because the lateral-recharge freshwater flows almost entirely through this layer when there is an upper layer of very high permeability. In the lower layers, the recharge water almost does not penetrate, thus favouring the rise of the mixing zone and notably reducing its slope (Figs. 2.11C and D). On the other hand, when the aquifer is homogeneous, there is no preferential flow through the upper layer; thus the deep freshwater is able to maintain a higher head, thus repelling the mixing zone, reducing saltwater intrusions and moving it towards the salt flat (Figs. 2.11A and B). In the homogeneous case the largest slope of the interface is reached.
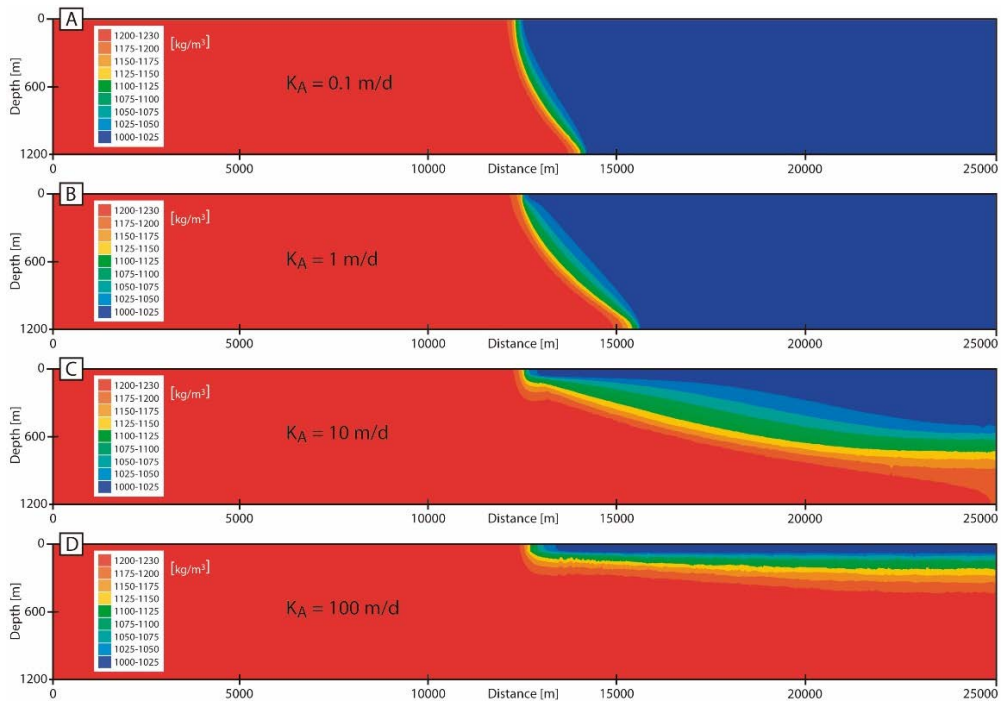
Figure 2.11. *Sensitivity analysis of the hydraulic conductivity of the upper aquifer. A) 0.1 m³/d (homogenous case). B) 1 m³/d. C) 10 m³/d. D) 100 m³/d. The vertical scale was exaggerated by a factor of three.*

The hydraulic conductivity of the upper layers greatly influences the geometry of the regional saline interface. This explains the low slope and great intrusion of the mixing zone in the Salar de Atacama, unlike in previous works (Tejeda et al., 2003; Vásquez et al., 2013), where the mixing zone did not penetrate the alluvial fans and had a much higher slope. All of these studies considered a homogenous porous medium without a high-permeability top layer. Additionally, theoretical works (Fan et al., 1997; Hamann et al., 2015; Holzbecher, 2005) always addressed a homogenous case of study. Only Fan et al. (1997) made a first approximation of the effect of heterogeneity in the mixing zone by taking into account a more realistic geology, however these authors focused their efforts on explaining the free convection differences between both cases and did not focus on the geometry of the mixing zone.

The presence of aquitards can also modify the position of the mixing zone. This is because the aquitard further hinders the flow of groundwater through the deeper layers and forces the flow through the upper aquifer at up flow areas. Thus, the relative deepening and reduced thickness of the mixing zone may be observed.

The effects described above may explain the most abrupt deepening of the mixing zone observed in the central-eastern area (East of Soncor) of the Salar de Atacama (Figs. 2.5 and 2.6B). Near this zone, some studies (Cornellà et al., 2009; Ortiz et al., 2014) have described several less-permeable layers at different levels.

2.5. Conclusions

The two (2D) and three-dimensional (3D) geometry and hydrodynamics of the salt flat freshwater-brine mixing zone were studied, using the Salar de Atacama as case study.

The three-dimensional mapping of the actual mixing zone was carried out for the first time in a salt flat, showing the irregularities of the mixing zone in both the vertical and horizontal directions.

Using the 3D mixing zone mapping data, the application of a water head correction to the freshwater and mixed water heads in order to compensate for density variations and transform them into brine water heads was proposed to reduce the computational cost of the 3D regional models of salt flats. By applying

this methodology, it was possible to reproduce the vertical fluxes in the lagoons and wetlands, which are located in the minimum regional piezometric area.

An idealized two-dimensional model of a vertical cross-section in the Salar de Atacama general structure was carried out to reproduce the mixing zone at a regional scale and to evaluate how heterogeneity affects the mixing zone geometry. The higher the permeability of the upper aquifer is, the lower the slope is and the shallower the mixing zone becomes. This occurs because the freshwater that is recharged is forced to flow through the upper aquifer and thus have a lower head at the mixing zone. Thus, hydraulic conductivity of the upper aquifer, generally constituted by karstified evaporites and alluvial deposits in the salt flats, is critical to the geometry of the resulting saline interface.

Chapter 3

Hydrodynamics of salt flat basins: The Salar de Atacama example

3.1. Introduction

Salt flats are saline and endorheic hydrogeological systems that are frequently associated with arid to hyperarid climates, in which the water table is several centimetres or decimetres below the ground surface. The largest salt flats in the world are on the Altiplano-Puna plateau of the Central Andean Range, which includes northwestern Argentina, southwestern Bolivia and north-eastern Chile (Risacher et al., 2003; Warren, 2010). The salt flats and their brines are a major source of lithium, boron, sodium chloride, iodine, potassium and magnesium (Evans, 1978; Kesler et al., 2012; Munk et al., 2016). Some of these elements are highly valued in the modern economy. For example, lithium is a main constituent in batteries for mobile phones, electric cars (Marom et al., 2011; Tarascon, 2010; Vikström et al., 2013) and even pharmacological treatments (Cipriani et al., 2005).

The Salar de Atacama (SdA) is the third largest salt flat in the world after the Salar de Uyuni (Bolivia) and Salinas Grandes (Argentina). Its brine contains a lithium concentration (~5,000 ppm) that is much higher than that of the other salt flats, and makes the SdA the main lithium reserve in the world. In addition, it is located in the most arid area of the Earth and houses exceptional ecosystems, such as the Reserva Nacional de los Flamencos (Ramsar site). These ecosystems are threatened because of the mining exploitation of the brine that has been occurring since the 1980s. In contrast, the brine pumping carried out have allowed to dispose of the best monitoring network in the world, which makes the SdA a reference for the scientific community.

The origin of the SdA dates to the Oligocene-Miocene boundary, synchronous with the increase in volcanic activity and Altiplano uplift (Arriagada et al., 2006). The uplift of the plateau marked the paleoclimatology history as a consequence of the strong topographic gradient reached, giving rise to a more humid plateau and a hyperarid salt flat (Rech et al., 2006). From this ancient time until the mid-1980s, the hydrodynamics of the system were controlled by the different climatic cycles. However, from the 1980s onward, the pumping of the brine for commercial purposes has altered its natural dynamics. Most of the studies that have been carried out in the SdA have analysed the current anthropogenic regime of the system (Salas et al., 2010), in which the water table of the salt flat has been drawn down. However, studies of the natural regime of the system, prior to exploitation, are lacking. Only

the water table contour map of the eastern alluvial fans performed by HARZA (1978) is available. Unfortunately, this work does not take density differences into account.

Under the natural regime, the water table depth of the SdA was determined by a complex balance between the water inputs and outputs that tended to be zero (Rosen, 1994; Yechieli and Wood, 2002). The main recharge was precipitation (rainfall) that occurred in the mountains of the basin. The evaporation was controlled by the water table depth, which was a few decimetres below ground (Kampf et al., 2005; Kampf and Tyler, 2006; Tyler et al., 2006). The salt deposits accumulated because of the strong evaporation rates that were maintained for several thousands of years (Corenthal et al., 2016; Hardie, 1991; Wood and Sanford, 1990). These complex systems tend to be very sensitive to climatic and anthropogenic changes (Godfrey et al., 2013).

Although progress has been made in the last few decades to understanding the hydrogeology of the SdA, there are still many uncertainties in the water balance, and no water balance has been validated with numerical models. Thus, some authors present divergences about key factors to calculate the flow discharge: water table depth, areas of discharge and evaporation rates. The first study that addressed evaporation in the SdA (Mardones, 1986) quantified the volume of evaporated water as 5.29 $m^3 \cdot s^{-1}$. Assuming that in the basin-scale balance the inputs (recharge) are equal to the outputs (evaporation), this value should correspond to the recharge value. Subsequent works used this value as a reference and, obtained water balances in the range of 5.17-5.58 $m^3 \cdot s^{-1}$ (Dirección General de Aguas, 2013, 2010, 1986; Muñoz-Pardo et al., 2004). Kampf and Tyler (2006) obtained values of evaporation in a range of 1.6-22.7 $m^3 \cdot s^{-1}$, depending on the multiple calculation methods that were applied, which were based on remote sensing and evaporation zoning. Recently, Corenthal et al. (2016) used an approximated value of recharge from Bookhagen and Strecker (2008), applied the recharge model of Houston (2006a) and obtained a net recharge of 0.9 $m^3 \cdot s^{-1}$ (26.5 $m^3 \cdot s^{-1}$ of rainfall with 3.5 % of infiltration). However, the same authors predicted that evaporation should have been 21.7 $m^3 \cdot s^{-1}$ to explain the amount of accumulated salts, and they proposed as a probable explanation that the estimated recharge deficit is compensated by contributions from the Altiplano outside the SdA basin. However, this approach is not consistent with the scarce presence of vegetation that would facilitate evapotranspiration and with the scarce evidence of surface runoff that would favour evaporation. If the evapotranspiration is very low and

surface runoff almost non-existent, the recharge rate to aquifers should be very high. Therefore, there is still great uncertainty regarding the values of recharge and evaporation in the basin of the SdA under the natural regime.

Numerical models constitute a powerful tool to justify and validate the water balance. The steady-state models offer a hydrogeological reference for the system around which the system will naturally oscillate. These models also serve as a basis to incorporate natural oscillations (e.g., cycles of evaporation, precipitation, etc.) and anthropogenic impacts (pumping and artificial recharge) in future transient-state models. However, determining the average water balance under the natural regime is not trivial and requires an analysis of a sufficiently large time interval that includes several dry and humid climatic cycles. In addition, three-dimensional (3D) numerical models represent a much more powerful tool than two-dimensional (2D) models as they allow to include recharge and evaporation processes within a geometry that faithfully reproduces the hydrostratigraphy of the basin in its three spatial components. This allows to quantify the total water balance at the basin scale.

The density contrast between the rainwater (freshwater) and the evaporated water (brine) results in a mixing zone (saline interface) that represents the dynamic equilibrium of both miscible fluids and has a strong influence on the groundwater flow (Marazuela et al., 2018) (Fig. 3.1). To date, only 2D models of the mixing zone have been published in scientific manuscripts (Duffy and Al-Hassan, 1988; Fan et al., 1997; Holzbecher, 2005; Marazuela et al., 2018; Tejeda et al., 2003; Vásquez et al., 2013; Wooding et al., 1997). To the best of our knowledge, 3D numerical models that integrate the complex recharge-evaporation interaction within a salt flat do not exist. Moreover, no detailed studies have been conducted to provide a numerical response on a regional scale to the role that is played by the mixing zone and its lakes in a salt flat system. The principal reason for this lack of specific studies is probably the high computational cost and the absence of methodologies to consider the effects of density variations. In the case of the SdA, regional models have neglected the effects of density on the flow (Anderson et al., 2002; Muñoz-Pardo et al., 2004), despite of the large density contrasts (1 to 1.23 kg·L^{-1}). To overcome this problem, Marazuela et al. (2018) proposed a methodology based on the correction of freshwater and mixed water heads by density variations in salt flats. This method allows the reproduction of the vertical flows that occur in the mixing zone at a low computational cost.
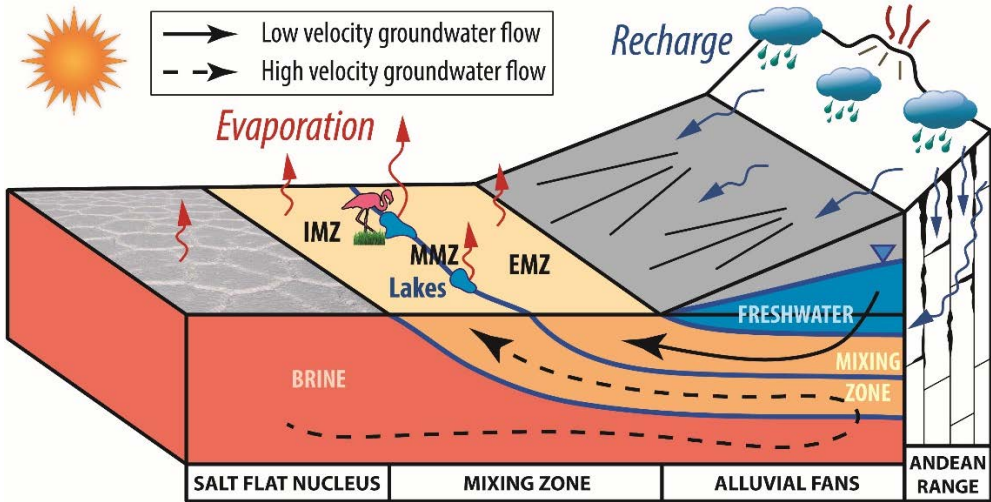
Figure 3.1. *Hydrodynamics of the mixing zone. IMZ - internal mixing zone; MMZ - middle mixing zone; EMZ - external mixing zone. Modified from Marazuela et al. (2018).*

The objective of this study is to characterize the hydrogeological behaviour of the SdA and to quantify its complex water balance, prior to brine exploitation, to establish a reference for the salt flats studies. To reach the objective, firstly, the hydrogeological conceptual model of the system is defined and quantified to subsequently proceed to its 3D numerical modelling, which allows to validate the estimated water balance and to determine its uncertainties. The recent methodology proposed by Marazuela et al. (2018) for 3D numerical modelling of salt flats that is based on the 3D mapping of the salt interface is used. This leads to a discussion about the recharge and hydrodynamics of the salt flat basins, and how the SdA basin can serve as a reference for the hydrogeological conceptualization of other salt flat basins and its 3D numerical modelling.

3.2. Materials and methods

The methodology followed in this work mixes experimental and numerical modelling techniques. First, it is performed a synthesis of the SdA location and its regional hydrodynamics, especially of its saline interface which was studied previously by Marazuela et al. (2018), and which serves as a basis for the correction of hydraulic heads by density variations applied in the 3D model of the present work. Second, the stratigraphy of the SdA focused on defining the geometry of the 3D

numerical model is addressed. Third, the obtaining of experimental data such as precipitation and evaporation data, as well as the collection of isotope values that are included in the basin recharge discussion, is addressed. Fourth, the modelling strategies that are proposed for the salt flats modelling and which can be applied in the future to other analogous systems are defined. Fifth, all the characteristics of the 3D numerical model and the calibration are described.

3.2.1. Study area

The SdA basin, with a north-south elongated shape, is between 23° and 24° S latitude and 68° and 69° W longitude (Fig. 3.2). To the east, it is enclosed by the main chain of the Andean Range (>5,500 m a.s.l., metres above sea level), while to the west, lies a secondary mountain range called the Cordillera de Domeyko. The salt flat, including the mixing zone, encompasses 3,000 km², and it is approximately 100 km in length and 50 km in width.

Four geomorphological zones from the depocenter to the watershed can be identified as follows: (1) salt flat nucleus; (2) mixing zone; (3) alluvial fans; and (4) volcanic and basement rocks (Figs. 3.1 and 3.2). The salt flat nucleus is mainly made up of halite and it has an elevation of approximately 2,300 m a.s.l., whose topography exhibits a high level of roughness because of evaporation and ephemeral surface water. The mixing zone comprises calcite, gypsum and halite (Boschetti et al., 2007; Pueyo et al., 2017; Vásquez et al., 2013). The alluvial fans and particularly the volcanic and basement rock reach the highest altitude and constitute the main recharge area of the basin.

The hydrographic network is rather sparse and consists of two rivers, some streams and lakes; most of the lakes are in the mixing zone. The main tributaries are the San Pedro and Vilama Rivers, which originate to the north of the basin. Streams descend from the highest mountains to disappear through infiltration in the highly permeable alluvial fans. The lakes are grouped into four systems, namely, Soncor, which is fed by the Burro Muerto channel, Aguas de Quelana, Peine and Tilopozo (Fig. 3.2). In addition, the Tebinquiche and the Cejar lakes can be distinguished in the northern part of the San Pedro alluvial fan. The lakes have an extent of no more than several hectares.
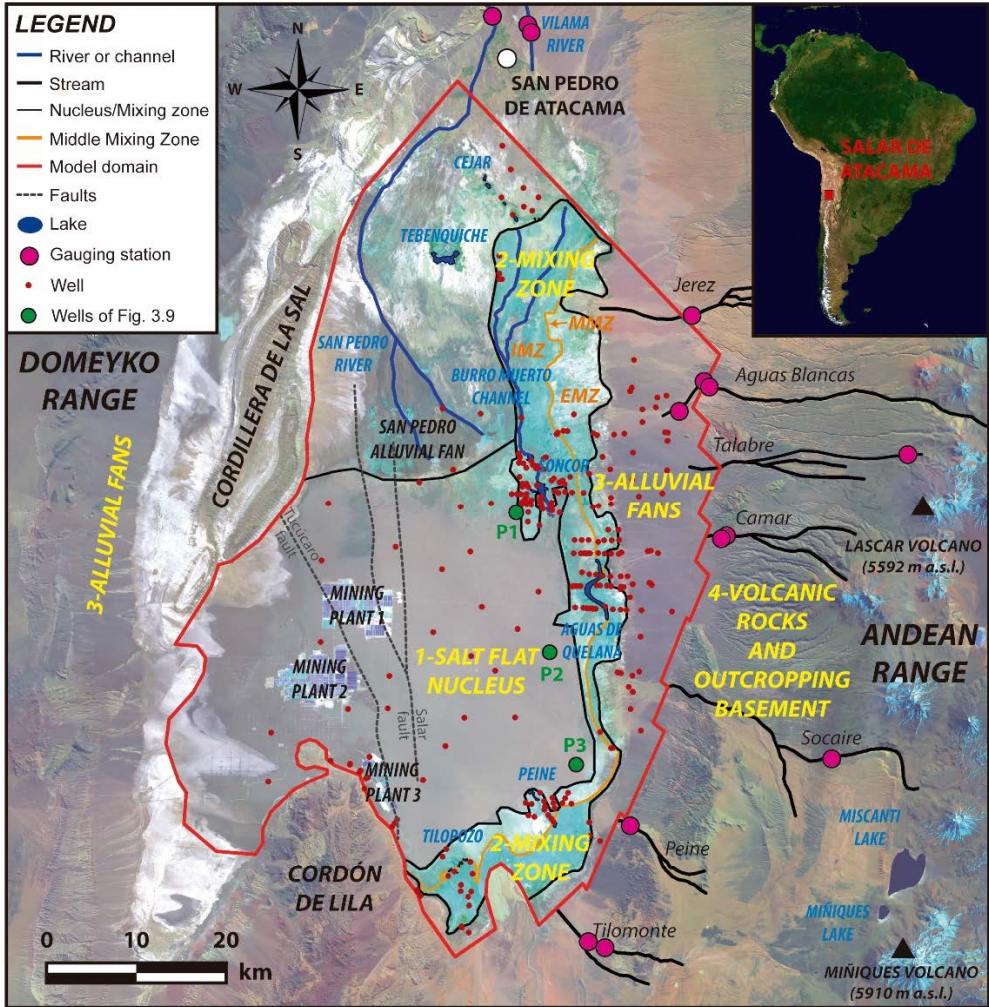
Figure 3.2. *Location of the SdA (LANDSAT 8, 27 September, 2016). The three sub-zones of the mixing zone are shown in orange lettering (internal, IMZ, middle, MMZ and external, EMZ).*

The exploitation of the brine is carried out in three plants constituted by evaporation pools, where the pumped brine is transported. The pumping wells associated with the mining plant 1, belonging to Albermale company, began in 1984 while those associated with mining plants 2 and 3, belonging to the Sociedad Química y Minera de Chile (SQM) company, began in 1994 and 1996, respectively.

3.2.2. Hydrogeology of the saline interface (mixing zone)

The density contrast between the recharged rainwater (freshwater) and the evaporated water (brine) results in a mixing zone (saline interface) that represents the dynamic equilibrium of both miscible fluids and has a strong influence on the groundwater flow (Marazuela et al., 2018) (Fig. 3.1). The brine that is evaporated in the salt flat nucleus sinks because of gravity. The sinking of the denser fluid causes the rise of less dense fluid. On the freshwater side of the mixing zone, the groundwater that originates from the recharge area (mountains) is forced to rise to the surface by the mixing zone because of its lower salinity. On the brine side of the mixing zone, the brine also rises to the surface and is pushed by a convection cell that is similar to the seawater intrusion process in coastal aquifers (Post and Werner, 2017; Werner et al., 2013). Through this mechanism, the main discharge occurs in the freshwater-brine mixing zone, where some lakes may appear, and the water table is very near the surface, which results in higher evaporation rates (Cornellà et al., 2009; Tejeda et al., 2003).

Marazuela et al. (2018) differentiate three zones within the mixing zone depending on its hydraulic characteristics: the internal mixing zone (IMZ) corresponds to the mixed water that is pushed by the marginal convection cell of the nucleus and the middle mixing zone (MMZ) and the external mixing zone (EMZ) are characterised by upward fluid flow from the mountains, with high and medium flow velocities, respectively (Fig. 3.1). This zoning is also evident on the surface, and the corresponding lakes and wetlands are in the MMZ (Fig. 3.2). The Los Flamencos National Reserve occupies the northeastern and eastern mixing zone associated with the upward groundwater flow that provides the water to the lakes and wetlands.

3.2.3. Stratigraphy of the Salar de Atacama

According to the lithological data of more than one thousand cores (IDAEA-CSIC, 2017; XTERRAE, 2011), with lengths that rang between less than 10 m and more than 200 m, six stratigraphic units can be distinguished in the salt flat nucleus as follows: (1) Unit A (Upper halite); (2) Unit AB (Upper gypsum with carbonates); (3) Unit B (Intermediate halite); (4) Unit C (Middle gypsums); (5) Unit D (Lower halite); and (6) Unit E (Clays) (Fig. 3.3). The three upper hydrogeological units are of paramount importance for mineral resources and ecological sustainability, and these units are

considered to be the main hydrological system. These layers constitute the more permeable area of the salt flat, the mineral exploitation domain, and they interact directly with the lakes of the mixing zone. Units C, D and E do not play any important hydrological role because of their lower permeability.

UNIT	DESCRIPTION
A	Upper halite
AB	Upper gypsum with carbonates
B	Middle halite
C	Middle gypsum
D	Lower halite
E	Clays
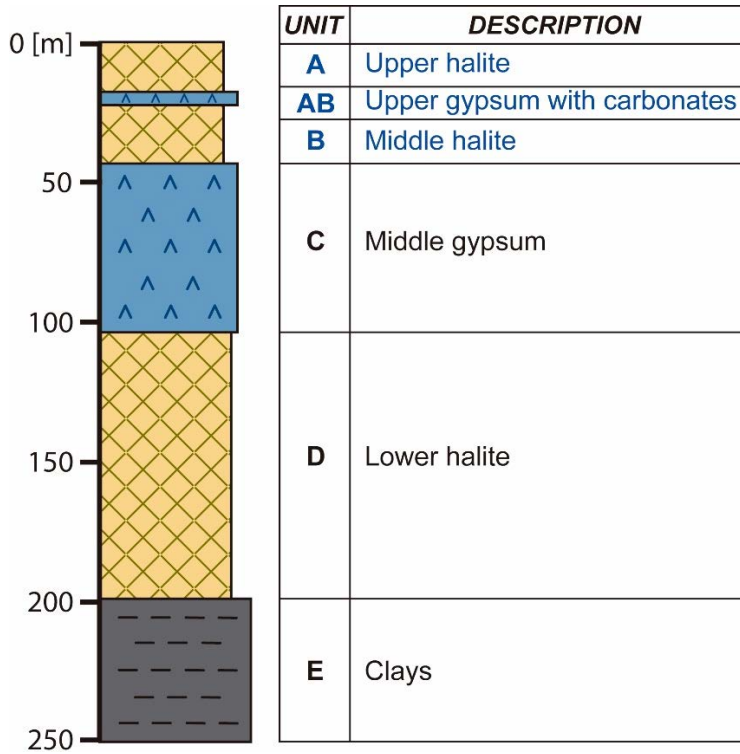
Figure 3.3. Type stratigraphic profile of the western salt flat nucleus. The blue letters highlight the main hydrogeological units considered in the numerical model.

Furthermore, the stratigraphy of the SdA has been seriously affected by the synsedimentary tectonics, particularly by the Salar fault (Arriagada et al., 2006; Jordan et al., 2007; Mpodozis et al., 2005) but also slightly by the Tucúcaro fault (see their location in Fig. 3.2). As a consequence, the thickness of the hydro-stratigraphic units has been affected and ranges from 50-250 m on the western side of the Salar fault to 400-500 m on the eastern side.

Unit A or aquifer A comprises pure halite with sediments and gypsum. Its porosity is higher than the underlying units. The sediments are clays, silts and sands of a brown to red colour. This unit is affected by the Salar fault; thus, in the western

part, it has a thickness between 14 and 20 m, while in the eastern part, its thickness ranges between 25 and 40 m.

Unit AB or aquitard AB corresponds to a group of lithologies that present continuity through lateral facies changes, with a gradation from clays in the marginal zones to gypsum with carbonates in the nucleus. The thickness ranges between 0.2 m and 3 m, although in some areas it may be thicker.

Unit B or aquifer B comprises halite with sediments and gypsum in the western part. In the eastern part, the unit consists mainly of pure halite and lenses of organic matter and gypsum. In the western part, this unit has a variable thickness between 20 m and 25 m, while in the eastern part, the unit reaches up to 400 m in thickness.

3.2.4. Experimental data

A meteorological analysis was performed from January 1986 to December 2015. This interval was considered representative to stablish the average natural regime of the SdA basin as it includes several wet and dry cycles.

The rainfall study was based on the daily meteorological data that has been collected by 14 weather stations since the 1970s (see their location in Fig. 3.4A). An interpolation that is consistent with the topography and meteorological data was performed for the average rainfall values of the basin. The interpolation of these meteorological data allowed to create the average isohyets map of the SdA for the 1986-2015 period (Fig. 3.4A). Topographic factors were the dominant criterion for this interpolation. These estimated values may have a small uncertainty because not all of the weather stations records were continuous and complete, but in general, the amount and distribution of the data was considered good enough.

To quantify the recharge, the basin was discretized into 11 sub-basins and 30 zones (Fig. 3.4). The sub-basin division was performed based on geomorphological and topographical features and watersheds. Each of these sub-basins captures the water that is recharged by rainfall in the mountains and moves it to the salt flat. In the salt flat and surroundings, the definition of zones was based on soil features. The recharge produced by rainfall infiltration was estimated subtracting the detention – defined below- from the total rained water in each rainfall event. One rainfall event comprises the integration of rainfalls that occurred in some consecutive days, mostly

during the summer season. Detention is an equivalent term for the "initial abstraction" defined in the Runoff Curve Number methodology (Mishra and Singh, 2003) as the water held by interception, surface detention and infiltration at the beginning of a storm and that finally back to the atmosphere through evaporation. This detention value was applied to each event. Furthermore, previous $\delta^{18}O$ and δ^2H values of the groundwater of the SdA were used to discuss the location of its recharge (Huerta-Vásquez, 2012; Rissmann et al., 2015).

The potential evaporation data were obtained from the measurements that were taken at evaporation trays or evaporimeter tanks installed at the weather stations. Furthermore, several lysimeters collected evaporation data from the water table of the eastern mixing zone. The water table depth was the most critical factor in the evaporation rate in the SdA. Water table depth values were obtained from old reports and field campaigns (IDAEA-CSIC, 2017; Marazuela et al., 2018). To consider the depth of the water table, the methodology of Philip (1957) was used. This method correlates the evaporation value that is measured at the surface with the water table depth through an exponential adjustment. The evaporation rate difference that is caused by solute concentration was directly included in the measurements. To quantify the evaporation flow, the zoning of Mardones (1986) was used as reference. This was slightly modified considering the new data and the availability of high-resolution satellite images, we improved this zoning (Fig. 3.4C).

The stream flows was daily monitored by 15 gauging stations (see their location in Fig. 3.2) during most of the analysed time. The missing data in the time series were filled with the average flow rate of each stream and were joined to the meteorological data of the weather stations and the ranges of oscillation in the nearby streams.

The hydraulic conductivity reference values were stablished considering previous studies and the interpretation of the pumping and packer test that was completed in the field by SQM. Over the last few decades, numerous scientific and technical studies have been conducted to assess the hydraulic properties of the study area (IDAEA-CSIC, 2017; Muñoz-Pardo et al., 2004; Rio Chilex S.A, 1997; Rockwood-Lithium, 2015). Furthermore, hydraulic tests, including packer tests, were conducted by SQM and then re-interpreted by the authors to obtain reference values. The parameter zoning (Fig. 3.5) was based on geological features and pumping test results.
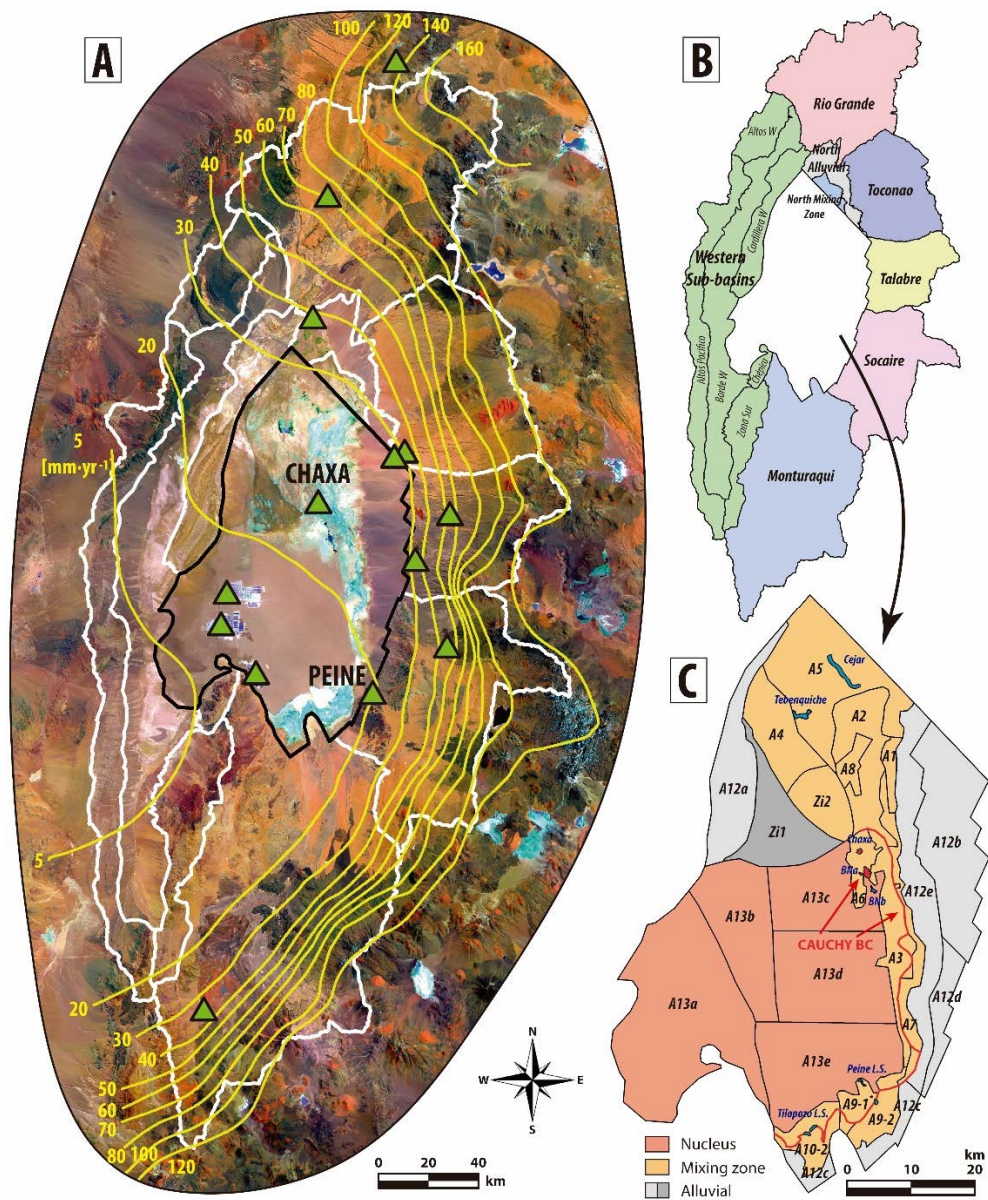
Figure 3.4. *A) Isohyets map of the SdA basin. The white lines show the sub-basin zoning, and the green triangles show the weather stations. B) Regional recharge sub-basins. The values of each sub-basin are listed in Table 3.1. C) Recharge zones in the surface of the model domain. The values of each sub-basin are listed in Table 3.2.*
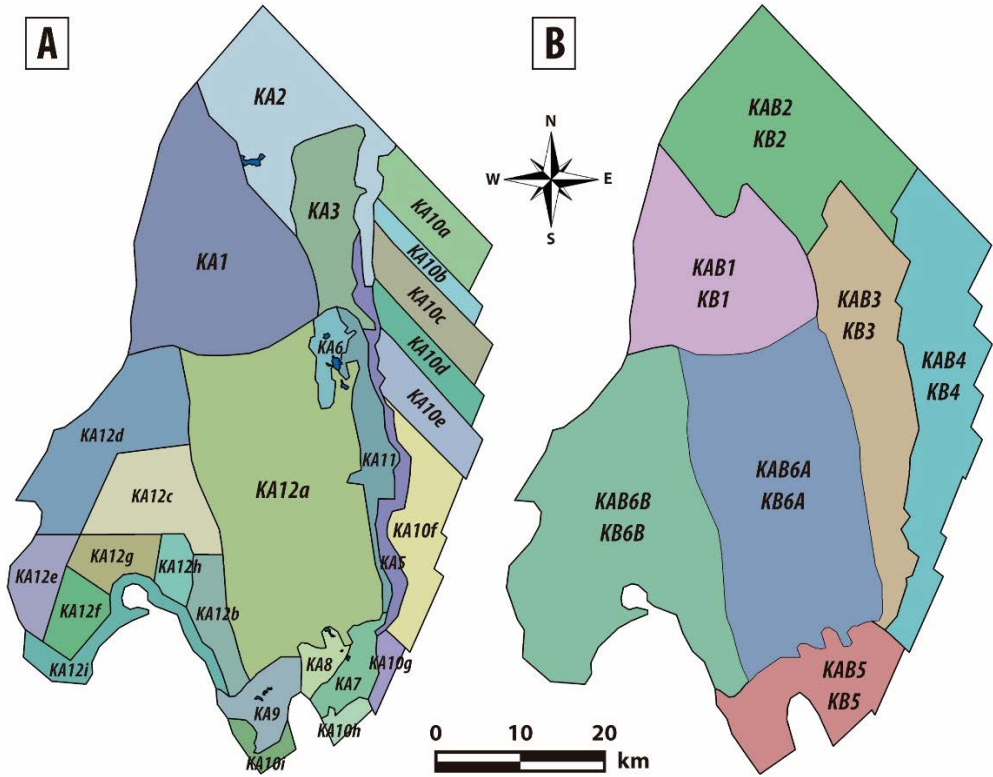
Figure 3.5. *A) Zoning of hydraulic conductivity in aquifer A (KA). B) Zoning of hydraulic conductivity in aquitard AB (KAB) and aquifer B (KB). The hydraulic conductivity values of each zone are listed in Appendix D.*

3.2.5. Criteria for the 3D modelling of the mixing zone of salt flats

3.2.5.1. Double boundary condition for modelling the mixing zone

Among the main difficulties in the modelling of salt flats is the presence of a freshwater-brine mixing zone within the modelled domain. In the similar case of coastal aquifers (Custodio and Bruggeman, 1987; Ferguson and Gleeson, 2012; Post et al., 2013; Post and Werner, 2017; Werner et al., 2013), the mixing zone is usually used as the outer boundary of the model and the sea level is prescribed. However, no numerical solution has been proposed for the regional modelling of the mixing zone of salt flats. In the available 2D numerical models of salt flats, almost the only ones made to date, two modelling strategies have been used: (1) reactive transport models taking into account evaporation and dissolution-precipitation processes

(Hamann et al., 2015; Vásquez et al., 2013) and (2) to simplify the modelling strategies when the hydrochemical reactions are not the objective through the use of fixed hydraulic head in the saline interface (Duffy and Al-Hassan, 1988; Fan et al., 1997; Marazuela et al., 2018; Tejeda et al., 2003).

In the present work, the outflow from the mixing zone was treated by a double boundary condition (BC): (1) the main outflow was considered through the Neumann BC that is imposed in the entire surface mixing zone area as in the salt flat nucleus and (2) the rest of the outflow was considered through the Cauchy BC with the hydraulic head fixed along the MMZ. This methodology is valid as long as the mixing zone is not affected by pumping or strong perturbations. This option for modelling the saline interface is favoured for two reasons: the water table is fairly constant along the entire mixing zone that surrounds the salt flat nucleus, and this allows to close the total water balance with the balance component of greatest uncertainty. Although the evaporation of the salt flat nucleus and especially the recharge of each zone can be estimated and introduced to the model with high accuracy, the water that is ejected in the mixing zone may be more difficult to evaluate in the conceptual model because of the complex processes that occur in this area. In this approach, the balance can be reliably closed and adjusted to reality if the other calculations for recharging and evaporation have been correctly estimated. In addition, the boundary of the model must be located far enough from the mixing zone, being an efficient choice the contact between the alluvial fans and the basement, where the permeability is markedly reduced.

3.2.5.2. Hydraulic head corrections for density variations

Because of the presence of two miscible fluids of different density, i.e., freshwater and brine, the hydraulic heads that refer to each of the fluids cannot be co-modelled at a constant density without applying a correction, since the resulting groundwater flow would not be representative of reality (Maas and Emke, 1989; Oude-Essink, 2001; Strack, 1976). In coastal aquifers, where the area of interest is the land side (freshwater side), the seawater heads may be corrected to freshwater heads (Lusczynski, 1961; Post et al., 2007). Nevertheless, because the salt flat nucleus and its mixing zone are the areas of greatest interest, Marazuela et al. (2018) proposed to correct the fresh and mixed water heads to brine heads. This methodology was based

on the 3D mapping of the regional mixing zone of the SdA, and the equations for the correction in each type of well are shown in detail there.

Thus, the hydraulic head data were corrected for variable density effects following the methodology proposed by Marazuela et al. (2018). A correction of the fresh and mixed water heads was applied to compensate for density variations, using the brine density, 1.23 kg·L⁻¹, as reference. Thus, the water head of the observational points in the salt flat nucleus or very near it did not require any correction. The hydraulic heads that were measured in the mixing zone generally required a small compensation because the saline interface is very near the surface. The hydraulic heads of the observational points in the alluvial and recharge zones required a greater correction because the interface is deeper. The depth of screening and the local stratigraphy were analysed as thoroughly as possible for each well.

The result of this hydraulic head correction is the existence of a regional minimum water head in the mixing zone or near it. If this correction was not applied to the hydraulic heads, the minimum piezometric head would be displaced to a more central position within the salt flat nucleus. Then, the flow pathways would cross the mixing zone without considering the effects of the variable density that drives an ascending flow in this area and feeds the lake ecosystems. Alternatively, if the correction is applied, a minimum piezometric head is reached in this area and reproduces the upward flow in the marginal zone at a low computational cost.

3.2.6. Numerical modelling

3.2.6.1. Model set-up

A steady-state model was built to reproduce the average water table of the natural regime of the SdA and to justify the water balance before intensive brine extraction. The steady-state flow equation was solved with the FEFLOW code (Diersch, 2014).

The model domain (see location in Fig. 3.2) encompassed an area of 3,303 km², which included the nucleus, mixing zone and alluvial fans, and its bounds were defined on the basis of hydrogeological features. The northern boundary corresponded to a structural lineament of the basement, the eastern and southern boundaries largely represented the contact between alluvial fans or the salt flat

nucleus with the basement and volcanic rocks, and the western boundary was the limit between the nucleus and the Cordillera de la Sal.

A 3D domain was used to model the regional groundwater flow of the SdA because a vertical component of the flux and a vertical heterogeneity were identified. The three upper hydrogeological units were considered: unit A is a free aquifer, unit AB is an aquitard, and unit B acted as a semi-confined aquifer. The geometry of the hydrostratigraphic units was provided by the correlation of cores and geophysical data (IDAEA-CSIC, 2017). Fig. 3.6 shows the geometry and topography of each geological unit.
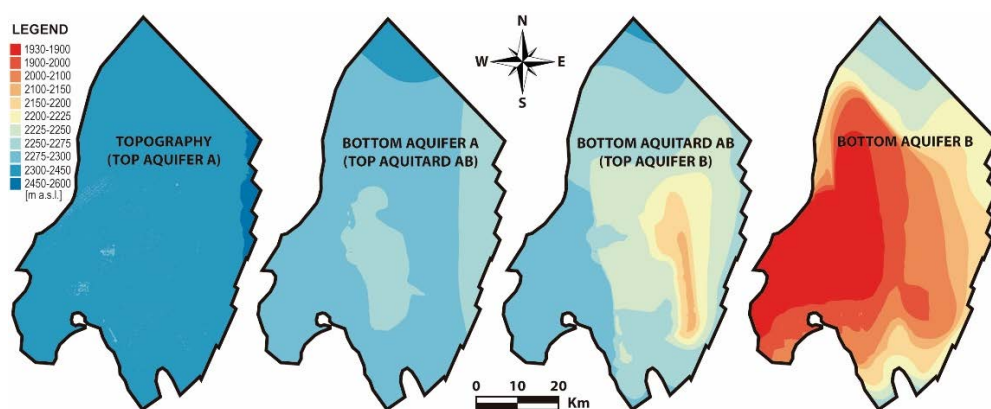
Figure 3.6. *Geometry of each of the geological surfaces that define aquifer A, aquitard AB and aquifer B.*

The finite element mesh consisted of 168,025 nodes that were, arranged in 266,340 triangular prismatic elements of variable size, and were distributed in four layers (Fig. 3.7). Aquifer A and aquitard AB were represented with one layer each one. Aquifer B was represented by two finite element layers to smooth the mesh in the strong jump of the Salar fault. As a consequence, the south-western part of the bottom layer was deactivated. The grid was refined in the areas of greatest interest, such as the mixing zone and lakes.

3.2.6.2. Boundary conditions (BCs)

The inflows (the surface recharge, lateral groundwater recharge, streams and Soncor lake system) and outflows (evaporation) of the model were implemented by using several BCs as described below.

Surface recharge was applied in each zone of the domain through a Neumann BC (Fig. 3.4C).
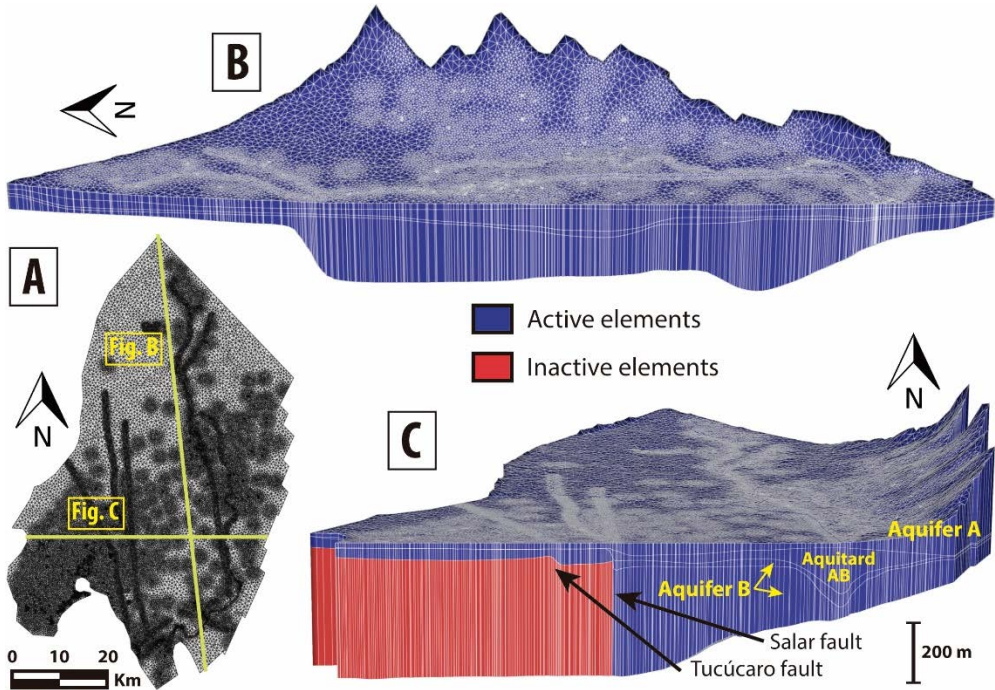
Figure 3.7. *Three-dimensional mesh of the numerical model. A) Top view of the mesh. In yellow is the vertical cross-section of figures B and C. B) North-South vertical cross-section. C) East-west vertical cross-section.*

A fixed flow rate condition was applied to the lateral groundwater recharge and streams. The lateral recharge of each sub-basin was applied to the nodes of Unit B, which represented the groundwater flow that originates from the recharge occurring outside the model domain (Fig. 3.4B). Only the North Alluvial and North Mixing Zone areas were applied to Unit A. The flow rates of the Jerez, Aguas Blancas, Talabre, Camar, Socaire, Peine and Tilomonte streams (their locations are shown in Fig. 3.2) were fixed in the nodes of the Unit A, except for the Jerez stream. The San Pedro and Vilama Rivers and the Jerez stream were included in the lateral recharge value of the North Alluvial and North Mixing Zone areas.

A special case of recharge occurred in the complex Soncor lake system. The historical data of the water table showed a constant inter-annual hydraulic head of

2,300 m a.s.l. (with oscillations of only ± 0.1 m). This value was chosen to fit (Cauchy BC) the hydraulic head in Soncor lake system (Fig. 3.4C).

The evaporation was treated with two BCs. On the one hand, for each defined zone of the salt flat nucleus and the mixing zone, an evaporation rate was imposed. On the other hand, part of the evaporation that occurs in the mixing zone was represented by a Cauchy BC along the MMZ (Fig. 3.4C). The fixed water head was 2,299.9 m a.s.l., which corresponds to the average value in the mixing zone, and it was fairly constant during the considered time. The northern stretch of the mixing zone mapped in Fig. 3.2 was not taken into account for the Cauchy BC (Fig. 3.4C) because its hydraulic heads considerably changed with respect to the nucleus and the eastern mixing zone. The outflow from this zone was considered in the calibrated value of the Neumann boundary condition.

3.2.6.3. Model calibration

The mean of the hydraulic head value of the historical series at each observational point from January 1986 to December 1994 were used in the calibration. These values were corrected for density variations (see section 3.2.5.2). The data closest to Mining Plant 3 (see their location in Fig. 3.2) were not considered because they were already affected by small local pumping during this period of time. Furthermore, the measurements of the hydraulic head measured since January 1995 were included only if they did not show perturbations due to mining activities. These observational points were mainly in the mixing zone and alluvial fans, far from the mining exploitation area, and they contributed to improve the calibration in the areas where no data prior to 1994 were available. Thus, a total of 299 observational points were used in the model calibration (Fig. 3.2).

The lateral groundwater recharge was calibrated manually, while the evaporation rates for each zone and the hydraulic conductivities (K_x, K_y and K_z) were calibrated through steady-state inverse modelling with the parameter estimation code PEST (Doherty, 2015). The core of the PEST engine is the GLMA search algorithm, which iteratively optimizes the model parameters to improve its fit to observed data.

3.3. Results

3.3.1. Hydrogeological behaviour

The SdA is an endorheic basin in which the inputs correspond to the recharge that is produced by rainfall, and the outputs are represented by the evaporation that is produced from the salt flat nucleus and particularly in the surface mixing zone (Fig. 3.8).
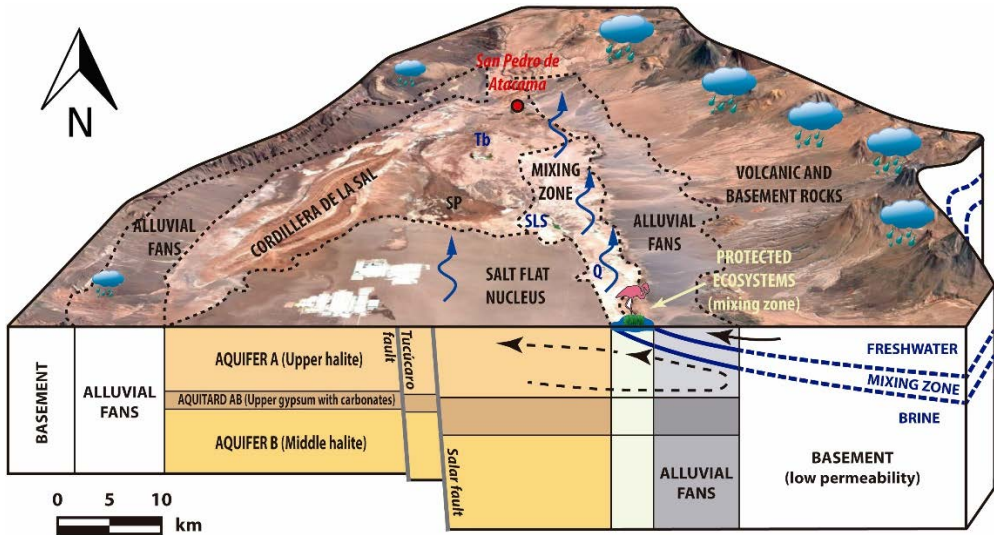
Figure 3.8. *Hydrogeological behaviour of the SdA basin. Q is Quelana lake, SLS is the Soncor lake system, Tb is Tebenquiche lake and SP is the San Pedro alluvial fan. The black lines show the groundwater flow in the mixing zone. The vertical scale was deformed to better show the main hydrogeological features.*

The Andean Range acts as a barrier to the cold Humboldt Current of the Pacific coast. Because it is under a subtropical high pressure zone, the SdA has a hyperarid climate, with low precipitation (Bookhagen and Strecker, 2008; Garreaud et al., 2010; Hartley and Chong, 2002). The main recharge is produced in the eastern side of the basin, in the Altiplano, particularly during the austral summer when the main rainfall events occur and particularly during wetter La Niña (ENSO) years. The water that is recharged in the mountains arrives mainly to the salt flat through lateral groundwater flow. When the lateral groundwater reaches the brine, it ascends to the surface as forced by the mixing zone, where a mixing and flow that is dominated by

convection processes occur. Only a small portion of the recharge occurs through direct rainfall events on the salt flat or through the infiltration of water from rivers and streams.

The individualized results of the recharge, evaporation, streams and hydraulic parameters that characterize the SdA basin are described in detail below.

3.3.1.1. Recharge

The resulting isohyet map shows that precipitation in the highlands of the Andean Range exceeds 160 mm·yr^{-1}, while in the salt flat nucleus, precipitation barely reaches 10 mm·yr^{-1}. The most western area of the basin show precipitation values of less than 5 mm·yr^{-1}. Therefore, the SdA basin exhibits precipitation values that are typical of hyperarid zones, while in the mountains, the rainfall rates are much higher.
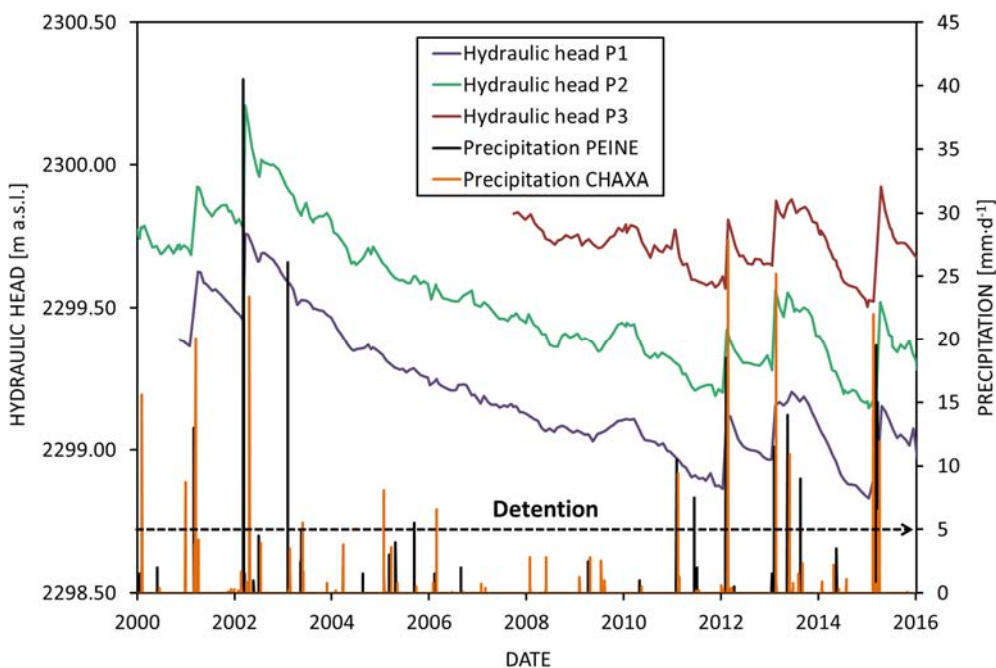
Figure 3.9. Precipitation data of the Peine and Chaxa weather stations (see their locations in Fig. 3.4A) and their effect on the hydraulic heads of the observational points P1, P2 and P3 (see their location in Fig. 3.2). The dashed black line shows the average detention value.

There are no experimental works that quantify the values of detention in the Atacama region. The high degree of fracturing of the ignimbrites and volcanic rocks

in the mountains (recharge area) and the predominant coarse-grained composition of the alluvial fans results in a little developed surface runoff and a very high infiltration. Additionally, the sparse vegetation also contribute to very low evapotranspiration from the soil. Some direct observations in several piezometers of the salt flat show that rainfall events of less than 5 mm do not produce any response in the groundwater heads (Fig. 3.9). This value was selected as representative of the detention in the salt flat; it was also extrapolated for the entire basin in the absence of previous experimental data on the recharge in the mountains and it was based on the previous criteria (sparse vegetation and a high degree of fracturing). After detracting 5 mm from the rainfall, the estimated detention for the sub-basins was between 25 % and 85 % (Table 3.1), and for the zones of the salt flat and surroundings, this value was 35 % (Table 3.2).

Table 3.1. Rainfall and recharge values for each sub-basin. The estimated and calibrated values are shown for the recharge. The sub-basin locations are shown in Fig. 3.4B.

Sub-basin	Area [km²]	Rainfall [mm·yr⁻¹]	Rainfall [m³·s⁻¹]	Detention [%]	Estimated recharge [m³·s⁻¹]	Calibrated recharge [m³·s⁻¹]
Rio Grande	2165	95	6.54	25	4.91	6.50
Toconao	1263	77	3.07	25	2.30	
Talabre	845	74	1.97	25	1.48	1.48
Socaire	1574	60	2.97	25	2.23	2.23
Monturaqui	3378	44	4.68	25	3.51	2.15
Altos Pacífico	1093	9	0.30	85	0.05	
Altos W	354	37	0.41	85	0.06	
Borde W	1575	13	0.66	85	0.10	0.31
Cordillera W	515	24	0.40	85	0.06	
Chépica	91	6	0.02	85	<0.01	
Zona Sur	521	9	0.15	85	0.02	
North Alluvial	279	35	0.31	35	0.20	0.25
North Mixing Zone	83	30	0.08	35	0.05	

Therefore, the calculated average precipitation in the SdA basin was 23.5 m³·s⁻¹, and the recharge (precipitation minus detention) to the aquifers was 16.2 m³·s⁻¹. The precipitation value is quite reliable and it is only submitted to the small uncertainty of the interpolation technique. The recharge estimation has a somewhat greater uncertainty because the exact detention is more difficult to quantify.

Table 3.2. *Rainfall, recharge and evaporation values for each zone of the model domain. The recharge zones locations are shown in Fig. 3.4C.*

Zone	Sub-zone	Area [km²]	Rainfall [mm·yr⁻¹]	Rainfall [m³·s⁻¹]	Detention [%]	Recharge [m³·s⁻¹]	Evaporation [mm·yr⁻¹]		Evaporation [m³·s⁻¹]	
							Initial	Calibrated	Initial	Calibrated
Alluvial Zone	A12a	162	23	0.12	35	0.08	1	1	0.01	0.01
	A12b	274	24	0.21	35	0.14	0	0	0.00	0.00
	A12c	61	16	0.03	35	0.02	0	0	0.00	0.00
	A12d	57	23	0.04	35	0.03	0	0	0.00	0.00
	A12e	202	22	0.14	35	0.09	1	1	0.01	0.01
Mixing Zone	A1	21	24	0.02	35	0.01	97	113	0.06	0.07
	A2	127	25	0.10	35	0.07	1066	825	4.31	3.33
	A3	90	21	0.06	35	0.04	744	213	2.12	0.61
	A4	114	25	0.09	35	0.06	97	113	0.35	0.41
	A5	268	28	0.23	35	0.15	97	112	0.82	0.96
	A6	34	22	0.02	35	0.02	1066	514	1.16	0.56
	A7	71	21	0.05	35	0.03	97	764	0.22	1.72
	A8	25	25	0.02	35	0.01	1066	952	0.83	0.75
	A9-1	29	14	0.01	35	0.01	1355	174	1.27	0.16
	A9-2	51	16	0.03	35	0.02	1066	411	1.73	0.67
	A10-2	63	11	0.02	35	0.01	744	172	1.49	0.35
	BNa	1	21	0.00	35	0.00	2190	2190	0.09	0.09
	BNb	1	21	0.00	35	0.00	2190	2190	0.03	0.03
	Chaxa	1	22	0.00	35	0.00	2190	2190	0.02	0.02
	Tebenquiche	2	26	0.00	35	0.00	2190	2190	0.14	0.14
	Cejar	1	26	0.00	35	0.00	2190	2190	0.02	0.02
	Peine	1	16	0.00	35	0.00	2190	2190	0.05	0.05
	Tilopozo	1	11	0.00	35	0.00	2190	2190	0.03	0.03
Salt Flat Nucleus	A13a	507	8	0.13	35	0.09	20	20	0.33	0.33
	A13b	210	16	0.11	35	0.07	20	20	0.14	0.14
	A13c	178	20	0.11	35	0.07	20	20	0.11	0.11
	A13d	260	18	0.14	35	0.09	20	20	0.17	0.17
	A13e	273	14	0.12	35	0.08	20	20	0.18	0.18
	Zi1	140	22	0.10	35	0.06	0	7	0.00	0.03
	Zi2	78	23	0.06	35	0.04	2	8	0.01	0.02

3.3.1.2. Evaporation

According to the data that were collected at the different weather stations, the average annual temperature was 14 °C, with a maximum of 24 °C during February (summer) and a minimum of 4 °C during July (winter).

The measurements show an annual evaporation rate that oscillates between 1,100 mm·yr⁻¹ and 4,500 mm·yr⁻¹. The variation was attributed to the seasonal behaviour of the potential evaporation. These potential values of evaporation decrease exponentially until they disappear when the water table reaches depths between 0.5 and 2 m.

The evapotranspiration that was produced by vegetation was neglected because the surface that is covered by vegetation is less than 5 %; it is also not a continuous and dense cover, which makes it difficult to predict with traditional methods. Therefore, taking into account the depth of the water table and integrating the different evaporation zones (Fig. 3.4C), the total discharge of water by evaporation in the studied area was initially estimated in 16.0 $m^3 \cdot s^{-1}$. This result is significantly larger than the discharge of 5.0 to 6.0 $m^3 \cdot s^{-1}$ obtained by Mardones (1986), that has been used as reference in many water mass balances up to now (Dirección General de Aguas, 2013, 2010, 1986) . Nevertheless, using the original Mardones' exponential curves and the groundwater depth data obtained from old reports and surveys, the discharge results in 15.0 $m^3 \cdot s^{-1}$ (HARZA, 1978; Marazuela et al., 2018; Rio Chilex S.A, 1997), a value close that obtained in the present study.

3.3.1.3. Streams

The surface drainage network develops from the highlands to the salt flat during intermittent rainy periods. The water that originates from the rainfall in the mountains moves downhill until it disappears through infiltration in the alluvial fans. These drainages are in the northern and eastern areas of the basin. The average value of each stream is shown in Table 3.3. The highest flows are in the San Pedro and Vilama Rivers, with average values of 0.72 $m^3 \cdot s^{-1}$ and 0.28 $m^3 \cdot s^{-1}$, respectively. The flow of the eastern streams ranges between 0.15 $m^3 \cdot s^{-1}$ and 0.01 $m^3 \cdot s^{-1}$.

Table 3.3. Location (Coordinates in Universal Transverse Mercator, UTM) and flow of each stream.

River or Stream	UTM East	UTM	Flow [$m^3 \cdot s^{-1}$]
San Pedro river	582083	7475499	0.72
Vilama river	583595	7470601	0.28
Jerez stream	602845	7435114	0.06
Aguas Blancas	600733	7425563	0.09
Talabre stream	623250	7420102	0.01
Camar	606284	7411161	0.01
Socaire stream	617452	7387854	0.15
Peine stream	596005	7380506	0.01
Tilomonte stream	590688	7368361	0.04

3.3.1.4. Hydraulic parameters

The evaporites and cemented detrital materials of the salt flat nucleus and the mixing zone have a low hydraulic conductivity. However, the karstification that occurs because of dissolution can increases these values by several orders of magnitude, which results in preferential underground channels (Bakalowicz, 2005). In a simplified manner, these materials can be treated as a discretized equivalent porous media (Scanlon et al., 2003). The hydraulic test performed in the nucleus showed transmissivities between almost zero to more than 10,000 $m^2 \cdot d^{-1}$. In the case of the alluvial fans, the hydraulic tests show transmissivity values from 2,000 $m^2 \cdot d^{-1}$ to 9,000 $m^2 \cdot d^{-1}$. The reference hydraulic conductivity values are shown in Appendix D.

3.3.2. Groundwater flow dynamics

The hydraulic head contour map that was obtained from the natural steady-state model is shown in Fig. 3.10. The fit of the observational data to the simulation data is expressed through the objective function (the weighted sum of the squares of the residuals between the observations and the simulation results). The results of the hydraulic head calibration are shown in Fig. 3.11, and the lateral recharge, superficial recharge and hydraulic conductivity values that were obtained are shown in Tables 3.1, 3.2 and Appendix D, respectively. The results show a very accurate fit of the data with an average error of 0.48 m and a root mean square and a standard deviation of 0.64 m. The errors of the model are not spatially concentrated which indicate that the calibration is accurate for all model zones.

The resulting water table is representative of the average climate under natural regime. Therefore, this is the water table around which the hydraulic heads oscillates due to natural perturbations (e.g., rainfall events or evaporation cycles).

The hydraulic gradients cause the flow to converge from the mountains to the mixing zone and to the eastern and south-eastern area of the salt flat nucleus. Higher hydraulic gradients are identified in the northern, eastern and southeastern zones, which coincides with the main lateral recharge sub-basins. The lower hydraulic gradients occur in the salt flat nucleus because of the low rainfall, flat topography and high hydraulic conductivities. The specific characteristics of each zone defined in Fig. 3.10 and are described as follows.
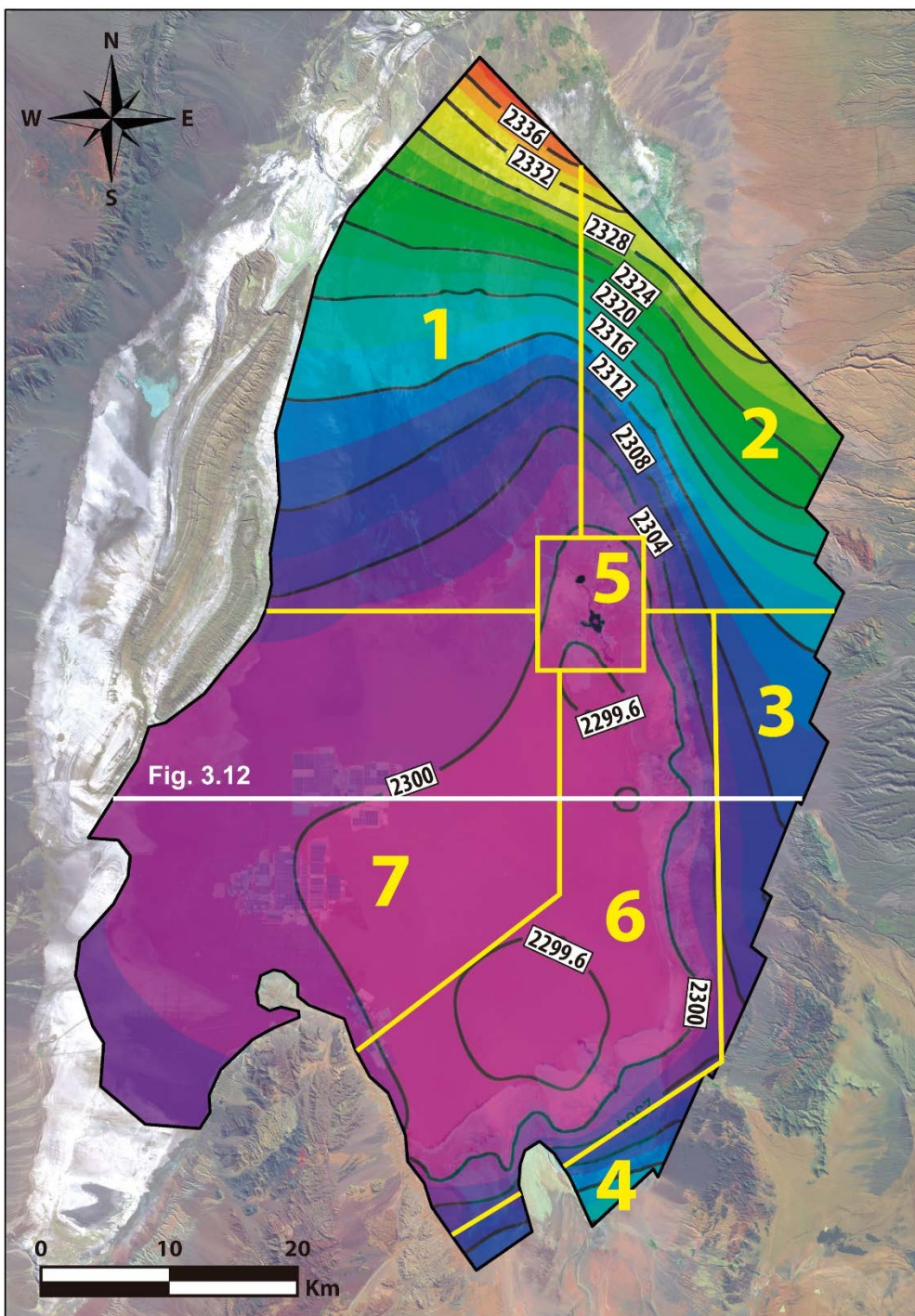
Figure 3.10. *Map of hydraulic heads of aquifer A that results from the numerical model.*

In the northwestern sector of the domain (Zone 1 of Fig. 3.10), groundwater flows from the northeast to the southwest in its northernmost zone, which gives way to a north-south flow and finally to a northwestern-southeastern flow in the San Pedro alluvial fan. The hydraulic heads oscillate between 2,340 m a.s.l. in the north and up to 2,300 m a.s.l. near the nucleus. Of particular importance are Tebinquiche and Cejar lakes (their locations are shown in Fig. 3.2) that constitute the relative minimum piezometric heads and act as local discharge zones through evaporation.

In the northeastern sector (Zone 2), groundwater flows from the northeast to the southwest. The flow follows to a great extent the geometry of the alluvial fans to their end at the mixing zone, where the hydraulic heads are approximately 2,300 m a.s.l. Zone 3 is the southward extension of the trend that is described in Zone 2 where the groundwater flow move in east-west direction, from the Andean Range to the mixing zone (Zone 6).
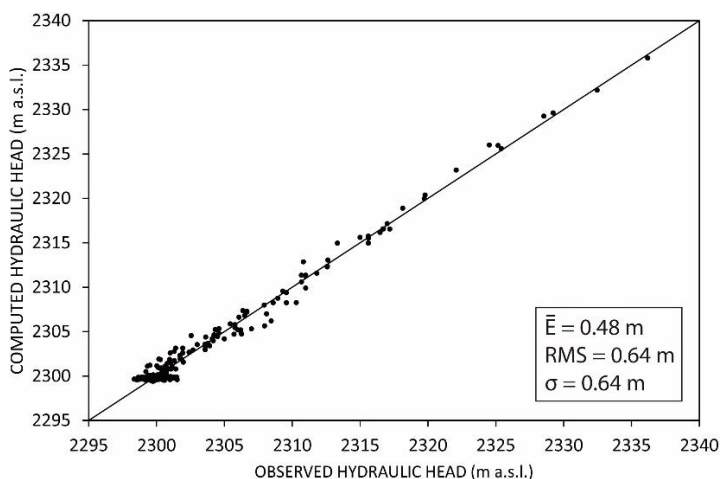
Figure 3.11. *Calibration results of the numerical model. The average error ($\bar{E}$), root mean square (RMS) and standard deviation (σ) are shown.*

Zone 4 corresponds to the discharge of the Monturaqui aquifer (Anderson et al., 2002; Boutt et al., 2016; Rissmann et al., 2015). It shows more pronounced hydraulic gradients than in nearby areas, with a SE-NW flow direction and water heads that ranges from 2,316 m a.s.l. to 2,300 m a.s.l.

A sector of special interest because of its hydrogeological location and ecology is the Soncor lake system (Zone 5). This zone is characterized by water heads of

approximately 2,300 m a.s.l. Although a great part of the water is evaporated, another part infiltrates aquifer A.

The regional minimum water head is located in the mixing zone or in the eastern and south-eastern part of the salt flat nucleus, near the mixing zone (Zone 6). An upward flow of freshwater from the eastern side discharges the mixing zone, as the vertical hydraulic gradients show in Fig. 3.12. In addition, the brine from the nucleus also follows an upward flow in this area although with much lower hydraulic gradient.
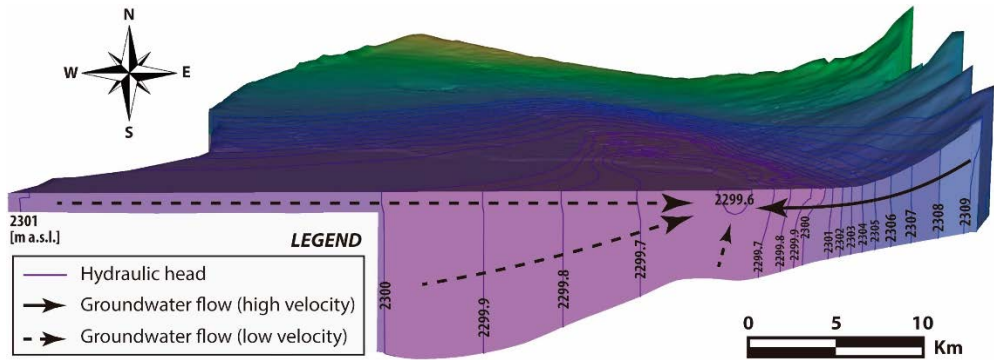
Figure 3.12. *Three-dimensional hydraulic head contour map of the vertical cross-section showed in Fig. 3.10. Black lines show the high velocity freshwater flow and dashed black lines show the slow velocity brine flow.*

The nucleus of the SdA (Zone 7) is characterized by very low hydraulic gradients, as in an area of approximately 1,360 km², the difference between the maximum and minimum hydraulic heads is barely 4 m. The western part of the nucleus presents somewhat higher gradients than the eastern part, particularly in the southwestern sector. The groundwater flows from southwest to northeast in the western sector. Once the flow path lines reach the eastern part of the nucleus, they continue to rotate toward southeast, where the regional minimum water head is reached.

3.3.3. Water balance

The water balance of the system was quantified through the numerical model in 14.9 m³·s⁻¹ for both the inflows and outflows of the SdA basin, which leaves the net balance equal to zero (Fig. 3.13).

The total recharge comprised lateral recharge from peripheral sub-basins (87.2 %), surface recharge that was produced by rainwater on the modelled domain (8.6 %), streams (2.2 %), and water that returned to the upper aquifer through infiltration from the Soncor lake system (2.0 %).
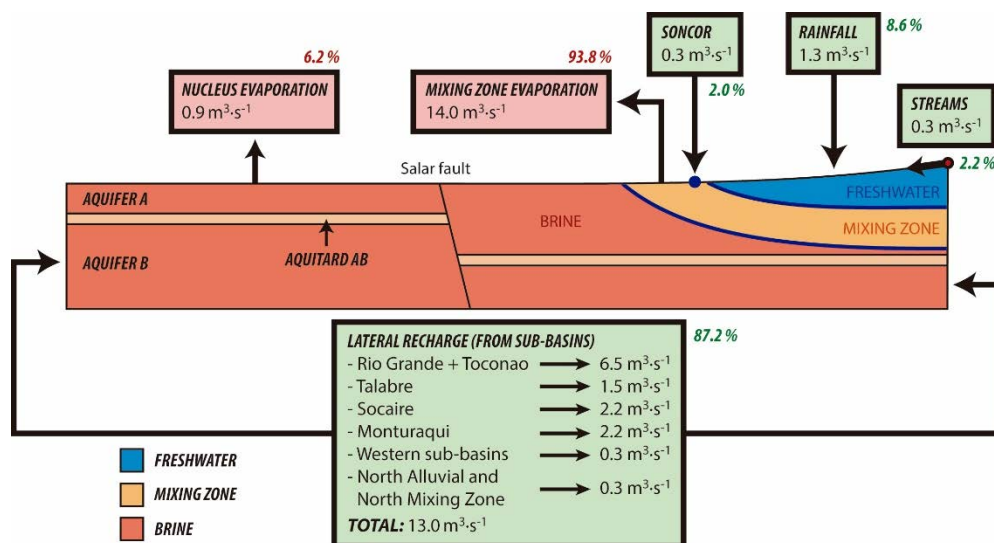
Figure 3.13. Water balance that results from the 3D numerical model.

The total lateral recharge from the peripheral sub-basins was 13.0 m³·s⁻¹. The main lateral recharge of the modelled domain was produced by the northern area that includes the Rio Grande and Toconao sub-basins, followed by the sub-basins of the Socaire, Monturaqui and Talabre; the least water was provided by the western sub-basins. Therefore, the main recharge was produced in the northern, eastern and south-eastern parts of the system, with very little lateral recharge from the western section because the heights of the western mountains are much smaller, and the mountains thus receive less precipitation.

The direct rainfall on the modelled area was much less than in the peripheral sub-basins because of its lower topography. However, the amount of water that was recharged was not negligible and reached 1.3 m³·s⁻¹. The streams from the zones outside the domain also made a small contribution to the system, with a total of 0.3 m³·s⁻¹.

A component of particular interest in the hydrodynamics of the system is the Soncor lake system. It collected water from the mixing zone. All of these water contributions converged in the Burro Muerto channel and later arrived at the different lakes of Soncor. The surface system ends up overflowing to the south of Barros Negros lake (the largest lake of Soncor) and, it constituted a water return of 0.3 m³·s⁻¹ to aquifer A.

The outputs of the system were produced entirely through evaporation, with a total of 14.9 m³·s⁻¹. The salt flat nucleus evaporated 0.9 m³·s⁻¹, while the mixing zone evaporated a total of 14.0 m³·s⁻¹. A part of the water that evaporated in the mixing zone corresponds to that was produced through the Neumann BC on the surface (9.7 m³·s⁻¹), and another part corresponds to the water that was produced through the Cauchy BC in the MMZ (4.3 m³·s⁻¹). The small inputs that were locally produced by the Cauchy BC are negligible.

3.4. Discussion

As any endorheic basin, the water table of the SdA under natural regime is the result of the balance between the inputs that mainly occur in the highlands and the outputs that occur in the mixing zone and in the salt flat nucleus by evaporation. The recharge of the basin occurs mainly in the north, east and southeast parts of the basin where the highest topography is reached. No external water entries were considered from outside the basin. The water table was characterized by strong hydraulic gradients in the zones of higher topography and low hydraulic gradients in the salt flat (Fig. 3.10). As a consequence of the topography and the geological features, the resulting water table evidences an asymmetry respect to the north-south axis. The minimum hydraulic head is located in the mixing zone or in the eastern part of the nucleus.

The main vertical groundwater flows that result from the 3D numerical model occurs in the mixing zone or in the easternmost zone of the nucleus, near to the mixing zone where the lower hydraulic head is located (Figs. 3.10 and 3.12). The location of the regional piezometric minimum in the eastern and southeastern sector of the nucleus, which was near the mixing zone but not always in the mixing zone itself, may be due to the evaporation that occurs in the nucleus of the salt flat under its natural regime. The water that reaches the mixing zone from the mountains

largely evaporates in the lakes of the mixing zone or directly from the water table that is very shallow in this area (less than 1 m depth). Therefore, the eastern mixing zone constitute the main outflow of the system. Another part of this upward water mixes with the brine and reaches the nucleus because of the convection cell. This flow pattern is consistent with the increase in densities in the nucleus from the eastern zone (1.18-1.20 kg·L^{-1}) to the west-central zone (1.23 kg·L^{-1}). This consistency indicates that the regional flow that is controlled by the variable density of the fluid was satisfactorily reproduced at a constant density, which validates the methodology that was proposed by Marazuela et al., (2018) for the numerical modelling of salt flats with low computational effort. The outflow produced through the mixing zone reached 14.0 m^3·s^{-1} what equals to 94 % of the total water balance outputs. Only the 6 % of the outflow was produced through the salt flat nucleus in the natural regime.

In the northeastern mixing zone, the presence of vertical fracturing planes favours the upwelling of groundwater (Marazuela et al., 2018). This water that rises in the northeastern mixing zone is channelled in part by the Burro Muerto channel and flows to the Soncor lake system, which not only favours evaporation from the surface water but also generates a re-entry of water into the aquifer through overflowing and infiltration. However, this mixing zone was not mirrored in the western margin because of the presence of the Cordillera de la Sal, made up of salt rocks, produces enrichment in salts. Therefore, this enrichment causes a gradual increase in the density of the small amount of water (lower topography) that is recharged in the western sector of the basin. As a consequence, the mixing zone was much further to the west from the salt flat and possibly much more gradual.

The nearly absent hydraulic head gradients in the salt flat nucleus, coupled with the presence of the saline interface that acts as a barrier on the eastern side, leads the salt flat nucleus to act as quasi-isolated area, where the small flows that occur are induced by the density contrasts. The main responsible for the low hydraulic gradients is the topography that conditions the recharge and the strong karstification of the evaporitic materials. Due to the karstification processes, the hydraulic conductivities obtained from the pumping tests and the calibration of the numerical model for the equivalent porous medium was very high. This barrier effect that is exerted by the saline interface could have a decisive influence on the hydraulic response of the water table when a recharge or pumping event occurred between the

nucleus and the EMZ such as the events described by Boutt et al. (2016) in the southeastern mixing zone.

The total water balance, which was estimated as 16.2 $m^3 \cdot s^{-1}$ for the rainfall recharge (section 3.3.1.1) and 16.0 $m^3 \cdot s^{-1}$ for the evaporation (section 3.3.1.2), was slightly higher than the water balance that is obtained with the calibrated numerical model which was computed as 14.9 $m^3 \cdot s^{-1}$ for both of them. This small difference (<8 %) corresponds mainly to a reduction in the lateral recharge from the Monturaqui sub-basin during the calibration process. In this sub-basin, the shortage of weather stations prevented a more detailed isohyetal mapping of the zones of greater precipitation. Therefore, the recharge water could be slightly overestimated in the initial conceptual model.

The water balance studies that have been conducted by the Chilean government (Dirección General de Aguas, 2013, 2010, 1986) and researchers (Muñoz-Pardo et al., 2004) have used as reference the 5.29 $m^3 \cdot s^{-1}$ value estimated by Mardones (1998). This value is much less than the value that was obtained from our study (16.0 $m^3 \cdot s^{-1}$). Nevertheless, using the original Mardones' exponential curves and the groundwater depth data obtained from old reports and surveys, the discharge results in 15.0 $m^3 \cdot s^{-1}$ (HARZA, 1978; Marazuela et al., 2018; Rio Chilex S.A, 1997), a value close that obtained in the present study.

On the other hand, according to the later estimation of Kampf and Tyler (2006), the discharge could reach 22.7 $m^3 \cdot s^{-1}$. Corenthal et al. (2016) estimated a long-term discharge rate of 21.7 $m^3 \cdot s^{-1}$ to explain the accumulation of halite deposits. According to our water table depths data and considering the application of the Philip (1957) fitting curve, the evaporation that was obtained for the salt flat is reasonable and the main controversy is the infiltration rate considered in each case. The same authors estimated the gross recharge as 26.5 $m^3 \cdot s^{-1}$ based on the TRMM 2B31 data set of Bookhagen and Strecker (2008). Our specific recharge study slightly refined this value to 23.5 $m^3 \cdot s^{-1}$. This shows the high sensitivity of the evaporation with the water table depth and the need of its accurate measurements in endorheic basin studies.

The main discussion to estimate the amount and location of the recharged water is the infiltration rate. Traditionally, it has been assumed that the infiltration rate in arid to hyperarid zones is very low, with values that can range between 0.1-5 %, with the most part being evaporated from the soil (Scanlon et al., 2006). Following this

common assumption, Corenthal et al. (2016) concluded that an infiltration rate of 3 %, which was obtained by applying the Houston (2009) recharge model, would results in an effective recharge of only 0.9 $m^3 \cdot s^{-1}$ and cannot explain the amount of halite that has accumulated in the basin. According to these authors, a possible explanation would be a much wider recharge area from the Altiplano towards the SdA basin. However, this hypothesis assumes that most of the recharge occurs from outside the basin, and there is no clear evidence of this. In addition, this hypothesis would imply that the water that recharges the SdA from the Altiplano would have relatively heavy $\delta^{18}O$ and δ^2H values because of the low infiltration and high evaporation rates is assumed by these authors and the presence of numerous salt flats in the Altiplano.

In contrast, we assumed in our model that most of the rainfall infiltrates with a minor fraction being evaporated from the soil. Indeed, the main recharge zone comprises ignimbrites, lava flows and different basement rocks. All these rocks evidence a low degree of incision by superficial hydric erosion, which indicates that most of the rainwater infiltrates preventing its rapid evaporation. The sparse vegetation in these zones neither favours evapotranspiration from the soil. In addition, all these rocks are strongly affected by fractures and deep grooves because of tectonics and the cooling process of volcanic rocks. A high infiltration rate (i.e., low detention) is also consistent with the isotopic values of the recharge water. The $\delta^{18}O$ and δ^2H values of the groundwater from the wells and boreholes of the eastern and southeastern recharge area of the SdA, prior to the mixing zone, plot very close to the Local Meteoric Water Line, and show nearly no evaporation (Fig. 3.14). This result is also consistent with the isotopic values of Herrera et al. (2016), which show exactly the same characteristics in an area (Laguna Tuyajto) of the Altiplano several kilometres to the east of the watershed of the SdA. Only one of the samples that was analysed by these authors showed evidences of evaporation, but they explained it as a sample that was taken from nearly still water in a small pond. Therefore, all these reasons indicate that rainwater quickly infiltrate, without sufficient time to evaporate. In addition, this result disprove the presence of evaporated primary water flows from the other salt flats of the Altiplano (outside the basin) as the main source of the enriched elements in the brine, which is in any case, a very specific process and scarcely important at a regional scale.

For all these reasons, it can be inferred that the infiltration rates of 0.1-5 % that are traditionally associated with hyperarid systems, with evaporation rates of less than 35 mm·yr⁻¹ in many cases, are not applicable to the SdA basin where the topography reaches 5,000 m a.s.l., with precipitation rates of 160 mm·yr⁻¹ (Fig. 3.4A).
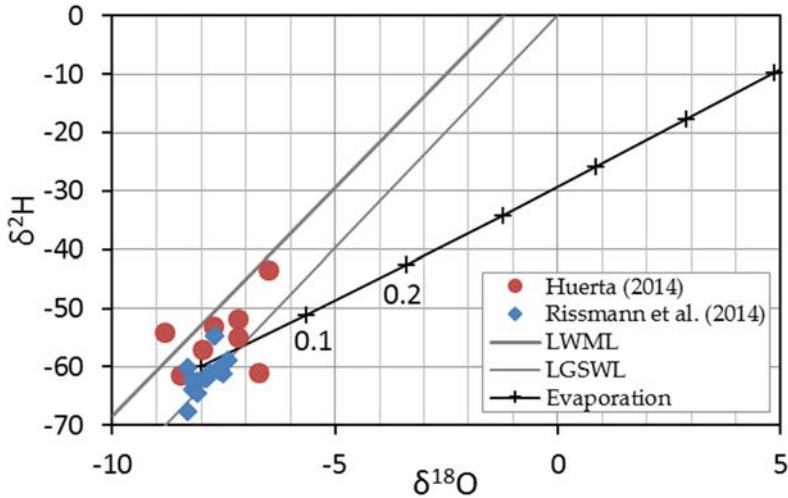
Figure 3.14. Plot of the δ¹⁸O and δ²H values of the groundwater from the eastern SdA recharge area. Values are from Huerta-Vásquez (2012) and Rissmann et al. (2015). Also plotted is the Local Meteoric Water Line (LMWL) from Aravena et al. (1999), Local Ground and Spring Water Line (see several authors collected in Rissmann et al., 2015), and evaporation trend that was calculated according to Skrzypek et al. (2015).

3.5. Synthesis and conclusions

The regional groundwater flow and the complex water balance of the SdA under its natural regime, previous to mining exploitation, were characterized and quantified. A three-dimensional groundwater flow model was used to assess the coherence of the water balance. The model uses a low computational effort method based on hydraulic head corrections by density variations to reproduce the vertical fluxes of the mixing zone (saline interface) in salt flats.

The recharge of the system occurs mainly in the north, east and southeast sub-basins where the highest elevations are reached. The lowest hydraulic head is located near the eastern mixing zone. Thus, the mixing zone constitutes the main outflow of the system and it is motivated by the vertical hydraulic gradients. The groundwater flow that reaches the mixing zone from the mountains is largely evaporated in both,

the lakes of the mixing zone or directly from the shallow water table. The nearly absent hydraulic gradients in the salt flat nucleus, coupled with the presence of the mixing zone that operate as barrier lead the salt flat nucleus to act as a hydrodynamically quasi-isolated area. This is a general trend that can be expected in the hydrodynamics of any salt flat system.

The basin water balance was quantified as 14.9 $m^3 \cdot s^{-1}$ in natural regime for both, the inflows and outflows. The water balance considered the basin as an endorheic system which was consistent with the isotopic data. The very low infiltration values that are generally assumed for hyperarid basins are not consistent with the hydrogeology of the SdA and very high infiltration rates occur because of the high degree of fracturing of rocks and the scarce vegetation. The existence of evaporated inflows from the Altiplano (outside the basin) as the main source of the enriched elements in the brine therefore seems to be unlikely. This behaviour of the recharge in the SdA basin with high infiltration rates in hyperarid climates, should serve as reference for future studies in other continental saline systems of the world. This is also of great importance to know the origin and renewal rate of chemical elements that are extracted from the salt flat brines.

Chapter 4

The effect of brine pumping on the natural hydrodynamics of the Salar de Atacama: The damping capacity of salt flats

4.1. Introduction

The Salar de Atacama is the largest source of lithium in the world, containing approximately a quarter part of the global reserves. It is, behind the Salar de Uyuni (Bolivia) and Salinas Grandes (Argentina), the third largest salt flat of the Altiplano and of the world (Risacher et al., 2003). Brine of salt flats is also a source of large amounts of boron, potassium, iodine, sodium chloride and bischofite (Evans, 1978; Hardie, 1991; Kesler et al., 2012; Lowenstein and Risacher, 2009; Munk et al., 2016; Rissmann et al., 2015). These elements and minerals are essential for the production of batteries, fertilizers, ceramics, detergents and other important industrial utilities (Marom et al., 2011; Vikström et al., 2013). The exploitation of lithium and other chemical elements is executed through brine pumping. The extracted brine is channelled into large pools where it evaporates and precipitates salts, returning a part of the excess brine to the aquifer via infiltration. The boom in clean energy production forecasts an increase in the demand for these elements and minerals that could trigger significant ecological impacts on salt flat ecosystems. Therefore, understanding the hydrodynamics of these hydrogeological systems is important for predicting their response to anthropogenic pressure and for proposing solutions for their sustainable management.

Salt flats are saline dry lakes often associated with arid to hyperarid environments in which the water table is located close to the land surface, allowing phreatic evaporation from groundwater. Under the natural regime, the depth of the water table is a result of the balance between the recharge produced mainly by rainfall in the mountains and the evaporation produced in the salt flat (Yechieli and Wood, 2002). The high evaporation rates maintained for thousand or millions of years allow the accumulation of large amounts of salts (Corenthal et al., 2016; Warren, 2010; Wood and Sanford, 1990).

As a consequence of the density contrast between the brine produced from evaporation and the freshwater recharged in the mountains, a saline interface with a mixing zone is often present in the margins of the salt flats (Fan et al., 1997; Hamann et al., 2015; Holzbecher, 2005; Nield et al., 2008; Wooding et al., 1997). When the groundwater recharged in the mountains arrives at the marginal zone of the salt flat, it is forced upward by its lower density. In the marginal zone where the mixing zone is located, many lakes and wetlands with valuable ecosystems exist, favoured by the

upward groundwater flow. Moreover, in the salt flat, the evaporated brine sinks due to its high density, and when it arrives at the mixing zone, it can be forced to return to the land surface of the mixing zone by convection cells, causing mixing with the freshwater that comes from the mountains (Marazuela et al., 2018).

As the salt flats water table is controlled by evaporation and recharge processes, these systems are very sensitive to climatic and anthropogenic changes (Rosen, 1994). Climatic cycles may cause a direct response in hydraulic heads at different scales (Bowen et al., 2017; Duffy and Al-Hassan, 1988). Moreover, the anthropogenic pressure upstream of the salt flats or directly in the same salt flat can generate large disturbances to the water table (Acosta and Custodio, 2008; Tyler et al., 2006) and therefore in the ecosystems depending on it. The study of some of these processes that join in the hydrodynamics of salt flats has been addressed in a separate manner in previous studies. Such is the case for the evaporation and rainfall in the Altiplano. Evaporation occurs directly from the groundwater due to the shallow water table, which favours the rise of water by capillarity. The evaporation in salt flats can reach the potential evaporation rate in open water reservoirs, but this rate decreases exponentially until extinguishing in the range of 0.6-2 meters of depth (Kampf et al., 2005; Kampf and Tyler, 2006; Muñoz-Pardo et al., 2004). This causes the fluctuations of the water table due to natural or anthropogenic processes to modify the evaporation rate. Rainfall in the Altiplano basins is conditioned by topography, which, due to the Altiplano uplift, results in two rainfall domains, one more arid at lower elevations and another wetter one at high elevations (Bookhagen and Strecker, 2008; Boutt et al., 2016; Houston, 2006; Rech et al., 2006). To the best of the authors' knowledge, there are no studies that integrate in a coupled manner all natural processes with the pumping of brine. Based on numerical models, Muñoz-Pardo et al. (2004) developed a direct relationship between the water table depth and recharge and evaporation and investigated how this relationship could contribute to keeping the water table stable, but a detailed study of this process and the effect of brine pumping is still lacking. Acosta and Custodio (2008) evaluated the environmental impacts under different pumping rates in the exploitation of the Salar de Huasco (Chile), although they could not compare with measured data for the case studied.

Numerical models are the best tool capable of integrating all components of the water balance to analyse its interactions and to quantify the effects that brine pumping has on the water table. No previous study has integrated all natural and

anthropogenic processes at the same time to reproduce the water table evolution of a salt flat in a three-dimensional (3D) numerical model. Additionally, no study has analysed the response of salt flats to the intensive pumping of brine and how this affect the natural regime of the water table. The high computational cost and the difficulty of quantifying the water balance of these basins are the reasons why these systems have rarely been quantitatively modelled.

To fill this scientific gap, the Salar de Atacama is a suitable case study. The monitoring network of the Salar de Atacama is considered the largest in the world (Tyler et al., 2006), and it has hydraulic head and density data spanning more than 30 years. The range of the continuous data record covers a first period (1986-1994) in which the hydrodynamics of the system were dominated by natural processes (the pre-operational period in an almost-natural regime) and a second period (1994-2015), in which the effect of the intensive extraction of brine was added (the operational period in the anthropogenic regime).

Marazuela et al. (2018) used the Salar de Atacama to describe the hydrodynamics of the mixing zone in salt flats and to propose a methodology of hydraulic head corrections based on density variations to approximate the vertical fluxes of the mixing zone in constant-density 3D numerical models at the regional scale. This allows overcoming the limitation of the high computational cost of 3D models with variable density. Furthermore, the 3D steady-state numerical model of Marazuela et al. (2019a) established the average water balance and groundwater flow of the Salar de Atacama in its natural regime, which serve to evidence that the infiltration in hyperarid basins reaches values much higher than what was previously believed. In their work, the water balance of the Salar de Atacama basin was established to be 16 $m^3 \cdot s^{-1}$ for both the recharge and evaporation, allowing a 0 $m^3 \cdot s^{-1}$ net balance. However, the temporal evolution of the water table and the effect of the hydrodynamics of the natural processes coupled to the brine pumping were outside the scope of the research and have not yet been studied. Understanding how brine pumping has affected the natural hydrodynamics of the Salar de Atacama for more than three decades is of great importance to know how salt flats respond to anthropogenic pressure and how this may affects their ecosystems. This is of paramount importance because salt flats (and their ecosystems) are becoming increasingly targeted for mining raw material critical for modern industry.

The objective of this paper is to study the interaction between the natural and anthropogenic processes that coexist in salt flats, using the Salar de Atacama as a case study, and to abstract natural and anthropogenic patterns to other salt flats. For this purpose, a 3D transient-state numerical model is used as a tool to describe and quantify the water table response to these coupled processes.

4.2. Study area

The Salar de Atacama basin is located in a large endorheic basin of the current forearc of northern Chile. The surface area of the basin is approximately 17,000 km², and its depocenter (2300 m a.s.l., meters above sea level) is the Salar de Atacama. It belongs to the Antofagasta Region, located 55 km south of San Pedro de Atacama and 320 km northeast of Antofagasta (Fig. 4.1). The basin may be divided into four geomorphological domains: salt flat nucleus, mixing zone, alluvial fans and basement and volcanic rocks.

The eastern limit of the basin is represented by the Western Cordillera, which is the current volcanic arc of the Andean Range and reaches 5,000 m a.s.l. The western limit of the basin is the Cordillera Domeyko, which has an average elevation of 3,000 m a.s.l. and is constituted by Palaeozoic and Mesozoic rocks (Arriagada et al., 2006; Pananont et al., 2004). At its southern boundary, the basin is limited by the Cordón de Lila, which includes igneous and sedimentary rocks from the Ordovician to the Carboniferous (Muñoz et al., 2002). The Miocene and Pliocene ignimbrites along with some Upper Paleozoic rocks outcrop on the slope of the Western Cordillera (Mpodozis et al., 2005).

The current depocenter of the basin is mainly filled by clastic and evaporite sediments that, due to the continuous lateral groundwater recharge coming from the mountains and permanent evaporation, have generated a nucleus enriched in sodium chloride of area 1,360 km². The nucleus is surrounded by a marginal zone that corresponds to the intersection between the mixing zone and the land surface. The mixing zone has an area of approximately 2,000 km², and it is constituted by halite, gypsum and calcite (Vásquez et al., 2013).
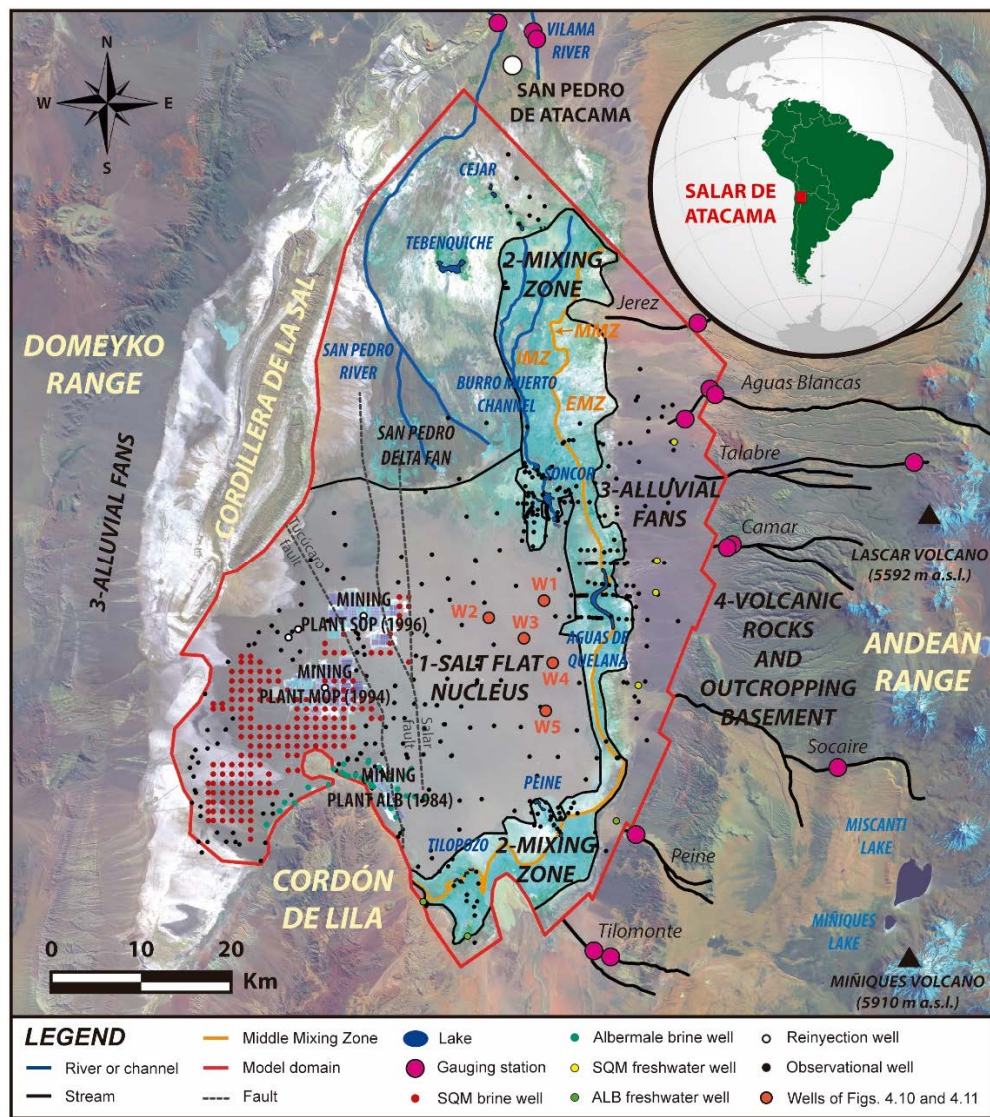
Figure 4.1. *Location of the Salar de Atacama (LANDSAT 8: 27 September, 2016). The black lines border the salt flat nucleus and the mixing zone. The three sub-zones of the mixing zone are shown in orange lettering (internal, IMZ; middle, MMZ and external, EMZ).*

4.2.1. Hydrogeology

As an endorheic basin, all recharge that occurs in the aquifers of the Salar de Atacama is produced by infiltration of rainfall. Because the Andean Range acts as a barrier to the cold Humboldt Current of the Pacific coast, the Salar de Atacama is

under a subtropical high-pressure zone, and it has a hyperarid climate that is characterized by low precipitation rates.

The surface hydric network is scarce, and the highest flows occur in the San Pedro and Vilama rivers (Fig. 4.1). The San Pedro River forms an alluvial fan (San Pedro alluvial fan) when arriving at the northern margin of the salt flat, where water infiltrates detrital sediments. Additionally, there are some intermittent streams that drain, across the eastern margin, the water from the mountains such as the Toconao, Aguas Blancas, Talabre, Camar, Socaire, Peine and Tilomonte streams. At a short distance from San Pedro alluvial fan, and in the east direction, the Burro Muerto Channel connects and feeds the Chaxa and Barros Negros Lakes which constitute the Soncor Lake system.
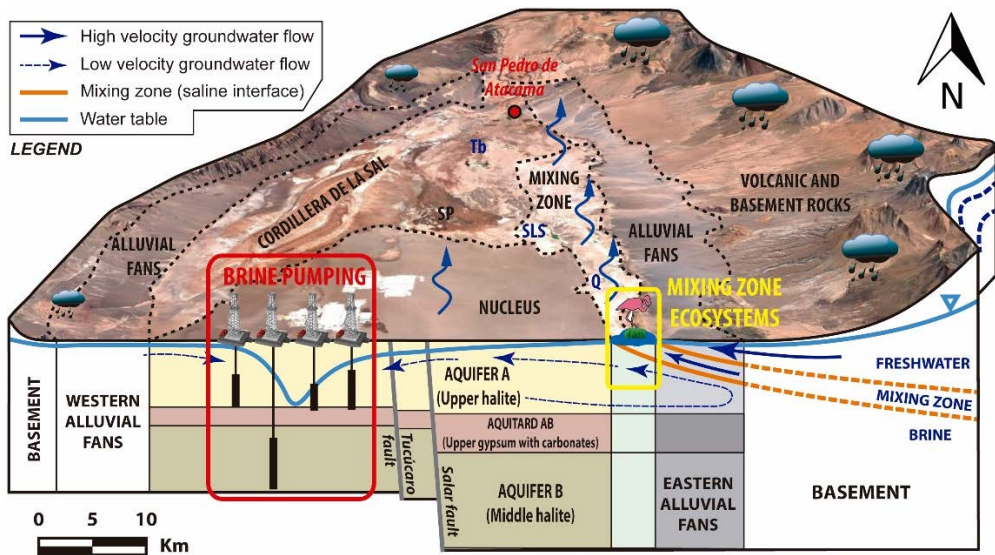
Figure 4.2. *Hydrogeological performance of the Salar de Atacama basin (modified from Marazuela et al., 2019a). Q is the Quelana Lake, SLS is the Soncor Lake system, Tb is the Tebenquiche Lake and SP is the San Pedro alluvial fan.*

In addition to Soncor, there are several lakes (Cejar, Tebenquiche, Aguas de Quelana, Peine and Tilopozo) in the mixing zone associated with the upward flows that constitute highly valuable ecosystems that serve as a habitat or nesting centre for Andean flamingos and other species (Cornellà et al., 2009; Ortiz et al., 2014; Salas et al., 2010; Tejeda et al., 2003) (Fig. 4.2). Marazuela et al. (2018) differentiated three hydrodynamic zones inside the mixing zone: an internal mixing zone (IMZ), middle

mixing zone (MMZ) and external mixing zone (EMZ). Most of the lakes are located in the upstream flows associated with the middle mixing zone (MMZ), which separates the internal mixing zone (IMZ) from the external mixing zone (EMZ) (Fig. 4.1). The IMZ exhibits a hydrodynamics dominated by groundwater movements associated with density contrasts. On the other side, the EMZ is controlled by the groundwater flows coming from the recharge in the mountains (Marazuela et al., 2019a). The water table depth in the natural regime ranges from 0.1-1 m in the salt flat nucleus and 0-1.5 m in the mixing zone.

In the nucleus, the most permeable aquifer is the upper stratigraphic unit of halite (Fig. 4.2) (IDAEA-CSIC, 2017; Marazuela et al., 2019a). Below, a second halite aquifer is confined by a low permeability stratigraphic unit of gypsum that constitutes an intermediate aquitard. Towards the margins, the hydro-stratigraphic sequence aquifer-aquitard-aquifer is transferable to the alluvial fans as a regional simplification, where the upper and lower high-permeability detrital deposits are detached from the lower ones by a poorly permeable layer constituted mainly by sands, silts and ashes. Two main faults affect the thickness and geometry of these stratigraphic units, the Salar and Tucúcaro faults.

4.3. Materials and methods

In this section, the methodology followed to obtain the data used for the estimation and calibration of the inflows and outflows of the numerical model is described. First, the meteorological data considered for the estimation of recharge, evaporation and flow of streams are explained. Second, we address the hydrogeological data, which include the pumping rate of the brine and freshwater wells, the hydraulic heads of the observational wells and the hydraulic parameters involved in the calibration process of the numerical model. Finally, the geometry and performance of the 3D transient-state numerical model are described.

4.3.1. Meteorological data

4.3.1.1. Recharge

The rainfall data were provided by 14 weather stations located in the Salar de Atacama basin (see their locations in Fig. 4.3A). Some rain events affect a very local

area, and analysing the rainfall over time in an integrated manner is not possible. Therefore, each rain event from January 1986 to December 2015 was mapped individually. Thus, an isohyets map of each event was created, taking into account topographic factors as the dominant criteria for the interpolation.

Two multivariate methods were used to fill gaps in the rainfall time series: weighted linear combination (Peterson and Easterling, 1994) and the Karl methodology (Karl and Williams, 1987). The first method allows filling the gaps from the data of statistically proximal series by means of a weighted linear combination of the series that are used. The second method replaces the gap of a record by the corresponding value of another nearby station that has a high linear correlation index, it being necessary to know the behaviour of precipitation in the basin (e.g. rainfall gradient).

The recharge by infiltration of rain water was calculated by subtracting the detention from the total precipitation following the criteria of Marazuela et al., (2019a). In accordance with this previous work, the Salar de Atacama basin cannot be treated as a typical hyperarid area with very low infiltration rates and a homogeneous precipitation rate. The sparse vegetation, the underdeveloped surface hydrological network and the high degree of fracturing of the rocks of the mountains (the main recharge area) imply that the great part of the rainfall infiltrates in the mountains. Detention is the proportion of rainfall that will not arrive to infiltrate and recharge the aquifers. At the beginning of each precipitation event, approximately 5 mm are detained in the soil and return to the atmosphere by evaporation. This value is justified because rain events lower than 5 mm almost never affect the water table of the salt flat because the water is detained in the soil and subsequently evaporated. This value was subtracted for each rain event.

The zoning to quantify the recharge by rainfall was performed at two levels: (1) peripheral sub-basins and (2) the salt flat nucleus, mixing zone and alluvial fans. The first correspond to the most elevated areas located between 2,400 and 5,500 m a.s.l. The sub-basins of greater extension and elevation are found in the eastern half of the basin. In these areas, andesite and ignimbrite rocks appear interspersed with continental sedimentary facies. They constitute aquifers of low hydraulic conductivity and storage capacity, although they can increase their effective hydraulic conductivity due to the high degree of fracturing. As explained above, the

high degree of fracturing together with the scarce vegetation and the processes of physical-chemical weathering on the surface make the infiltration rate very high. A total of 11 sub-basins were defined based on a morphometric study that included a digital elevation model and satellite images (LANDSAT 7 and 8) (Fig. 4.3A). On the other hand, the domain that encompasses the salt flat nucleus, mixing zone and alluvial fans was discretized into 30 zones according to geomorphological and soil features (Fig. 4.3B). The recharge values for sub-basins are listed in Table 3.1, and those for surface zones are presented in Table 3.2.
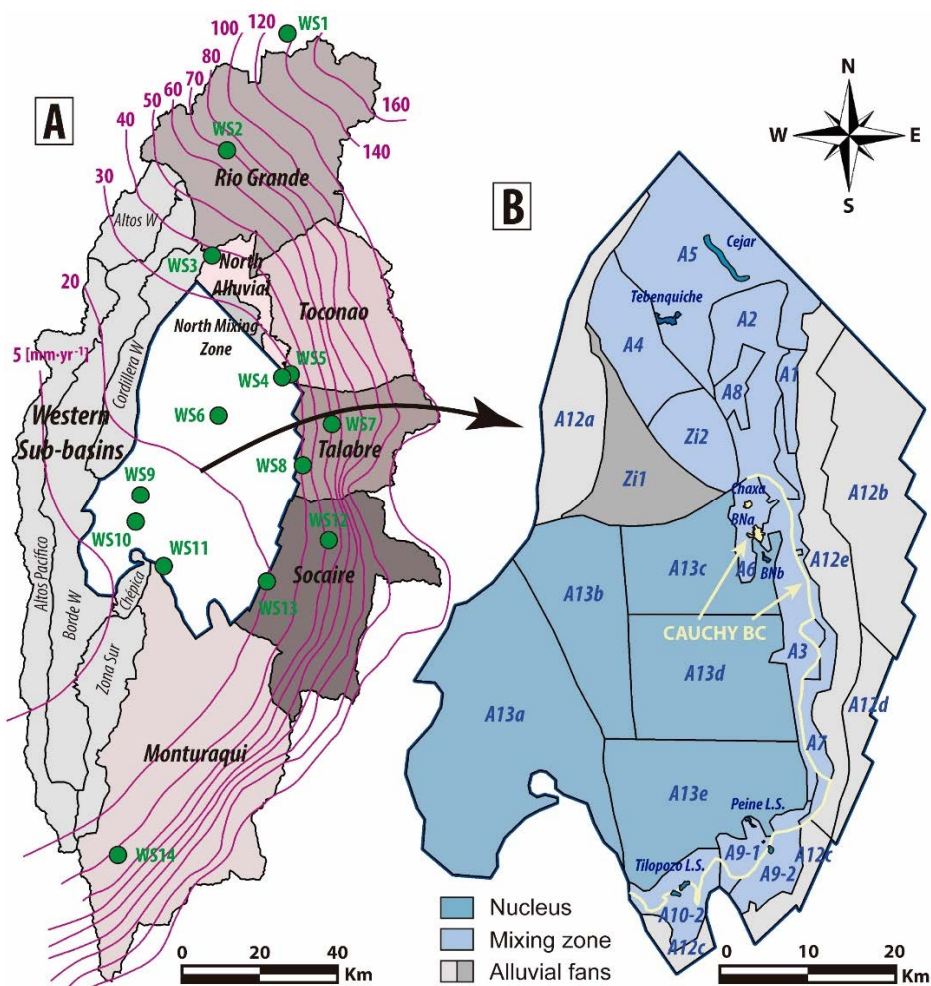
Figure 4.3. *Superficial recharge and evaporation zones (modified from Marazuela et al., 2019a). A) Regional recharge sub-basins and isohyets map. Green points indicate the positions of the weather stations. The basin recharge values of each zone are listed in Table 3.1. B) Recharge zones at the surface of the model domain. The recharge and evaporation values of each zone are listed in Table 3.2.*

4.3.1.2. Evaporation

The evaporation in the Salar de Atacama occurs from the water table which is very close to the ground (phreatic evaporation). The higher evaporation rates, however, occur in the mixing zone where the water table is closer to the land surface and where some lakes allow direct evaporation. In the salt flat nucleus, the polygonal structure of the salt crusts allows the rise of the groundwater by capillarity and favours evaporation from the water table when it is close to the surface. Although the evaporation rate in the nucleus is much less than in the mixing zone, this should not be neglected because the surface area is very large.

Evaporation rates were estimated from the experimental data registered by evaporation trays and lysimeters. Evaporation trays were installed in the weather stations. Lysimeters were installed in the mixing zone to measure the evaporation from the groundwater. Evaporation rates were correlated with the water table depth by fitting the experimental data of the lysimeters with the Philip (1957)-type curve. This method relates the evaporation rate that is measured to the water table depth through an exponential fit.

Considering the characteristics of each type of soil and the data collected by the evaporation trays or evaporimeter tanks, the annual evolution of the evaporation rate in each zone of the Fig. 4.3B was established. The average values for each zone are listed in Table 3.2.

4.3.1.3. Streams

Although the surface drainage network is undeveloped in the Salar de Atacama basin, two rivers and some streams may be identified. Streams descend from the eastern mountains until the alluvial fans, where the often intermittent flows infiltrate as a consequence of the high permeability. These streams were continuously monitored using 15 gauging stations (see their locations in Fig. 4.1). Time series gaps were filled through data correlation between nearby gauging stations, taking into account the average value of each stream and the meteorological data of the weather stations. The highest flows are in the San Pedro River, with 0.72 $m^3 \cdot s^{-1}$, and the Vilama River, with 0.28 $m^3 \cdot s^{-1}$, both of them at the north of the Salar de Atacama. The other streams, such as Toconao, Aguas Blancas, Talabre, Camar, Socaire, Peine and Tilomonte, are located on the eastern or south-eastern side of the Salar de Atacama,

with flow rates that range between 0.15 m³·s⁻¹ and 0.01 m³·s⁻¹. The average values of streams are presented in Table 3.3.

4.3.2. Hydrogeological data

4.3.2.1. Pumping wells

At present, two mining companies pump the brine of the Salar de Atacama. These companies are Sociedad Química y Minera de Chile S.A. (SQM), owner of mining plants MOP and SOP and Albemarle Corporation (ALB), owner of mining plant ALB.

The pumping network of SQM consists of several hundred brine pumping wells located in the southwestern salt flat nucleus, 5 freshwater wells in the eastern alluvial fans and 4 reinjection points associated with infiltration from the evaporation pools (Fig. 4.1). Daily flow rates are available from the beginning of the pumping in 1994.

The pumping network of the ALB mining company comprised 62 brine wells in the southern salt flat nucleus and 3 freshwater wells in the southern alluvial fans. Historical flows were seasonally represented based on the data presented in Rockwood-Lithium (2015).

The brine pumping performed by ALB began in 1983 at a rate of 0.05 m³·s⁻¹ and increased to 0.13 m³·s⁻¹ by 2015. The extraction of brine performed by SQM began in November 1994 at a rate of 0.07 m³·s⁻¹ and reached 1.37 m³·s⁻¹ in 2015, with the maximum extraction in summer and minimum in winter (Comisión Regional del Medio Ambiente, 2006; IDAEA-CSIC, 2017). The freshwater pumping performed by ALB ranged between 0.01 m³·s⁻¹ in 1999 and 0.02 m³·s⁻¹ in 2015, and for SQM, it ranged between 0.07 m³·s⁻¹ in 2000 and 0.21 m³·s⁻¹ in 2015. The SQM reinjections increased from 0.1 m³·s⁻¹ in 1996 to 0.38 m³·s⁻¹ in 2015. Therefore, a pre-operational period (1986-1994) and an operational period (1994-2015) were differentiated. In the pre-operational period some brine extractions occurred, but they were insignificant compared with those that have occurred since 1994.

4.3.2.2. Observational wells

The hydraulic head time series were recorded manually or with a data logger in a total of 549 wells (see their locations in Fig. 4.1). The data were corrected for variable density variations following the methodology of Marazuela et al., (2018). This

methodology is based on the application of a correction to the fresh and mixed water heads to compensate for the density variations, taking as reference the density of the brine (1.23 kg·L^{-1}).

4.3.2.3. Hydraulic parameters

Evaporites and cemented detrital deposits of salt flats have low hydraulic conductivities if they are not altered. However, the dissolution and karstification increase the permeability by several orders of magnitude, resulting in preferential channels (Bakalowicz, 2005). These deposits can be treated as discretized equivalent porous media in regional studies (Scanlon et al., 2003).

The reference values of the hydraulic conductivity and specific storage were deduced from the hydraulic tests performed by mining companies and in some cases reinterpreted by other authors (IDAEA-CSIC, 2017; Marazuela et al., 2019a; Rockwood-Lithium, 2015). The zoning of the hydraulic parameters and specific storage was performed based on lithological and soil features, pumping test results and the previous study (Fig. 4.4).

4.3.3. Numerical modelling

A transient-state groundwater flow model was constructed to reproduce the hydrogeological behaviour of the Salar de Atacama between January 1986 and December 2015, considering the natural (recharge and evaporation) and anthropogenic processes (freshwater and brine pumping and reinjections). For the initial condition, the steady-state water table presented by Marazuela et al. (2019a) was used, which represents the average hydraulic heads in the natural regime, prior to brine pumping, similar to the 1986 regime. A time step limited to 10 days was applied. The FEFLOW code (Diersch, 2014) was used to solve the three-dimensional groundwater flow equation.

4.3.3.1. Model set-up

The model domain (Fig. 4.1) has an area of 3,303 km^2 and covers the salt flat nucleus, the mixing zone and a large part of the eastern alluvial fans. The eastern boundary is the contact between the alluvial fans and the basement or volcanic rocks, the southern boundary is the contact between the salt flat nucleus and the Cordón de

Lila, the western boundary is the contact with the Cordillera de la Sal and the northern boundary correspond with a deep structural lineament, sufficiently far from the area of interest (IDAEA-CSIC, 2017).
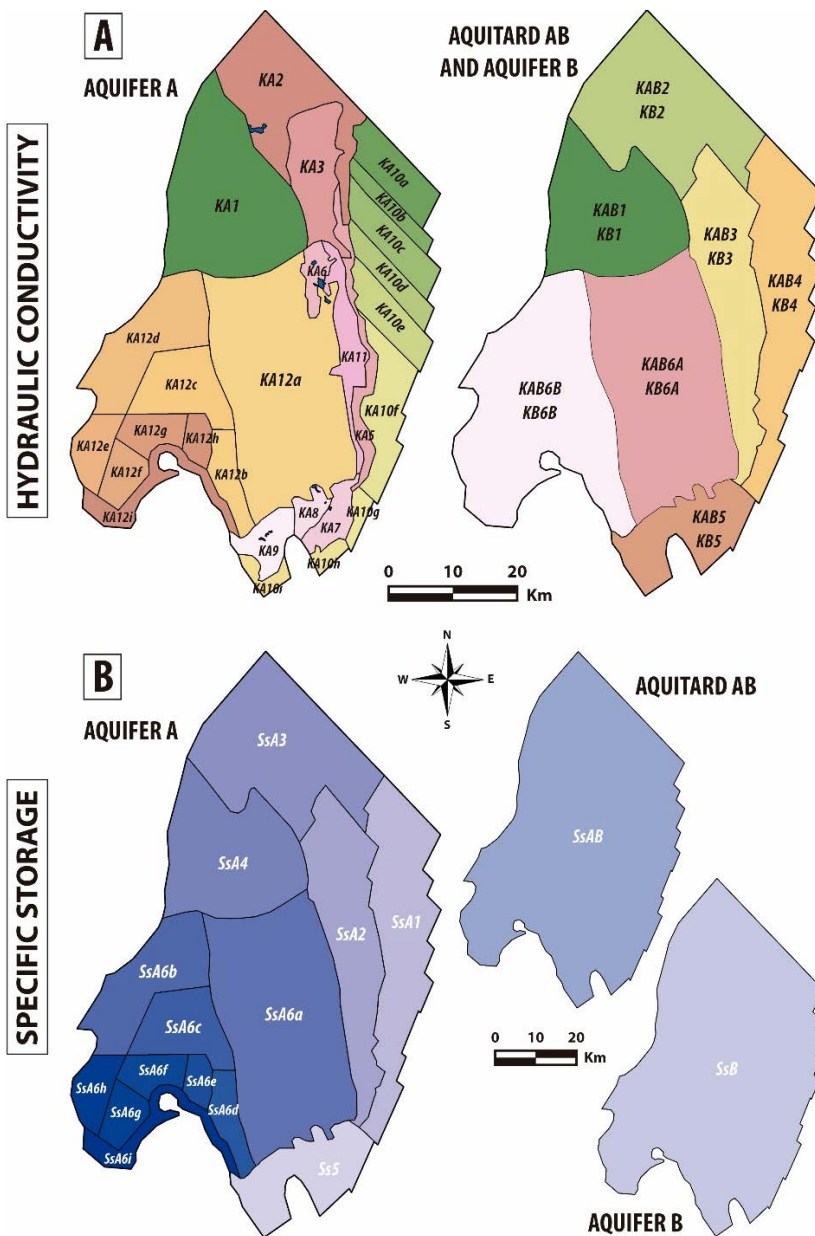
Figure 4.4. *Zoning of the hydraulic conductivity (A) and specific storage (B) for each hydrogeological unit (modified from Marazuela et al., 2019a). The hydraulic conductivity values are listed in Appendix D and the specific storage values in Appendix E.*

The three-dimensional mesh contains four layers with a total of 266,340 triangular prism elements to represent aquifer A, aquitard AB and aquifer B (Fig. 4.5). Aquifer A and aquitard AB are represented with one layer each. Aquifer B is represented through the two lower layers to correctly reproduce the strong fault jump caused by the Salar fault. The mesh is refined near fault jumps, lakes, pumping wells and observational wells. The sizes of the elements range between 10 and 300 m.
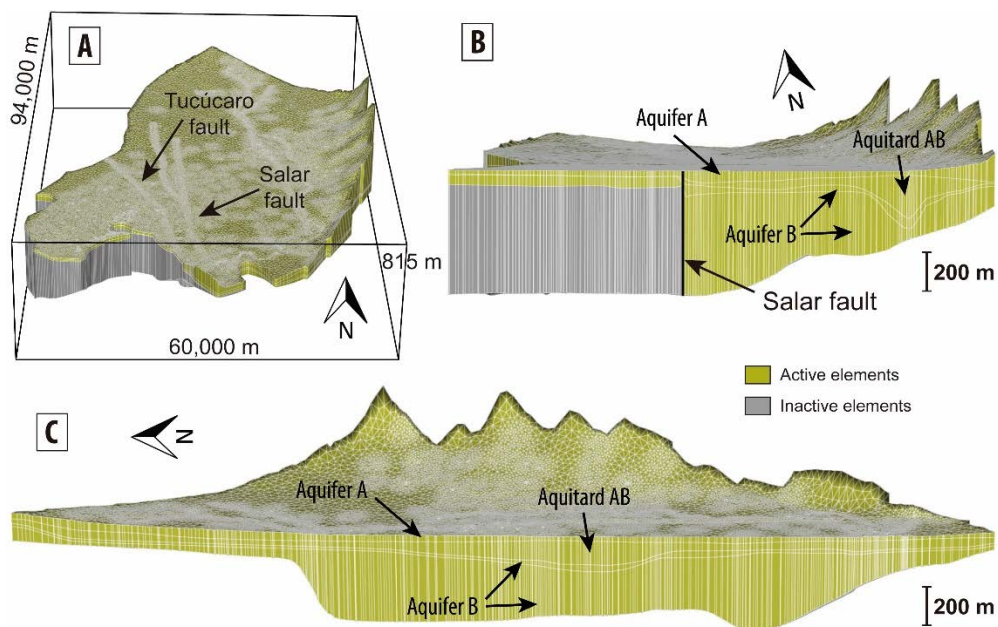
Figure 4.5. Mesh of the 3D numerical model. A) 3D view. B) East-West vertical cross section. C) North-South vertical cross section.

4.3.3.2. Boundary conditions

The lateral groundwater recharge that represents the flows coming from the water recharged in the mountains was implemented through the well-type boundary condition around the domain for each sub-basin. Due to the distance between the mountains and the model domain and due to the thick unsaturated zone in the mountains, these values were constant over time. The recharge produced by the rainfall events that occurred directly in the model domain, due to the thin unsaturated zone, was incorporated as a Neumann-type boundary condition.

Therefore, for each defined recharge zone on the top boundary of the model, a time series with the estimated recharge values of each rain event was obtained.

The evaporation was incorporated through double boundary conditions, outflow on top and Cauchy-type. The outflow on top was used to implement the time series of the evaporation rate in each zone of the nucleus and mixing zone, including lakes. The evaporation time series included a progressive non-linear reduction in the salt flat nucleus due to the deepening of the water table produced by the pumping. The Cauchy-type boundary condition with a high leakage served to prescribe the hydraulic head in the Soncor Lake system and in the MMZ, where the water head was similar to the salt flat nucleus over time. The northern stretch of the mixing zone mapped in Fig. 4.1 was not taken into account for the Cauchy boundary condition (Fig. 4.3B) because the water heads change with respect to the nucleus, and it would be necessary to apply density corrections to the prescribed water heads. The outflow from this zone was considered based on the calibrated value of the Neumann-type boundary condition.

$$Q_W = Q_1 + Q_2 + Q_3 + ... + Q_n$$
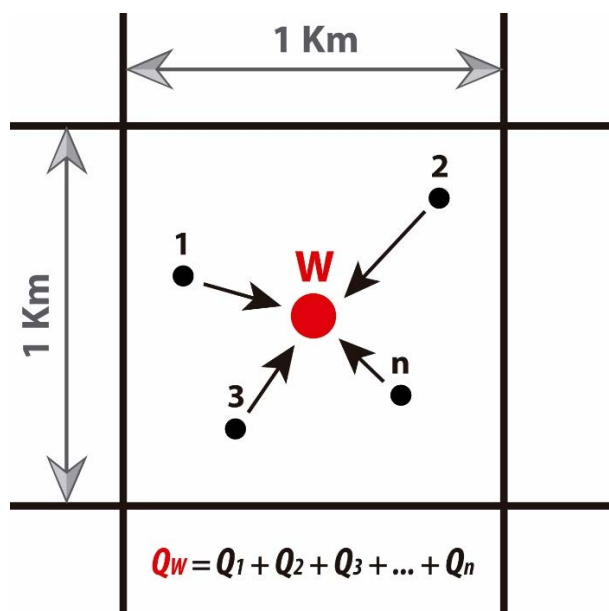
Figure 4.6. Methodology used for the definition of the equivalent wells.

Finally, a well-type boundary condition was used to reproduce the extractions and reinjections. The brine pumping wells were adjusted to a simplified network of

equivalent wells to facilitate their implementation in the numerical model. This network of equivalent wells was made using a regular mesh with cells of 1 km^2 resolution, assigning the accumulated pumping of the wells in each cell to its centroid (Fig. 4.6). This methodology was performed independently for aquifer A and aquifer B. A total of 245 equivalent wells were used.

4.3.3.3. Model calibration

The calibration process was performed through inverse modelling with the parameter estimation code PEST (Doherty, 2015). The core of the PEST engine is the Gauss-Levenberg-Marquardt algorithm (GLMA), which iteratively optimizes the model parameters to improve their fit to observed data by means of an objective function.

The calibration of the hydraulic conductivity, lateral recharge and average evaporation was a joint process based on the steady-state model of Marazuela et al. (2019a). The specific storage was calibrated for the transient-state model.

The hydraulic conductivities in aquifer A exhibited values ranging between 80 and 300 m·d^{-1} for the alluvial fans and between 60 and 300 m·d^{-1} for the salt flat nucleus and mixing zone (Appendix D). The hydraulic conductivities in aquitard AB ranged between 0.01 and 5 m·d^{-1}, and in aquifer B, they ranged between 0.1 and 20 m·d^{-1}. The specific storage values (Appendix E) ranged between 0.007 m^{-1} and 0.012 m^{-1} in aquifer A. For aquitard AB and aquifer B, the specific storage was 10-4 m^{-1} and 10-5 m^{-1}, respectively.

4.4. Results and discussion

In this section, the field data combined with the results of the 3D transient-state numerical model are used to discuss the natural hydrodynamics of the Salar de Atacama and how the brine pumping has impacted the natural water table to abstract patterns applicable to other salt flats.

First, the individualized natural processes, recharge and evaporation, that occurred in the Salar de Atacama and their coupled behaviour are addressed separately. Subsequently, the effects that caused brine pumping are evaluated and discussed to extrapolate general patterns to other salt flats.

4.4.1. Natural hydrodynamics of the Salar de Atacama

The results of the numerical model simulation show the evolution of the water table of the Salar de Atacama from 1986 to 2015, taking into account the brine pumping (Figs. 4.7 and 4.8). The brine pumping was almost non-existent until 1994, and therefore it is very interesting to first establish the natural hydrodynamics of the salt flat during this period (1986-1994) to be able to discuss in the following section the anthropogenic impacts of brine pumping.
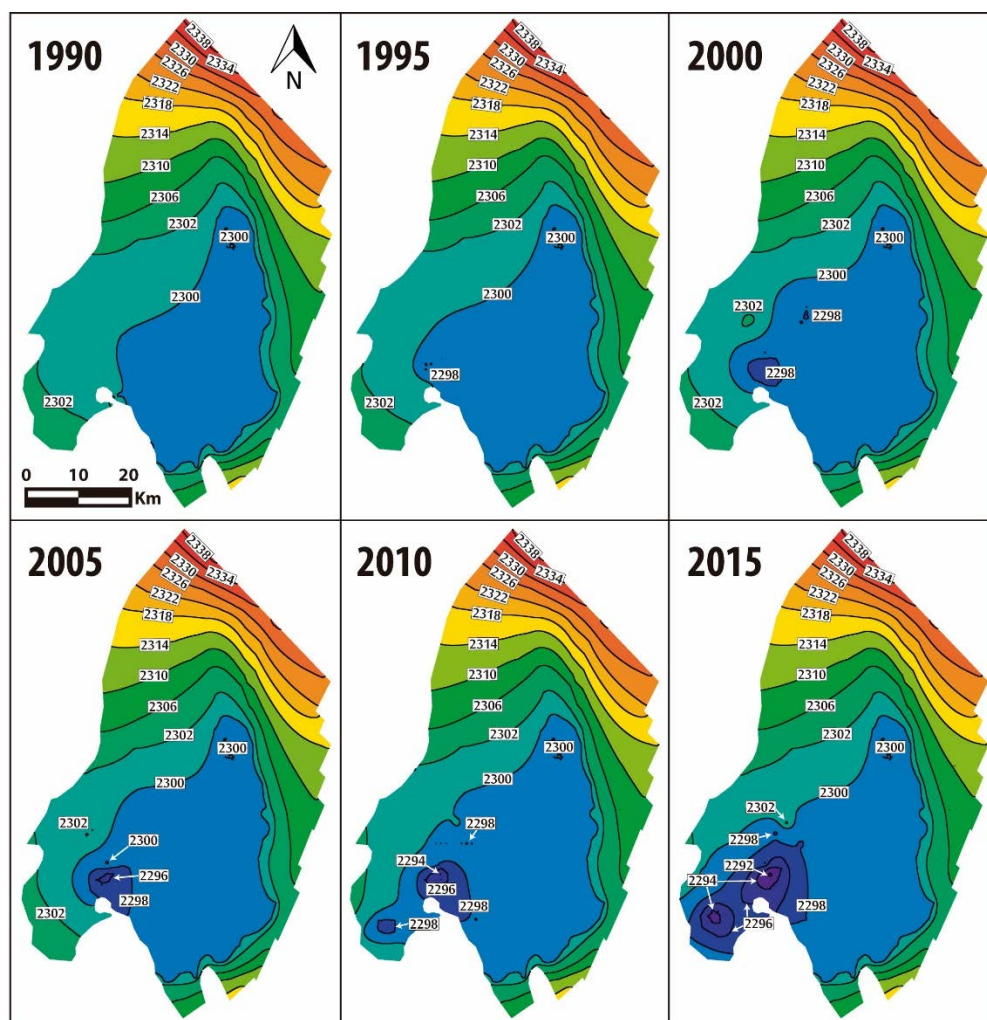
Figure 4.7. *Hydraulic head contour maps resulting from the 3D transient-state numerical model. The results are shown every five-year periods from December 31st, 1990 to December 31st, 2015. The black letters indicate the value of each hydraulic head contour line in meters above sea level (m a.s.l.).*
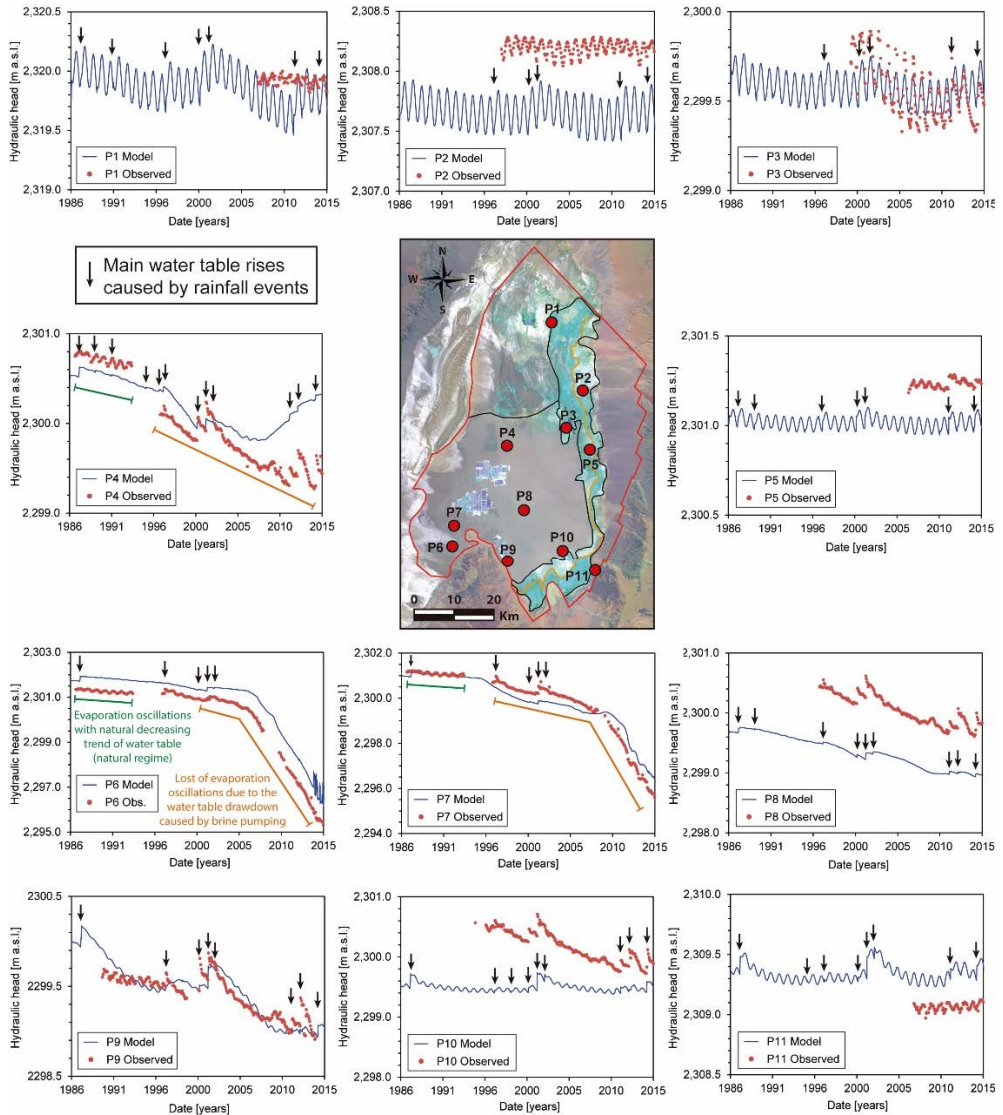
Figure 4.8. *Hydraulic head evolution at eleven observational wells showing the modelled versus measured (observed) data. The measured data outside the mixing zone were corrected for density variations following the methodology of Marazuela et al. (2018). The location of the piezometers are shown in the centre of the figure.*

In the natural regime, the water table is controlled by evaporation and recharge processes. The experimental data reveal that the evaporation has a clearly seasonal behaviour, with average minimum values of 1050 mm·yr^{-1} from June-July and maximum values of 4450 mm·yr^{-1} from December-January. In addition to this annual

evaporation wave, there is a daily day-night cycle that also modulates the evaporation rate. These values decrease exponentially until extinguishing at water table depths between 0.5 and 2 m, as evidenced by the lysimeter data (Fig. 4.9).
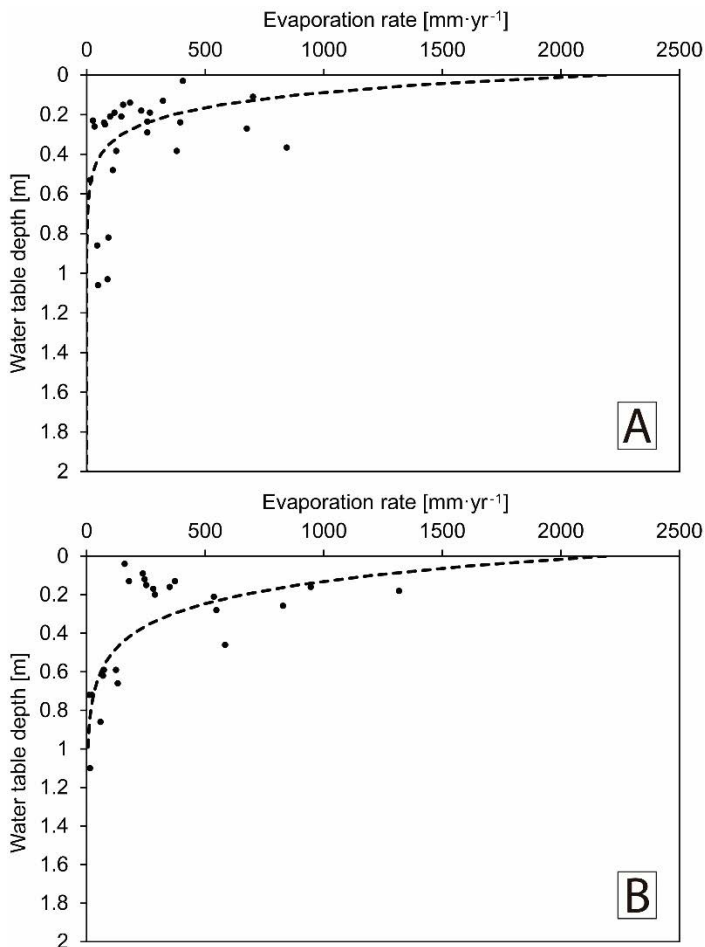
Figure 4.9. Experimental data of evaporation rates taken by lysimeters located in the evaporation zones A3 and A7. The fit of the average exponential curve was based on the Philip (1957) type curve.

The evaporation process is apparent in the water table evolution mainly as an annual cycle. Thus, the greater evaporation in summer than in winter causes a gradual drawdown from December to June and a gradual rise from June to December. The phase of the sinusoidal effect may change slightly depending on the salt flat zone if any external factor, such as the lateral groundwater recharge that arrives from the mountains, generates a change in the water table depth. In Fig. 4.10,

the correlation between the hydraulic heads and the normalized evaporation function applied for each average value of evaporation is shown. This normalized function was computed based on the evaporation data of the open water reservoir (evaporation trays data). The water table oscillations due to the annual cycle of evaporation reach a half metre in the mixing zone, where the water table is closest to the topographic surface and the evaporation rate is higher (Fig. 4.8). However, in most modelled areas the maximum oscillation caused by evaporation is centimetres or a few decimetres. This effect can be observed in detail in the observed and modelled hydraulic heads shown in Fig. 4.8 during the pre-operational period. The wells P1, P2 and P3 located in the north-eastern mixing zone exhibit higher oscillation ranges due to evaporation, which is approximately 0.10 to 0.50 m. Additionally, the annual cycle of evaporation is evidenced in the wells P5, P10 and P11, with amplitudes from approximately 0.10 to 0.30 m for the eastern and south-eastern mixing zones. Furthermore, during the pre-operational period, this cycle is also evidenced in the wells P4, P6, P7 and P9 of the brine pumping area, with oscillation rates between 0.10 and 0.20 m. These field data confirm that in the natural regime, both the nucleus and the mixing zone evaporated the groundwater. The mixing zone experienced a higher evaporation rate due to the shallower water table and the existence of lakes connected to the water table. This is coherent with the lower amplitude of the evaporation cycle in the salt flat nucleus relative to the mixing zone.
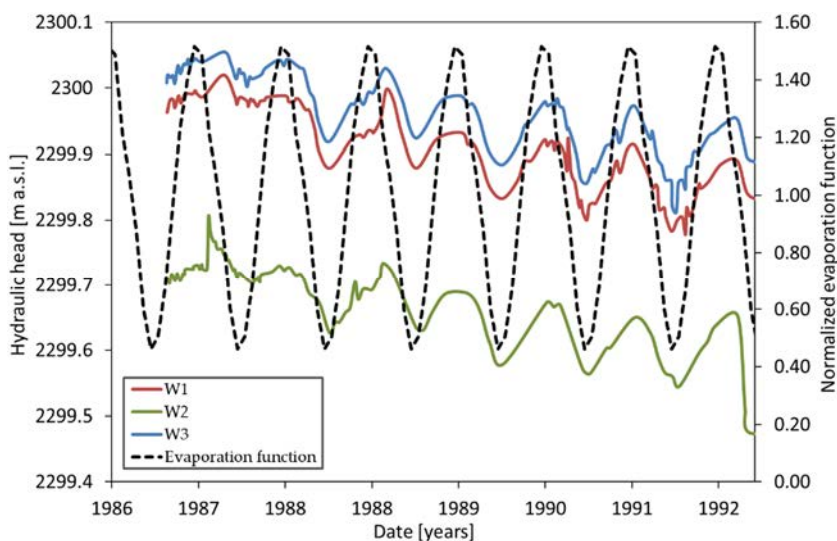
Figure 4.10. *Correlation between hydraulic head data from observational wells W1, W2 and W3 (see its location in Fig. 4.1) and the normalized evapotranspiration function.*

The meteorological data provided by the weather stations reveal that rainfall rate ranged from less than 10 mm·yr^{-1} in the salt flat nucleus to greater than 160 mm·yr^{-1} in the eastern mountains (Fig. 4.3A). The rainfall events are very scarce, and they are concentrated from December to March. The amount of precipitation is controlled by the climatic cycles, and it is subject to cycles of 5, 10 or more years, coinciding also with the El Niño – Southern Oscillation (ENSO). In the salt flat nucleus, the precipitation decreases from north to south and from east to west, since the clouds discharge the water before reaching the south-western end of the salt flat.

The effect of the rainfall recharge on the water table depends on its location. Rain events can occur both directly on the salt flat nucleus and mixing zone or in the mountains. An abrupt and instantaneous rise in water table is observed with each direct rain event on the salt flat nucleus and the IMZ due to the small thickness of the unsaturated zone. However, some rain events exhibit no direct impact on the water table or a linear relationship between the amount of rainfall and the disturbance of the water table (Fig. 4.11). This behaviour is a consequence of the type of soil, the spatial distribution of the rain event and the temporal lag between rainfall events which modify the detention. Owing to the great extent of the basin, the rain events did not present a homogeneous distribution along the entire basin, making it necessary to analyse the isohyets map for each event and translate this into the time series of the numerical model. Thus, rain events with high rainfall rates and great spatial extent (rain events identified at several weather stations) are those that give rise to greatest abrupt rises of the water table (Fig. 4.11). This type of perturbation can trigger abrupt ascents of several decimetres of the water table, as observed in Figs. 4.8 and 4.11. Black arrows denotes each of the rain events than caused a strong rise of the water table, with eight being the most important during the last 30 years.

Regarding the rain events that occurred in the mountains, however, the perturbation that they produced in the water table of the salt flat is not obvious. There, the rain water infiltrates the soil and recharges aquifers. The amount of water recharged in the eastern mountains is very large due to the low detention in the soil caused by the presence of fractured soils (ignimbrites) and the scarce vegetation. However, despite the large volume of water recharged, the perturbations to the water table were not evident in the salt flat. This is because due to the greater thickness of the unsaturated zone in the mountains and the distance from the mountains to the salt flat nucleus, the effect of the rain events is damped.
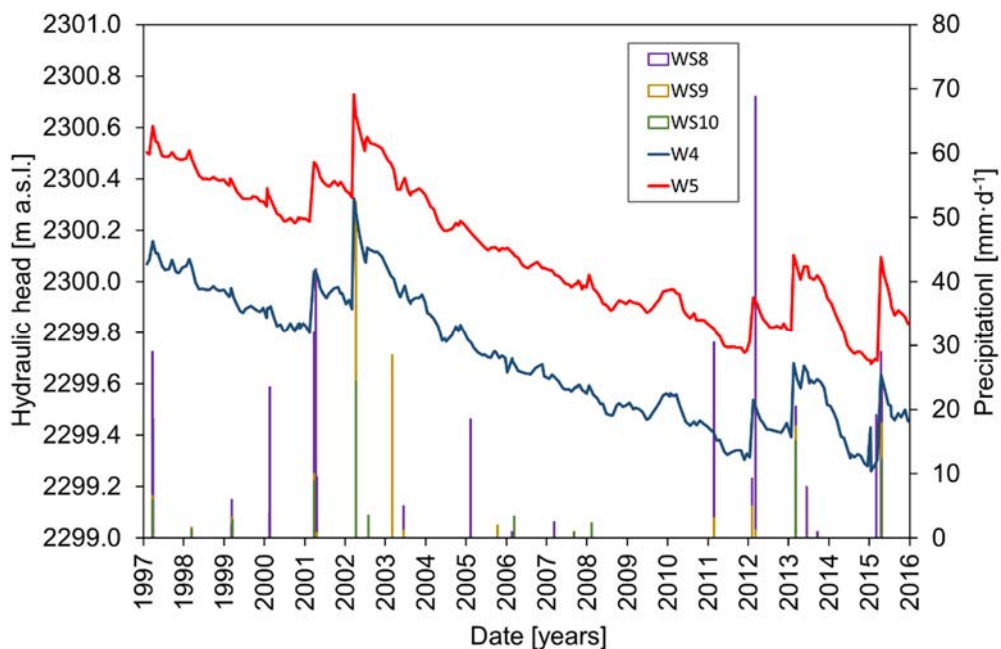
Figure 4.11. *Correlation between rain events registered at three weather stations (WS8, WS9 and WS10) (see its location in Fig. 4.3A) and the hydraulic head values of the observational wells W4 and W5 (see its location in Fig. 4.1).*

In the salt flat nucleus and the IMZ, the coupling of both natural processes, evaporation and recharge, results in a water table evolution dominated by a gradual decay due to evaporation which is disrupted by sudden level rises caused by episodic rain events. The natural trend of the water table is to gradually decay because the evaporation is greater than the recharge for most of the time period studied. This effect is evidenced by the evolution of the hydraulic heads of the P4, P8, P9 and P10 wells (Fig. 4.8), where the decreasing natural trend due to evaporation is only perturbed by the episodic rain events.

In the EMZ, the gradual decay caused by evaporation is damped even though the evaporation rate is the highest. This is because the mixing zone acts as a hydraulic barrier that isolates the two systems, the salt flat nucleus and the IMZ on one side and the main recharge area (mountains), the alluvial fans and the EMZ on the other, with the domains separated by the MMZ. In the EMZ, the rain events did not exhibit such a direct response in the water table, especially those far away from the intersection of the mixing zone with the land surface. The lateral groundwater

recharge dominates the surface recharge, and the unsaturated zone becomes wider, weakening the direct effect of the rain. This process results in fairly constant hydraulic heads over time even though they are affected by evaporation and surface recharge (see the evolution of the hydraulic heads of the P2, P3 and P5 wells in Fig. 4.8). As a consequence of the barrier effect exerted by the mixing zone, the hydrodynamics of the salt flat nucleus and the IMZ are those of pools that are quasi-isolated from the groundwater that arrives from the mountains as lateral recharge. The groundwater movement in these areas (nucleus and IMZ) is much slower and is controlled mainly by density-driven forces.

4.4.2. Anthropogenic impacts

Under the natural regime, evaporation and recharge control the hydrodynamics and water table of the salt flat. However, in the Salar de Atacama there has been intensive brine exploitation, whose potential impacts on the natural hydrodynamics require analysis and quantification to extrapolate its behaviour to other salt flats.

4.4.2.1. Water table evolution

The water table evolution results from the numerical model shows the origin and evolution of different water table drawdowns as a consequence of the pumping of brine (Figs. 4.7 and 4.8). Prior to 1994, the brine pumping performed in the southern area of the salt flat nucleus by ALB did not produce large disturbances in the natural regime. In 1994, the first effects of the pumping appeared, although they were still incipient and only located in the southern zone of the nucleus. In 2000, the affected area spread and more acute pumping depressions developed in the southern area. In addition, the effects of the reinjections in the central-western zone of the nucleus were also evident. This situation was accentuated in 2005, when the southern water table drawdowns caused water heads lower than 2296 m a.s.l. In 2010, the southern drawdown cone continued to increase, and a new cone of depression was evident in the south-western sector. Both cones reached minimum hydraulic heads in 2015, with values below 2,292 m a.s.l.

This gradual drawdown of the water table produced a change in the location of the regional minimum hydraulic head, which moved from the eastern mixing zone or close to it to the southwestern salt flat nucleus (the main brine pumping area).

However, the water heads in the mixing zone and outdoor areas remained practically constant throughout this period. This is the same as saying that until now, the salt flat nucleus has been the only one that has clearly suffered the effects of brine pumping. This may be explained by both the isolating effect of the mixing zone already described above and the important reduction of the evaporation rate in the nucleus caused by the drawdown of the water table. Indeed, as the evaporation rate from the groundwater is a function of the water table depth, the brine pumping causes an exponential decay in the evaporation rate, which results in a dampening of the water table. This effect of the water table is clearly evidenced in the piezometers P7 and P8 (Fig. 4.8), which are located in the pumping area. The hydraulic heads of these piezometers clearly described the annual oscillations of evaporation during the pre-operation period, similar to the piezometers located far from the influence area of the pumping, but during the operational period, these oscillations disappeared as a consequence of the drawdown of the water table, indicating that evaporation process stopped as a result of the brine pumping. It is undeniable that the dependence of the evaporation rate on the water table depth enables any salt flat to counterbalance the increase and decrease of the entries of their basins. This makes salt flats and their ecosystems fairly stable over time on a geological scale, since wet periods with more rainfall would imply a rise in the water table that would automatically trigger an increase in the evaporation rate and therefore slow down this water table rise. In the same manner, a drier period would lead to inflows reduction in the basin due to rainfall, which would lead to a drawdown of the water table. The decrease in water table would cause a reduction in evaporation rate, which would slow down this water table drawdown. This effect is termed in the present work the damping capacity of the water table, which is a property of all salt flats that acts attenuating both natural and anthropogenic oscillations.

The damping capacity of the salt flats water table for natural oscillations is partially effective for anthropogenic perturbations of the basin water balance. However, to understand how the damping capacity responds to anthropogenic disturbances generated by brine pumping, it is necessary to delve into how the water balance has evolved at the basin scale during its transition. Thus, brine pumping beyond the natural evaporation outflow would cause irreversible depletions of the water heads until recharge was able to replace the pumped brine.

4.4.2.2. Water balance evolution

Therefore, it is necessary to analyse the water balance evolution computed by the 3D numerical model during the pre-operational and operational periods to advance the knowledge of the damping capacity of a salt flat when anthropogenic perturbations occur. First, the evolution of each inflow and outflow of the basin during the natural and the anthropogenic regimes is shown and discussed. Second, the effects of brine pumping in the water balance and the counterbalance that the damping capacity has produced in water balance are evaluated.

In the case of Salar de Atacama, the system was dominated by a negative water balance, which was counteracted punctually with rain events, especially during wet periods. The total inputs along the modelled period were $1.39 \cdot 10^{10}$ m³, and the total outputs were $1.44 \cdot 10^{10}$ m³ (Fig. 4.12). The resulting negative imbalance was $5.00 \cdot 10^8$ m³, which was less than the volume of pumped brine.
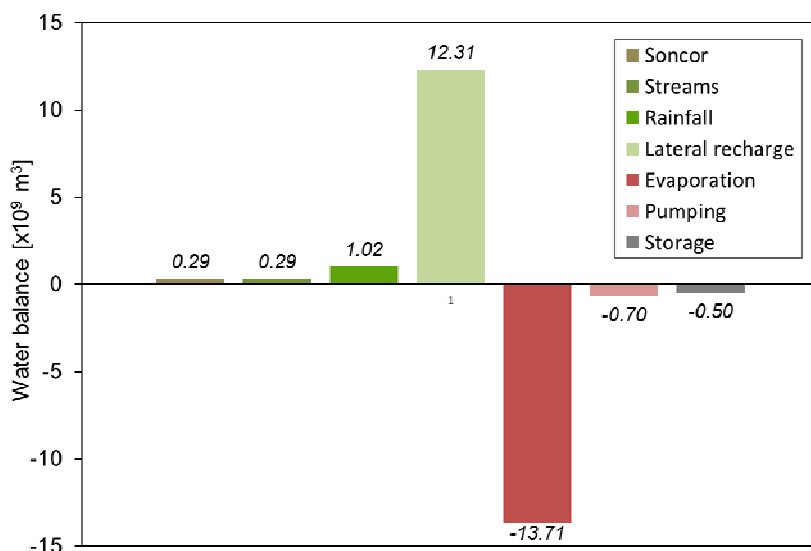
Figure 4.12. *Total water balance resulting from the 3D transient-state numerical model.*

As observed in the total water balance of the numerical model for the period from 1986-2015 (Fig. 4.12), 89 % of the inflows to the salt flat were produced through the deep lateral recharge from the water infiltrated into the mountains. The remaining 11 % comprised rainwater fallen directly on the domain (7 %), infiltration from streams (2 %) and infiltration from the overflow of the Soncor Lake system (2 %).

The outflows of the system were produced by evaporation (95 %) and by extraction of brine (5 %). The Cauchy-type boundary condition exhibited adequate performance as the inflow produced through this boundary condition was less than 5 % of the outputs, and both remained constant during the total modelled period.
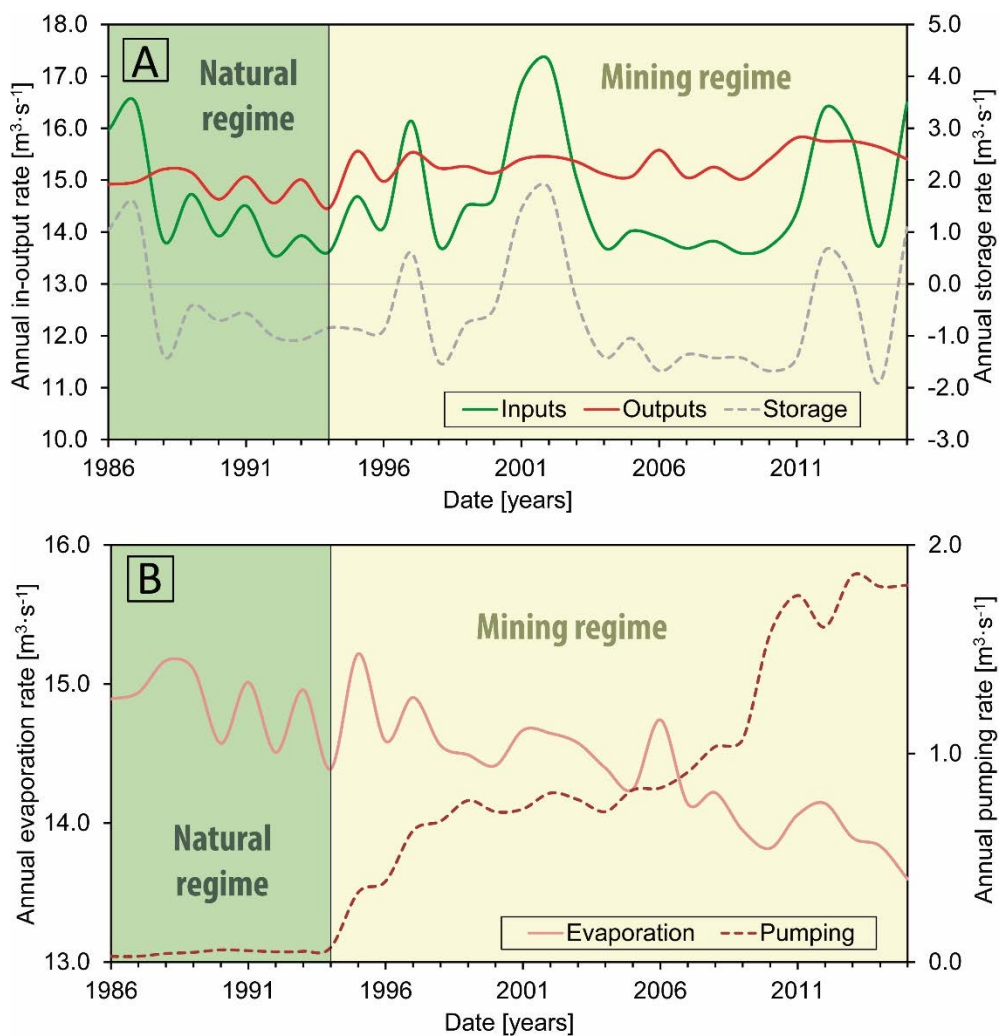
Figure 4.13. *Water balance evolution. Continuous lines correspond to the primary vertical axis and dashed lines correspond to the secondary vertical axis. A) Total inputs, outputs and storage rates. B) Total evaporation and pumping rates.*

The temporal evolution of the inflows, outflows and storage over time is shown in Fig. 4.13. The annual inflows oscillated between 13.54 $m^3 \cdot s^{-1}$ and 17.31 $m^3 \cdot s^{-1}$, whereas the outflows had a lower oscillation range, between 14.46 $m^3 \cdot s^{-1}$ and 15.82

m$^3 \cdot$s^{-1}. The inflows to the system were mainly represented by the rainwater recharge, which depends on the climate cycles. This results in inflow oscillations over time. On the other hand, the evaporation depends on the potential evaporation, which may be considered similar every year (taking into account interannual variability), and on the water table depth, which decreased throughout the modelled period but was countered by the brine pumping (Fig. 4.13B). Consequently, the outflows of the system exhibit lower oscillation amplitudes than the inflows.

In the Salar de Atacama, the natural water balance was modified by the beginning of the brine exploitation. From then on, a new negative component was added to the water balance of the system. However, there is no linear relationship between the water pumped and the decrease in storage. This behaviour is associated with the damping capacity of salt flats. When a certain volume of brine is extracted, a drawdown in the water table is generated, which causes a reduction in the evaporation rate due to an increase in the thickness of the unsaturated zone. Therefore, an increase in the brine pumping rate implies a decrease in the evaporation rate, counteracting, in part, the effect of brine pumping on the total water balance (Fig. 4.13B). Although the drawdown of the water table may favour the influx of water from the side of the salt flat or from the depth, which are difficult to assess, the main factor responsible for the damping capacity is the modification of the evaporation rate. From an ecological point of view this damping effect may reduce the impacts of the mixing zone on lake and wetland ecosystems. However, it must be considered that the damping capacity is limited to the movement of the water table at depths shallower than 2 m. Below this depth, the evaporation rate goes to zero, and the damping capacity is lost.

The biggest contributor to the damping capacity of the salt flat water table is the nucleus, at least when the natural or anthropic disturbances are small or moderate. This is due to two reasons: (1) the large extent of the nucleus and (2) the location of the brine pumping wells. The nucleus of the salt flats generally has a large extent, which implies that even though the evaporation rate is much lower than that of the mixing zone, a small rise or fall of the water table leads to a significant change within the total water balance. This is applicable for both natural and anthropogenic disturbances. In addition, because the brines are more evaporated and therefore have a higher economic value in the salt flat nucleus, the brine pumping wells are located

in that sector. Due to brine pumping, the nucleus suffers the greatest impact in terms of hydraulic heads and consequently evaporation rates.

4.5. Conclusions

The coupled natural and anthropogenic processes that control the hydrodynamics of many salt flats were addressed using the Salar de Atacama as a case study. A three-dimensional groundwater flow model was used to reproduce the water table evolution of the Salar de Atacama from 1986 to 2015. This also permitted quantifying the water balance impacts. The three-dimensional approach for the modelling of the groundwater flow in salt flats was demonstrated to be a power tool to evaluate natural processes and anthropogenic impacts and to be of great utility for the management of these systems.

The natural hydrodynamics of the Salar the Atacama was evidenced during the pre-operational period (1986-1994). In the natural regime, the water table exhibited a gradual drawdown because the evaporation was greater than the recharge most of the time. This negative balance was counteracted by some sharp rises produced by direct rainfall events on the salt flat. The lateral recharge that arrived from the mountains did not produce abrupt perturbations to the water table because the rainfall events in the mountains were damped by the distance from the recharge zone and the great thickness of the unsaturated zone.

The natural regime of the water table was disturbed by the brine pumping performed in the Salar de Atacama during the operational period (1994-2015). The pumping causes a fall in the water table, which results in a decrease of the evaporation rate that at least partially compensates for the pumped brine. This effect is termed in the present work the damping capacity of the salt flats. Due to this process, salt flats have a capacity for damping their water tables in response to both natural and anthropogenic disturbances, which is of great importance for the management of lake and wetland ecosystems and brine mining. The limit of the damping capacity of salt flats is defined by the evaporation extinction depth, which is between 0.5 and 2 m.

Chapter 5

Towards more sustainable brine extraction in salt flats: Learning from the Salar de Atacama

5.1. Introduction

Salt flats are zones of discharge by phreatic evaporation often located in arid to hyperarid climates. Long-term evaporation has allowed the accumulation of a large thicknesses of evaporite rocks and has enriched pore brines in lithium, potassium, boron, iodine and nitrates (Corenthal et al., 2016; Risacher et al., 2003; Warren, 2010; Yechieli and Wood, 2002). These brines contain essential raw materials for batteries, fertilizers and detergents among others (Evans, 1978; Hardie, 1991; Kesler et al., 2012; Lowenstein and Risacher, 2009; Rissmann et al., 2015). The brine is pumped and then transported to evaporation pools where is progressively concentrated until the salts of interest precipitate (Flexer et al., 2018).

The shallow water table favours salt flats usually harbour lake and wetland ecosystem recognized worldwide for their uniqueness. However, the ecological richness of these sensitive ecosystems can be affected by brine pumping as a consequence of the reduction in the discharge by evaporation that causes the drawdown of the water table (Acosta and Custodio, 2008; Scheihing and Tröger, 2018). The free water surface evaporation occurs from lakes and the phreatic evaporation takes place from the shallow water table of salt flats as a function of the water table depth (Philip, 1957). Thus, the increase in thickness of the unsaturated zone caused by brine pumping breaks the natural water balance of the basin (Marazuela et al., 2019b). In addition to the pumped outflow and the hydraulic parameters that are characteristic of each salt flat (Houston et al., 2011), the distribution of the pumping wells is the factor that determines the spatio-temporal evolution of these impacts.

Until now, concessions made by public authorities to mining companies almost always establish limits in terms of the maximum volume of brine that can be extracted. The design of the operation, that is, the distribution of pumping wells, is not usually considered and is ultimately based on the interests of the mining company. Thus, it is of great importance to advance the knowledge of the impacts that brine pumping induces in the evaporation discharge of salt flats to establish the most efficient designs for brine exploitation in terms of ecological impact.

The Salar de Atacama, which is the third largest salt flat globally and it is located in the Central Andean Range (Northeast of Chile), was chosen as a case study to

evaluate the impacts caused by brine pumping on the water table and evaporation discharge of salt flats, since it is the best known from the hydrogeological point of view favoured by its outstanding ecosystems and the intense mining pressure carried out to extract Li-rich brines worldwide (Ide and Kunasz, 1990; Kesler et al., 2012; Liu et al., 2019; Munk et al., 2016).

The hydrodynamics of the Salar de Atacama was stablished under natural and anthropogenic regimes (Marazuela et al., 2019a and 2019b). In this endorheic basin, the main recharge occurs by infiltration of rainfall in the eastern volcanic arc and the discharge is produced by phreatic evaporation in the marginal zone and salt flat nucleus. The marginal zone matches the saline interface and its mixing zone which results from the density contrast between the laterally recharged freshwater and the evaporated brine of the nucleus (Boutt et al., 2016; Marazuela et al., 2018; Tejeda et al., 2003). Because rainfall recharge can be considered undisturbed by the effects of mining, the focus in terms of brine pumping impacts on the water balance should be the evaporation rate. Evaporation occurs mainly from the water table, which is very close to the land surface and tends to rise by capillarity (Grilli, 1985; Grilli and Vidal, 1986; Houston, 2006b; Kampf et al., 2005; Kampf and Tyler, 2006; Muñoz-Pardo et al., 2004).

The evaporation discharge of the Salar de Atacama has been widely discussed during the last decades. Mardones (1986) quantified the evaporation discharge as 5.29 $m^3 \cdot s^{-1}$. Some subsequent manuscripts and technical reports have used this estimation as a reference what has led them to calculate evaporation discharge in the range of 5.17-5.58 $m^3 \cdot s^{-1}$ (Dirección General de Aguas, 2013, 2010, 1986; Muñoz-Pardo et al., 2004). Kampf and Tyler (2006) obtained values of evaporation in a range of 1.60-22.7 $m^3 \cdot s^{-1}$, depending on the multiple calculation methods that were applied, which were based on remote sensing and evaporation zoning. The last quantification established the natural evaporation discharge in 14.90 $m^3 \cdot s^{-1}$ (Marazuela et al., 2019a). Establishing a methodology for estimating evaporation discharge in salt flats and analysing the sensitivity of its uncertainties is, therefore, necessary.

Furthermore, as the evaporation discharge depends on the water table depth and backwards, salt flats have a damping capacity of water balance that makes very complex to predict the impact generated by the pumping. Any natural or

anthropogenic perturbation of the water table causes a change in the evaporation discharge in the opposite direction of the perturbation.

The objectives of this work are (1) to establish a methodology for the estimation of the evaporation discharge in salt flats and to evaluate its sensitivity to the accuracy of the water table depth data, (2) to quantify the spatio-temporal impacts of the brine pumping in the Salar de Atacama case of study and 3) to evaluate the best distribution of brine pumping wells to reduce the ecological impacts on salt flats.

The workflow of the methodology followed to reach these objectives included (1) field measurements of water table depth and evaporation rate (lysimeters and evaporation trays), (2) spatio-temporal analysis of the field data and (3) the application of the knowledge acquired to a numerical model that allows to evaluate the ecological efficiency of brine exploitations (Fig. 5.1). The spatio-temporal analysis was performed for two extreme snapshots of the Salar de Atacama case study: the natural regime prior to brine pumping (year 1986) and (2) the present regime under intensive brine pumping (year 2018). First, the drawdown caused in the water table by brine pumping was quantified. Second, the distribution of evaporation rates in the whole basin and the subsequent reduction in evaporation discharge were estimated.
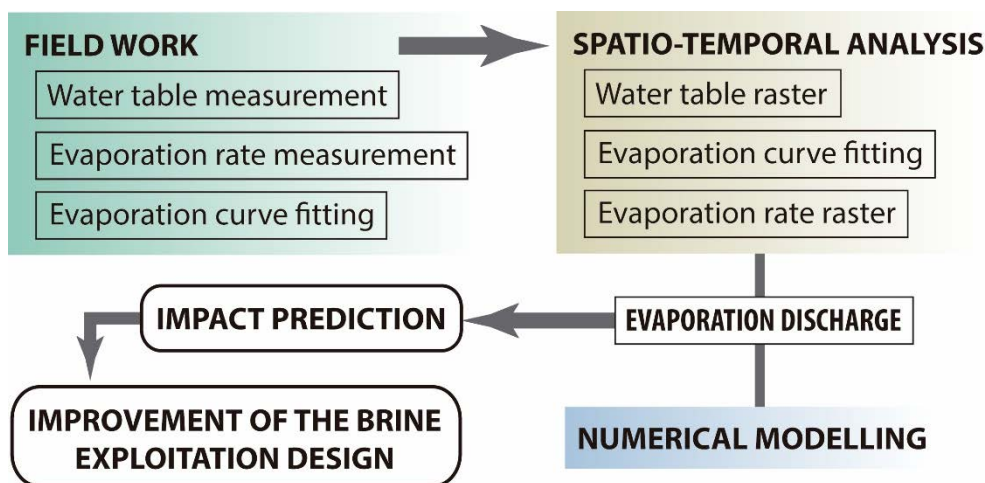
Figure 5.1. *Flowchart of the methodology proposed to assess the evaporation discharge in salt flats and improve the ecological management of brine exploitations.*

5.2. Material and methods

5.2.1. Hydrogeological setting

The Salar de Atacama is located in the Central Andean Range within the Antofagasta Region (Chile), 55 km south of San Pedro de Atacama and 315 km northeast of Antofagasta (Fig. 5.2). The overall shape of the basin has the long axis in the N-S direction and an area of approximately 17,000 km². From the centre to the boundary of the basin, four sub-domains can be distinguished: the salt flat nucleus, the marginal zone or mixing zone, the alluvial sub-domain, and the basement and volcanic rocks.

The Andean Range suffered numerous tectonic phases that have generated reliefs controlled by faults and folds at local and regional scales and depocenters where many of the Andean salt flats developed (González et al., 2009). The Salar de Atacama basin was subjected to an extensive phase during the Oligocene-Lower Miocene, which was followed by a compressive phase that is still ongoing (Arriagada et al., 2006). The basin is delimited by inverse faults that affect the rocks of Palaeozoic age that constitute the basement of the current cover (Jordan et al., 2007). The space generated by the movements of these faults has controlled the deposition of filling materials, including the Vilama Formation which constitutes the nucleus of the Salar de Atacama (> 2300 m a.s.l., metres above sea level) (Muñoz et al., 2002). The geometry of the layers is strongly affected by the Salar and Tucúcaro Fault Systems, which make the eastern block of the salt flat nucleus reach a thickness of approximately 1,400 m against the only 500 m thickness of the western block (Fig. 5.3).

The salt flat nucleus is mainly composed by halite. The deposits that border the salt flat nucleus and that are associated with the mixing zone are composed of carbonates and gypsum according to the precipitation sequence by evaporation (Vásquez et al., 2013). The most external zone of the basin is composed of the basement and the volcanic rocks of the current volcanic arc (> 5,500 m a.s.l.) (González et al., 2009). Previous works have reported a strong variability of the soil characteristics that may condition the evaporation process. Kampf and Tyler (2006) defined the crust of the nucleus as rough halite crust while the crust of the mixing zone was identified as moderately rough crust ranging between soft and hard.
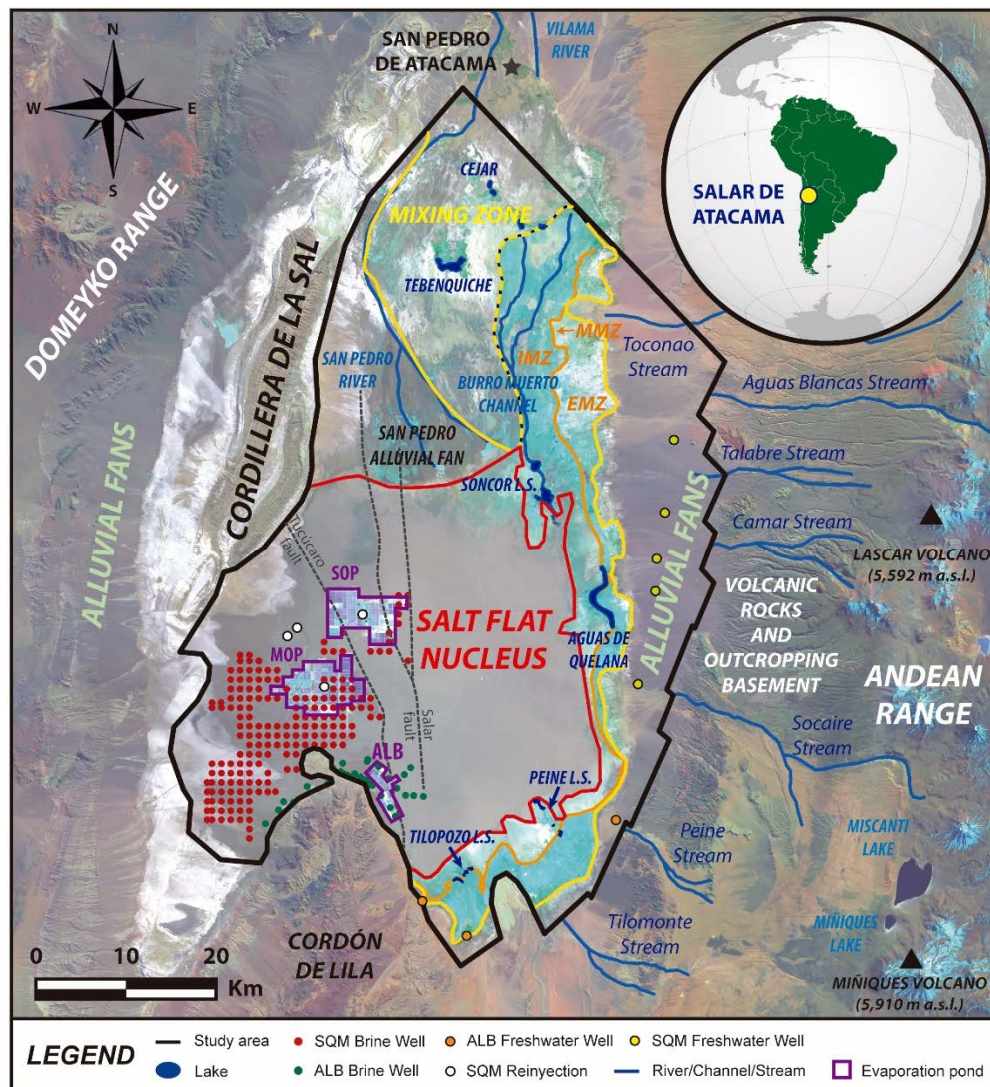
Figure 5.2. *Location of the Salar de Atacama (LANDSAT 8: 27 September, 2016). The three sub-zones of the mixing zone are indicated by orange lettering (internal, IMZ; middle, MMZ and external, EMZ, mixing zone).*

The precipitation reaches more than 120 mm·yr^{-1} in the volcanic arc and it is reduced to less than 10 mm·yr^{-1} in the salt flat nucleus (Marazuela et al., 2019a). The saline interface (mixing zone) located in the marginal zone isolates the hydrodynamics of the system in two environments: the salt flat nucleus and the recharge area. The salt flat nucleus acts as a quasi-isolated area, similar to a pool with very slow flows driven by density contrasts. The groundwater flows coming from

the eastern mountains conducted by potentiometric gradients converges with the convection cell of the salt flat nucleus and push the groundwater to the surface feeding the lakes of the marginal zone (Marazuela et al., 2019a). Thus, the maximum evaporation rates are reached in the marginal zone where the water table is at the minimum depth in the study area. Three zones inside of the mixing zone were differentiated based on hydrodynamics by Marazuela et al. (2018): the internal mixing zone (IMZ), middle mixing zone (MMZ) and external mixing zone (EMZ) (Fig. 5.2). The lake systems Aguas de Quelana, Peine (Salada and Saladita Lakes) and Tilopozo (La Punta and La Brava Lakes) are located in the MMZ associated with the main upward groundwater flows. A special case is the Soncor Lake System (Barros Negros, Chaxa and Puilar Lakes) because it is located in the IMZ, and different sources of groundwater and surface water contribute to maintaining its water level (Ortiz et al., 2014).
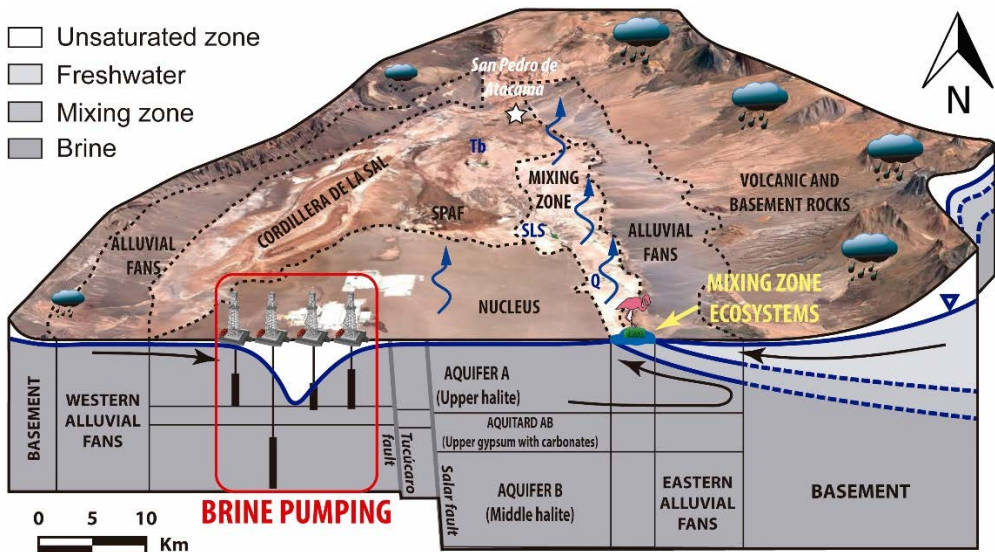
Figure 5.3. *Conceptual model of the Salar de Atacama basin. Q is Quelana Lake, SLS is the Soncor Lake System, Tb is Tebenquiche Lake and SPAF is the San Pedro alluvial fan. Black arrows show the groundwater flow movement direction.*

During the natural regime, prior to brine pumping, the water balance of the basin was established as 14.9 $m^3 \cdot s^{-1}$, which was approximately equal for the recharge and evaporation (Marazuela et al., 2019a). However, the natural regime has been perturbed by brine pumping. The exploitation of the lithium and other raw materials in the Salar de Atacama is carried out by means of pumping along a very dense

network of wells. Several hundred of wells are drilled in the Salar de Atacama at present. The brine pumping was started in 1984 by the Albermale Company (ALB), and since 1994 the Sociedad Química y Minera de Chile (SQM) Company has also conducted brine pumping in the area (Fig. 5.4) (IDAEA-CSIC, 2017). The mining plants MOP and SOP (Fig. 5.2), both of which belonged to SQM, began to pump in 1994 and 1996, respectively. Before 1994, the volume of brine pumped did not exceed 0.05 $m^3 \cdot s^{-1}$; however, from 1994 to 2009, the pumped rates reached values between 0.5-1 $m^3 \cdot s^{-1}$, and from 2010 to the present, they have exceeded 1.5 $m^3 \cdot s^{-1}$, with a greater increase expected in the coming years that will reach to values higher than 2 $m^3 \cdot s^{-1}$.
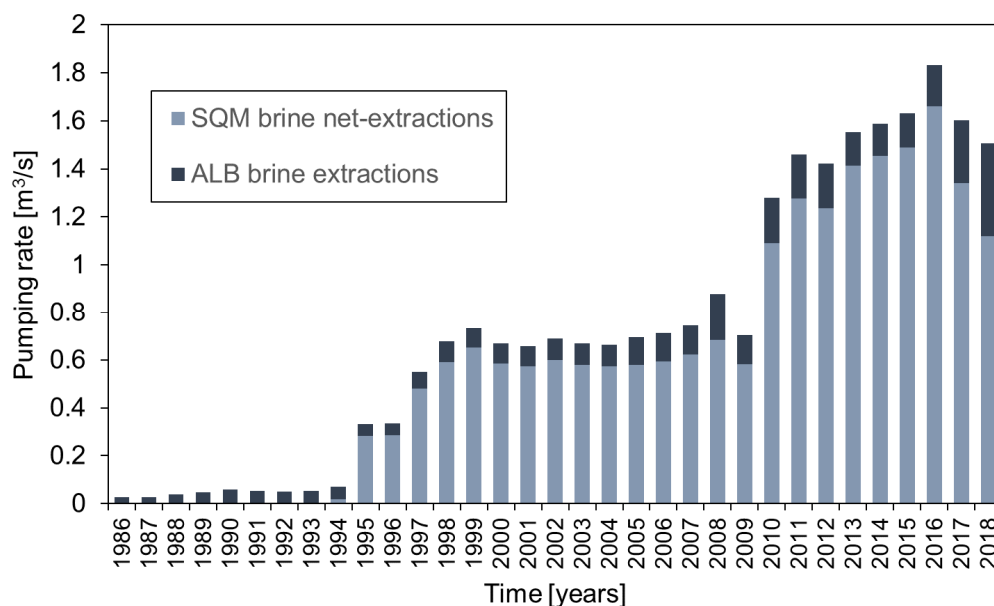
Figure 5.4. Temporal evolution of the brine extractions in the Salar de Atacama. In the case of the SQM Company, the pumping rate consider the net value that is to say the brine pumping minus the reinjections from the evaporation ponds.

5.2.2. Measurement of evaporation rates

The estimation of the evaporation rate required two different approaches depending on the type of evaporation, i.e., evaporation from free water surface or phreatic evaporation. The first type of evaporation occurs in areas occupied by water bodies open directly to the atmosphere. This type of evaporation occurs in the perennial lakes located in the marginal zone and extends a total area of 3.57 km^2. In the remaining areas of the mixing zone and in the nucleus, the main responsible for

the groundwater discharge is the phreatic evaporation favoured by the shallow water table.

The rates of both, free water surface and phreatic evaporations, were measured in the field. The first one was measured with evaporation pans, and the second one with lysimeters. Furthermore, a spatio-temporal analysis of the evaporation discharge, which included these measurements, was performed.

The zoning adopted for this study is shown in Fig. 5.5. This zoning considered the different types of soil reported by Mardones (1998) and the after modifications performed by Marazuela et al. (2019a).
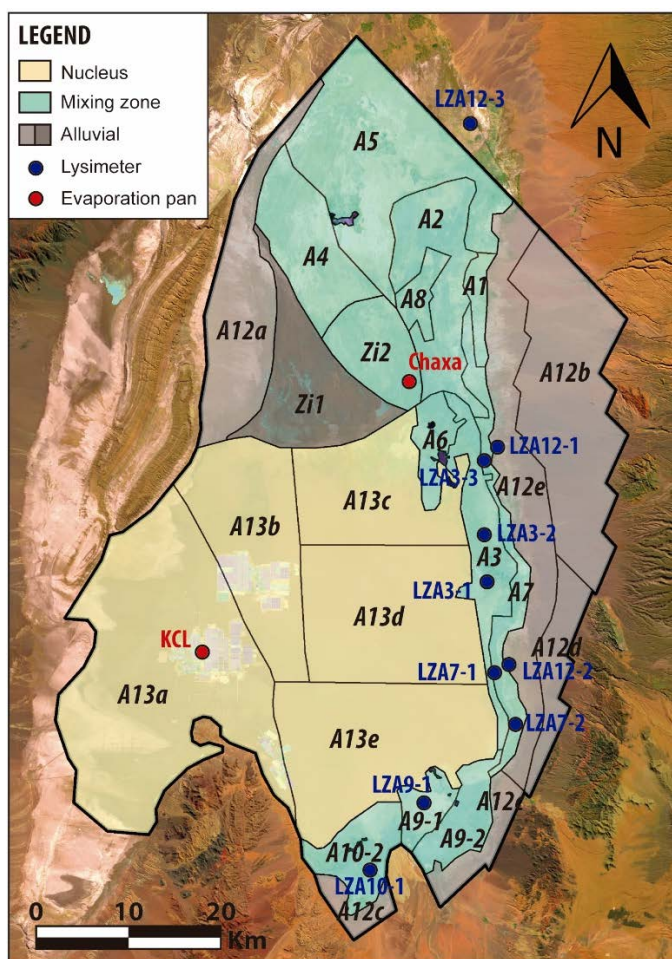
Figure 5.5. Evaporation zoning of the Salar de Atacama basin. The locations of the pan evaporation and lysimeters are shown.

5.2.2.1. Evaporation from free water surface: evaporation pans

The evaporation rate in the free water surface was measured in three evaporation pans located in the nucleus and mixing zone (see their locations in Fig. 5.5). Evaporation pans were used to measure the water evaporating from a tank of regular dimensions. The Class A model of the U.S. National Weather Service was chosen for this purpose (Brutsaert, 1982) (Fig. 5.6A). Tanks were cylindrical in shape and were 120.65 cm in diameter and 25.4 cm deep. They were installed on a wooden platform, positioning the bottom of the tanks 10 cm above the surface of the soil to allow the flow of air below the tank. The tanks were filled with freshwater up to 5 cm from the top edge and were refilled when 2.5 cm of water had evaporated. The evaporation rate was estimated using a data logger that measured the water level oscillations. Because the dimensions of the tanks were known, the calculation of the evaporation rates was direct.
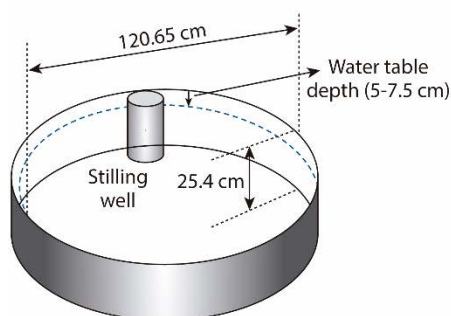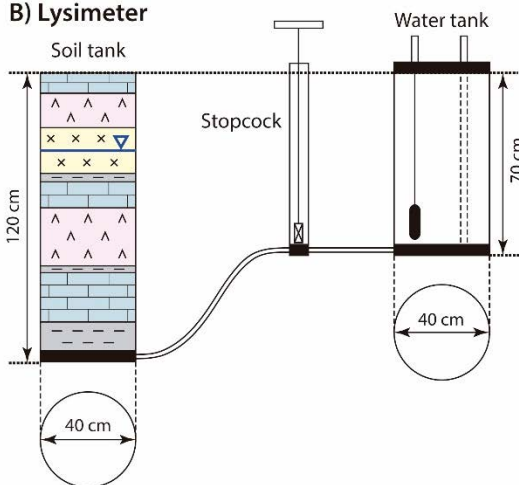
Figure 5.6. *Designs of the A) pan evaporation and B) lysimeter installed in the Salar de Atacama.*

Measurements of pan evaporation (E_p) are, in general, greater than the potential evaporation (E_0) due to the characteristics of the instrumentation and the salinity of the water. The first limitation is compensated through an empirical correction coefficient known as the pan coefficient (K_p). This coefficient was estimated in previous works around 0.75 for the Salar de Atacama considering its climatic and environmental features (Dirección General de Aguas, 2014, 2010; HARZA, 1978). The salinity coefficient (K_s) accounts for the effect of salinity on the water activity

(Obianyo, 2019). An annual average value of 0.94±0.02 was calculated from major element concentration analysed in the Chaxa lagoon using the PHREEQC software and the pitzer.dat database (Parkhurst and Appelo, 2013). This value is close to 0.95 calculated from average salinity values (Ide, 1978). Therefore, the calculation of the potential evaporation was performed as follows:

$$E_0 = E_p \cdot K_p \cdot K_s \tag{5.1}$$

5.2.2.2. Phreatic evaporation: lysimeters

The measurement of the phreatic evaporation rate was carried out using 10 lysimeters (lysimeter locations are shown in Fig. 5.5). Lysimeters data corresponded to the period from August 2015 to June 2018. The lysimeters were distributed in order to occupy the largest possible area of the mixing zone, where the highest evaporation rates occur and the largest range of water table depths is currently available.

Each lysimeter is composed of two connected tanks buried in the ground (Fig. 5.6B). The first tank was filled with local water (water tank) and the second tank (soil tank) contained an unaltered soil sample to maintain the hydraulic characteristics under natural conditions. The water level in both tanks was the same because, when connected, the pressures were equalized. Evaporation from the ground occurred in the soil tank, and the level variations were measured by the pressure data logger installed in the water tank. The lysimeter measured the variation in the water level due to evaporation. Determining the level difference for a known time interval and considering the measurements of the water tank allowed us to calculate the volume of water that evaporated over this time interval; therefore, the evaporation rate was obtained.

For the estimation of the evaporation rate (E) with the water table depth, the methodology of Philip (1957) was adopted. This method correlates the evaporation rate measured at the surface with the water table depth through an exponential adjustment:

$$E = E_0 \cdot e^{(-b \cdot z)} \tag{5.2}$$

Where E_0 is the potential evaporation from free water surface, z is the water table depth, and b is an adjustment parameter that was obtained by fitting the

experimental data with the linearized form of the equation (2) via the Gnuplot 5.2 software (Williams and Kelley, 1986).

The data obtained of each lysimeter were plotted together representing the maximum variability. This variability was limited by adjusting the envelopes that represented the minimum and maximum evaporation values, similar to other works (Dirección General de Aguas, 2014, 1986; Johnson et al., 2009). The adjustment of each curve was performed by fitting the minimum, average and maximum values of the parameter b.

5.2.2.3. Spatial analysis of the water table depth

Two raster maps that represented the spatial distribution of water table depths and phreatic evaporation rates with a resolution of 200 x 200 m were performed for the years 1986 and 2018 to evaluate the temporal evolution of the discharge produced by phreatic evaporation in the Salar de Atacama basin. These two temporal snapshots represented, in the first case, the natural regime, prior to brine pumping and, in the second case, the current regime under brine exploitation.

The hydraulic head data necessary to perform the water table depth raster were provided by the historical record of SQM S.A. and was complemented with data of Bevacqua (1988), Rio Chilex S.A (1997), Golder Associates (2017a, 2017b) and Rockwood-Lithium (2015). The calculation of the water table depth from the hydraulic heads was conducted by considering the elevation of the ground. This elevation was measured in a topographic campaign with differential GPS due to the necessary precision and the difficulty of estimating ground elevation by satellite images as a consequence of the scarce topographic gradient and the irregularity of the salt crust. Moreover, control points in the lakes connected to the water table (water table depth equal to 0 m) and in the boundary of the domain were incorporated to properly inter- and extrapolate the measured data. A total of 1066 data points were considered for the 1986 raster, and 1816 data points for the 2018 raster, of which 60 and 401 data points, respectively, corresponded to direct measurements, 856 data points corresponded to boundary conditions in free water surface bodies each case and 53 and 31 data points, respectively, corresponded to the domain boundary to facilitate the extrapolation in the peripheral area. In the cases in which more than one data point was available, the average of the data was

considered. The interpolation between data was performed using the natural neighbour method.

Once the water table depths were estimated for 1986 and 2018, the evaporation rates for both years were estimated. The local evaporation curves for each evaporation zone was fitted using equation 5.2 in which lysimeter data were available (zones A3, A7, A9-1, A9-2, A10-2 and A12). For the salt flat nucleus the mean values of lysimeters LZA3-2 and LZA3-3 were selected based on their proximity to the nucleus and soil characteristics. For the rest of the evaporation zones, the general evaporation curve resulting from the fitting of data from all lysimeters was used.

In addition, the sensitivity of the evaporation discharge to the water table depth accuracy was evaluated considering a gradual deepening of the water table until 0.5 m below the estimated water table for the years 1986 and 2018. The discharge from the lakes remained constant in all cases.

5.2.3. Numerical modelling

A synthetic parallelepiped model of 12,000 m of sides and 30 m of depth was performed to evaluate the improved brine exploitation design (Fig. 5.7). The model consisted of 6 layers with a total of 76,000 triangular prism elements and was considered a confined aquifer. The mesh was enough fine to avoid numerical oscillations and scale-effects. Finer meshes was evaluated to confirm the accuracy of the results. The hydraulic conductivity was 250 m·d^{-1} and the specific storage was 5·10^{-3} m^{-1}. The FEFLOW code (Diersch, 2014) was used to solve the three-dimensional groundwater flow equation.

Six simulations were carried out considering three initial water table depths and two spatial distributions of the brine pumping wells. The simulations were run over 500 days. The outflows of the model were produced through the top as a consequence of the phreatic evaporation which was implemented using equation 5.1 and the fitting parameters of the nucleus of the Salar de Atacama. For the initial conditions, water table depths of 0, 0.2 and 0.4 m were considered. The inflows of the model were implemented in the bottom and corresponded with the phreatic evaporation value associated with the three different initial water table depths, with rates of 5.84, 2.15

and 0.79 mm·d⁻¹ for the 0, 0.2 and 0.4 m depths, respectively. The sides of the model were considered as impervious.
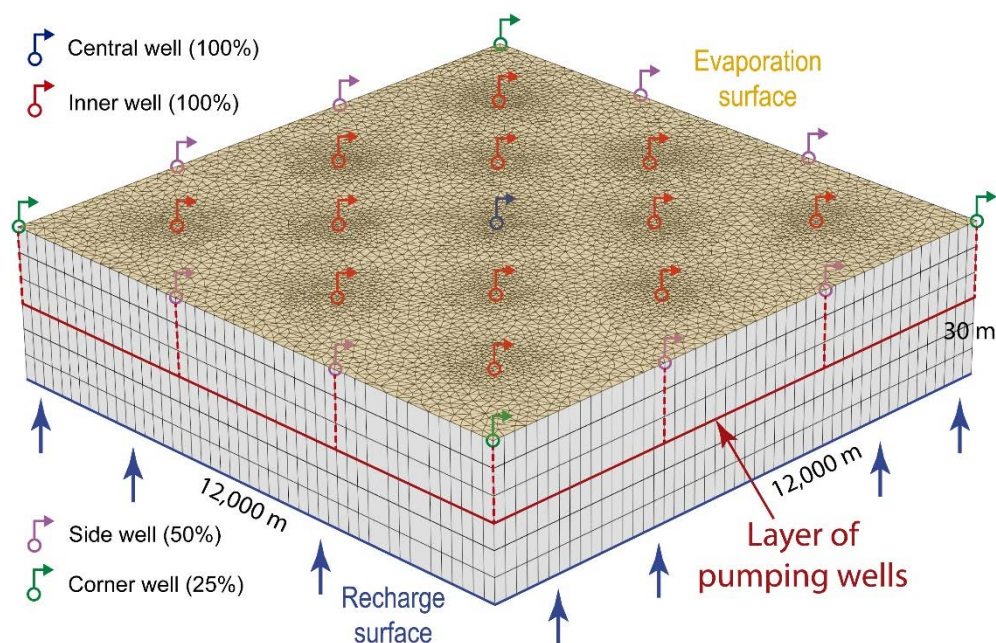
Figure 5.7. *Three-dimensional mesh of the synthetic model performed to study the efficiency of the brine exploitation in salt flats.*

The pumping was implemented with the well-type boundary condition and two extreme distributions were considered: (1) a single-well in the centre of the parallelepiped and (2) a regular network of multiple-wells with a separation distance of 4,000 m. In the second case, the wells located in the sides and corners were analysed considering only a flow pumping of 50 % and 25 %, respectively. A total flow pumping rate of 2 m³·s⁻¹ was implemented in slice 4 (15 m of depth) in both cases.

It is important to highlight that brine pumping is currently carried out in several hundred of wells in the Salar de Atacama based on the distribution of permeability and the lithium concentration (Houston et al., 2011). This numerical model seeks to quantify the effect and possible benefit of a decentralization of the pumps to consider it into future management plans of this or other salt flats.

5.3. Results and discussion

5.3.1. Evaporation rates in the Salar de Atacama

The measured values of the free water surface evaporation rates measured in the pans of KCL and Chaxa are shown in Fig. 5.8. The average value of pan evaporation was 8.2 mm·d^{-1} which after salinity and pan coefficient corrections was reduced to a potential evaporation rate of 5.84 mm·d^{-1}. There was a marked seasonal oscillation, i.e., the maximum potential evaporation rates were recorded in the month of December (summer) and the minimum rates were recorded in the month of June (winter), with values ranging between 8.7 and 2.6 mm·d^{-1}, respectively. The historical series showed no trend of the average evaporation rate in the last two decades, so no impact of climate change on it was appreciated.
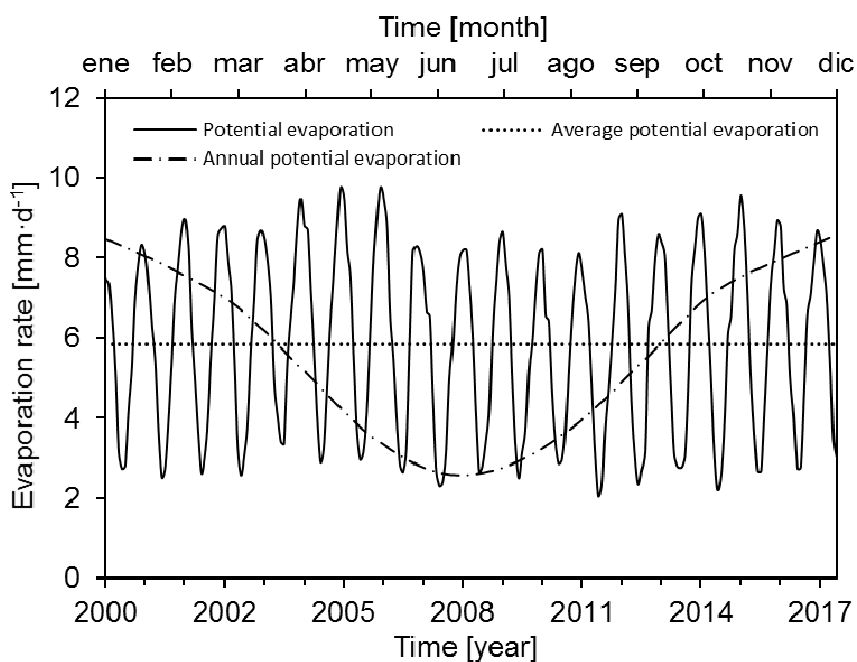
Figure 5.8. *Potential evaporation in the Salar de Atacama considering the data of the evaporation pans KCL and Chaxa.*

The local evaporation curves resulting from the adjustment of the lysimeter data are shown in Fig. 5.9. The measured data show a good fit through the Philip curve except for some anomalous values in the measures closest to the ground of the LZA3-

3, LZA7-2 and LZA12-3 lysimeters. In these three lysimeters record, a data set values follows a vertical trend with depth which could be associated with residual measurement errors when evaporation rates are low. Furthermore, the Philips curve slightly undervalue the measured data for depths close to 0 m in LZA7-1, LZA9-1 and LZA12-1 cases, similar to the results obtained by Grilli and Vidal (1986). This suggests that the potential evaporation could be even slightly greater than the calculated and also an improvement of the Philip curve should be evaluated in future works. The general good agreement between calculated and observed data allows to confirm that the pan coefficient (K_p) adopted for the correction of the evaporation pan is within range. It is usually assumed that the pan coefficient can be as low as 0.35 in hyperarid climates close to cropping areas, depending on the wind speed and the distance of dry fallow (Doorenbos and Pruitt, 1975). However, a value of 0.75 was considered a good approximation for the Salar de Atacama because crops are absent in the area and, moreover, lower values would further accentuate the undervaluation of evaporation rates when the water table is close to the ground surface leading to unrealistic estimations of the evaporation flow. Unlike surface evaporation, no clear seasonality was observed here in the measured data. Most of the exponential curves showed the strongest variability at water table depths between 0 and 0.5 m. In this range the evaporation rate decreased from 5.84 mm·d^{-1} at 0 m to less than 1 mm·d^{-1} at 0.5 m of depth. Only for lysimeter LZA9-1 the measured data showed an evaporation rate greater than 1 mm·d^{-1} at depths greater than 0.5 m. This lysimeter was located in the "soft moderately rough crust" described by Kampf and Tyler (2006) which can explain its greater evaporation rates with respect to the other lysimeters that are located in or near "hard moderately rough crusts". At the other end, the lysimeter LZA3-2 showed the fastest reduction of the evaporation rate with the depth. In this case, the evaporation rate is close to extinction at only 0.3 m of depth which correspond to a very hard crust. In the rest of the lysimeters, the evaporation rates approached the extinction value at depths ranging between 0.5 and 1 m. According to these results, within the same type of soil (Kampf and Tyler, 2006) or zoning (Mardones, 1998) there is a high variability in the evaporation rate. This leads us to think that it is difficult to establish a homogenous evaporation curve for each zone possibly motivated by the fact that there are sharp contrasts of the soil type even within the same zone of defined soil type.
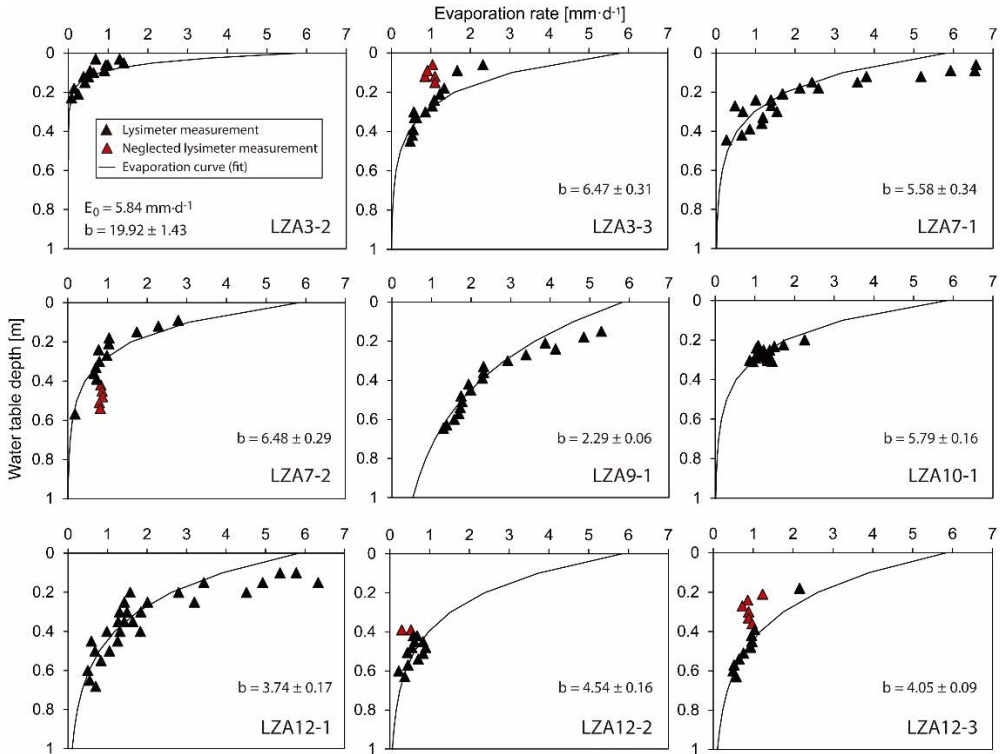
Figure 5.9. Exponential relationship between evaporation rate and water table depth for each lysimeter (see their locations in Fig. 5.4). The data are given in Appendix F. The fit parameters and its error are shown.

Due to the great variability of the measures and the unfeasibility of installing as many lysimeters as sub-types of soils exist, the set of all lysimeter data was used to build the general evaporation curve showed in Fig. 5.10. This general curve represents the maximum variability of the evaporation rate in the Salar de Atacama and may be of great interest when the local curve is not available or a general estimation of the evaporation is required. Because the dispersion is greater when considering a greater number of data, three fits were chosen similarly to (Johnson et al., 2009): lower, average and upper fit. The average fit match fairly well with the fit performed by Grilli and Vidal (1986) for the silt and sulphate crust (marginal zone). At depths very close to 0 m the undervaluation of their fit is higher than showed in the present work. This is mainly because the potential evaporation considered in the present work is higher than the adopted by these authors, 5.84 mm·d^{-1} in front of 4.27 mm·d^{-1}. Even so, our adjustment still shows a certain undervaluation of the measured

values, which can only be solved using the evaporation measured by the evaporation pans without applying correction (Fig. 5.10). Future work should explain this fact. The measurement performed by Grilli and Vidal (1986) pointed the minimum evaporation rate in the salt flat nucleus due to its hard crust. Furthermore, the fit performed for the salt flat nucleus and chloride crust by Grilli and Vidal (1986) is located between our average and lower fits. Summarizing, the average extinction depth at which evaporation can no longer occur may be established at 1 m, although in a conservative estimation this value could increases to 1.5-2 m considering the exception of lysimeter LZA9-1, or even reduces to 0.3 m considering the LZA3-2 lysimeter.
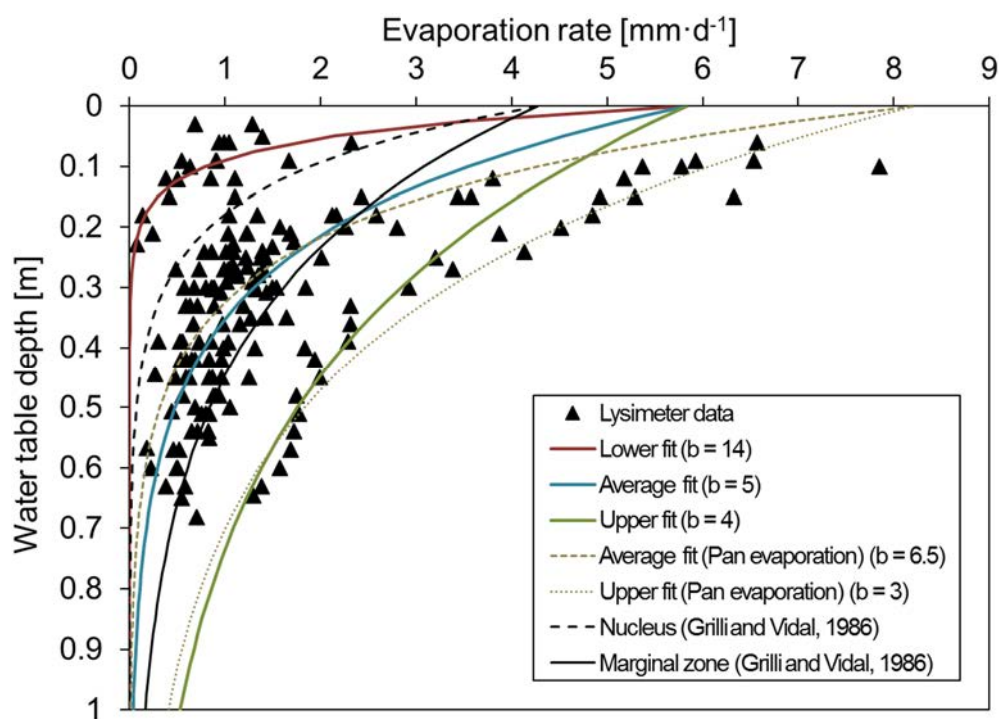
Figure 5.10. *General evaporation curve that shows the decreasing of the evaporation rate with the water table depth considering the total measurements. The fit parameter b is shown in parenthesis.*

5.3.2. Evolution of the discharge by evaporation in the Salar de Atacama basin

The estimation of the evaporation discharge in the Salar de Atacama requires an accurate analysis of the water table depth besides the estimation of the evaporation rate performed in the previous section. Moreover, this spatial estimation needs to

incorporate the temporal evolution of evaporation if determining the impacts of brine pumping on the evaporation discharge is an objective. In a first step, we perform a detailed spatial analysis of the water table depths which, subsequently, is used to quantify the spatial distribution of the evaporation discharge. These estimations were performed for both the natural regime prior to intensive brine pumping (year 1986) and the present regime under intensive brine pumping (year 2018) to quantify the impact in the water balance of the basin.
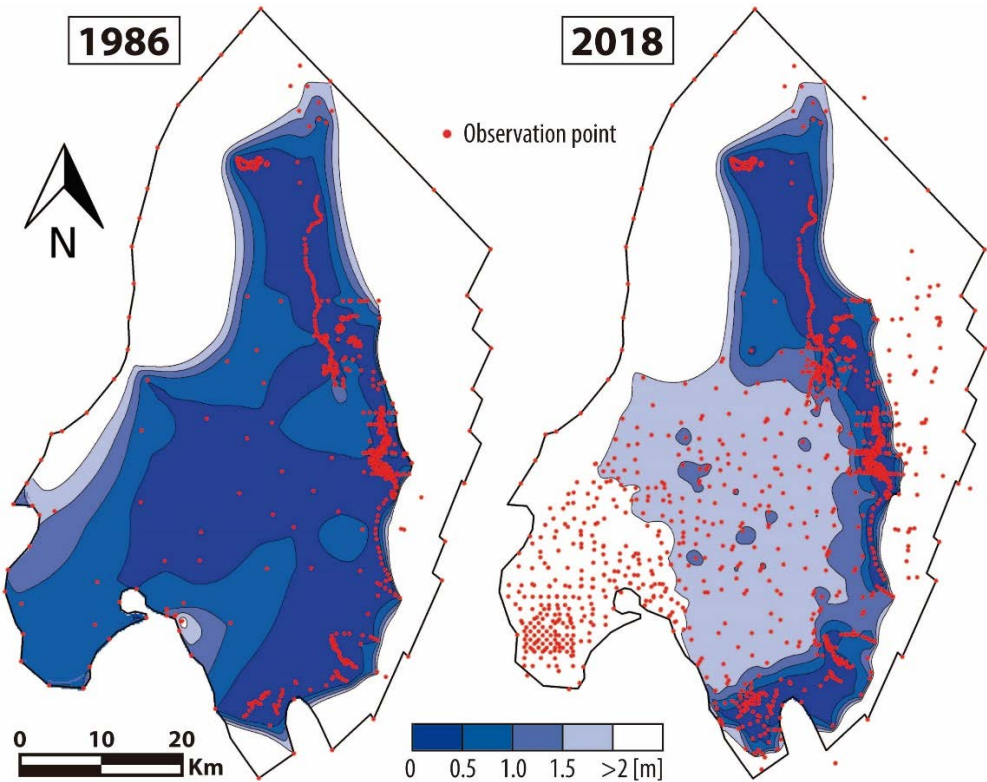
Figure 5.11. Raster maps of the water table depth for the years 1986 and 2018.

5.3.2.1. Water table depth evolution from 1986 to 2018

The water table depths for the years 1986 and 2018 are shown in the rasters maps of the Fig. 5.11. In 1986, the mixing zone had water table depths shallower than 0.5 m. The salt flat nucleus showed depths ranging between deeper than 2 m on the western side, near the western alluvial fans, and shallower than 0.5 m on the eastern side, near the mixing zone. The northwestern and eastern alluvial fans had water

table depths deeper than 2 m in all cases. However, when this water table depth distribution was compared with the present distribution (year 2018), important changes stand out in almost all areas (Fig. 5.12). At present, the water table depths in the northern mixing zone are equivalent to the values in 1986. Something similar happens with the eastern and southeastern mixing zone where only a small increase in depth was identified locally. However, the salt flat nucleus was, quantitatively, the most affected area. The eastern salt flat nucleus evolved from water table depths shallower than 0.5 m in 1986 to depths below 1.5 m in 2018. The western salt flat nucleus had deeper water tables reaching depths below 2 m. This drawdown of the water table was caused by the brine pumping carried out in the south and southwest of the salt flat nucleus.
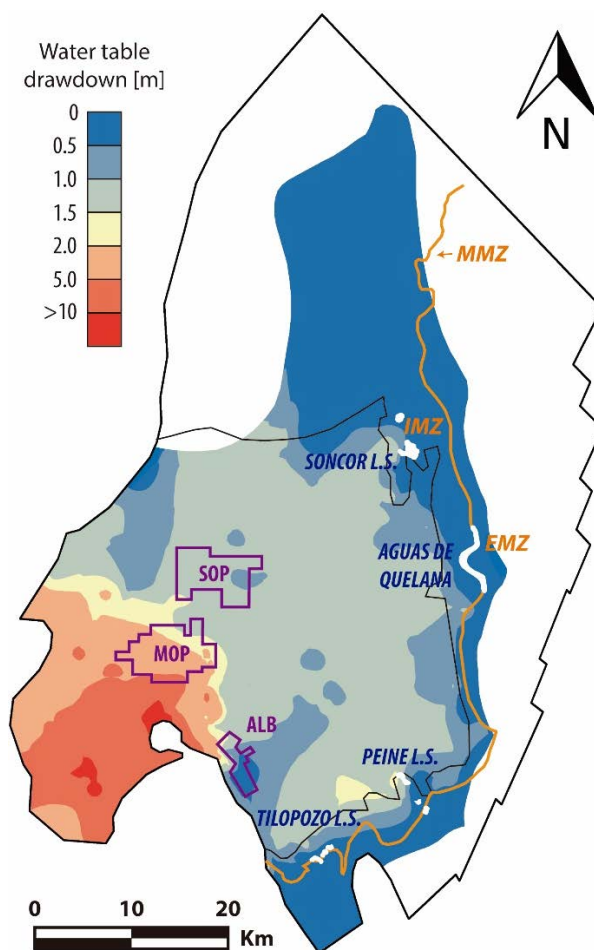
Figure 5.12. Raster maps showing the drawdown evidenced in the Salar de Atacama from 1986 to 2018.

5.3.2.2. Evaporation rates and water balance impacts

The deepening of the water table has an indirect impact in the water balance of the basin as because the phreatic evaporation rate depends on the water table depth, as described above. Thus, the calculation of the evaporation rate for each pixel of the water table depth rasters considering the most adequate evaporation curve for each zone in 1986 and 2018, was performed (Fig. 5.13). The spatial distribution of the phreatic evaporation rates also permitted the accurate estimation of the discharge flows for each evaporation zone. These values are shown in Table 1 for 1986 and 2018.
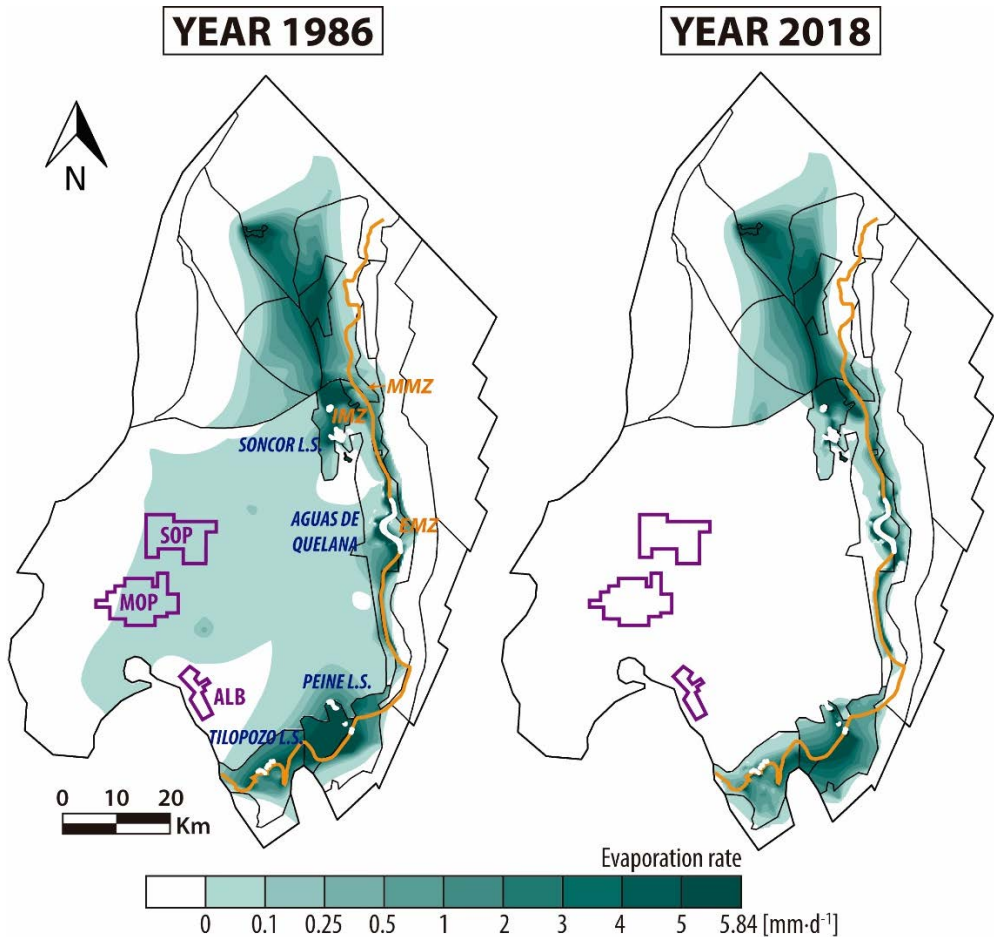
***Figure 5.13.** Raster maps of the evaporation rates in 1986 and 2018.*

Table 5.1. *Evaporation discharge [m³·s⁻¹] quantified for each evaporation zone of the Salar de Atacama (see Fig. 5.5 for the distribution of the evaporation zones) assuming an error of 0 to -0.5 m in the water table measurement.*

Domain	Zone	Calculated		Error -0.1 [m]		Error -0.2		Error -0.3		Error -0.4		Error -0.5	
		1986	2018	1986	2018	1986	2018	1986	2018	1986	2018	1986	2018
Mixing zone	A1	**0.00**	**0.00**	0.00	0.00	0.00	0.00	0.00	0.00	0.00	0.00	0.00	0.00
	A2	**1.38**	**1.80**	0.88	1.18	0.58	0.80	0.40	0.58	0.29	0.44	0.23	0.35
	A3	**1.02**	**0.88**	0.71	0.70	0.67	0.67	0.66	0.67	0.66	0.67	0.66	0.67
	A4	**0.13**	**0.12**	0.08	0.08	0.05	0.05	0.03	0.03	0.02	0.03	0.02	0.02
	A5	**1.63**	**1.81**	1.11	1.23	0.80	0.87	0.61	0.66	0.50	0.53	0.43	0.45
	A6	**1.17**	**0.96**	0.92	0.83	0.77	0.76	0.67	0.71	0.62	0.68	0.59	0.67
	A7	**0.73**	**0.65**	0.46	0.41	0.32	0.29	0.25	0.22	0.21	0.19	0.19	0.17
	A8	**1.04**	**0.88**	0.78	0.68	0.62	0.56	0.52	0.48	0.46	0.44	0.43	0.41
	A9-1	**1.82**	**0.87**	1.67	0.70	1.55	0.56	1.46	0.46	1.39	0.37	1.33	0.31
	A9-2	**0.96**	**1.32**	0.82	1.11	0.72	0.94	0.63	0.81	0.56	0.71	0.51	0.62
	A10	**1.53**	**0.57**	0.97	0.35	0.65	0.22	0.47	0.14	0.37	0.10	0.32	0.08
	Zi2	**1.09**	**0.97**	0.68	0.61	0.43	0.39	0.28	0.25	0.19	0.17	0.13	0.12
Total mixing zone		*12.49*	*10.82*	*9.08*	*7.88*	*7.16*	*6.11*	*5.98*	*5.01*	*5.27*	*4.33*	*4.84*	*3.87*
Alluvial	Zi1	**0.09**	**0.06**	0.06	0.04	0.03	0.02	0.02	0.01	0.01	0.01	0.01	0.00
	A12a	**0.00**	**0.00**	0.00	0.00	0.00	0.00	0.00	0.00	0.00	0.00	0.00	0.00
	A12b	**0.00**	**0.00**	0.00	0.00	0.00	0.00	0.00	0.00	0.00	0.00	0.00	0.00
	A12c	**0.00**	**0.00**	0.00	0.00	0.00	0.00	0.00	0.00	0.00	0.00	0.00	0.00
	A12d	**0.00**	**0.00**	0.00	0.00	0.00	0.00	0.00	0.00	0.00	0.00	0.00	0.00
	A12e	**0.11**	**0.06**	0.07	0.04	0.04	0.02	0.03	0.01	0.02	0.01	0.01	0.01
Total alluvial		*0.20*	*0.12*	*0.13*	*0.08*	*0.07*	*0.04*	*0.05*	*0.02*	*0.03*	*0.02*	*0.02*	*0.01*
Nucleus	A13a	**0.00**	**0.00**	0.00	0.00	0.00	0.00	0.00	0.00	0.00	0.00	0.00	0.00
	A13b	**0.00**	**0.00**	0.00	0.00	0.00	0.00	0.00	0.00	0.00	0.00	0.00	0.00
	A13c	**0.01**	**0.01**	0.00	0.00	0.00	0.00	0.00	0.00	0.00	0.00	0.00	0.00
	A13d	**0.01**	**0.00**	0.00	0.00	0.00	0.00	0.00	0.00	0.00	0.00	0.00	0.00
	A13e	**0.15**	**0.00**	0.02	0.00	0.00	0.00	0.00	0.00	0.00	0.00	0.00	0.00
Total nucleus		*0.16*	*0.01*	*0.02*	*0.00*	*0.00*	*0.00*	*0.00*	*0.00*	*0.00*	*0.00*	*0.00*	*0.00*
Total [m³·s⁻¹]		*12.85*	*10.95*	*9.23*	*7.96*	*7.23*	*6.15*	*6.03*	*5.03*	*5.30*	*4.35*	*4.86*	*3.88*

The deepening of the water table caused a non-homogenous reduction in the evaporation rate of the salt flat basin. In the nucleus, prior to brine pumping, the average evaporation rate was approximately 0.03 mm·d⁻¹. In 1986, the minimum evaporation rate, which had values close to 0 mm·d⁻¹, occurred in the western area due to the relative high thickness of the unsaturated zone and near the ALB evaporation pond where early brine pumping had already started. The maximum evaporation rates in the nucleus were located near the Peine and Soncor Lake Systems, locally reaching values higher than 0.5 mm·d⁻¹. After brine pumping, in 2018, almost the total area of the water table in the nucleus experienced a drawdown below the extinction depth. Only near the Peine and Soncor Lake Systems still some outflows remain at present. The drawdown in the nucleus led to a reduction of 96 % of the evaporation flow that characterized the natural regime, resulting in an impact of 0.48 m³·s⁻¹ in the water balance.

The evaporation rate in the mixing zone, in both periods, reached values of 5.84 mm·d^{-1} in the lakes and values less than 0.5 mm·d^{-1} in areas near the nucleus and the alluvial fans where the thickness of the unsaturated zone increases. Considering the total area covered by the free water surface in the Salar de Atacama basin, an average evaporation flow of 0.24 m^3·s^{-1} was obtained for the lakes. This value remained almost constant between both dates because the evaporation rate and the extension area covered by lakes remained almost constant. In the northern mixing zone, where the water table depth was fairly constant between 1986 and 2018, evaporation rates overall remained quite similar. In the eastern and southeastern mixing zones, the evaporation rate also remained constant in the EMZ and MMZ areas, but in the IMZ area, especially towards the nucleus side of this sub-zone, the slight drawdown of the water table caused a reduction in the evaporation rate. In percentage, the mixing zone experienced a minor reduction (14 %) in the discharge flow than the nucleus, but this was enough to cause an impact in the evaporation flow of 1.78 m^3·s^{-1}, which was higher than the produced in the nucleus. Finally, the alluvial zone scarcely contributed to the water balance in 1986 and 2018 because the depth of the water table was always deeper than 2 m.

When the total evaporation discharge estimated for the year 1986, 13.38 m^3·s^{-1}, is compared with the evaporation flow calculated for the year 2018, 11.02 m^3·s^{-1}, a reduction of 2.36 m^3·s^{-1}, equivalent to 17 %, is evidenced. This reduced flow is relatively similar to the flow pumped in recent years (Fig. 5.4), even somewhat higher. This means that the damping capacity has allowed practically all the brine that is pumped to be compensated with an equivalent reduction in evaporation. The water expelled by evaporation may be greater than the brine pumped because the estimation of the water table requires interpolating the water table depth data which adds a little uncertainty even though the data density is high. It can also influence the water table to be slightly above average as a result of a rainy period (Marazuela et al., 2019a). In 2018, part of the water that had been discharged naturally from the basin in 1986 was removed from the system by pumping. This possibly diminished the impact of the lakes and wetlands in the MMZ. From the MMZ to the boundary of the basin, the impact of brine pumping was seemingly almost null, even though the salt flat is a closed basin. It seems logical to conclude that the anthropogenic or natural exit of brine from the nucleus should not modify the hydraulic regime of the marginal zone as long as the amount of brine leaving the nucleus is the same.

However, the damping capacity only works when the water table oscillates between the ground and the extinction depth (1-2 m) of the phreatic evaporation. In addition, the main damping capacity occurs in the first decimetres of depth, when the evaporation rate changes more rapidly. Below 0.5 m, due to the exponential change in the evaporation curve, the damping capacity is substantially reduced. The damping capacity played first in the nucleus, where the first drawdown of the water table occurred. However, as the extinction depth was reached, the damping capacity had ceased to be effective in the nucleus. This seems to be the current scenario. Our understanding of the system behaviour leads to think that the forward increase of the brine pumping and the drawdown caused in the water table suppose a potential risk to the lakes. In the case of the Soncor Lake System, the increase in the vertical hydraulic gradient could favour the infiltration from the lakes to the aquifer. To avoid or at least delay this regime as much as possible and to anticipate it, in the following section, we discuss one option of salt flat management through an improved distribution of wells.

5.3.2.3. Sensitivity analysis

The strong dependence of the methodology followed for the estimation of the evaporation discharge on the water table depth implies that the accuracy of the water table measurement is critical. In addition, the low topographic gradient and the presence of a rough surface crust in salt flats hinders the elevation measurement of the ground.

The sensitivity analysis evaluated the impact of an error of 0.1 to 0.5 m in the water table on the evaporation rate for the years 1986 and 2018. In the most adverse scenario evaluated, assuming an error of -0.5 m and keeping constant the outflow from lakes, the evaporation discharge decreased from 12.85 and 10.95 $m^3 \cdot s^{-1}$ to 4.86 and 3.88 $m^3 \cdot s^{-1}$ for 1986 and 2018, respectively (Fig. 5.14 and Table 5.1). Thus, an error of only 0.5 m was enough to reduce in more than 60% the calculated evaporation discharge. The results confirmed the critical dependency of the evaporation discharge estimation to the water table depth accuracy. The accuracy of the groundwater level measurements and the evaporation zoning considered in each study have been the main reason why the historical estimations of the evaporation discharge in the Salar de Atacama have ranged between 1.6 $m^3 \cdot s^{-1}$ and 22.7 $m^3 \cdot s^{-1}$ (Kampf and Tyler, 2006; Marazuela et al., 2019a; Mardones, 1986). Therefore, despite the high efficiency of the methodology

applied, it is critical to invest efforts in a sufficient number of observation wells and precise measurement of groundwater levels to accurately quantify the evaporation discharge of any salt flat.
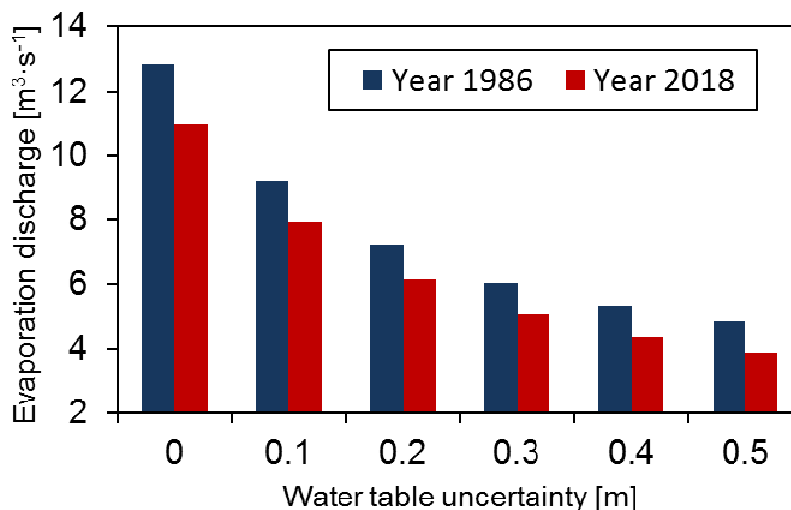
Figure 5.14. Evaporation discharge values obtained from the sensitivity analysis of the water table accuracy.

5.3.3. Minimizing the impacts of brine pumping

The most efficient spatial-distribution of brine pumping wells to minimize the impact of pumping on the water balance and water table was determined using a 3D groundwater flow model. This numerical model reproduced a synthetic salt flat nucleus in which two extreme distributions of pumping wells, single- and multiple-wells extracting the same water flow were evaluated. The evaporation curve representative of the nucleus of the Salar de Atacama and similar to the evaporation curve of other salt flats (e.g. Grilli and Vidal, 1986) was incorporated in the top of the model to regulate the evaporation discharge as the water table is depleted by brine pumping. Furthermore, as not all salt flats have water tables at the same depth, three initial water table depths of 0.30, 0.15 and 0 m were considered. The depth of 0.3 m implied an initial evaporation rate of 0.10 mm·d^{-1} within the evaporation range of the Salar de Atacama in its natural regime (Fig. 5.15). The depth of 0 m represented an extreme case, in which the system would be a lake with an evaporation rate of 5.84 mm·d^{-1}.
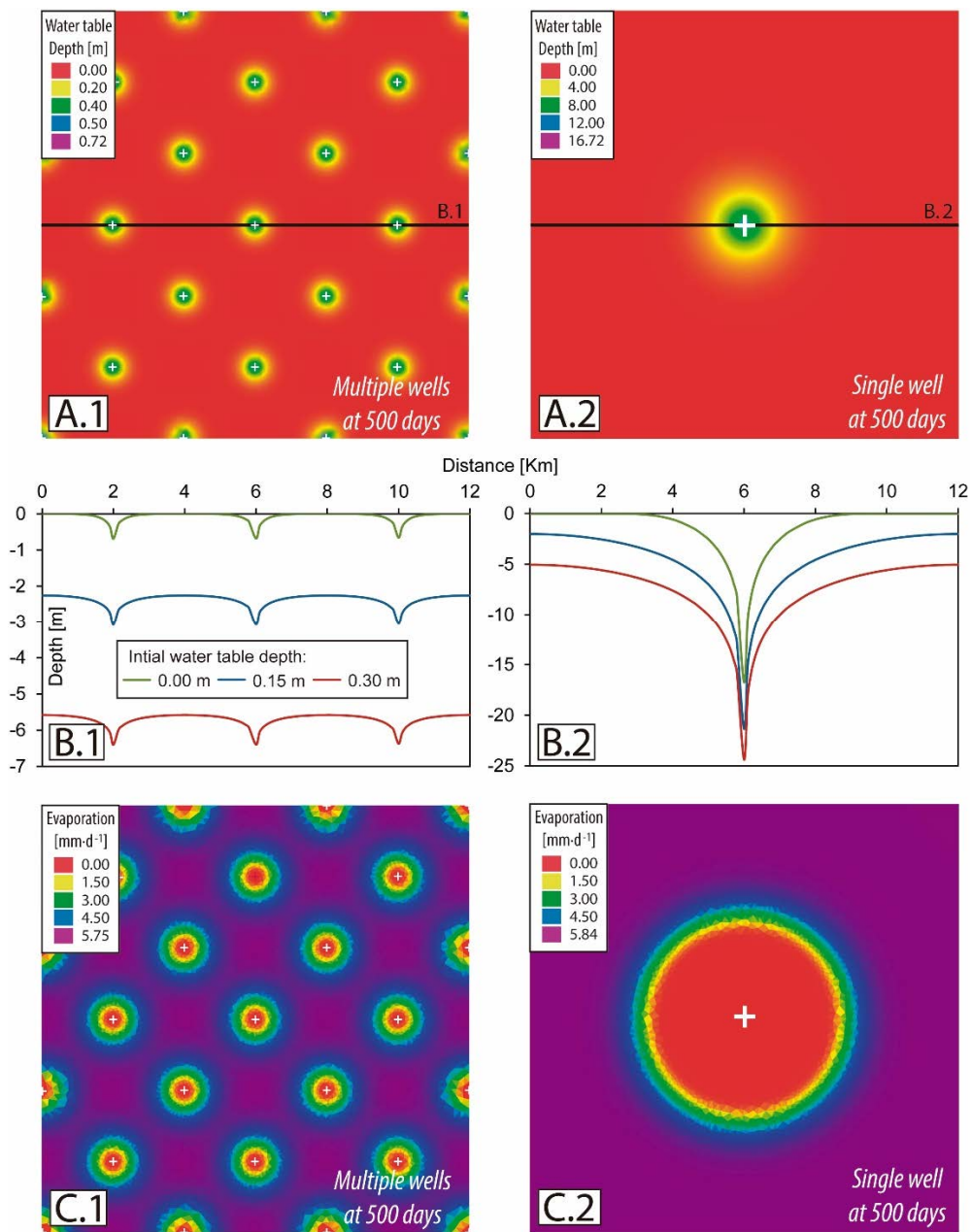
Figure 5.15. *Spatial distribution of the hydraulic heads and evaporation rates from the 3D numerical model. A) Hydraulic heads at 500 days. B) Hydraulic heads in the section at 500 days. Note the different vertical scales. The location of the section is shown in Fig. 5.15A. C) Evaporation rates at 500 days. The left three figures refer to the single-well design, and the right three figures refer to the multiple-wells design. The white crosses indicate the locations of the pumping wells.*

The initial evaporation rate was reduced depending on the distribution of the pumping wells (Fig. 5.15). In the multiple-wells case, several small cones of depression deepened the water table more homogeneously than in the single-well case, in which the brine pumped at one point caused a unique and deep cone of depression. This resulted in a different reduction in the evaporation rates. The reduction in the evaporation rate was more homogeneous and affected a greater area when the brine pumping was distributed in several wells than when brine pumping was conducted in a single-well (Fig. 5.15C). In the single-well case, the reduction in the evaporation rates was concentrated around the well, and far away, the evaporation rate remained close to the natural regime.

The temporal evolution of the evaporation rate reduction and the storage loss is shown in Fig. 5.16. In all cases, the initial evaporation rate was rapidly reduced as a result of the water table drawdown caused by the pumping. The new evaporation rate reached 0 mm·yr^{-1}, i.e. the extinction depth, for the initial 0.15 and 0.30 depths. In these two cases, the reduction in the evaporation discharge could not compensate for the brine pumped and the extinction depth of the phreatic evaporation was reached. For the initial water table depth of 0 m (lake case), the deepening of the water table allowed a reduction in the evaporation rate high enough to compensate for the brine pumped. Then, the new evaporation rate was equilibrated below the initial evaporation rate and above zero (Fig. 5.16). On the other hand, for each of the three initial depths, a difference in the evaporation rate between single- and multiple-well cases was clearly observed. The distribution of multiple-wells resulted in a faster decrease in evaporation, indicating a more efficient use of the damping capacity. In the case of the single-well, as the pumping was concentrated at one point, the extinction depth was quickly reached in the area closest to the pumping site, while in the most distant areas, the decrease in the evaporation rate was relatively slow.

Additionally, the changes in the evaporation rate had a direct impact on the storage of the aquifer and, as a consequence, on the stabilization of the water table. In all cases, the initial loss of storage coincided with the brine pumping of 2 m^3·s^{-1}, but this value immediately dropped until stabilizing concomitantly with the evaporation rate. This stabilization reached zero loss of storage in the 0 m depth case because the reduction in the initial evaporation rate allowed full compensation for the brine pumped. In the 0.3 and 0.15 m depth cases, as the evaporation rate reduction did not completely compensate for the brine pumped, the stabilization of

the storage loss occurred when the phreatic evaporation stopped due to water table deepening. In these two cases, the water table continued to fall indefinitely because there was no longer any damping capacity. If this result is compared with the observations performed in the nucleus of the Salar de Atacama, where the extinction depth of the phreatic evaporation has been already reached, the reduction in the evaporation rate will not be sufficient to compensate for the brine pumped.
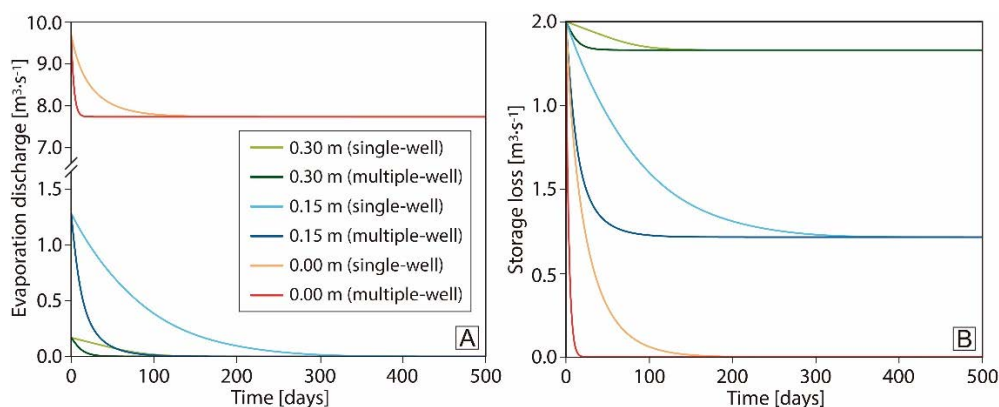
Figure 5.16. *Evaporation rates and storage resulting from the synthetic numerical model. A) Evolution of the total evaporation. B) Evolution of the storage.*

While it is true that the difference between the two distributions of wells became null when the system stabilized, in a real case, the system will not reach stabilization, since the pumps are not constant over time and the recharge is neither constant nor homogeneous. Therefore, it is evident that the use of a multiple-wells system takes better advantage of the damping capacity of the water table and balance and the water table of salt flats than the use of a single-well system. In accordance with the results of these six simulations, the use of a multiple-wells design instead of a single-well design allowed to compensate for an extra of 65 %, 33 % and 5 % of the pumped brine in the cases with initial water table depths of 0, 0.15 and 0.3 m, respectively. These percentages refer to the maximum storage difference between the single- and multiple-wells distributions with respect to the maximum storage (2 $m^3 \cdot s^{-1}$). Furthermore, because the evaporation curve decreases exponentially with the water table depth, the more superficial the water table, the greater the damping capacity that is harnessed.

5.4. Synthesis and conclusions

The methodology proposed to quantify the evaporation discharge in the Salar de Atacama and to evaluate the impacts caused by its brine exploitation allowed to improve the design of the brine exploitation in salt flats. The methodology included (1) field measurements of water table and evaporation rate, (2) its spatio-temporal analysis and (3) numerical modelling to improve the brine exploitation design.

First, evaporation pans and lysimeters were used to measure the evaporation rates from the free water surface of lakes and the phreatic evaporation, respectively. The potential evaporation rate was estimated in 5.84 mm·d^{-1}. The lysimeter measurements allowed to define the exponential decrease of the evaporation with respect to the water table depth. The strongest decrease occurred in the 0.5 m closest to the ground and the extinction of the evaporation was usually reached at 1 m of depth.

Second, the quantification of the evaporation discharge for the year 1986, prior to brine pumping, and 2018, under intensive brine extraction, was carried out through spatio-temporal analysis of the water table depth and the evaporation rate measurements. The evaporation discharge decreased from 12.85 to 10.95 m^3·s^{-1} between 1986 and 2018 that is around 15 %. This reduction compensated part of the extractions and could contribute to the preservation of the mixing zone ecosystems. The damping capacity was more efficient at water table depths between 0 and 0.5 m where the evaporation experienced the strongest decrease. At present, the damping capacity of the salt flat nucleus is already amortized. The sensitivity analysis showed that an average error of the water table depth of 0.5 m is enough to reduce the evaporation discharge of the basin by more than 60 %. The sensitivity of the phreatic evaporation on the water table imposes that considerable effort should invested to faithfully quantify the discharge by evaporation which is critical to the water balance of the salt flat basins.

Third, the 3D groundwater flow model of a hypothetical salt flat under brine exploitation allowed to optimize the designs for the pumping wells in terms of water balance impact. The results showed that the damping capacity can reach to compensate the total pumped brine through a reduction of the initial evaporation discharge as a consequence of the water table drawdown. To take better advantage

of the damping capacity and to minimize impacts on the water balance and water table, brine exploitations should consider to distribute the pumping outflow in the largest possible area.

Chapter 6

From the origin to the mature stage of a salt flat: hydrogeological constraints to explain the extreme Li-enrichment in the Salar de Atacama

This chapter constitutes the basis of the paper: **Marazuela, M.A.**, Ayora, C., Olivella, S., Vázquez-Suñé, E., García-Gil, A. (in preparation). From the origin to the mature stage of a salt flat: hydrogeological constraints to explain the extreme Li-enrichment in the Salar de Atacama.

6.1. Introduction

The strong evaporation that take place in salt flats (*salars*) contributes to the enrichment in Li, B, I, K, Mg and NaCl that are very attractive for mining exploitation (Eugster, 1980; Hardie et al., 1978; Rosen, 1994; Wood and Sanford, 1990; Yechieli and Wood, 2002). The brines of salt flats account for the 80 % of the world's reserves of Li. This element is essential for the development of mobile phone and electric vehicle batteries as well as in the pharmacology industry (USGS, 2019). The largest salt flats in the world are located in the Altiplano-Puna plateau of the Central Andean Range, which includes northwestern Argentina, southwestern Bolivia and northeastern Chile. Around 25 % of the worldwide Li reserves are located in the Salar de Atacama (in what follows referred as SdA) (NE Chile) where concentrations above 5,000 mg/L are reached around the Salar Fault System (in what follows referred as SFS) (Kesler et al., 2012; Liu et al., 2019) (Figs. 6.1 and 6.2). However, although strong evaporation occurs, it seems unlikely that such extreme Li-concentration is achieved from the evaporation of the freshwater inflows (<5 mg/L) reaching the Andean salt flats (Risacher and Fritz, 2009).

The origin of solutes in salt flats and the extreme Li-enrichment of the SdA have been intensively discussed in the recent decades. Practically all the high Li-concentrations take place in continental brines formed in endorheic basins fed with surface and/or groundwater with direct or indirect contribution of geothermal waters (Warren, 2016, 2010). Geothermal springs from the Northern Chile region contain Li concentrations from 7 to 46 mg/L, being the highest from El Tatio, to the N of SdA (Garrett, 2004). Even so, according to this data, whatever the origin of solutes a strong evaporation is needed for water to acquire Li concentrations higher than 5,000 mg/L. Thus, several hypothesis has been proposed to explain the extreme Li-enrichment in the SdA:

Risacher and Fritz (1991) pointed out the origin of solutes in Bolivian salt flats as combination of meteoric or hydrothermal alteration of volcanic rocks leading to Na-HCO_3-S inflow waters and leaching of ancient evaporites trapped below the extensive volcanic structures that leads to Na-Cl inflow waters. A similar behaviour was also described by Alpers and Whittemore (1990) in nearby salt flats of northern Chile. Based on Cl/Br ratios and $\delta^{18}O$-δ^2H isotope concentrations, Risacher et al. (2003) concluded that, rather than leaching ancient evaporites, the saline inflows of

the Chilean salt flats are mixtures of dilute meteoric water with present salt flat brines that leak though bottom sediments. Risacher et al. (2011) suggested that many thermal springs in Northern Chile contain some fraction of brine leaked from salt flats. In addition, hydro-thermo-haline circulation would act as driving force for the deep leaking brines to leave the basin and to be transported elsewhere, resulting possibly in very complex mixings. Carmona et al. (2000) supported the existence of two types of brines in the SdA, one rich in SO_4 to the East coming from the Western Cordillera of the Andean Range (volcanic arc) and another one rich in Ca to the W originated from the leaching of the Cordillera de la Sal. Risacher et al. (2003) and Risacher and Fritz (2009) proposed that the SO4-rich inflow waters and their derived SO_4-rich brines should be found in the intravolcanic basins of the Western Cordillera associated to the oxidation of native sulphur, while Ca-rich brines should prevail in sedimentary basins where Ca-rich minerals are abundant. To explain Ca-rich brines in several salt flats of the Western Cordillera they proposed that they might acquire their Ca-rich composition in Pleistocene time when their drainage basins were mainly sedimentary and before the lava flows and ignimbrites covered the sedimentary formations. Then, the weathering of volcanic sulphur would tend to shift progressively the brine geochemistry from Ca-rich to SO_4-rich.

For the specific case of the SdA, this set of hypotheses that relate the extreme Li-enrichment with the leaching of volcanic rocks, buried salt flats or leaking from current salt flats needs to assume that there is a deep groundwater flow from the Altiplano-Puna to the SdA. Jordan et al. (2002) hypothesized that highly evaporated brines leaking from the present salt flats of the Altiplano-Puna could reach the SdA through deep flow paths and ascend through the SFS. Corenthal et al. (2016) proposed that the topographic watershed does not coincide with the hydrogeological watershed and inflows from beyond the border of Chile-Argentina frontier feed the SdA. However, this assumption is very risky from a hydrodynamic point of view because of (1) the highest elevation of a E-W cross-section of the Andean Range matches with the volcanic arc mountains that constitute the Eastern boundary of the SdA basin and which should constitute a regional watershed and (2) the mixing zone should vanish in deep so that those flow lines reach the SFS of the SdA where the highest Li-concentration is located.
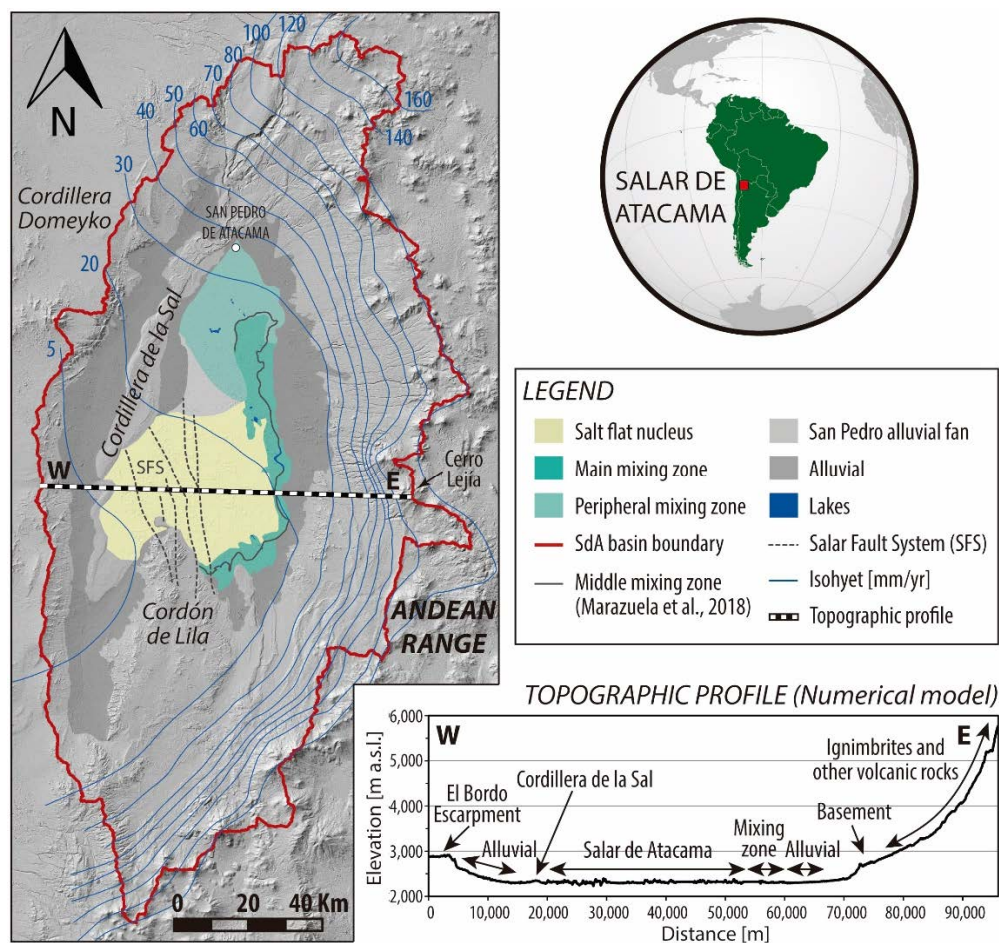
Figure 6.1. *Location of the Salar de Atacama basin. The topographic profile of the vertical cross-section chosen for the numerical simulations is shown.*

An alternative explanation to the Ca-rich brines found in the SFS of the SdA nucleus is the upflow of Li-rich hydrothermal solutions. Lowenstein and Risacher (2009) hypothesized that Li could be related to the inflow of hydrothermal solutions of Ca-Cl type through the SFS. This would explain the link of the higher Li concentration to the faults located in the SW part of the nucleus. The He isotope values measured by Munk et al. (2016) keep open a possible magmatic origin of these solutions because Li contents of around 1,000 mg/L are common in the fluid and melt inclusions associated to volcanic and magmatic rocks (Hofstra et al., 2013; Lindsay, 2001; Schmitt, 2001). However, Munk et al. (2018) suggested that the fault planes located within the salt flat are not necessarily good candidates because here the

lithosphere is cold and rigid (Schurr and Rietbrock, 2004) and better option faults would be the located between the salt flat and the volcanic arc in the southern-half of the SdA basin. Recently, González et al. (2009) related some of the SdA basin faults to the migration of hydrothermal fluids from deep magma reservoirs to the surface. The contribution of hydrothermal fluids to the brine compositions has been described in many parts of the world such as Salar de Uyuni in Bolivia (Ericksen et al., 1978), Fox Creek Area in Canada (Eccles and Berhane, 2011), Salton Sea, Death Valley and Bristol Dry Lake in California (EEUU) (Lowenstein et al., 2016; Lowenstein and Risacher, 2009), Quaidam basin (Tibet) in China (Li et al., 2018; Lowenstein and Risacher, 2009; Yu et al., 2013), and many other magmatic zones in the world (Benson et al., 2017). Karmanocky and Benison (2016) evidenced the hydrothermal-magmatic pulses control in the geochemistry of the Salar Ignorado, located 200 km S of the SdA, though the study of the inclusions in gypsum crystals. The study carried out in several salt flats of NW Argentina by López Steinmetz et al. (2018) confirmed the positive linear correlations between Li, K and Mg, suggesting a common source for these ions, probably as thermal contribution.

As a summary of these background, three origins have been proposed to explain the extreme Li-enrichment in the SdA: (1) leaking of brines from the present salt flats of the Altiplano-Puna (Risacher et al., 2003; Risacher and Fritz, 2009), (2) leaching of hypothetical salt flats buried by volcanic eruptions in the Altiplano-Puna (Risacher et al., 2011; Risacher and Fritz, 2009) and (3) rising of hydrothermal brines from deep reservoirs through faults (Lowenstein and Risacher, 2009).

Almost these works have focused their efforts on detailed hydrochemical and isotopic data of the brines. This has led to hypothesize on the hydrodynamics of the SdA basin but without having validated these hypotheses through quantitative models that take into account the complex hydro-thermo-haline circulation of these systems. At the same time, due to the conceptual and non-quantitative nature of all of them, could not be invalidated by the next hypotheses proposed. Therefore, the origin of Li in the SdA and other salt flats remains unknown and quantitative uncertain.
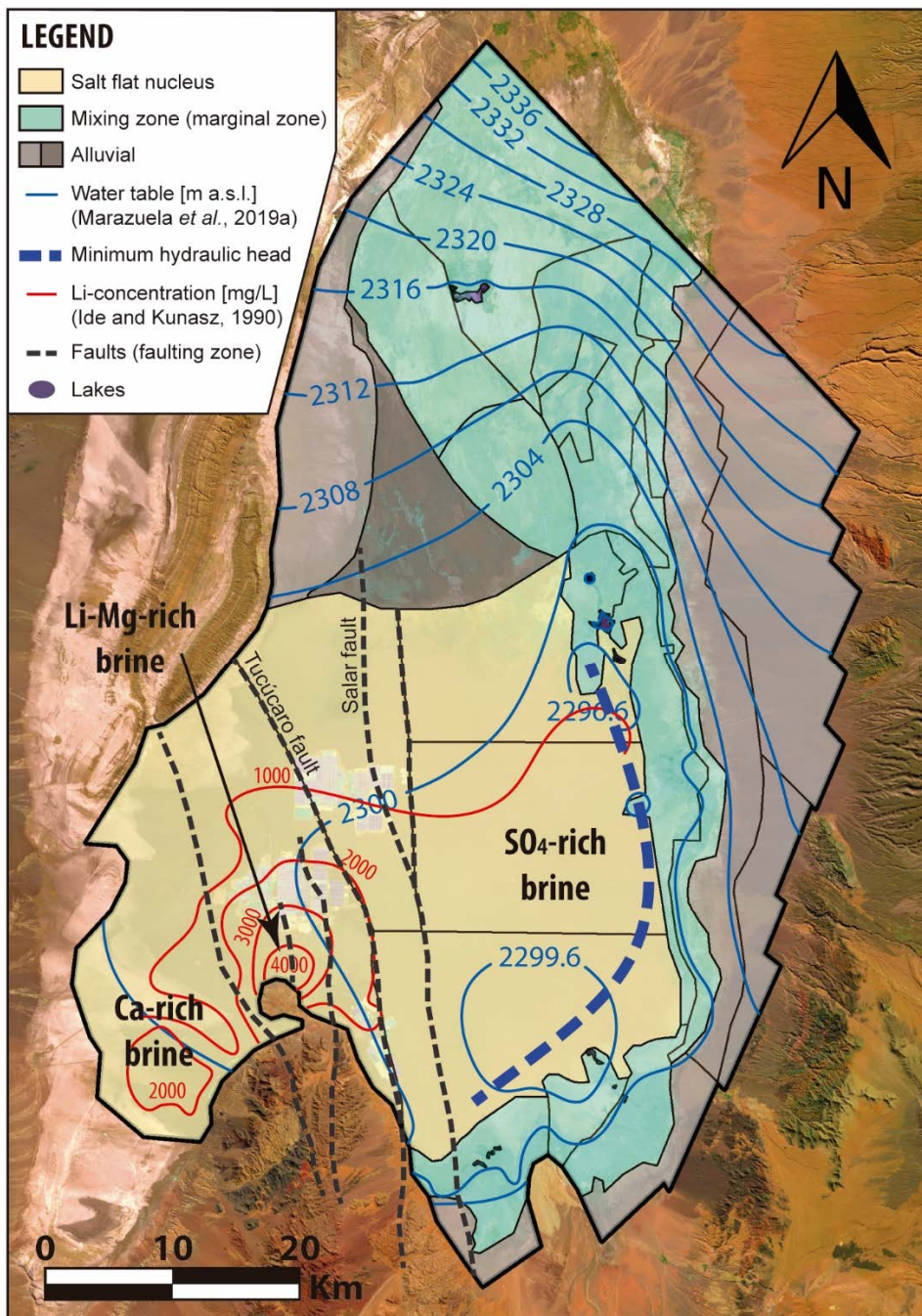
Figure 6.2. *Hydrogeological and hydrogeochemical framework of the Salar de Atacama. The decoupling between the minimum hydraulic head of the water table (prior to brine pumping) and the highest Li-concentration is evidenced. Highlight the strong overlap between the SFS and the highest Li-concentration.*

The groundwater flow modelling of salt flat basins indispensably needs to take into account the strong coupling of flow, mass and heat transport and the density and viscosity dependency of pressure, mass-concentration (salinity) and temperature (Driesner and Heinrich, 2007; Klyukin et al., 2016; Kohfahl et al., 2015). In hydro-thermo-haline systems the density and viscosity variations are very strong and they have a significant role to groundwater flow that is regulated by Darcy's law. Hydro-thermo-haline convection implies that dense brine may counters the upward buoyant flow and convective cells promoted by thermally-driven flow (Magri et al., 2015, 2012). This process may have a great importance during the origin and evolution of the salt flats since in that moment the previous thermal-driven regime is altered by the instability produced by the formation of a heavy brine on top (Wooding et al., 1997). Furthermore, fault planes are frequently associated to preferential flow paths due its higher permeability combined with the development of convective cells (e.g. Li et al., 2016; Magri et al., 2015, 2010; Simms and Garven, 2004). The brine inflows related to faults has been modelled in other places such as the Lake Tiberias (Israel) where paleo-heating processes related to magmatic intrusions may explain a Ca-rich brine (Koltzer et al., 2017). However, to date, although previous work have highlight the necessity to address hydro-thermo-haline circulation in salt flats (Hardie, 1991, 1990; Magaritz et al., 1990; Munk et al., 2016; Risacher et al., 2003; Rosen, 1994) only synthetic models reproducing the saline interface resulted by salinity contrast in continental saline environments has been performed (Duffy and Al-Hassan, 1988; Fan et al., 1997; Hamann et al., 2015; Marazuela et al., 2018; Nield et al., 2008; Simmons et al., 1999; Tejeda et al., 2003; Vásquez et al., 2013). The complexity and high computational cost of these models is probably what has prevented the development of quantitative models for the understanding of the origin and evolution of salt flat basins and the role that faults can play in the geochemistry of brines.

The main goal of this work is to discuss the feasibility of the different hypotheses proposed to explain the formation of the one of the world's largest lithium reserve. To achieve this objective, two sets of numerical simulations have been carried out to define (1) the origin and evolution of a salt flat and how climate cycles can affect the location of the most Li-concentrated brines by evaporation and (2) the development of the hydro-thermo-haline circulation of a mature salt flat basin.

6.2. Material and methods

6.2.1. Hydrogeological setting

The internally-drained SdA basin is a prominent morphological depression of 17,000 km² located in the western flank of the Altiplano–Puna plateau of the Central Andes at 2,303 m a.s.l. (metres above sea level), in the hyper-arid Atacama Desert (Fig. 6.1). The SdA basin is in the proximal fore-arc between the present volcanic arc (Western Cordillera) to the E and the North Chilean Precordillera (Cordillera de Domeyko) to the W. The SdA basin, specially its western half part, is located in the arc shaped region of high heat flow described in the literature between latitudes 15 and 30 S (Hamza et al., 2005). The strong positive anomalies in the isostatic residual gravity of the de SdA were caused by dense bodies magmatically or tectonically emplaced during Cretaceous rift episode at 4-6 km and 10-15 km (González et al., 2009; Reutter et al., 2006).

Successive extensional and compressional regimes have strongly fractured the basin, being the SFS the most outstanding feature (Arriagada et al., 2006). The SFS affects the salt flat from the Cordon de Lila at the S until the San Pedro River alluvial fan and it remains active at least since the Paleogene until present (Jordan et al., 2007). This strike-slip faulting zone has caused the stratigraphic units of the east block of the SdA to be much thicker than in the west block and can determine the regional groundwater flow (Jordan et al., 2002). At least, three other major faults are also described in the literature: Tucúcaro, that like the other minor faults of the SdA nucleus we consider included in the SFS to simplify the wording, Peine and a here named East (Muñoz et al., 2002; Reutter et al., 2006).

The hyper-arid climate of the SdA remains long before its origin, dating to 5.8 Ma (González et al., 2009), although some relatively wetter short periods have been occurred (Bobst et al., 2001). These climatic cycles have been able to modify the hydrogeology operation of the basin over time. The larger precipitation rate, above 120 mm/yr, occurs in the volcanic arc where elevations above 5,000 m a.s.l. are reached (Houston, 2006a; Marazuela et al., 2019a). In the salt flat nucleus, the precipitation rate reduces hardly until 5 mm/yr.

From a hydrogeological point of view, three great domains have been identified by Marazuela et al. (2018). These are: the salt flat nucleus (composed by halite and filled by brine), the marginal zone around the nucleus that match with the mixing zone (saline interface) outcrops (composed by gypsum and carbonates) and the recharge zone that encompass the alluvial fans and the basement and volcanic rock outcrops toward the volcanic arc. The mixing zone results from the density contrast between the freshwater (1,000 kg/m³) coming from the recharge in the mountains and the dense brine (1,200 kg/m³) of the halite nucleus (Marazuela et al., 2018; Muñoz-Pardo et al., 2004; Tejeda et al., 2003; Vásquez et al., 2013). The main discharge (evaporation rates until 5.84 mm/d) occurs in the outcrop of the mixing zone where the water table is closest to the ground or directly above the ground in the lakes and wetlands. However, in spite of the relative greater depth of the water table in the nucleus, it can also contribute slightly to the discharge of the basin with small evaporation rates (< 0.1 mm/d) (Marazuela et al., 2020, 2019a). Therefore, under the current climatic conditions, a clear asymmetry in the discharge by evaporation influences and conditions the water table of the upper aquifers which minimum hydraulic head is located in the easternmost nucleus, close to the mixing zone outcrop (Fig. 6.2).

The groundwater recharged in the volcanic arc moves toward the eastern marginal zone where is forced to rise until the surface by the mixing zone. On the other side of the eastern mixing zone, the quantitatively less groundwater that inflow the nucleus along the SW and W margin moves towards the nucleus until it reaches the minimum hydraulic head where collides with the eastern recharge groundwater. The upwelling flows associated to the mixing zone feeds lakes and wetlands that serve as habitat to a number of endemic and migratory birds and other animals (Ortiz et al., 2014; Salas et al., 2010).

6.2.2. Stratigraphy

The upper crustal lithology and structure of the basin needed to support the model are well known from industry seismic data and a deep exploration well drilled in the center of the basin (a synthetic profile is shown in Fig. 6.3) (Jordan et al., 2007; Muñoz et al., 2002; Pananont et al., 2004).
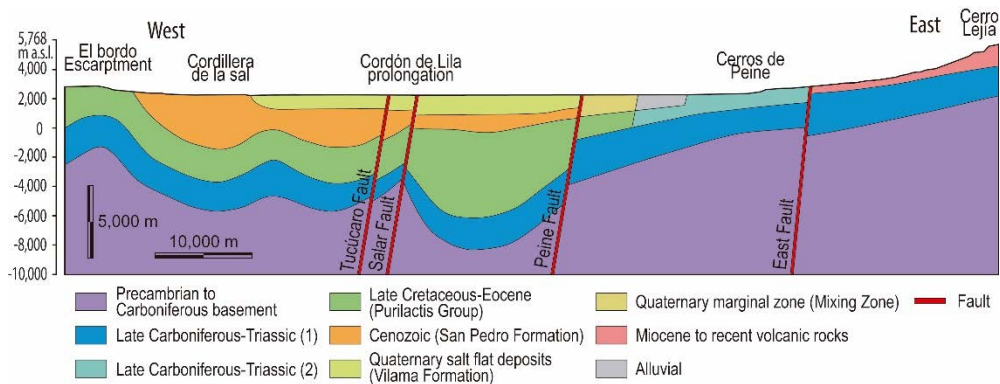
Figure 6.3. *Stratigraphy and structural features of the vertical profile chosen for the numerical simulations (vertically scaled x1.5 like all profiles shown hereinafter) (see its location in Fig. 6.1).*

The Pre-Cretaceous basement is represented by sedimentary and igneous rocks that outcrop in the Cordón de Lila peninsula and also by widely distributed, stratified volcanic and sedimentary rocks of late Paleozoic to Triassic age. The early Paleozoic rocks are composed by clastic sediments with intercalations of pillow-lavas of Ordovician age and Ordovician to Carboniferous plutonic rocks.

The Cretaceous to Eocene sequences that underlie the actual SdA were deposited in the back-arc of the volcanic arc from before 38 Ma (Reutter et al., 2006). The Purilactis Group (Cretaceous to Eocene) which outcrops in the fold and thrust belt of the El Bordo Escarpment, underlies the late Eocene to recent sedimentary fill of the basin. The lowest part of the Purilactis Group is constituted limestones, gypsum and halite and the upper part by conglomerates. Also basaltic to andesitic lavas, dykes, sills and subvolcanic intrusive rocks were described into these sequences as a consequence of the strong volcanic activity through fissures of N-S direction.

The Cenozoic rocks correspond to continental clastic sediments and ignimbrites (liparites) of great extension. The San Pedro Formation (Eocene-Early Miocene) that outcrops in the Cordillera de la Sal is constituted by continental deposits both clastic (clays, siltstones, sandstones and fine-grained conglomerates) and evaporitic (halite and gypsum). The equivalent Tambores Formation is composed by para-conglomerates and poorly consolidated sandstones.

The Quaternary is mainly represented by the Vilama Formation (Late Pliocene-Recent) that constitutes the SdA halite nucleus. Five ignimbrite layers associated to

the ignimbrite flows extruded from large caldera systems (stratovolcanoes) located
in the Altiplano-Puna during this period permitted to know the age of this deposits
(De Silva, 1989; Gardeweg and Ramírez, 1987; González et al., 2009).

6.2.3. Numerical model

The numerical modelling works encompassed three hydro-thermo-haline
simulations based on the geological profile shown in Fig. 6.3. This profile includes
the main stratigraphic and structural features described by previous works (Jordan
et al., 2007; Muñoz et al., 2002; Reutter et al., 2006). The first two simulations aim to
analyse the effect of evaporation on the location of the brine most enriched in solutes
and how it has been able to evolve over time. The third simulation allows to
understanding the hydro-thermo-haline operation of the SdA in its mature stage.

6.2.3.1. Coupled formulation

The FEFLOW code (Diersch, 2014) allows modelling the strong coupling of
groundwater flow, solute transport and heat transfer based on the following
governing equations. See Appendix G for explanation of equations.

The equation of fluid mass conservation in equivalent hydraulic heads is defined
as:

$$S_s \frac{\partial h}{\partial t} + \nabla \cdot \mathbf{q} = 0 \tag{6.1}$$

Where S_s is the specific storage, h the equivalent hydraulic head and $\mathbf{q}$ the Darcy's
law that describes the flow of a fluid through a porous medium:

$$\mathbf{q} = -\mathbf{K}\left[\nabla h + \frac{\rho^f - \rho_o^f}{\rho_0^f}\mathbf{u}\right] \tag{6.2}$$

Being K the hydraulic conductivity tensor, ρ^f the fluid density and ρ_o^f the
reference density. The second adding term of this law is the product of the density
ratio and the gravitational unit vector $\mathbf{u}$ (=-$\mathbf{g}$/$\|\mathbf{g}\|$, where $\mathbf{g}$ is the gravitational
acceleration vector) that represents the buoyancy force induced by density
variations.

The energy-balance equation for the fluid and porous medium is given by the
expression:

$$\frac{\partial}{\partial t}\left((\phi\rho^f c^f + (1-\phi)\rho^s c^s)T\right) + \nabla \cdot (-\boldsymbol{\lambda}\nabla\mathrm{T} + \rho^f c^f T\mathbf{q}) = 0 \tag{6.3}$$

Where ϕ denotes porosity, ρ^s density of the solid, T temperature c^f specific heat of the fluid, c^s specific heat of the solid and $\boldsymbol{\lambda}$ the thermal conductivity of the saturated porous medium as a whole.

The equation of solute-mass conservation in its convective form:

$$\phi\frac{\partial C}{\partial t} + \mathbf{q}\nabla C - \nabla \cdot (\mathbf{D}\nabla C) = 0 \tag{6.4}$$

Where C is the mass-concentration and $\mathbf{D}$ the tensor of hydrodynamic dispersion.

The tensor of hydraulic conductivity, $\mathbf{K}$, is defined as:

$$\mathbf{K} = \frac{\mathbf{k}\rho_0^f g}{\mu^f(C,T)} \tag{6.5}$$

Where $\mathbf{k}$ is the intrinsic permeability tensor. The dynamic viscosity of the fluid phase, μ^f, is regarded as a thermodynamic function of mass fraction ω and temperature T. Combining the high-concentration dependency as given by Lever and Jackson (1985) with the empirical temperature dependency of Mercer and Pinder (1974), the following expression is reached employing reference values of concentration, C_0, and temperature, T_0:

$$\mu^f(C,\ T) = \mu_0 \ x \ \frac{1+1.85\omega-4.1\omega^2+44.5\omega^3}{1+1.85\omega_{(C=C_0)}-4.1\omega^2_{(C=C_0)}+44.5\omega^3_{(C=C_0)}} \ x \ \frac{1+0.7063\varsigma_{(T=T_0)}-0.04832\varsigma^3_{(T=T_0)}}{1+0.7063\varsigma-0.04832\varsigma^3}$$

$$\tag{6.6}$$

With $\varsigma = (T-150)/100$ at T in °C and $\omega = C/\rho^f$.

The equation of state used for the fluid density is given by the *BrineDensity* plug-in implemented in the FEFLOW code (Magri, 2009):

$$\rho^f = \rho_0^f\left(1 - \bar{\beta}(T,p)(T-T_0) + \bar{\gamma}(T,p)(p-p_0) + \frac{\bar{\alpha}(T,p)}{C_s-C_0}(C-C_0)\right) \tag{6.7}$$

This polynomial expression dependent on the coefficients of thermal expansion, $\bar{\beta}$, compressibility, $\bar{\gamma}$, and mass-concentration ratio, $\bar{\alpha}$ has been applied and validated in several geothermal and brine systems (Irvine et al., 2014; Magri et al., 2015, 2012, 2009).

6.2.3.2. Mesh and model parameters

The modelled profile extends from the E to the W of the basin going through the center of the SdA (Fig. 6.1). The profile is quite parallel to the main direction of the groundwater flow and reaches the Precambrian-Carboniferous basement in all its extension (Fig. 6.3). The maximum elevation is reached at the eastern boundary (Cerro Lejia) with 5,769 m a.s.l. while on the other side, the Border Escarpment reaches only 2,871 m a.s.l. The center of the profile that corresponds to the current SdA remains in approximately 2,303 m a.s.l. Although the groundwater flow shows a rotation component from the SW nucleus toward the eastern marginal zone (Fig. 6.2), this has been simplified to a W-E profile. This rotation of the flow affects only the western end of the salt flat, the one with the lowest contribution to the water balance, being able to benefit the simplified W-E profile.

The finite-element mesh was built using the "Triangle" algorithm and satisfying the Delaunay criterion (Shewchuk, 1996). The whole profile compresses approximately 120,000 triangular elements. The element-size ranged from approximately 25 m in the evaporation zones and faults to an average value of 150 m in the less critical areas to avoid the numerical errors.

Faults were taken into account using the Equivalent Porous Media (EPM) approach which allows to model faults with lower computational effort than the discrete-fracture technique and to model the density-driven flow inside the faults (Magri et al., 2016, 2012, 2010). The fault aperture of 300 m was very small compared to the basin-scale groundwater flow. Faults were disabled in the simulations that allowed evaluating the effect of the evaporation in the location of the maximum solute-enrichment.

Each stratigraphic unit (Fig. 6.3) was considered homogenous and isotropic with respect to the physical properties (hydraulic conductivity, porosity, thermal conductivity and volumetric heat capacity) listed in Table 6.1. Average values of each parameter taken from previous field works (Marazuela et al., 2019a and 2019b) and bibliographic reference values of each type of rocks (Eppelbaum et al., 2014) were assigned. The basement was considered as impermeable and then, neglected for the modelling task. The longitudinal and transverse dispersivities for both, mass and heat transport, were 100 and 10 m, respectively.

Table 6.1. Hydraulic and thermal parameters considered for the numerical simulations. The colours are in accordance with the geological profile of the Fig. 6.3.

Hydrostratigraphic Units	K [m·d⁻¹]	φ [-]	λ [J·m⁻¹·s⁻¹·°C⁻¹]	ρˢ cˢ [MJ/m⁻³/°C⁻¹]
Precambrian to Carboniferous basement			Impermeable	
Late Carboniferous-Triassic (1)	$5 \cdot 10^{-4}$	0.02	2.8	2.1
Late Carboniferous-Triassic (2)	$2 \cdot 10^{-2}$	0.02	2.8	2.1
Late Cretaceous-Eocene	$1 \cdot 10^{-3}$	0.03	2.6	2.1
Cenozoic	$1 \cdot 10^{-2}$	0.04	3.0	2.0
Quaternary salt flat deposits	0.1	0.02	3.5	1.8
Evaporation zone of the nucleus	0.5	0.05	3.5	1.8
Quaternary marginal zone	0.1	0.02	3.2	1.8
Evaporation zone of the marginal zone	0.5	0.05	3.2	1.8
Miocene to recent volcanic rocks	1	0.10	2.8	2.1
Alluvial	2	0.10	1.8	1.7
Fault (EPM)	1	0.25	2.0	1.8
Fluid	-	-	0.65	4.2

6.2.3.3. Boundary (BC) and initial (IC) conditions

The groundwater flow and mass-transport BC encompasses a freshwater inflow in the eastern and western recharge areas and a freshwater sink along the salt flat and mixing zone (Fig. 6.4). The inflow rate was based on the recharge values presented by Marazuela et al. (2019a). The main recharge is produced in the eastern side with values that increase from 34 mm/yr in the contact between the alluvial and the outcrop of Triassic rocks to 85 mm/yr in the Cerro Lejía. These values correspond with the present rainfall rates of 40 to 100 mm/yr minus the 15 % that is detained by the soil. In the western side a recharge of 5.5 mm/yr was considered. On the eastern recharge zone (volcanic arc), the freshwater inflow had a concentration of 5,000 mg/L which represented a recharge water slightly enriched in solutes after having gone through volcanic rocks. On the western recharge zone the same approach was used, however, on the stretch occupied by the Cordillera de la Sal (San Pedro Formation) (Fig. 6.3) the inflow reaches automatically the maximum solute-concentration in the third simulation (hydro-thermo-haline regime of the mature SdA stage), representing the saturation in halite produced by dissolution of the salt rocks.

The evaporation was implemented as a freshwater sink along a rectangle of 200 m of thickness that extends along the salt flat nucleus and mixing zone. This sink allows to extract pure freshwater (0 mg/L) without solutes triggering the solutes increase by evaporation (Nield et al., 2008). The outflow in the salt flat nucleus and mixing zone was 0.3 and 5.4 m^3/d, respectively, in accordance with the evaporation rate estimated by Marazuela et al. (2019a and 2020). Additionally, a mass-concentration BC with a constraint served to limit the maximum concentration (350,000 mg/L that correspond with the saturation index of halite) that brine can reach in each node inside of the evaporation rectangle (Kohfahl et al., 2015). The normalization range for concentration was stablished between 0 mg/L, equivalent to pure freshwater of density 1,000 Kg/m^3 and 350,000 mg/L, equivalent to a brine saturated in halite of density 1,200 Kg/m^3.
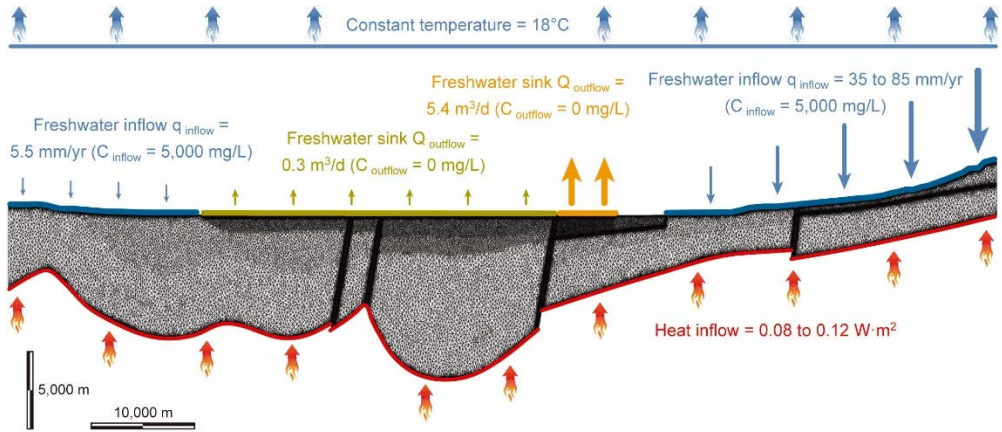
Figure 6.4. *Mesh and sketch of the main flow, mass and heat boundary condition considered for the different numerical simulations.*

The heat-transport BC allowed to reproduce the geothermal gradient considering the heat flow values of Hamza et al. (2005). A heat inflow at the bottom increasing from 0.08 in the eastern side to 0.12 W/m^2 in the western side represented the more cold crust below the salt flat than below the volcanic arc (Fig. 6.4). The average atmospheric temperature, 18°C, was fixed at the top of the model. Lateral boundaries were closed to fluid, heat and mass flow because they constitute basin-scale watersheds.

The IC for hydraulic head and temperature were derived from a convective hydro-thermal model led to its quasi steady-state regime performed previously to

the fully coupled model. The initial mass-concentration was 5,000 mg/L in the entire domain, representing a hypothetical basin filled completely by freshwater. The third simulation was run until the quasi-steady state regime was achieved. This was reached before the 5.8 Ma in which the origin of the SdA was dated (González et al., 2009).

6.3. Results

6.3.1. The salt-enrichment by evaporation in salt flats

The SdA basin was occupied probably by a freshwater-lake just prior to the salt flat development. Under this hypothetical regime, the flow paths would move from the mountains to the bottom of the freshwater-lake due to the topographic gradient between the recharge and discharge zones similar to other endorheic basins (Yechieli and Wood, 2002). However, this regime must have changed drastically when a salt lake or salt flat was developed and the differential solute-concentration changed the density of the groundwater. This transition could happen through (1) a gradual evolution that had an intermediate stage of salt lake or salt flat system where the evaporation or phreatic evaporation was homogenous throughout the surface, or (2) a rapid change towards a salt flat with characteristics very similar to the current one where the main discharge by phreatic evaporation already occurred in the eastern marginal zone. In addition, successive stages between both types linked to paleoclimate evolution of system could have occurred.

Assuming a homogeneous evaporation rate on the free surface of a salt lake or on a salt flat, the minimum hydraulic head appears in a central position within the nucleus or slightly western considering the present day asymmetry in the recharge (Fig. 6.5). The minimum hydraulic head determines the direction in which the evaporated brine tends to move and accumulate and therefore, it has a capital significance for the enrichment of brines in Li and any other conservative element, as well as for the precipitation of salts. The density contrast generated by the solute-concentration gradient leads the system to a salt-bulge convection cell. The groundwater coming from the recharge is enriched in solutes by evaporation and when arrive to the minimum hydraulic head it enters in the salt bulge convection cell. The evaporated groundwater sinks due to its higher density but the convection cell returns this groundwater quickly to the point of minimum hydraulic head and,

therefore, favouring the increase in solutes of the salt-bulge. The salt-bulge evolving down until it reaches relative-more impermeable rocks where expands horizontally. In spite of this deepening slowdown, the salt-bulge gradually sinks until it reaches the impermeable basement. Although this sinking process is sensitive to the hydraulic parameters of the rocks, it seems that this can occur even before the saturation in halite is achieved in the upper aquifer (350,000 mg/L) (Fig. 6.5B). That is, the leakage of evaporated brine from the salt flat toward deep layers is favoured with respect to lateral expansion even when the rocks have low permeability. This occurs because the density gradient is very strong in this type of systems and the density-driven flow overcomes the topographic-driven flow. In addition, the effect of heat on brine density enhances this deepening as discussed below. This leads to think that many thousands or millions of years would be necessary to reach the dimensions of the current SdA. In fact, it still seems unlikely that this is the only process that has resulted in a salt flat of these dimensions.
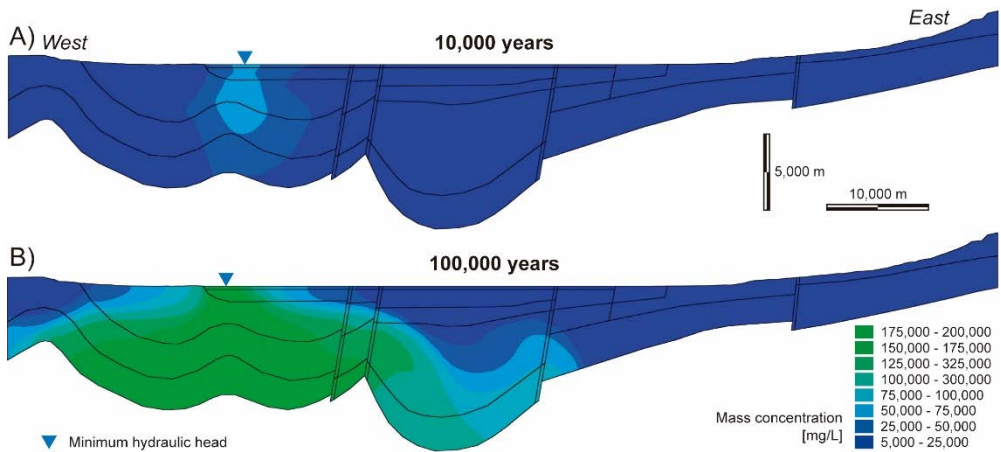
Figure 6.5. Mass-concentration evolution of a salt flat from its origin considering a homogenous evaporation (equal evaporation rate for the nucleus and the eastern marginal zone). The minimum hydraulic head is located in the western side of the salt flat nucleus.

However, if the present day asymmetric evaporation is considered, the minimum hydraulic head is located around the contact between the nucleus and the eastern marginal zone (Fig. 6.6). A salt-bulge develops similarly to that described for the homogeneous evaporation case. The symmetric or asymmetric evaporation affects significantly the location of the most concentrated and evaporated brines and small changes in the water table may be sufficient to modify the position of the regional

minimum hydraulic head. In fact, only reducing slightly the asymmetry between the evaporation of the nucleus and the mixing zone, the displacement of the minimum hydraulic head from the wester nucleus to the central nucleus already occurs.
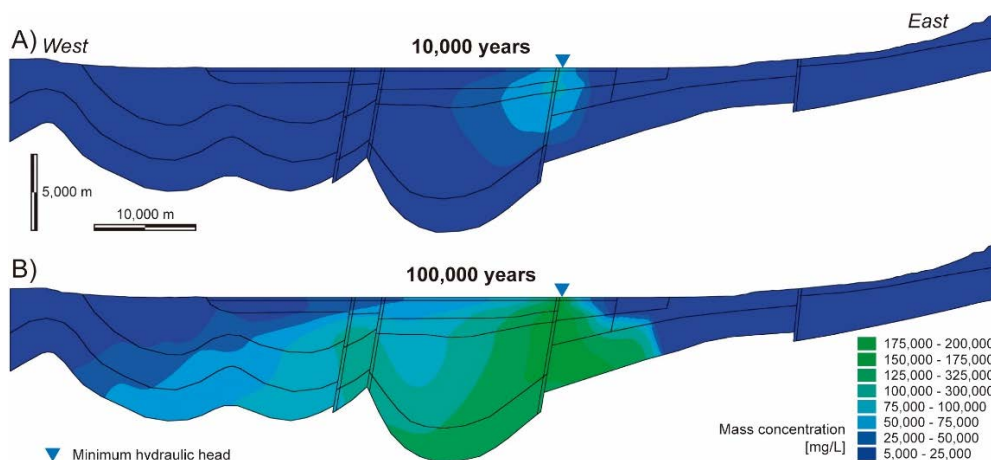
Figure 6.6. Mass-concentration evolution of a salt flat from its origin considering the present asymmetric distribution of the evaporation (higher evaporation rate for the eastern marginal zone than the nucleus). Note that the minimum hydraulic head is located in the eastern side of the nucleus.

6.3.2. The hydro-thermo-haline circulation of the Salar de Atacama

Groundwater flow of the salt flat basin at regional scale is strongly conditioned by the effect of the temperature and salinity in the density of the fluid (freshwater or brine) (Fig. 6.7). The computed temperature field shows that the central part of the basin is cooler than the mountains, as previous studies suggested (Fig. 6.7A). The temperature field is constrained by the synclinal geometry of the hydrostratigraphic units, which determine the distribution of the hydraulic and thermal parameters. The computed temperatures are within the range of the obtained by Jayne et al. (2016) for the Salar de Huasco further to N. The temperature field is distorted by the presence of faults and the mixing zone developed in the marginal zone of the salt flat.

In a mature stage, a saline interface and the associated mixing zone is located around the salt flat nucleus (Fig. 6.7B). The density of the brine below the nucleus, because of the increase in temperature with depth, reduces from 1,200 to 1,100 kg/m³ (Fig. 6.7C). However, in spite of this, the saline interface that is consequence of the density contrast caused by the salinity gradient between the nucleus brine and the recharge freshwater does not vanish in depth. The persistence of the mixing zone in

depth is a critical factor for the basin-scale hydrodynamics because prevents any flow path coming from the recharge in the mountains directly reach the salt flat nucleus. The eastern mixing zone due to its constrained groundwater flow modifies the temperature field with an increasing in the brine side and a decreasing in the freshwater side (Fig. 6.7A). In addition, the heat also favours the brine leakage from the top of the salt flat, which contributes to explain why the porosity and permeability of the aquifers have not reduced drastically due to salt precipitation.
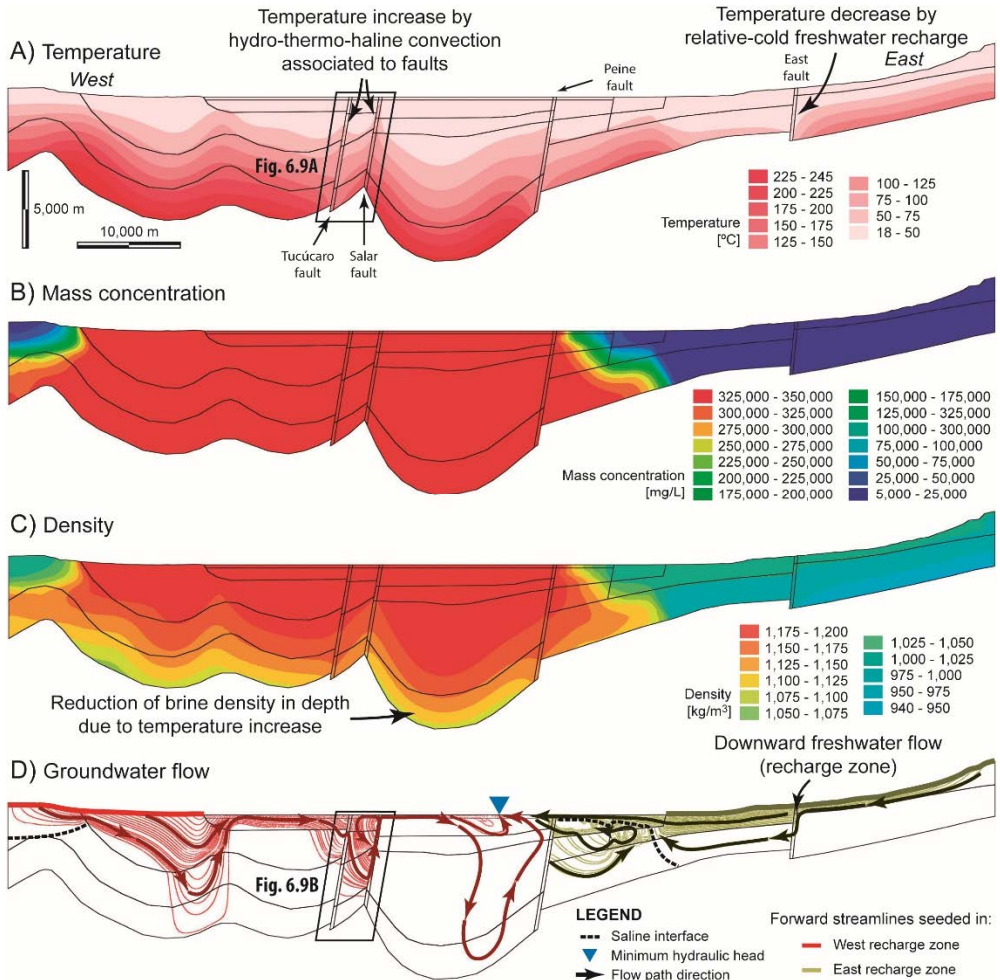
Figure 6.7. *Computed temperature field (A), mass-concentration (B), density field (C) and groundwater flow (D) for the hydro-thermo-haline simulation of the mature stage of the Salar de Atacama basin. The SFS zones showed in Fig. 6.9 are framed with two black parallelepipeds.*

The geometry of the mixing zone is controlled by the recharge-discharge rate and the hydraulic parameters of the basin rocks. Thus, the permeability of the upper aquifer controls the geometry of the mixing zone in the most superficial layers. The surficial layers of salt flats are often the most permeable ones due to the karstification process that usually affects the salt rocks and the frequent presence of low compacted detrital sediments in the salt flat surroundings (Marazuela et al., 2018). This is the case of the eastern mixing zone that outcrops into high-permeability Quaternary deposits unlike the western mixing zone that is placed directly over relative low-permeability Cenozoic rocks (Fig. 6.3 and Table 6.1). Thus, the slope of the eastern mixing zone in the upper aquifers is lower than in the western mixing zone because the high permeability of the upper aquifers reduces the freshwater heads contributing to the advance of the brine out of the nucleus. However, in depth, where the permeability is lower and it is almost similar in both mixing zones, the eastern mixing zone reaches a more pronounced slope than the western one due to the higher recharge coming from the volcanic arc.

A key factor is that the minimum hydraulic head of the water table divides completely the system into two hydrodynamic domains, the eastern and western domain (Fig. 6.7D). The minimum hydraulic head is located in the easternmost part of the salt flat nucleus, close to the eastern mixing zone. The groundwater flow in these two hydrodynamic domains is antisymmetric, that is, the flow lines come from their respective recharge zones, on both sides of the basin, and tend to die towards the zone with the minimum hydraulic head of the water table.

The freshwater coming from the recharge in the volcanic arc is forced to ascend by the saline interface and it outcrops in the eastern marginal zone (Fig. 6.7D). The flow paths turn very horizontal in the upper aquifers of the marginal zone due to the very low slope of the mixing zone described above. Along this quasi-horizontal flow path, the shallow water table close to the surface causes the groundwater to suffer an intense evaporation, rapidly increasing the concentration in solutes and reaching saturation in halite before reaching the minimum hydraulic head where the last eastern flow paths die. The little water that reaches the nucleus does not surpass the point of minimum hydraulic head and, as a consequence, it tends to recirculate by convection on the inner side of the saline interface (Fig. 6.8).

The fault located in the recharge area, the East Fault, shows a downward flow direction and hydrodynamics are controlled by the topographic gradient (Fig. 6.7D). The groundwater recharged in the mountains moved along surficial aquifers but when it reached a high-permeable fault, the flow path changed toward the deep. Due to the downward direction of the flow of the relative-cold water recharged in the mountains, this fault generated a negative anomaly in the temperature field, cooling the thermal gradient compared with the simulation with faults disabled (Fig. 6.7A).
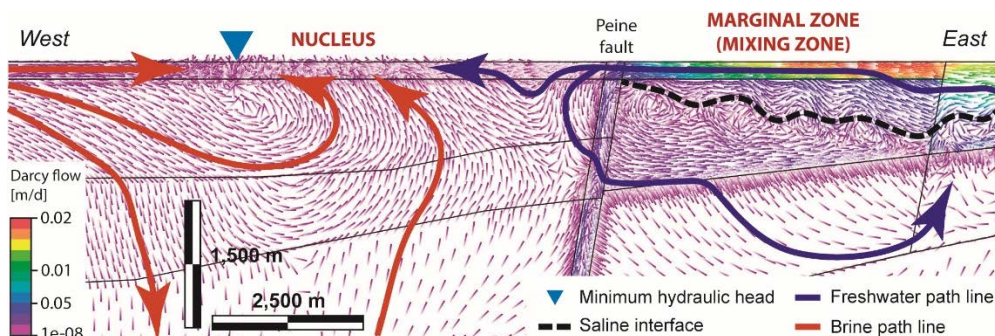
Figure 6.8. *Darcy flow and groundwater flow streamlines of the marginal zone and eastern salt flat nucleus.*

On the other side of the basin, the quick saturation in halite by the western recharge water is a process quite likely to occur due to the geology of the area. As described in the "Geological setting" section, the San Pedro Formation outcrops throughout the western margin of the salt flat through the Cordillera de la Sal and extends in deep below the entire salt flat (Arriagada et al., 2006; Jordan et al., 2007). The consideration of the San Pedro formation as a saline domain in which the pore water is saturated in halite leads to get a brine of homogenous density in the entire salt flat nucleus (Fig. 6.7C). A consequence of the leaching of the water-soluble rocks of the recharge area was that the groundwater entering the western margin of the salt flat nucleus really was brine of density 1,200 kg/m^3. The brine is enriched in solutes only by dissolution of salts and not by evaporation, as occurs in the eastern margin, because in this case, the water table is deeper and the phreatic evaporation does not occur. However, when the leaching-enriched brine coming from the W is incorporated to the nucleus, a slight evaporation can occur until the last flow path dies toward minimum hydraulic head. The brine crosses the entire nucleus from the W to the E although with very low velocity due to the small hydraulic gradient. The

almost non-existent hydraulic gradients together with the presence of a salt interface that borders the nucleus throughout its marginal zone make the nucleus behave like a pool almost hydrodynamically isolated from the rest of the basin. For this reason, a hydrodynamics dominated by hydraulic gradients induced by topography outside the nucleus and a hydrodynamics dominated by density gradients and convective fluxes in the salt flat nucleus can be distinguished.
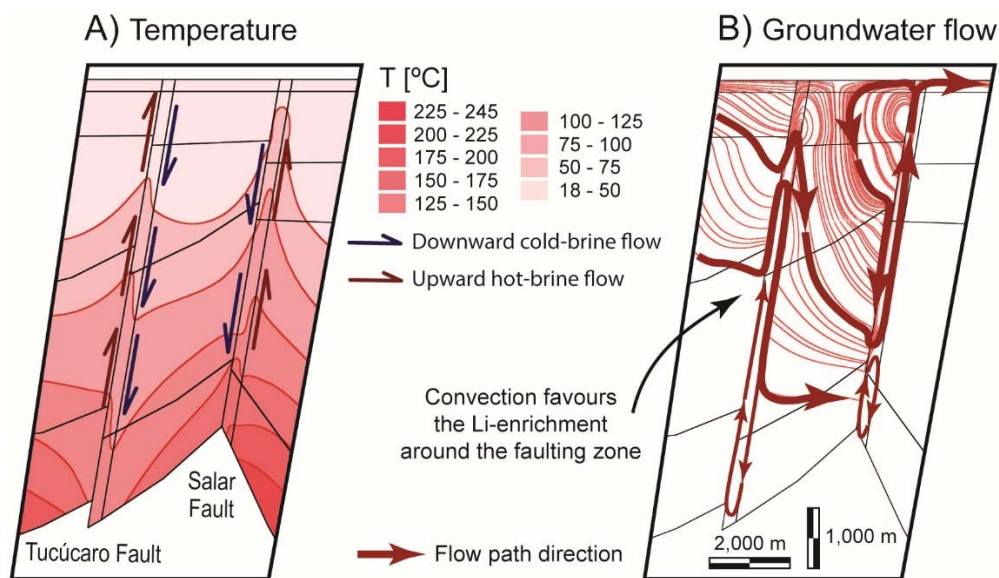
Figure 6.9. *Temperature (A) and groundwater flow (B) of the SFS located in the Salar de Atacama resulted from the hydro-thermohaline simulation. The location of this figure is shown in Fig. 6.7.*

The faults located inside the salt flat nucleus, showed a more complex and unpredictable hydrodynamics because they are located in an area of flat topography and, as a consequence, the density-driven flow dominates (Fig. 6.9). The density contrast induced by temperature and salinity gradients was the driving force of this hydro-thermo-haline circulation (Fig. 6.9A). The resulting streamlines evidenced the complex hydro-thermo-haline circulation that took place in the Tucúcaro and Salar faults located inside the salt flat nucleus. The brine enriched by leaching of salts coming from the W sinks when it reaches a fault. The circulation is complex and internal convection cells develop not only around the faults but also inside the faults similar to those described in other hydro-thermo-haline systems (Magri et al., 2012, 2010) (Fig. 6.9B). This produces a deformation of the temperature field with a

temperature decrease in the eastern side of the Tucúcaro fault and western side of the Salar Fault and an increase in the opposite sides of these faults (Fig. 6.9A).

Finally, the brine already saturated in halite coming from both hydrodynamic domains reaches the minimum hydraulic head. In this point, both antagonist flow paths converge and close the two large convection cell of each hydrodynamics domain (Fig. 6.7D).

6.4. Discussion

6.4.1. *The minimum hydraulic head constraint*

According to the modelling results, the minimum hydraulic head determines the direction in which the evaporated brine tends to move and accumulate (Figs. 6.5 and 6.6). As the highest concentration of Li and the densest brines are found in the SFS (Fig. 6.2), it would be necessary for the minimum hydraulic head to be located in that area in order to explain the extreme concentration of Li by evaporation. Only, if the evaporation was homogenous in the entire surface of the salt flat, the minimum hydraulic head would be located in a central to western position within the nucleus (Fig. 6.5). This hypothetical scenario could occur in the past and it is very likely that in the early stages of the salt flat, the most concentrated brine was located in the present SFS and that this was evidenced in deep layers buried today under the current salt flat. However, actually the minimum hydraulic head is located close to the eastern mixing zone (Fig. 6.7D) which implies that the most evaporated brines are located in that zone and not in the SFS of the nucleus where the highest Li-concentration occurs. In addition, due to the high hydraulic conductivity of the upper karstified aquifers (Marazuela et al., 2019a; Muñoz-Pardo et al., 2004), the hydrogeochemistry of these aquifers is in equilibrium with the present hydrological regime and it seems unlikely the Li-anomaly in the SFS was a brine vestige of a hypothetical old hydrological regime. Therefore, it is ruled out that the geochemistry of the brines of the upper aquifers is a vestige of a previous hydrodynamics in which, for example, the minimum hydraulic head was located in the fault zone. Therefore, it is not possible to explain the Li (and Mg, K, B)-high concentrated brines of the SFS only by evaporation and an alternative hypothesis should be addressed.

6.4.2. The mixing zone as regional hydraulic barrier for deep groundwater flow

Several previous works hypothesised that the Li-Mg-rich brines could have its origin in the leaching of the eastern volcanic arc or in the leakage of ancient salt flats from the Cordillera (Alonso and Risacher, 1996; Corenthal et al., 2016; Jordan et al., 2002; Risacher et al., 2003; Risacher and Alonso, 1996). However, under the current hydrodynamic setting of the SdA, no flow path can enter the nucleus of the salt flat through the eastern margin. The computed hydro-thermo-haline circulation confirmed that, although it may be slightly distorted by the temperature gradient, the eastern mixing zone keeps in depth (Fig. 6.7). The persistence in depth of the mixing zone has important implications for the regional hydrodynamics of the basin because it forces all groundwater coming from the eastern recharge produced in the volcanic arc to ascend until the surface in the eastern marginal zone of the salt flat. This would prevent that a flow path coming from the volcanic arc reaches the SFS as proposed Jordan et al. (2002). For the same reason, it would also not be consistent that the rise of Li-rich hydrothermal fluids would occur in the faults located between the nucleus and the volcanic arc as Munk et al., (2018) hypothesized. In addition, these previous hypothesis would necessarily imply that the highest concentration of Li would be located at the eastern part of the nucleus where the eastern flow paths end and the minimum hydraulic head of the water table are located. Once again, the hydro-thermo-haline-dynamics of the SdA points to the need to incorporate an extra process to explain the Li anomaly, as the minimum hydraulic head constrain pointed.

6.4.3. The possible role of fractures and hydro-thermo-haline convection in the formation of Li-rich brines

As discussed above, the recent minimum hydraulic head in the Eastern side is not compatible with the location of the higher Li-Mg concentrations in the SW of the nucleus. Moreover, the deep mixing zone prevents the inflow of lateral recharges to the nucleus. Therefore, new processes must be considered to explain such anomalous hydrochemistry. The location of the Li-rich brines in the nucleus closer to fractures of the Cordón de Lila (Fig. 6.2), suggests that fractures could have played an active role in the Li and Mg accumulation as already pointed out Lowenstein and Risacher (2009) with respect to the Ca-Cl-type brines.

According to the geological setting, the previous literature background, and the numerical modelling results, two hypotheses are open that deserve to be discussed. Thus, the original source of Li and Mg could be (1) rising of Li-rich brines from a deep hydrothermal reservoir similar to the proposed by González et al. (2009) or (2) mobilization of an old deposit (salts or clays) below the present salt flat which was formed during an hyperarid climate that favoured the extreme enrichment in Li-Mg.

In the case of Li-Mg enrichment by mobilization of an old deposit (salts, clays), the water recharged in the West of the salt flat basin quickly increases its salt-concentration by dissolution of the salts of San Pedro Formation that outcrops in the Cordillera de la Sal. During the path flow followed by this non-evaporated brine coming from the West towards the minimum hydraulic head of the water table, the presence of the Tucúcaro and Salar Faults would favour the sink and later rise of this brine (Fig. 6.11). In accordance with the model results, the western brine tends to sink down to several hundred or thousands of meters in the Tucúcaro Fault, and then return to the upper aquifer of the salt flat through the Salar Fault due to the convective circulation. Along this path, the brine can be enriched Li and Mg if any layer of old salt or exchangeable positions of clay enriched in these elements exists in depth although the density would remain undisturbed. Likely, the low Li/Na ratios and the $\delta^{18}O$-$\delta^{2}H$ values of the subsurface brine in the Salar del Hombre Muerto plot in the Meteoric Water Line indicating the deep inflow of non-evaporated water and that its salt comes from halite dissolution (Godfrey et al., 2013).

The existence of Li-salts as a source of Li has never been reported in the evaporite geological record of Central Andes (Risacher and Fritz, 2009). Indeed, although K, Mg and B are known to accumulate in soluble salts under advanced evaporation stages (chlorides, sulfates and borates), Li can be scarcely part of the salt structures and the majority remains in the liquid phase (Garrett, 2004; Pueyo et al., 2017; Song et al., 2017). Thus, in order to precipitate as LiCl, the brine must evaporate up to 38% w/w LiCl brine beyond the formation of sylvite, carnallite and bischofite (Garrett, 2004). The existence of Li-rich clays has been, however, more commonly reported. Thus, hectorite formed from the alteration of rhyolitic glass is described together with salt-beds in Pleistocene lacustrine sediments in Clayton valley, Nevada (Araoka et al., 2014; Munk et al., 2011). Hectorite halos interpreted as remains of ancient lacustrine brines have been reported from several other locations in the North American Basin and Range (Vine and Dooley, 1980). Also, the existence of Li-bearing

clays is hypothesized to explain the concentration and isotopic values of Li in deep strata of the Salar de Olaroz, Argentina (Garcia et al., 2020). Li-bearing smectitic clays have been also reported in the Birka and Bigodic boron salt flats, Turkey (Büyüburç and Köksal, 2005). No hectorite has been described to know in the SdA, although Ide and Kunasz (1990) emphasized the existence of Li concentrations as high as 484 ppm in the argillaceous sediments underlying the tuffs of the Miocene El Campamento formation, present in the Cordillera de la Sal and the Cordon de Lila areas. Up to 200 mg/L of exchangeable Li were removed from synthetic Li-bearing smectites with 1 M NH_4Cl and Ca_2Cl solution prior to Li isotope fractionation experiments (Vigier et al., 2008).

A study of deuterium and oxygen isotopes will easily discern if the Li-Mg rich brine comes from a brine highly evaporated and leaked down in ancient stages of the salt flat or a non-evaporated recharge water acquiring its salinity by dissolution of salt rocks. Also a detailed study of noble gases around the SFS could contribute to identify a possible deep hydrothermal sources although brine mixtures in the fracture could mask a clear distinction.

An indirect test for dissolution of Li-salts or leaching of Li-clays can be the Br concentration of Li-rich brines. Thus, due to the increasing concentration in solution with evaporation and the higher solid/liquid partition coefficient in Mg-salts (Marion et al., 2010), Br is expected to be enriched in the advanced evaporated salts accompanying hypothetical Li-salts (see Krupp, 2005 for a Permian example). Therefore, Br is expected to be present in the analyses of Li-rich brines. On the contrary, Br is poorly scavenged by halite, and the brines formed by recharge water dissolving halite and then extracting Li from clays are not expected to have Br concentrations very different from the dilute inflows.

Ultimately, it is important to highlight that the hydro-thermo-haline convection of salt flats could not be easily detected in the field observations. The upper aquifer of the nucleus does not show any appreciable increase of the hydraulic heads, thus, the groundwater coming from the W recharge zone goes beyond the fault zone without changes until it reaches the regional minimum hydraulic head. Moreover, the basic physical-chemical parameters (density, CE, TDS, etc.) would not be differentiated from those of the salt flat in which only evaporation contributed to enrichment of the brine.

6.5. Conclusions

Hydro-thermo-haline modelling revealed useful to understand the origin of the extreme Li-enrichment in the Salar de Atacama and rule out some previous hypothesis. Thus, the present minimum hydraulic head located in the Eastern side of the nucleus prevents to consider advanced evaporation as a present day mechanism of reaching the high Li content of the brines located in the Salar Fault System within the nucleus. Moreover, the persistence of mixing zones in depth also enables 1) lateral recharge from the Altiplano-Puna (and its possible leaching of buried salt flats below the volcanic rocks), and 2) the leaking of the present salt flats in the Altiplano-Puna as sources for high Li brines.

The results of the hydro-thermo-haline modelling are compatible with other alternative genetic hypotheses: 1) rising of Li-rich brines from a deep hydrothermal reservoir, and 2) remobilization of ancient layers of Li-enriched salts and/or clays by non-evaporated recharge waters. In both cases, the role of fractures is very important to allow efficient down and up flow rates. No reason to rule out any of the two hypotheses was deduced from the hydrodynamic analysis. However, a study of deuterium and oxygen isotopes will easily discern if the Li-Mg rich brine comes from a brine highly evaporated and leaked down in ancient stages of the salt flat or a non-evaporated recharge water acquiring its salinity by dissolution of salt rocks. Also a detailed study of noble gases around the SFS could contribute to identify a possible deep hydrothermal sources although brine mixtures in the fracture could mask a clear distinction.

Future modelling works of salt flats should avoid considering an impermeable bottom boundary immediately below the upper aquifers and should include the coupled effects of the mass-concentration and temperature gradients at regional scale. Thus, the density-driven flow allows the leakage of dense brines even through very low permeability and contributes to explain the hydrogeochemistry of the salt flat systems.

Chapter 7

General Conclusions

The aim of this thesis has been to establish and validate through numerical models the hydrogeological functioning of salt flats under natural and anthropogenic regimes, taking the Salar de Atacama as case of study. This has allowed to evaluate the impacts of the brine extraction on the natural hydrodynamics of the basin and discuss the extreme Li-enrichment of their brines.

The results of this thesis have allowed to answer the questions posed in the introduction section:

- **How is the geometry and the groundwater flow of the mixing zone (saline interface) of salt flats?**

The first 3D mapping of the Salar de Atacama mixing zone was completed and it evidenced a much lower slope of the mixing zone than previous predictions. The 2D modelling of an idealized vertical cross-section of the mixing zone allowed to explain the shallow location of the mixing zone. Thus, as the permeability of the upper aquifer increases, the slope of the mixing zone decreases, resulting in a shallower mixing zone. This occurs because the freshwater that is recharged in the mountains is forced to flow through the upper aquifer and thus have a lower head at the mixing

zone. Therefore, the permeability of the upper aquifer, generally constituted by very conductive karstified evaporites and alluvial deposits, is critical to the geometry of the mixing zone.

Moreover, a methodology based on the density correction applied to freshwater and mixed water heads has been proposed to transform them into brine heads. This methodology allows to reproduces the vertical fluxes of the mixing zone in 3D groundwater flow models with low computational cost.

- **How is the hydrogeological functioning of the Salar de Atacama under natural conditions?**

The hydrogeological model and the water balance of the Salar de Atacama, prior to the brine pumping (natural regime), was established and validated using a 3D steady-state groundwater flow model that included the methodology proposed to reproduce the vertical fluxes of the mixing zone.

The water balance of the endorheic basin was quantified between 12.8 and 14.9 $m^3 \cdot s^{-1}$ for both, the inflows and outflows. The existence of evaporated inflows from the Altiplano-Puna (outside the basin) as the main source of the enriched elements in the brine seems to be unlikely according to previous isotopic data collected and reinterpreted.

The recharge of the basin occurs mainly in the eastern half sub-basins due to its higher topographic level. The very low infiltration rate that is frequently assumed for hyperarid basins is not consistent with the hydrogeology of the Salar de Atacama. Here, a high infiltration rate occurs as a consequence of the high degree of fracturing of the rocks and the scarce vegetation. The discharge takes place mainly from the free water surface of the lakes or from the shallow water table of the mixing zone, and minority the nucleus, as phreatic evaporation. This results in a water table whose minimum hydraulic head is located in the easternmost nucleus, close to the eastern mixing zone. The presence of the surrounding mixing zone that operates as hydraulic barrier and the almost absent hydraulic gradients leads the nucleus to act as a hydrodynamically quasi-isolated area.

- **What impact does the brine pumping on the hydrodynamics and the water balance of salt flats?**

The 3D transient-state groundwater flow modelling of the Salar de Atacama basin from 1986 to 2018 allowed to explain the hydrodynamics and water balance of salt flats under natural and mining regimes.

From 1986 to 1994, under the natural regime, the gradual drawdown of the water table resulting from the negative water balance (greater evaporation than recharge) was counteracted by the sharp rises caused by rainfall events occurred directly on the salt flat. The groundwater coming from the mountains remained quite constant because the pulses were damped by the great distance and the thick unsaturated zone of the mountains.

From 1994 to 2015, under mining regime, the brine pumping caused an additional drawdown of the water table that triggered a decrease of the phreatic evaporation. This effect was defined as "damping capacity". The damping capacity is of great importance for the sustainable management of salt flats and their ecosystems because it allows to counteract the disturbances occasioned by natural or anthropogenic events on the water table and water balance.

- **Can the impacts caused by brine extraction be spatio-temporally quantified? Is it possible to improve the design of mining operations to reduce environmental impacts?**

A methodology based on field data and spatio-temporal analysis was proposed and applied to the Salar de Atacama to quantify the impacts caused by brine pumping on the water table and the evaporation discharge of salt flats.

First, the measurements carried out with evaporation pans and lysimeters allowed to estimate the potential evaporation from the free water surface of lakes (5.84 mm·d^{-1}) and to define the exponential decrease of the evaporation with respect to the water table depth.

Second, the spatio-temporal analysis of the water table depth and the evaporation rate allowed to quantify the decrease of the evaporation discharge in 15 % from 1986 to 2018. The damping capacity compensated, at least in part, the decrease of the evaporation discharge in the nucleus but it is already amortized nowadays and the mixing zone begins to be impacted.

Third, the 3D groundwater flow modelling of several distributions of pumping wells showed that brine exploitations should consider to distribute the pumping outflow in the greatest extent possible to take full advantage of the damping capacity and minimize environmental impacts.

- **What is the origin of the extreme Li-enrichment in the Salar de Atacama?**

The hydro-thermo-haline modelling proved useful to understand the origin of the extreme Li-enrichment in the Salar de Atacama and rule out some previous hypothesis. On one side, the minimum hydraulic head is located in the easternmost part of the nucleus where the most evaporated brines are found. On the other side, highest Li-concentrated brines are located in the faulting zone (central-southwestern nucleus). This decoupling prevents to consider advanced evaporation as the present day mechanism of Li-enriching.

The persistence of mixing zones in depth also prevents (1) the leaking of brines from the present salt flats of the Altiplano-Puna and (2) the leaching of hypothetical salt flats buried by volcanic eruptions in the Altiplano-Puna as sources for Li-enriched brines. By contrast, the results of the hydro-thermo-haline modelling are compatible with other alternative genetic hypotheses: (1) the rising of Li-rich brines from a deep hydrothermal reservoir and (2) the remobilization of ancient layers of Li-enriched salts and/or clays by non-evaporated recharge waters. In both cases, the role of the Salar Fault System is capital to allow down and up efficient flow rates.

Appendix A

Scientific and technical production.

Scientific articles

Scientific articles directly related with the PhD thesis:

1. **Marazuela, M.A.**, Vázquez-Suñé, E., Custodio, E., Palma, T., García-Gil, A., Ayora, C. (2018). 3D mapping, hydrodynamics and modelling of the freshwater-brine mixing zone in salt flats similar to the Salar de Atacama (Chile). *Journal of Hydrology*, 561, 223-235. DOI: 10.1016/j.jhydrol.2018.04.010.

2. **Marazuela, M.A.**, Vázquez-Suñé, E., Ayora, C., García-Gil, A., Palma, T. (2019). Hydrodynamics of salt flat basins: The Salar de Atacama example. *Science of the Total Environment*, 651, 668-683. DOI: 10.1016/j.scitotenv.2018.09.190.

3. **Marazuela, M.A.**, Vázquez-Suñé, E., Ayora, C., García-Gil, A., Palma, T. (2019). The effect of brine pumping on the natural hydrodynamics of the Salar de Atacama: The damping capacity of salt flats. *Science of the Total Environment*, 654, 1118-1131. DOI: 10.1016/j.scitotenv.2018.11.196.

4. **Marazuela, M.A.**, Vázquez-Suñé, E., Ayora, C.; García-Gil, A. (2020). Towards more sustainable brine extraction in salt flats: Learning from the Salar de Atacama. *Science of the Total Environment*, 703, 135605. DOI: 10.1016/j.scitotenv.2019.135605.

5. **Marazuela, M.A.**, Vázquez-Suñé, E., Custodio, E., Palma, T., García-Gil, A., Ayora, C. (2020). Cartografía 3D, hidrodinámica y modelación numérica de la interfaz salina del Salar de Atacama. *Boletín Geológico y Minero de España* (in press).

6. **Marazuela, M.A.**, Ayora, C., Olivella, S., Vázquez-Suñé, E., García-Gil, A., Ayora, C. From the origin to the mature stage of a salt flat: hydrogeological constraints to explain the extreme Li-enrichment in the Salar de Atacama. In preparation.

Other scientific articles where the author had collaborated during the PhD thesis:

1. Vázquez-Suñé, E., **Marazuela, M.A.**, Velasco, V., Diviu, M., Pérez-Estaún, A., Álvarez-Marrón, J. (2016). A geological model for the management of subsurface data in the urban environment of Barcelona and surrounding area. *Solid Earth*, 7, 5, 1317-1329. DOI: 10.5194/se-7-1317-2016.

2. García-Gil, A., Epting, J., Garrido, E., Vázquez-Suñé, E., Lázaro, J.M., Sánchez-Navarro, J.A., Huggenberg, P., **Marazuela, M.A.** (2016). A city scale study on the effects of intensive groundwater heat pump systems on heavy metal contents in groundwater. *Science of the Total Environment*, 572, 1047-1058. DOI: 10.1016/j.scitotenv.2016.08.010.

3. Muela-Maya, S., García-Gil, A., Garrido-Schneider, E., Mejías-Moreno, M., Epting, J., Vázquez-Suñé, E., **Marazuela, M.A.**, Sánchez-Navarro, J.A. (2018). An upscaling procedure for the optimal implementation of open-loop geothermal energy systems into hydrogeological models. *Journal of Hydrology*, 563, 155-166. DOI: 10.1016/j.jhydrol.2018.05.057.

4. Soriano, M.A., Pocoví, A., Gil, H., Pérez, A., Luzón, A., **Marazuela, M.A.** (2019). Some evolutionary patterns of palaeokarst developed in Pleistocene deposits (Ebro Basin, NE Spain): Improving geohazard awareness in present-day karst. *Geological Journal*, 54, 1, 333-350. DOI: 10.1002/gj.3181.

5. García-Gil, A., Muela-Maya, S., Garrido-Schneider, E., Mejías-Moreno, M., Vázquez-Suñé, E., **Marazuela, M.A.**, Mateo-Lázaro, J., Sánchez-Navarro, J.A. (2019). Sustainability indicator for the prevention of potential thermal interferences between groundwater heat pump systems in urban aquifers. *Renewable Energy*, 134, 14-24. DOI: 10.1016/j.renene.2018.11.002.

6. García-Gil, A., Abesser, C., Gasco-Cavero, S., **Marazuela, M.A.**, Mateo-Lázaro, J., Vázquez-Suñé, E., Hughes, A.G., Mejías-Moreno, M. (2020). Defining the exploitation patterns of groundwater heat pump systems. *Science of the Total Environment*, 710, 136425. DOI: 10.1016/j.scitotenv.2019. 136425.

7. Folch, A., del Val, L., Luquot, L., Martínez-Pérez, L., Bellmunt, F., Le Lay, H., Rodellas, V., Ferrer, N., Palacios, A., Fernández, S., **Marazuela, M.A.**, Diego-Feliu, M., Pool, M., Goyetche, T., Ledo, J., Pezard, P., Bour, O., Queralt, P., Marcuello, A., García-Orellana, J., Saaltink, M.W., Vázquez-Suñé, E., Carrera, J. (2020). Combining Fiber Optic (FO-DTS), Cross-Hole ERT and time lapse formation electrical conductivity to characterize and monitor a coastal aquifer. *Journal of Hydrology* (under review).

8. Martinez-Pérez, L., Luquot, L., Carrera, J., **Marazuela, M.A.**, Goyetche, T., Pool, M., Palacios, A., Bellmunt, F., Ledo, J., Ferrer, N., del Val, L., Pezard, P., García-Orellana, J., Diego-Feliu, M., Rodellas, V., Saaltink, M., Vázquez-Suñé, E., Folch, A. (2020). Conceptual and methodological surprises in the

characterization of the Mediterranean coastal aquifer of Argentona. *Hydrology and Earth System Sciences* (under review).

Book chapters

1. García-Gil, A., **Marazuela, M.A.**, Velasco, V., Alcaraz, M., Vázquez-Suñé, E. and Corbera, A. (2016). Assessing shallow geothermal resources at Zaragoza, North-East Spain, with 3D geological models. In: *Applied Multidimensional Geological Modelling*. K. Turner, J. Ford, H. Kessler (Eds.), Wiley-Blackwell (2016). 450 pages. ISBN: 978-1-119-16312-1.

Proceedings in congresses

1. Soriano, M.A., Gil, H., Pocoví, A., Pérez, A., **Marazuela, M.A**. Usefulness of the study of palaeokarst affecting Quaternary deposits in the Central Ebro Basin. *Progress in Quaternary archive studies in the Iberian Peninsula*. 12-13 March 2015. Sevilla (Spain). Oral presentation.
2. **Marazuela, M.A.**, Vázquez-Suñé, E., Velasco-Mansilla, V., Diviu, M. La gestión de datos hidrogeológicos en entornos urbanos: el caso de estudio de la ciudad de Barcelona. *Meeting of 50th anniversary CIHS 1966-2016*. 12-13 May 2016. Barcelona (Spain). Poster presentation.
3. **Marazuela, M.A.**, Vázquez-Suñé, E., Criollo-Manjarrez, R., García-Gíl, A. The origin of the geothermal anomaly identified in the Barcelona underground (Spain): Future perspectives of this urban geothermal resource. *EGU General Assembly 2017*. 23-28 April 2017. Vienna (Austria). Poster presentation.
4. Criollo, R., Velasco, V., Vázquez-Suñé, E., Nardi, A., **Marazuela, M.A.**, Rosetto, R., Borsi, I., Foglia, L., Cannata, M., De Filippis, G. Open source GIS based tools to improve hydrochemical water resources management in EU H2020 FREEWAT platform. *EGU General Assembly 2017*. 23-28 April 2017. Vienna (Austria). Poster presentation.
5. Criollo, R., Vázquez-Suñé, E., Velasco, V., **Marazuela, M.A.**, Burdons, S., Enrich, M., Cardona, F. An approach of groundwater management in Barcelona City. *EGU General Assembly 2017*. 23-28 April 2017. Vienna (Austria). Poster presentation.

6. **Marazuela, M.A.**, Vázquez-Suñé, E., García-Gil, A. Tidal fluctuations in salt flats and its importance for the contingency plans. *44th Annual Congress of the International Association of Hydrogeologists (IAH)*. 25-29 September 2017. Dubrovnik (Croatia). Poster presentation.

7. Martínez-Pérez, L., **Marazuela, M.A.**, Luquot, L., Folch, A., García-Orellana, J., Ferrer, N., Rodellas, V., Bellmunt, F., Del Val, l., Fernández, S., Ledo, J., Pezard, P., Saaltink, M., Carrera, J., Vázquez-Suñé, E. New guidelines to describe seawater intrusion process: the experimental Argentona field site. *44th Annual Congress of the International Association of Hydrogeologists (IAH)*. 25-29 September 2017. Dubrovnik (Croatia). Poster presentation.

8. Folch, A., Del Val, L., Luquot, L., Martínez, L., bellmunt, F., Le Lay, H., Rodellas, V., Ferrer, N., Fernández, S., **Marazuela, M.A.**, Ledo, J., Pezard, P., Bour, O., Queralt, P., Marcuello, A., García-Orellana, J., Saaltink, M., Vázquez-Suñé, E., Carrera, J. Combining different techniques to monitor seawater intrusion integrating different observation scales. *44th Annual Congress of the International Association of Hydrogeologists (IAH)*. 25-29 September 2017. Dubrovnik (Croatia). Oral presentation.

9. García-Gil, A., Garrido-Schneider, E., Sánchez-Navarro, J.A., Vázquez-Suñé, E., **Marazuela, M.A.**, Muela-Maya, S. Reactive transport modelling for the study of geochemical impacts induced by shallow geothermal exploitation. *Congress on Groundwater and Global Change in the Western Mediterranean. Impacts of Global Change on Western Mediterranean Aquifers*. 06-09 November 2017. Granada (Spain). Oral presentation.

10. **Marazuela, M.A.** Freshwater-Brine Mixing Zone Hydrodynamics in Salt Flats (Salar de Atacama). *American Geophysical Union (AGU) 2017 Fall Meeting*. 11-15 December 2017. New Orleans (EEUU). Poster presentation.

11. **Marazuela, M.A.** 3D mapping, hydrodynamics and modelling of the freshwater-brine mixing zone in salt flats similar to the Salar de Atacama (Chile). *Seminar for the Hydrogeology Group (GHS)*. 1 March 2018. Barcelona (Spain). Oral presentation.

12. **Marazuela, M.A.**, Vázquez-Suñé, E., Ayora, C., Palma, T., García-Gil, A. The complex hydrogeological equilibrium of the Salar de Atacama (NE Chile): a numerical approach for the management of salt flats systems. *EGU General Assembly 2018*. 08-13 May 2018. Vienna (Austria). Poster presentation.

13. **Marazuela, M.A.**, Vázquez-Suñé, E., Custodio, E., Palma, T., García-Gil, A., Ayora, C. 3D mapping, hydrodynamics and modelling of the freshwater-brine mixing zone in salt flats similar to the Salar de Atacama (Chile). *25th Salt Water Intrusion Meeting*. 17-22 June 2018. Gdansk (Polonia). Poster presentation.

14. Martínez-Pérez, L., **Marazuela, M.A.**, Luquot, L., Folch, A., Del Val, L., Goyetche, T., Diego-Feliu, M., Ferrer, N., Rodellas, V., Bellmunt, F., Ledo, J., Pool, M., García-Orellana, J., Pezard, P., Saaltink, M., Vázquez-Suñé, E., Carrera. J. Integrated methodology to characterize hydro-geochemical properties in an alluvial coastal aquifer affected by seawater intrusion (SWI) and submarine groundwater discharge (SGD). *25th Salt Water Intrusion Meeting*. 17-22 June 2018. Gdansk (Polonia). Poster presentation.

15. Folch, A., Del Val, L., Luquot, L., Martínez-Pérez, L., Bellmunt, F., Le Lay, H., Rodellas, V., Ferrer, N., Fernández, S., **Marazuela, M.A.**, Diego-Feliu, M., Pool, M., Goyetche, T., Palacios, A., Ledo, J., Pezard, P., Bour, O., Marcuello, A., García-Orellana, J., Saaltink, M., Vázquez-Suñé, E., Carrera, J. Seawater intrusion dynamics monitoring with geophysical techniques combination. *25th Salt Water Intrusion Meeting*. 17-22 June 2018. Gdansk (Polonia). Oral presentation.

16. **Marazuela, M.A.**, Vázquez-Suñé, E., Custodio, E., Palma, T., García-Gil, A., Ayora, C. Cartografía 3D, hidrodinámica y modelación numérica de la interfaz salina del Salar de Atacama (Chile). *XIV Congreso latinoamericano de hidrogeología*. 23-26 October 2018. Salta (Argentina). Oral presentation and proceeding.

17. García-Gil, A., Gasco-Cavero, S., Garrido-Schneider, E., Mejías-Moreno, M., Vázquez-Suñé, E., **Marazuela, M.A.**, Navarro-Elipe, M., Alejandre, C., Sevilla-Alcaine, E. Procesos de pseudo-pasteurización de bacterias patógenas en agua subterránea inducidos por intercambiadores geotérmicos. *Congreso Ibérico sobre Agua subterránea, medio ambiente, salud y patromonio*. 12-15 November 2018. Salamanca (Spain). Oral presentation.

18. **Marazuela, M.A.**, Vázquez-Suñé, E., Ayora, C., García-Gil, A. The damping capacity of the water balance of salt flats subjected to brine pumping: The Salar de Atacama example. *EGU General Assembly 2019*. 07-12 April 2019. Vienna (Austria). Poster presentation.

19. Martínez, L., **Marazuela, M.A.**, Luquot, L., Folch, A., Del Val, L., Goyetche, T., Diego-Feliu, M., Saaltink, M., Rodellas, V., Pool, M., Bellmunt, F., García-Orellana, J., Pezard, P., Ledo, J., Vázquez-Suñé, E., Carrera. J. Facing geological heterogeneity impact on reciprocal coastal systems. *EGU General Assembly 2019*. 07-12 April 2019. Vienna (Austria). Poster presentation.

20. Folch, A., Del Val, L., Luquot, L., Martínez, L., Bellmunt, F., Le Lay, H., Rodellas, V., Ferrer, N., Fernández, S., **Marazuela, M.A.**, Diego-Feliu, M., Pool, M., Goyetche, T., Ledo, J., Pezard, P., Bour, O., Queralt, P., Marcuello, A., García-Orellana, J., Palacios, A., Saaltink, M., Vázquez-Suñé, E., Carrera, J. Do groundwater data from piezometers correlate with FO-DTS and CHERT in costal aquifers?. *EGU General Assembly 2019*. 07-12 April 2019. Vienna (Austria). Poster presentation.

21. Vázquez-Suñé, E., **Marazuela, M.A.**, Scheiber, L., Criollo, R., Diviu, M., Mayer-Anhalt, L., Botey-Bassols, J. Finding geothermal resources under and urban area (Barcelona). *46th Annual Congress of the International Association of Hydrogeologists (IAH)*. 22-27 September 2019. Malaga (Spain). Oral presentation.

22. **Marazuela, M.A.**, Ayora, C., Vázquez-Suñé, E., Olivella, S., García-Gil, A. From the origin to the mature stage of salt flats: implications for the extreme Li-enrichment of its brines. *American Geophysical Union (AGU) 2019 Fall Meeting*. 9-13 December 2019. San Francisco (EEUU). Poster presentation.

23. **Marazuela, M.A.**, Ayora, C., Vázquez-Suñé, E., Olivella, S., García-Gil, A. A hydro-thermo-haline numerical approach of the groundwater flow to explain the extreme Li-enrichment in the Salar de Atacama (NE Chile). *EGU General Assembly 2020*. 3-8 May 2020. Vienna (Austria). Poster presentation.

24. García-Gil, A., **Marazuela, M.A.**, Mejías-Moreno, M., Vázquez-Suñé, E., Garrido-Schneider, E., Sánchez-Navarro, J.A. The BSI indicator: preventing thermal interferences between groundwater heat pump systems. *EGU General Assembly 2020*. 3-8 May 2020. Vienna (Austria). Poster presentation.

25. Vázquez-Suñé, E., **Marazuela, M.A.**, Criollo, R., Mayer-Anhalt, L., Scheiber, L., Botey, J. Geothermal Anomaly Identified Under a Dense Urban Area in the Metropolitan Region of Barcelona, Spain. *Proceedings World Geothermal Congress 2020*. 26 April – 2 May 2020. Reykjavik (Iceland). Oral presentation and proceeding.

Scientific and technology transfer projects

1. Mezcla y dispersión en el transporte de energía y solutos (MEDISTRAES). Programa Estatal de I+D+i Orientada a los Retos de la Sociedad, Ministerio de Economía y Competitividad (MINECO). Grant agreement number: CGL2013-48869-C2-1-R (January 2014 – December 2017).

2. Evaluación de las posibilidades de aprovechamiento de la anomalía geotérmica detectada en el sector de Fondo de Santa Coloma de Gramanet. Consorcio del Besós (October 2014 – March 2015).

3. FREE and open source software tools for WATer resource management. FREE-WAT project. Horizon 2020 - EU.3.5.4. Grant agreement number: 642224. (January 2015 – December 2018).

4. Assistència tècnica per la realització de talls geològics, el mapa d'isòbates del basament prequaternari, i el mapa de basament prequaternari, de la zona del delta del Besòs i del Pla de Barcelona, dels fulls a escala 1:25000 de Badalona (73-31) i de Barcelona (73-72). Institut Cartogràfic i Geològic de Catalunya (ICGC) (July 2015- December 2015).

5. Seguimiento hidrogeológico de los procesos de agotamiento del freático en el ámbito de la ejecución del túnel de la Plaza de Glorias. Ayuntamiento de Barcelona and BIMSA S.A. (September 2015 – September 2016).

6. Estudio para determinar el potencial de aprovechamiento geotérmico en el sector de Fondo, Santa Coloma de Gramenet. Consorcio del Besós (January 2016 – September 2016).

7. Cuarta actualización del modelo de flujo de agua subterránea en el Salar de Atacama según RCA 226-2006. Sociedad Química y Minera de Chile (SQM) (April 2016 – January 2017).

8. Grupo de Hidrología Subterránea (GHS). Agència de Gestió d'Ajuts Universitaris i de Recerca (AGAUR) (January 2017 – December 2019).

9. Revisión de los modelos numéricos del Salar de Llamara, Chile. Sociedad Química y Minera de Chile (SQM) (September 2017 – January 2018).

10. Trabajos de modelación hidrogeológica SQM-Salar. Sociedad Química y Minera de Chile (SQM) (January 2018 – January 2019).

11. Revisión cálculos hidrogeológicos y seguimiento de los efectos producidos por el agotamiento del freático en el ámbito de la ejecución del túnel de la

Plaza de Glorias. Ayuntamiento de Barcelona and BIMSA S.A. (May 2018 – May 2020).

12. UrbaN Bio-geochemistry: Integrating the Air, water, Soil and microbiological sciEnce needed to unDerpin pollution management. (UNBIASED). Programa Estatal de I+D+I Orientada a los Retos de la Sociedad, Ministerio de Ciencia, Innovación y Universidades. Grant agreement number: TI2018-097346-B-I00. (September 2019 – March 2021).

Appendix B

Cover of the scientific articles already published.

Research papers

3D mapping, hydrodynamics and modelling of the freshwater-brine mixing zone in salt flats similar to the Salar de Atacama (Chile)

M.A. Marazuela[a,b,c,*], E. Vázquez-Suñé[a], E. Custodio[b,d], T. Palma[a,b,c], A. García-Gil[e], C. Ayora[a]

[a] Institute of Environmental Assessment and Water Research (IDAEA), CSIC, Jordi Girona 18-26, 08034 Barcelona, Spain
[b] Department of Civil and Environmental Engineering, Technical University of Catalonia (UPC), Jordi Girona 1-3, 08034 Barcelona, Spain
[c] Associated Unit: Hydrogeology Group (UPC-CSIC), Spain
[d] Royal Academy of Sciences of Spain, Spain
[e] Geological and Mining Institute of Spain (IGME), Manuel Lasala 44, 9° B, 50006 Zaragoza, Spain

ARTICLE INFO

ABSTRACT

Salt flat brines are a major source of minerals and especially lithium. Moreover, valuable wetlands with delicate ecologies are also commonly present at the margins of salt flats. Therefore, the efficient and sustainable exploitation of the brines they contain requires detailed knowledge about the hydrogeology of the system. A critical issue is the freshwater-brine mixing zone, which develops as a result of the mass balance between the recharged freshwater and the evaporating brine.

The complex processes occurring in salt flats require a three-dimensional (3D) approach to assess the mixing zone geometry. In this study, a 3D map of the mixing zone in a salt flat is presented, using the Salar de Atacama as an example. This mapping procedure is proposed as the basis of computationally efficient three-dimensional numerical models, provided that the hydraulic heads of freshwater and mixed waters are corrected based on their density variations to convert them into brine heads. After this correction, the locations of lagoons and wetlands that are characteristic of the marginal zones of the salt flats coincide with the regional minimum water (brine) heads.

The different morphologies of the mixing zone resulting from this 3D mapping have been interpreted using a two-dimensional (2D) flow and transport numerical model of an idealized cross-section of the mixing zone. The result of the model shows a slope of the mixing zone that is similar to that obtained by 3D mapping and lower than in previous models. To explain this geometry, the 2D model was used to evaluate the effects of heterogeneity in the mixing zone geometry. The higher the permeability of the upper aquifer is, the lower the slope and the shallower the mixing zone become. This occurs because most of the freshwater lateral recharge flows through the upper aquifer due to its much higher transmissivity, thus reducing the freshwater head. The presence of a few meters of highly permeable materials in the upper part of these hydrogeological systems, such as alluvial fans or karstified evaporites that are frequently associated with the salt flats, is enough to greatly modify the geometry of the saline interface.

1. Introduction

Salt flats (*salares*) are an important source of minerals. They account for half of the world's lithium production and contain the main economic reserves of this element (USGS, 2017). In addition, boron and potash are economically mined from salt flats. Lithium is a strategic commodity; its uses vary from light batteries to cancer treatment. Its demand has notably increased in the last decade, and this trend will probably continue in the future (Vikström et al., 2013), as large quantities may be needed to develop nuclear fusion reactors using tritium generated from lithium. This fact is evidenced by the large number of countries that are just now commissioning studies to determine the mineral potential of their salt flats (e.g., Salar de Uyuni in Bolivia or Salar del Hombre Muerto in Argentina) as well as to increase the amounts of resources that could be exploited during current mining activities (e.g., Salar de Atacama in Chile). This explains the current worldwide interest in salt flat hydrogeology, which is also due to the existence of peripheral brine and saline water lagoons that have high ecological, human and tourist value, in addition to their scientific value.

Salt flats are endorheic lagoon systems associated with arid or hyperarid climates, where the rate of evaporation is very high; in many

Hydrodynamics of salt flat basins: The Salar de Atacama example

M.A. Marazuela [a,b,c,*], E. Vázquez-Suñé [a], C. Ayora [a], A. García-Gil [d], T. Palma [a,b,c]

[a] Institute of Environmental Assessment and Water Research (IDAEA), CSIC, Jordi Girona 18, 08034 Barcelona, Spain
[b] Department of Civil and Environmental Engineering, Technical University of Catalonia (UPC), Jordi Girona 1-3, 08034 Barcelona, Spain
[c] Associated Unit: Hydrogeology Group, UPC-CSIC, Spain
[d] Geological and Mining Institute of Spain (IGME), Manuel Lasala 44, 9° B, 50006 Zaragoza, Spain

HIGHLIGHTS

- A new regional groundwater flow for the Salar de Atacama was proposed.
- The hydrodynamics can be extended to other salt flat systems.
- The regional 3D numerical model served to validate the water balance.
- The conventional infiltration values for the hyperarid zones were not valid.
- Infiltration rates of hyperarid basin that reach 75% are justified.

GRAPHICAL ABSTRACT
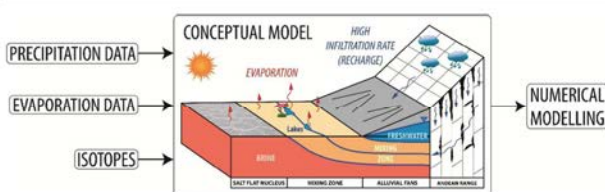
ARTICLE INFO

ABSTRACT

The Salar de Atacama is one of the most well-known saline endorheic basins in the world. It accumulates the world main lithium reserves and contains very sensitive ecosystems. The objective of this work is to characterize the hydrodynamics of the Salar de Atacama, and to quantify its complex water balance prior to the intense brine extraction. The methodology and results can be extrapolated to the groundwater flow and recharge of other salt flats. A three-dimensional groundwater flow model using low computational effort was calibrated against hundreds of hydraulic head measurements. The water infiltrated from the mountains ascends as a vertical flux through the saline interface (mixing zone) produced by the density contrast between the recharged freshwater and the evaporated brine of the salt flat nucleus. This water discharges and is largely evaporated from lakes or directly from the shallow water table. On the other hand, the very low hydraulic gradients, coupled with the presence of the mixing zone that operates as barrier, leads the salt flat nucleus to act as a hydrodynamically quasi-isolated area. The computed water table shows the lowest hydraulic head in the salt flat nucleus near the discharge at the mixing zone.

The groundwater balance of the Salar de Atacama in its natural regime was quantified resulting in an inflow/outflow of $14.9 \, \text{m}^3 \cdot \text{s}^{-1}$. This balance considers the basin as an endorheic system. The very low infiltration values that are generally assumed for hyperarid basins are not consistent with the hydrogeology of the Salar de Atacama. Indeed, very high infiltration rates (up to 85% of rainfall) occur because of the high degree of fracturing of rocks and the scarce vegetation. This high infiltration is consistent with the light isotopic composition of the water from the recharge area (Altiplano). Therefore, the existence of additional inflows outside the basin is unlikely.

1. Introduction

* Corresponding author at: Institute of Environmental Assessment and Water Research (IDAEA), CSIC, Jordi Girona 18, 08034 Barcelona, Spain.
E-mail address: mamarazuela@outlook.com (M.A. Marazuela).

Salt flats are saline and endorheic hydrogeological systems that are frequently associated with arid to hyperarid climates, in which the water table is several centimetres or decimetres below the ground

ELSEVIER

The effect of brine pumping on the natural hydrodynamics of the Salar de Atacama: The damping capacity of salt flats

M.A. Marazuela [a,b,c,*], E. Vázquez-Suñé [a], C. Ayora [a], A. García-Gil [d], T. Palma [a]

[a] Institute of Environmental Assessment and Water Research (IDAEA), CSIC, Jordi Girona 18-26, 08034 Barcelona, Spain
[b] Department of Civil and Environmental Engineering, Technical University of Catalonia (UPC), Jordi Girona 1-3, 08034 Barcelona, Spain
[c] Associated Unit: Hydrogeology Group (UPC-CSIC), Spain
[d] Geological and Mining Institute of Spain (IGME), Manuel Lasala 44, 9° B, 50006 Zaragoza, Spain

HIGHLIGHTS

- 3D groundwater flow modelling of the Salar de Atacama
- Damping capacity of salt flats water table was defined.
- Brine pumping causes reduction in the evaporation rate of salt flats.
- Reduction of evaporation due to brine pumping damping the water table drawdown
- The damping capacity ends up when the water table is depleted below 0.5–2 m deep.

GRAPHICAL ABSTRACT
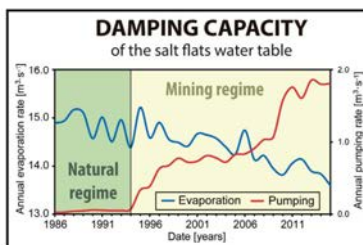
ARTICLE INFO

ABSTRACT

The Salar de Atacama is used as a case study to analyse and quantify coupled natural (evaporation and recharge) and anthropogenic processes (pumping of lithium-rich brine) to abstract their patterns to other salt flats using a three-dimensional groundwater flow model. Important changes in the dynamics of the water table between the pre-operational period (1986–1994) and operational period (1994–2015) are observed. The water table exhibited a gradual drawdown during the pre-operational period because the evaporation was greater than the recharge for most of these periods. This negative balance was counteracted by some sharp rises that were produced by direct rainfall events on the salt flat. The deep lateral recharge that arrived from the mountains did not produce abrupt changes in the water table because the rainfall events in the mountains were damped by the distance of the recharge zone and great thickness of the unsaturated zone.

The natural evolution of the water table was modified by the intensive brine pumping that was performed in the south-western Salar de Atacama during the operational period. As evaporation depends on the water table depth, the pumping caused a drawdown of the water table, resulting in an evaporation rate reduction that partially compensated for the pumped brine in the water balance of the basin. This effect is defined as the *damping capacity* of salt flats. Thus, salt flats have a high capacity for dampening oscillations in their water table in response to both natural and anthropogenic disturbances which is of great importance for the management of lake and wetland ecosystems and brine exploitation. The limit of the dampening capacity of salt flats is defined by the evaporation extinction depth, which is in the range of 0.5–2 m.

* Corresponding author at: Institute of Environmental Assessment and Water Research (IDAEA), CSIC, Jordi Girona 18, 08034 Barcelona, Spain.
E-mail address: mamarazuela@outlook.com (M.A. Marazuela).

Towards more sustainable brine extraction in salt flats: Learning from the Salar de Atacama

M.A. Marazuela [a,b,c,*], E. Vázquez-Suñé [a], C. Ayora [a], A. García-Gil [d]

[a] Institute of Environmental Assessment and Water Research (IDAEA), CSIC, Jordi Girona 18, 08034 Barcelona, Spain
[b] Department of Civil and Environmental Engineering, Technical University of Catalonia (UPC), Jordi Girona 1-3, 08034 Barcelona, Spain
[c] Associated Unit: Hydrogeology Group (UPC-CSIC), 08034 Barcelona, Spain
[d] Geological and Mining Institute of Spain (IGME), Manuel Lasala 44, 9° B, 50006 Zaragoza, Spain

HIGHLIGHTS

- A methodology to characterize the evaporation discharge in salt flats is proposed.
- The water table drawdown caused by Li-rich brine exploitation is evaluated.
- An exponential curve relating phreatic evaporation to water table depth is obtained.
- The impact on the evaporation discharge by brine pumping is quantified.
- A more ecologically efficient design of brine pumping is reported.

GRAPHICAL ABSTRACT
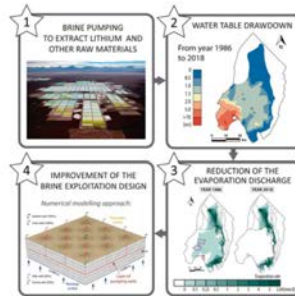
ARTICLE INFO

ABSTRACT

Salt flats are hydrogeological systems with highly valuable wetland and lake ecosystems. The brine pumping carried out to extract lithium is modifying the natural evaporation discharge of salt flats. A methodology to evaluate the impacts caused on water table and evaporation discharge by brine exploitation in salt flats is proposed and applied to the Salar de Atacama. The methodology included field measurements of water table and evaporation rate, followed by its spatio-temporal analysis and the application of the results to a numerical model to improve the brine exploitation design.

The spatio-temporal analysis of the water table depth and evaporation rates measured in the field concluded that the evaporation discharge decreased from 12.85 to 10.95 $m^3 \cdot s^{-1}$ between 1986 and 2018, that is around 15%. This reduction compensated part of the extractions and could contribute to the preservation of the mixing zone ecosystems. At present, this damping capacity is already amortized in the nucleus and the marginal zone is beginning to be affected by the brine pumping. The sensitivity of the phreatic evaporation on the water table depth justified the great uncertainty of the previous evaporation discharge estimations. Thus, an average error lower than 0.5 m was enough to modify the evaporation by >60%. Therefore, considerable effort should invested to faithfully quantify the discharge by evaporation which is critical in water balance of salt flat basins.

* Corresponding author at: Department of Civil and Environmental Engineering, Technical University of Catalonia (UPC), Jordi Girona 1-3, 08034 Barcelona, Spain.
E-mail address: mamarazuela@outlook.com (M.A. Marazuela).

A geological model for the management of subsurface data in the urban environment of Barcelona and surrounding area

Enric Vázquez-Suñé[1,2], Miguel Ángel Marazuela[1,2,3], Violeta Velasco[1,2], Marc Diviu[1,2], Andrés Pérez-Estaún[4], and Joaquina Álvarez-Marrón[4]

[1]Institute of Environmental Assessment and Water Research IDÆA – CSIC, Jordi Girona 18, 08034 Barcelona, Spain
[2]Associated Unit: Hydrogeology Group (UPC-CSIC)
[3]Department of Geotechnical Engineering and Geosciences, Universitat Politècnica de Catalunya (UPC), Jordi Girona 1-3, 08034 Barcelona, Spain
[4]Institute of Earth Sciences Jaume Almera ICTJA – CSIC, Lluís Solé Sabarís s/n, 08028 Barcelona, Spain

Correspondence to: Enric Vázquez-Suñé (enric.vazquez@idaea.csic.es)

Abstract. The overdevelopment of cities since the industrial revolution has shown the need to incorporate a sound geological knowledge in the management of required subsurface infrastructures and in the assessment of increasingly needed groundwater resources. Additionally, the scarcity of outcrops and the technical difficulty to conduct underground exploration in urban areas highlights the importance of implementing efficient management plans that deal with the legacy of heterogeneous subsurface information. To deal with these difficulties, a methodology has been proposed to integrate all the available spatio-temporal data into a comprehensive spatial database and a set of tools that facilitates the analysis and processing of the existing and newly added data for the city of Barcelona (NE Spain). Here we present the resulting actual subsurface 3-D geological model that incorporates and articulates all the information stored in the database. The methodology applied to Barcelona benefited from a good collaboration between administrative bodies and researchers that enabled the realization of a comprehensive geological database despite logistic difficulties. Currently, the public administration and also private sectors both benefit from the geological understanding acquired in the city of Barcelona, for example, when preparing the hydrogeological models used in groundwater assessment plans. The methodology further facilitates the continuous incorporation of new data in the implementation and sustainable management of urban groundwater, and also contributes to significantly reducing the costs of new infrastructures.

1 Introduction

The need for a groundwater supply has led people to settle near natural water sources since ancient times, usually near major rivers. For this reason, many of the world's major cities are located above alluvial or deltaic aquifers (Carlson et al., 2011; Davies, 2015; Gleeson et al., 2015; Tessler et al., 2015). Currently, particularly with the industrialization that began in the 1950s, most of these aquifers have been severely affected in terms of the quantity and quality of their waters (Aeschbach-Hertig and Gleeson, 2012; Gleeson et al., 2012b).

Urban expansion generates an enormous demand for infrastructure and, paradoxically, progressively less space for construction (Grimm et al., 2008). As a result, cities must grow downward, which requires subterranean construction (e.g. transportation networks and underground parking garages). These subterranean infrastructures usually interact with shallow aquifers, causing frequently negative repercussions for them (Attard et al., 2015; Ferguson, 2004; Ferguson and Woodbury, 2007; Kazemi, 2011; McDonald et al., 2014; Menberg et al., 2013; Taniguchi et al., 2008; Vázquez-Suñé et al., 2005; Vörösmarty et al., 2000). Various contamination pathways associated with this problem include spillways, sewage networks, and discharges into wells. Another result of urbanization is an abundance of hardscapes, which severely reduce the amount of aquifer recharge (Vázquez-Suñé et al., 2010).

A city scale study on the effects of intensive groundwater heat pump systems on heavy metal contents in groundwater

CrossMark

Alejandro García-Gil [a,*], Jannis Epting [b], Eduardo Garrido [a], Enric Vázquez-Suñé [c], Jesús Mateo Lázaro [d], José Ángel Sánchez Navarro [d], P. Huggenberger [b], Miguel Ángel Marazuela Calvo [c]

[a] Geological Survey of Spain (IGME), C/ Manuel Lasala n° 44, 9° B, 50006 Zaragoza, Spain
[b] Department of Environmental Sciences, Applied and Environmental Geology, University of Basel, Bernoullistr. 32, 4056 Basel, Switzerland
[c] GHS, Institute of Environmental Assessment & Water Research (IDAEA), CSIC, Jordi Girona 18-26, 08034 Barcelona, Spain
[d] Department of Earth Sciences, University of Zaragoza, c/ Pedro Cerbuna 12, 50009 Zaragoza, Spain

HIGHLIGHTS

- A city scale study on the effects of intensive geothermal resource use is presented.
- Effects on groundwater quality with emphasis on heavy metal contents were studied.
- Temperature changes are not the driving factor enhancing heavy metal contamination.

GRAPHICAL ABSTRACT
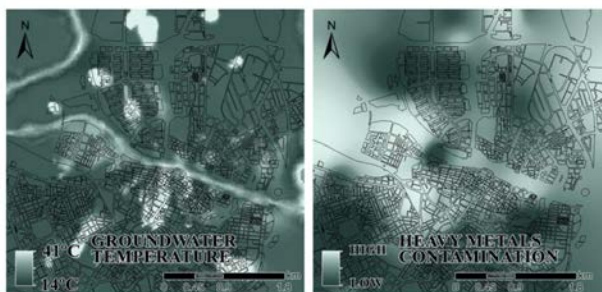
ARTICLE INFO

ABSTRACT

As a result of the increasing use of shallow geothermal resources, hydraulic, thermal and chemical impacts affecting groundwater quality can be observed with ever increasing frequency (Possemiers et al., 2014). To overcome the uncertainty associated with chemical impacts, a city scale study on the effects of intensive geothermal resource use by groundwater heat pump systems on groundwater quality, with special emphasis on heavy metal contents was performed. Statistical analysis of geochemical data obtained from several field campaigns has allowed studying the spatiotemporal relationship between temperature anomalies in the aquifer and trace element composition of groundwater. The relationship between temperature and the concentrations of trace elements resulted in weak correlations, indicating that temperature changes are not the driving factor in enhancing heavy metal contaminations. Regression models established for these correlations showed a very low reactivity or response of heavy metal contents to temperature changes. The change rates of heavy metal contents with respect to temperature changes obtained indicate a low risk of exceeding quality threshold values by means of the exploitation regimes used, neither producing nor enhancing contamination significantly. However, modification of pH, redox potential, electrical conductivity, dissolved oxygen and alkalinity correlated with the

* Corresponding author.
  E-mail address: a.garcia@igme.es (A. García-Gil).

Research papers

An upscaling procedure for the optimal implementation of open-loop geothermal energy systems into hydrogeological models

Sylvia Muela Maya[a], Alejandro García-Gil[b,d,*], Eduardo Garrido Schneider[b,d], Miguel Mejías Moreno[c], Jannis Epting[e], Enric Vázquez-Suñé[f], Miguel Ángel Marazuela[f], José Ángel Sánchez-Navarro[a,d]

[a] Department of Earth Sciences, University of Zaragoza (UZ), c/ Pedro Cerbuna 12, 50009 Zaragoza, Spain
[b] Geological Survey of Spain (IGME), C/ Manuel Lasala n° 44, 9° B, 50006 Zaragoza, Spain
[c] Geological Survey of Spain (IGME) Headquarters, C/ Ríos Rosas 23, 28003 Madrid, Spain
[d] Associated Unit in Earth Sciences IGME-UZ, Spain
[e] Department of Environmental Sciences, Applied and Environmental Geology, University of Basel, Bernoullistr. 32, 4056 Basel, Switzerland
[f] GHS, Institute of Environmental Assessment & Water Research (IDAEA), CSIC, Jordi Girona 18-26, 08034 Barcelona, Spain

ARTICLE INFO

ABSTRACT

Different aspects of management policies for shallow geothermal systems are currently under development. Although this technology has been used for a long time, doubts and concerns have been raised in the last years due to the massive implementation of new systems. To assess possible environmental impacts and manage subsurface energy resources, collecting data from operating shallow geothermal systems is becoming mandatory in Europe. This study presents novel advances in the upscaling of operation datasets obtained from open-loop geothermal energy systems for an optimal integration in hydrogeological models. The proposed procedure allows efficient numerical simulations to be performed at an urban scale. Specifically, this work proposes a novel methodology to optimize the data treatment of highly transient real exploitation regimes by integrating energy transfer in the environment to reduce more than 90% registered raw datasets. The proposed methodology is then applied to and validated on five different real optimization scenarios in which upscaling transformation of the injection temperature series of 15-min sampling frequency has been considered. The error derived from each approach was evaluated and compared for validation purposes. The results obtained from the upscaling procedures have proven the usefulness and transferability of the proposed method for achieving daily time functions to efficiently reproduce the exploitation regimes of these systems with an acceptable error in a sustainable resource management framework.

1. Introduction

Shallow geothermal systems are based on obtaining the heat energy from materials of the most superficial layers (< 250 m) of the Earths crust and the water that flows through them. The heat transfer from the Earth's core to the outer areas of the crust and the capacity of the ground to dampen thermal oscillations occurring on the surface make thermal stability possible, starting at a depth of approximately 15 m. After the damping of thermal oscillations with depth, the ground temperature is similar to the annual average temperature of the region plus 1 °C or 2 °C (Parsons, 1970). This terrain feature justifies the development of these important systems as an adaptative measure to climate change for renewable energy development (Bayer et al., 2012). The 'potential natural state of the aquifer' is defined as a state without anthropogenic influences (Epting and Huggenberger, 2013). Heat exchange with the ground can be performed by different types of ground source energy (GSE) systems, including closed or open systems, by using heat pumps coupled with heat exchangers. Open systems, also called groundwater heat pumps (GWHPs), take direct advantage of the heat or cold of pumped groundwater and subsequently reinject pumped water into the aquifer (García-Gil et al., 2014a). GWHPs, and GSE in general, are widely used worldwide and their demand is expected to increase in the next years (Epting et al., 2017; Jaudin, 2013; Lund and Boyd, 2016). The increasing trend of GWHPs has resulted in an additional heat load in urban aquifers, caused both by thermal interference between systems and interference between well doublets, that is, the thermal autointerference effect (Galgaro and Cultrera, 2013; Garrido et al., 2010b). Because the geothermal exploitation of the aquifer is not

RESEARCH ARTICLE

WILEY

Some evolutionary patterns of palaeokarst developed in Pleistocene deposits (Ebro Basin, NE Spain): Improving geohazard awareness in present-day karst

María Asunción Soriano[1] 🆔 | Andrés Pocoví[1] | Héctor Gil[2] | Antonio Pérez[1] | Aránzazu Luzón[1] | Miguel Ángel Marazuela[3,4,5]

[1] Grupo Geotransfer, Departamento de Ciencias de la Tierra, Facultad de Ciencias, Instituto de Investigación en Ciencias Ambientales (IUCA), Universidad de Zaragoza, Zaragoza, Spain

[2] Departamento de Ciencias de la Tierra, Universidad de Zaragoza, Zaragoza, Spain

[3] Institute of Enviromental Assessment and Water Research (IDAEA), CSIC, Barcelona, Spain

[4] Department of Civil and Environmental Engineering, Universidad Politécnica de Cataluña (UPC), Barcelona, Spain

[5] Associated Unit: Hydrogeology Group, UPC-CSIC, Barcelona, Spain

Correspondence
María Asunción Soriano, Departamento de Ciencias de la Tierra, Facultad de Ciencias, Instituto de Investigación en Ciencias Ambientales (IUCA), Universidad de Zaragoza, Pedro Cerbuna 12, 50009 Zaragoza, Spain.
Email: asuncion@unizar.es

Handling Editor: I. D. Somerville

Pleistocene detrital deposits in the central Ebro Basin frequently show deformation features due mainly to karstification in the underlying Neogene evaporites. In 123 cases, estimation of parameters of shape and minimum volume of materials involved was accomplished. Six of them were analysed in more detail to establish the main processes involved in their genesis and the succession of events. All the deformation features in the selected sites are synsedimentary. To achieve the objectives, intense fieldwork was made applying methods of sedimentology and structural geology. Usually, a complex evolutionary pattern was observed, with evidences of dissolution, sagging, collapse, gravity flow, suffosion, and plastic flow. In a schematic way, three main situations, independent of the age of the analysed deposits, can be distinguished: (a) slow subsidence, (b) collapse, and (c) temporal overlapping of both processes. In the first 2 scenarios, basins with smooth or abrupt borders, respectively, were generated on the land surface. In the third one, slow subsidence was followed by a collapse, located in the area of maximum flexure. These patterns are also observed in present-day dolines. Comparison of direct and indirect parameters between paleodolines and present-day dolines indicates a bigger size of the latter, probably caused by the different conditions of observation. This study helps to know the possibilities in the evolution of mantled karst features, to estimate the volume of material affected by karstification and to improve the knowledge of present-day dolines behaviour. Consequently, study of paleodolines must be considered to achieve a better urban planning in active karstic areas.

KEYWORDS

doline parameters estimation, evaporites, land-use planning, mantled karst, natural hazard, synsedimentary deformation features

1 | INTRODUCTION

Development of dolines with soil cover is a major geohazard related to karst because they may constitute small zones with very unstable ground, as Waltham, Bell, and Culshaw (2005) indicate. Different authors have considered that most of these landforms are inherited and induced or accelerated by man's activities (De Waele et al., 2017; Horwitz & Smith, 2003; Land & Asanidze, 2015; Mancini, Stecchi, Zanni, & Gabbianelli, 2009; Parise et al., 2015; Waltham, 2008; Waltham et al., 2005). Analysing hazards caused by karstification in mantled karst, that is, soluble rocks covered by unconsolidated sediments (Klimchouk, 2013), is not an easy task. Karst landforms are generated mainly by dissolution of soluble rocks and

dominant underground drainage. The hydraulic gradient and the properties of the involved rocks (lithology and structure) are determining factors in its development (Ford & Williams, 2007; Waltham et al., 2005; White, 1988; Williams, 2003). In addition, whenever mantled karst is considered, the behaviour of the detrital cover should be also taken into account (Ford, 1997). In these conditions, although dissolution is the main process in karst, others such as collapse, gravity, suffosion, and plastic flow can also be involved (Andrejchuk & Klimchouk, 2002; Beck, 1984; Beck & Pearson, 1995; Ford & Williams, 2007; Gutierrez, Guerrero, & Lucha, 2008; Waltham et al., 2005; White & White, 1969; Williams, 2003). At the surface, the most relevant landforms, consequence of these processes developed at depth, are dolines (sinkholes).
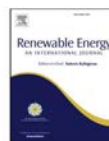
Sustainability indicator for the prevention of potential thermal interferences between groundwater heat pump systems in urban aquifers

Alejandro García-Gil [a, e, *], Sylvia Muela Maya [b], Eduardo Garrido Schneider [a, e], Miguel Mejías Moreno [c], Enric Vázquez-Suñé [d], Miguel Ángel Marazuela [d], Jesús Mateo Lázaro [b], José Ángel Sánchez-Navarro [b, e]

[a] Geological Survey of Spain (IGME), C/ Manuel Lasala n° 44, 9° B, 50006 Zaragoza, Spain
[b] Department of Earth Sciences, University of Zaragoza (UZ), c/ Pedro Cerbuna 12, 50009 Zaragoza, Spain
[c] Geological Survey of Spain (IGME) Headquarters, C/ Ríos Rosas 23, 28003 Madrid, Spain
[d] GHS, Institute of Environmental Assessment & Water Research (IDAEA), CSIC, Jordi Girona 18-26, 08034 Barcelona, Spain
[e] Associated Unit in Earth Sciences IGME-UZ, Spain

ARTICLE INFO

ABSTRACT

The steady increase of geothermal systems using groundwater is compromising the renewability of the geothermal resources in shallow urban aquifers. To ensure sustainability, scientifically-based criteria are required to prevent potential thermal interferences between geothermal systems. In this work, a management indicator (balanced sustainability index, BSI) applicable to groundwater heat pump systems is defined to assign a quantitative value of sustainability to each system, based on their intrinsic potential to produce thermal interference. The BSI indicator relies on the net heat balance transferred to the terrain throughout the year and the maximum seasonal thermal load associated. To define this indicator, 75 heating-cooling scenarios based in 23 real systems were established to cover all possible different operational conditions. The scenarios were simulated in a standard numerical model, adopted as a reference framework, and thermal impacts were evaluated. Two polynomial regression models were used for the interpolation of thermal impacts, thus allowing the direct calculation of the sustainability indicator developed as a function of heating-cooling ratios and maximum seasonal thermal loads. The BSI indicator could provide authorities and technicians with scientifically-based criteria to establish geothermal monitoring programs, which are critical to maintain the implementation rates and renewability of these systems in the cities.

© 2018 Elsevier Ltd. All rights reserved.

1. Introduction

Heating and cooling for buildings accounted for nearly half (544.2 Mtoe) of the final energy consumption in the European Union in 2010 [1]. To fulfill this modern society need, 81% of this energy was generated from combustion processes emitting carbon dioxide (CO_2) [2]. Technologies for heating-cooling using geothermal heat pumps (GHP) could provide such energy requirements by increasing the use of renewable energy sources. GHP installations presented a total installed power of more than 50 GW

in 2015 [3], thus presenting a large potential for the mitigation of climate change in this sector [4]. The growing awareness of GHP has resulted in a steady increase of installed capacity worldwide over the last 20 years, with a significant increase of around 10% [5,6]. This fast spreading of GHP systems all over the world can be explained by their economic and environmental feasibility [7–9], as they are especially economically advantageous when the price of electricity is low [10]. There are two main widespread types of configurations [11]: closed loop and open loop. In close loop or ground-coupled systems, the heat exchanger used to maximize heat transfer with the ground consists in a plastic pipe placed into the ground, either horizontally in a trench or vertically in a borehole. On the other hand, open loop or groundwater heat pump (GWHP) systems pump groundwater or surface water directly as a heat source and circulate it through heat exchangers placed in the

* Corresponding author. Geological Survey of Spain (IGME), C/ Manuel Lasala n° 44, 9° B, 50006 Zaragoza, Spain.
E-mail address: a.garcia@igme.es (A. García-Gil).

Defining the exploitation patterns of groundwater heat pump systems

Alejandro García-Gil [a,b,*], Corinna Abesser [b], Samanta Gasco Cavero [c], Miguel Ángel Marazuela [d], Jesús Mateo Lázaro [e], Enric Vázquez-Suñé [d], Andrew G. Hughes [b], Miguel Mejías Moreno [a]

[a] Geological Survey of Spain (IGME), C/Ríos Rosas 23, 28003 Madrid, Spain
[b] British Geological Survey, Maclean Building, Wallingford, Oxon OX10 8BB, UK
[c] MRC Harwell Institute, Mammalian Genetics Unit, Harwell Campus, Oxfordshire OX11 0RD, UK
[d] GHS, Institute of Environmental Assessment & Water Research (IDAEA), CSIC, Jordi Girona 18-26, 08034 Barcelona, Spain
[e] Department of Earth Sciences, University of Zaragoza, c/Pedro Cerbuna 12, 50009 Zaragoza, Spain

HIGHLIGHTS

- The exploitation regimes of 27 groundwater heat pump systems were examined.
- Exploitation patterns were identified from the cyclicality and cluster analysis.
- Different usage of the systems conditions the hourly and daily cycles.
- Monthly and yearly cycles are affected by the climatization strategy followed.

GRAPHICAL ABSTRACT
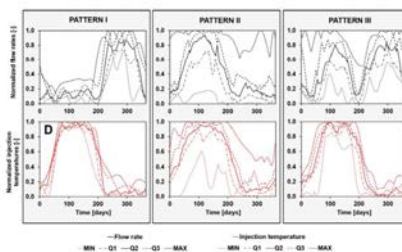
ABSTRACT

Shallow geothermal systems are the most efficient and clean technology for the air-conditioning of buildings and constitutes an emergent renewable energy resource in the worldwide market. Undisturbed systems are capable of efficiently exchanging heat with the subsurface and transferring it to human infrastructures, providing the basis for the successful decarbonisation of heating and cooling demands of cities. Unmanaged intensive use of groundwater for thermal purposes as a shallow geothermal energy (SGE) resource in urban environments threatens the resources' renewability and the systems' performance, due to the thermal interferences created by a biased energy demand throughout the year. The exploitation regimes of 27 groundwater heat pump systems from an alluvial aquifer were firstly examined using descriptive statistics. Linear relationships between abstraction and injection temperatures of the systems were assessed by calculating Pearson's r correlation coefficient, and used as an evidence of thermal interferences. Then, time series of flow rate, operation temperature and energy transfer were modelled by means of spectral analysis and sinusoidal regression methods, followed by the definition of the relative exploitation patterns. The exploitation regimes examined presented a clear cooling bias and a similar cyclicality. The amplitudes correlated with the different end-user's activities (e.g. medical centres) when high frequency cycles were observed, while climatization strategies (e.g. constant flow rates and modulation of injection temperatures) did so when low frequency cycles were detected. The time series models allowed defining the relative operational pattern of a system and the groups of systems following such patterns. The biases in exploitation regimes of groundwater heat pump systems existing in Mediterranean areas require

Appendix C

Locations and average physico-chemical parameters of the main observation points used for the 3D mapping of the mixing zone. EC = electrical conductivity, TDS = total dissolved solids.

Coordinate X	Coordinate Y	Elevation Z	EC [mS/cm⁻¹]	Density [g/cm³]	TDS [g/L]
570270	7380179	2301	234200	1.20	-
570521	7380563	2300	236500	1.22	-
570775	7380949	2300	234989	1.16	-
572422	7376975	2300	195525	1.18	390.59
572433	7376977	2300	199508	1.14	399.99
572913	7373356	2303	165300	1.11	-
572915	7373356	2303	42435	1.05	34.07
572970	7373199	2303	5903	-	-
573178	7417291	2301	100500	-	-
573296	7372777	2305	207649	1.16	377.39
573298	7372778	2305	7953	1.10	-
573770	7378723	2300	231700	1.22	-
573891	7377873	2302	229500	1.21	-
574720	7376454	2299	235014	1.06	-
575663	7376996	2300	231050	1.19	-
576091	7377780	2300	229613	1.16	379.19
576841	7380935	2300	242663	1.12	-
576894	7384044	2301	229050	1.21	-
576965	7375372	2301	27579	1.01	18.35
577629	7414639	2301	101500	1.22	-
577631	7373281	2303	35656	1.01	-
577651	7373947	2303	8087	1.00	4.59
577653	7373947	2303	202868	1.13	279.79
577715	7369511	2308	4147	1.06	-
577716	7369509	2309	4942	0.98	2.64
577717	7369513	2309	223233	1.19	369.19
578497	7368805	2311	212843	1.04	-
578506	7371715	2303	11108	1.01	6.10
578647	7376429	2301	23993	1.01	18.99
578650	7376430	2301	224193	1.15	398.59
578744	7373236	2303	226107	1.16	282.79
578747	7373235	2303	12183	1.03	7.85
579260	7384212	2301	237328	1.14	424.59
579752	7424698	2303	139400	1.20	-
580892	7414991	2301	105000	-	-
581183	7410996	2301	100500	-	-
583118	7416047	2301	66267	-	-
583568	7412046	2301	214224	1.15	239.62
583766	7413065	2301	101000	-	-
583852	7420405	2301	249833	-	-
583888	7419426	2302	198900	-	-
583937	7417902	2301	199100	-	-
583989	7414053	2301	212532	1.14	245.94
584095	7416018	2301	66233	-	-
584114	7414807	2301	-	1.15	-
584143	7424282	2302	129000	1.06	-
584156	7424265	2302	-	1.06	-
584160	7414914	2301	-	1.17	-
584234	7415017	2300	161756	1.06	171.00
584260	7415117	2301	75367	1.14	-
584319	7415196	2301	755	1.12	-
584433	7383998	2301	221036	1.15	-
584435	7415372	2301	1113	1.15	-
584560	7415521	2301	16450	1.17	-
584676	7415711	2301	76167	1.12	-
584706	7416080	2301	55400	-	-
584748	7411424	2301	100500	-	-
584841	7412989	2301	115100	-	-
584880	7416804	2301	66433	-	-
584892	7414013	2301	71667	-	-
584908	7381408	2302	128306	1.05	143.12

Coordinate X	Coordinate Y	Elevation Z	EC [mS/cm⁻¹]	Density [g/cm³]	TDS [g/L]
585210	7419631	2301	-	1.08	-
585211	7414817	2300	176447	-	217.35
585220	7414823	2300	226100	-	-
585233	7419627	2301	133000	-	-
585707	7418822	2301	167565	1.07	169.76
585803	7416976	2300	-	1.11	-
585852	7419096	2301	5170	-	-
585967	7405468	2301	218424	1.14	238.76
586095	7412578	2301	76400	-	-
586213	7415282	2301	-	1.23	-
586220	7415498	2300	-	1.22	-
586221	7415088	2301	71667	1.23	-
586244	7415762	2301	78000	1.22	-
586272	7414892	2301	-	1.22	-
586329	7414713	2301	-	1.23	-
586395	7414518	2301	-	1.23	-
586445	7414389	2301	75133	1.22	-
586723	7382312	2300	233233	1.18	415.59
586780	7420011	2302	59150	-	-
587170	7403823	2301	200000	-	-
587360	7381056	2300	231640	1.15	362.99
587361	7381053	2300	65864	1.02	50.79
587447	7414217	2301	109000	-	-
587730	7416378	2301	77000	-	-
588067	7422646	2302	21200	1.01	-
588137	7416166	2300	242000	-	-
588138	7416185	2301	209847	1.15	253.51
588272	7414004	2301	196706	1.11	208.52
588645	7422858	2303	14700	1.02	-
588870	7406100	2301	200000	-	-
589402	7417901	2302	117100	-	-
589607	7416216	2301	187038	1.08	193.79
589773	7409571	2302	110500	-	-
589797	7424645	2309	1854	-	-
590202	7406058	2301	-	1.12	-
590334	7406057	2301	149815	1.11	174.16
590533	7406056	2301	162600	-	-
590539	7409572	2302	-	1.05	-
590656	7407520	2302	140800	-	-
590791	7403723	2301	182100	-	-
591163	7403676	2301	-	1.11	-
591215	7409578	2302	-	1.04	-
591314	7409573	2302	-	1.04	-
591376	7411030	2302	45900	-	-
591440	7380661	2306	16800	0.98	19.80
591453	7418239	2307	1703	-	-
591524	7409579	2302	61300	-	-
591851	7414609	2305	10112	-	7.54
591858	7422583	2315	2138	-	1.71
591911	7403629	2302	-	1.15	-
592139	7403631	2302	189600	-	-
592187	7407286	2302	150300	-	-
592247	7406115	2301	80164	-	89.26
592287	7422403	2318	895	-	-
592412	7410800	2302	38700	1.01	-
592414	7409604	2302	201000	1.10	-
592440	7414727	2310	5650	-	-
592624	7406144	2302	105521	1.06	106.01
592879	7420047	2322	2183	-	-
592926	7407155	2302	-	1.14	-
593054	7410998	2305	-	1.00	-

Coordinate X	Coordinate Y	Elevation Z	EC [mS/cm^{-1}]	Density [g/cm^3]	TDS [g/L]
593121	7409555	2304	-	1.01	-
593160	7403838	2301	-	1.15	-
593360	7406128	2303	78615	1.02	75.34
593362	7406110	2303	158700	-	-
593471	7412131	2313	7580	-	-
593699	7407116	2303	47100	-	-
593725	7418708	2328	450	-	-
593769	7406038	2303	-	1.05	-
593776	7409547	2305	16740	1.01	-
593777	7415629	2324	2780	-	-
593834	7410994	2309	-	1.00	-
593971	7403544	2303	4853	0.99	3.67
594640	7411009	2319	2271	1.00	-
594827	7403503	2305	-	1.00	-
594842	7405987	2306	132500	-	-
594922	7409664	2320	3430	-	-
595207	7422552	2348	860	-	-
595449	7403481	2310	113800	1.00	-
595569	7407110	2317	2188	-	-
595818	7404843	2312	-	1.00	-
596087	7396429	2325	2827	1.00	2.03
596113	7406265	2321	20885	-	20.56
596154	7420525	2359	1610	-	-
596254	7430489	2356	597	-	-
596809	7415774	2367	3188	-	2.64
597046	7403455	2334	2169	1.00	-
597177	7425182	2369	743	-	-
598072	7409831	2380	2713	1.00	3.01
598164	7406166	2358	2565	0.99	2.83
598958	7414838	2404	4140	1.00	3.96
599733	7426657	2410	901	-	-
599801	7418613	2433	3240	-	-
599847	7421794	2410	1970	-	-
599919	7422645	2405	1938	1.00	1.41

Appendix D

Hydraulic conductivity values, both initial and calibrated by the numerical model. The location of each zone is shown in Fig. 3.5.

Unit	Domain	Zone	Hydraulic Conductivity [m·d⁻¹]	
			Initial	Calibrated
Aquifer A	Mixing Zone	KA1	100	80
		KA2	100	220
		KA3	100	150
		KA4	100	200
		KA5	100	60
		KA6	100	300
		KA7	100	225
		KA8	100	190
		KA9	100	190
		KA11	100	190
		Lakes	10000	10000
	Alluvial Zone	KA10a	100	100
		KA10b	100	80
		KA10c	100	80
		KA10d	100	80
		KA10e	100	80
		KA10f	100	80
		KA10g	100	200
		KA10h	100	300
		KA10i	100	250
	Nucleus	KA12a	200	300
		KA12b	200	140
		KA12c	200	160
		KA12d	200	160
		KA12e	200	100
		KA12f	200	100
		KA12g	200	100
		KA12h	200	140
		KA12i	200	140
Aquitard AB	Mixing Zone	KAB-1	0.1	0.01
		KAB-2	1	2
		KAB-3	1	5
		KAB-4	1	2
		KAB-5	1	5
	Nucleus	KAB-6	0.1	0.01
Aquifer B	Mixing Zone	KB-1	1	1
		KB-2	10	20
		KB-3	10	20
		KB-4	10	20
		KB-5	10	20
	Nucleus	KB-6	1	0.1

Appendix E

Specific storage values, both initial and calibrated by the numerical model. The location of each zone is shown in Fig. 4.4B.

Hydrostratigraphic unit	Zone	Specific Storage [m^{-1}]	
		Initial	Calibrated
Aquifer A	SsA1	0.004-0.012	0.007
	SsA2	0.004-0.012	0.012
	SsA3	0.004-0.012	0.01
	SsA4	0.004-0.012	0.01
	SsA5	0.004-0.012	0.01
	SsA6a	0.001-0.005	0.011
	SsA6b	0.001-0.005	0.01
	SsA6c	0.001-0.005	0.011
	SsA6d	0.001-0.005	0.011
	SsA6e	0.001-0.005	0.011
	SsA6f	0.001-0.005	0.01
	SsA6g	0.001-0.005	0.01
	SsA6h	0.001-0.005	0.01
	SsA6i	0.001-0.005	0.01
Aquitard AB	SsAB	0.0001	0.0001
Aquifer B	SsB	0.00001	0.00001

Appendix F

Lysimeter data.

LZA3-2		LZA3-3		LZA7-1		LZA7-2		LZA9-1		LZA10-1		LZA12-1		LZA12-2		LZA12-3	
WTD	Ev	WTD	Ev	WTD	Ev	WTD	Ev	WTD	Ev	WTD	Ev	WTD	Ev	WTD	Ev	WTD	Ev
0.03	0.68	0.06	2.32	0.06	6.57	0.09	2.78	0.15	5.29	0.20	2.26	0.10	5.78	0.39	0.30	0.18	2.16
0.03	1.29	0.06	1.04	0.09	5.93	0.12	2.29	0.18	4.85	0.22	1.72	0.10	7.85	0.39	0.53	0.21	1.24
0.05	1.39	0.09	0.91	0.09	6.54	0.15	1.74	0.21	3.87	0.23	1.08	0.10	5.36	0.42	0.69	0.24	0.86
0.06	0.94	0.09	1.67	0.12	5.18	0.18	1.04	0.24	4.13	0.23	1.49	0.15	3.44	0.42	0.59	0.27	0.73
0.06	0.99	0.12	1.10	0.21	3.80	0.21	1.03	0.27	3.39	0.24	1.04	0.15	6.33	0.45	0.84	0.30	0.89
0.09	0.54	0.12	0.85	0.15	2.43	0.24	0.78	0.30	2.92	0.25	1.22	0.15	4.93	0.45	0.62	0.33	0.88
0.09	0.91	0.15	1.10	0.15	3.57	0.27	0.99	0.33	2.32	0.25	1.38	0.20	1.57	0.48	0.90	0.36	0.97
0.10	0.63	0.18	1.34	0.18	2.12	0.30	0.80	0.36	2.32	0.26	1.08	0.20	2.80	0.48	0.56	0.39	1.03
0.12	0.38	0.21	1.23	0.18	2.59	0.33	0.71	0.39	2.28	0.27	1.23	0.20	4.52	0.51	0.44	0.42	0.96
0.12	0.50	0.24	1.09	0.21	1.69	0.36	0.67	0.42	1.94	0.27	1.12	0.25	3.20	0.51	0.84	0.45	0.97
0.15	0.41	0.27	1.03	0.21	1.68	0.39	0.73	0.45	1.99	0.27	1.08	0.25	2.01	0.51	0.84	0.48	0.93
0.18	0.14	0.30	0.86	0.24	1.39	0.42	0.83	0.48	1.75	0.28	1.34	0.25	1.42	0.54	0.72	0.51	0.76
0.21	0.25	0.30	0.57	0.24	1.01	0.45	0.86	0.51	1.77	0.28	1.13	0.30	1.30	0.57	0.46	0.54	0.65
0.23	0.08	0.33	0.59	0.27	1.40	0.48	0.88	0.54	1.73	0.29	1.01	0.30	1.50	0.60	0.22	0.57	0.52
		0.33	0.64	0.27	0.48	0.51	0.80	0.57	1.69	0.29	1.29	0.30	1.84	0.63	0.38	0.60	0.50
		0.39	0.55	0.30	0.68	0.54	0.82	0.60	1.57	0.30	1.32	0.35	1.43			0.63	0.58
		0.42	0.53	0.30	1.54	0.57	0.18	0.63	1.38	0.30	0.87	0.35	1.64				
		0.45	0.48	0.33	1.19			0.65	1.30	0.31	1.44	0.35	1.27				
				0.36	1.16					0.31	0.95	0.40	1.83				
				0.39	0.85							0.40	1.32				
				0.42	0.65							0.40	0.98				
				0.44	0.27							0.45	1.26				
												0.45	0.59				
												0.50	1.05				
												0.50	0.68				
												0.55	0.83				
												0.60	0.50				
												0.65	0.55				
												0.68	0.70				

* WTD = Water table depth [m]

** Ev = Evaporation rate [mm/d]

Neglected measurement

Appendix G

Development of simplified equations for variable density flow and transport.

a) Conservation of mass of water

The equation for mass conservation in porous media can be written as:

$$\frac{\partial(\phi\rho)}{\partial t} + \nabla \cdot (\rho\mathbf{q}) = 0 \tag{G1}$$

Where ϕ is porosity, ρ is density, and $\mathbf{q}$ is volumetric flux.

This equation can be transformed into:

$$\frac{\partial(\phi\rho)}{\partial t} + \mathbf{q} \cdot \nabla\rho + \rho\nabla \cdot \mathbf{q} = 0 \tag{G2}$$

As density is variable, the usual piezometric head cannot be used as it is only valid for constant density. Therefore, some additional development of Darcy's law is required. Darcy's law for variable density, can be written as (generalized Darcy's law):

$$\mathbf{q} = -\frac{\mathbf{k}}{\mu}(\nabla p + \rho g \nabla z) \tag{G3}$$

Where $g = 9.81$ N/kg is gravity force, $\nabla z = \begin{pmatrix} 0 \\ 0 \\ 1 \end{pmatrix}$ is a unit vector, $\mathbf{k}$ is intrinsic permeability, and μ is viscosity. Alternatively, the gravity term can be written as: $g\nabla z = -\mathbf{g}$ with the following definition of the gravity vector: $\mathbf{g} = \begin{pmatrix} 0 \\ 0 \\ -9.81 \end{pmatrix}$.

To introduce an equivalent piezometric head, the following transformation can be done:

$$\mathbf{q} = -\frac{\mathbf{k}}{\mu}(\nabla p + \rho g \nabla z) = -\frac{\mathbf{k}\rho_0 g}{\mu}\left(\nabla\left(\frac{p}{\rho_0 g}\right) + \frac{(\rho-\rho_0)g\nabla z + \rho_0 g\nabla z}{\rho_0 g}\right) = \tag{G4}$$

$$= -\frac{\mathbf{k}\rho_0 g}{\mu}\left(\nabla\left(\frac{p}{\rho_0 g} + z\right) + \frac{(\rho-\rho_0)}{\rho_0}g\nabla z\right) =$$

$$= -\frac{\mathbf{k}\rho_0 g}{\mu}\left(\nabla h + \frac{(\rho-\rho_0)}{\rho_0}\nabla z\right) =$$

$$= -\mathbf{K}\left(\nabla h + \frac{(\rho-\rho_0)}{\rho_0}\mathbf{u}\right)$$

Where ρ_0 is a reference constant density (for instance for pure water and at reference temperature). The following definitions have been introduced:

Direction unitary vector: $\mathbf{u} = -\frac{\mathbf{g}}{\|\mathbf{g}\|} = \nabla z = \begin{pmatrix} 0 \\ 0 \\ 1 \end{pmatrix}$

Hydraulic conductivity: $\mathbf{K} = \frac{\mathbf{k}\rho_0 g}{\mu}$

Equivalent piezometric head: $h = \frac{p}{\rho_0 g} + z$

It is important to note that hydraulic conductivity ($\mathbf{K}$) is calculated using the reference density (ρ_0), and that the equivalent piezometric head (h) is calculated using the reference density.

Equation G2, can be expanded in terms of the equivalent piezometric head:

$$\frac{1}{\rho}\frac{\partial(\phi\rho)}{\partial h}\frac{\partial h}{\partial t} + \frac{1}{\rho}\mathbf{q} \cdot \nabla\rho + \nabla \cdot \mathbf{q} = 0 \tag{G5}$$

Which can be transformed into:

$$S_y\frac{\partial h}{\partial t} + \nabla \cdot \mathbf{q} = 0 \tag{G6}$$

Assuming that the storage coefficient can be defined as: $S_y = \frac{1}{\rho}\frac{\partial(\phi\rho)}{\partial h} = \frac{\phi}{\rho}\frac{\partial\rho}{\partial h} + \frac{\partial\phi}{\partial h}$

And the following term is neglected: $\frac{1}{\rho}\mathbf{q} \cdot \nabla\rho$

This is possible if the product of a flux and a density gradient is assumed to be small (compared to other terms) because it is second order (product of two gradients).

b) Conservation of solute

The mass conservation of a solute can be written as:

$$\frac{\partial(\phi\rho\omega)}{\partial t} + \nabla \cdot (-\mathbf{D}\rho\nabla\omega + \omega\rho\mathbf{q}) = 0 \tag{G7}$$

Where ω is mass fraction and $\mathbf{D}$ the tensor of diffusion/dispersion.

After some algebra:

$$\phi\rho\frac{\partial\omega}{\partial t} + \frac{\partial(\phi\rho)}{\partial t}\omega + \nabla \cdot (-\mathbf{D}\rho\nabla\omega) + \rho\mathbf{q} \cdot \nabla\omega + \omega\nabla \cdot (\rho\mathbf{q}) = 0 \tag{G8}$$

The terms that are multiplied by ω correspond to water balance (Equation G1), and therefore can be eliminated because they sum 0. So, the final equation for transport is:

$$\phi\rho\frac{\partial\omega}{\partial t} + \nabla\cdot(-\mathbf{D}\rho\nabla\omega) + \rho\mathbf{q}\cdot\nabla\omega = 0 \tag{G9}$$

The mass conservation of a solute can be written also using concentration $C = \omega\rho$ as:

$$\frac{\partial(\phi C)}{\partial t} + \nabla\cdot(-\mathbf{D}\nabla C + C\mathbf{q}) = 0 \tag{G10}$$

In this case, it can be transformed into:

$$C\frac{\partial\phi}{\partial t} + \phi\frac{\partial C}{\partial t} + \nabla\cdot(-\mathbf{D}\nabla C) + C\nabla\cdot\mathbf{q} + \mathbf{q}\cdot\nabla C = 0 \tag{G11}$$

To simplify this equation (cancellation of the terms multiplied by C), equation G1 has to be used for constant density.

Then, it can be transformed into:

$$\phi\frac{\partial C}{\partial t} + \nabla\cdot(-\mathbf{D}\nabla C) + \mathbf{q}\cdot\nabla C = 0 \tag{G12}$$

In principle, equations G9 and G12 are similar, but there are additional assumptions to obtain G12 as compared to G9.

References

Acosta, O., Custodio, E., 2008. Impactos ambientales de las extracciones de agua subterránea en el Salar del Huasco (Norte de Chile). *Bol. Geol. y Min.* 119, 33–50.

Alonso, H., Risacher, F., 1996. Geoquímica del Salar de Atacama, parte 1: Origen De Los componentes y balance salino. *Rev. Geol. Chile* 23, 113–122. doi:10.5027/andgeoV23n2-a01.

Alpers, C.N., Whittemore, D.O., 1990. Hydrogeochemistry and stable isotopes of ground and surface waters from two adjacent closed basins, Atacama Desert, northern Chile. *Appl. Geochemistry* 5, 719–734. doi:10.1016/0883-2927(90)90067-F.

Anderson, M., Low, R., Foot, S., 2002. Sustainable groundwater development in arid, high Andean basins. *Geol. Soc. London,* Spec. Publ. 193, 133–144. doi:10.1144/GSL.SP.2002.193.01.11.

Araoka, D., Kawahata, H., Takagi, T., Watanabe, Y., Nishimura, K., Nishio, Y., 2014. Lithium and strontium isotopic systematics in playas in Nevada, USA: Constraints on the origin of lithium. *Miner. Depos.* 49, 371–379. doi:10.1007/s00126-013-0495-y.

Aravena, R., Suzuki, O., Peña, H., Pollastri, A., Fuenzalida, H., Grilli, A., 1999. Isotopic composition and origin of the precipitation in Northern Chile. *Appl. Geochemistry* 14, 411–422. doi:10.1016/S0883-2927(98)00067-5.

Arriagada, C., Cobbold, P.R., Roperch, P., 2006. Salar de Atacama basin: A record of compressional tectonics in the central Andes since the mid-Cretaceous. *Tectonics* 25, TC1008. doi:10.1029/2004TC001770.

Bakalowicz, M., 2005. Karst groundwater: A challenge for new resources. *Hydrogeol. J.* 13, 148–160. doi:10.1007/s10040-004-0402-9.

Bear, J., 1972. Dynamics of Fluids in Porous Media. *Soil Sci.* 120, 162–163. doi:10.1097/00010694-197508000-00022.

Benson, T.R., Coble, M.A., Rytuba, J.J., Mahood, G.A., 2017. Lithium enrichment in intracontinental rhyolite magmas leads to Li deposits in caldera basins. *Nat. Commun.* 8, 1–9. doi:10.1038/s41467-017-00234-y.

Bevacqua, P., 1988. Descripción de las unidades geológicas de superficie del Salar de Atacama.

Bobst, A.L., Lowenstein, T.K., Jordan, T.E., Godfrey, L. V., Ku, T.L., Luo, S., 2001. A 106 ka paleoclimate record from drill core of the Salar de Atacama, northern Chile. *Palaeogeogr. Palaeoclimatol. Palaeoecol.* 173, 21–42. doi:10.1016/S0031-0182(01)00308-X.

Bookhagen, B., Strecker, M.R., 2008. Orographic barriers, high-resolution TRMM rainfall, and relief variations along the eastern Andes. *Geophys. Res. Lett.* 35, L06403. doi:10.1029/2007GL032011.

Boschetti, T., Cortecci, G., Barbieri, M., Mussi, M., 2007. New and past geochemical data on fresh to brine waters of the Salar de Atacama and Andean Altiplano, northern Chile. *Geofluids* 7, 33–50. doi:10.1111/j.1468-8123.2006.00159.x.

Boutt, D.F., Hynek, S.A., Munk, L.A., Corenthal, L.G., 2016. Rapid recharge of fresh water to the halite-hosted brine aquifer of Salar de Atacama, Chile. *Hydrol. Process.* 30, 4720–4740. doi:10.1002/hyp.10994.

Bowen, B.B., Kipnis, E.L., Raming, L.W., 2017. Temporal dynamics of flooding, evaporation, and desiccation cycles and observations of salt crust area change at the Bonneville Salt Flats, Utah. *Geomorphology* 299, 1–11. doi:10.1016/j.geomorph.2017.09.036.

Brutsaert, W., 1982. Evaporation into the Atmosphere: Theory, History and Applications. Springer Netherlands. doi:10.1038/scientificamerican12121863-370.

Büyüburç, A., Köksal, G., 2005. An attempt to minimize the cost of extracting lithium from boron clays through robust process design. *Clays Clay Miner.* 53, 301–309. doi:10.1346/CCMN.2005.0530310.

Carmona, V., Pueyo, J.J., Taberner, C., Chong, G., Thirlwall, M., 2000. Solute inputs in the Salar de Atacama (N. Chile). *J. Geochemical Explor.* 69–70, 449–452. doi:10.1016/S0375-6742(00)00128-X.

Cipriani, A., Pretty, H., Hawton, K., Geddes, J.R., 2005. Lithium in the prevention of suicidal behavior and all-cause mortality in patients with mood disorders: a systematic review of randomized trials. *Am. J. Psychiatry* 162, 1805–1819. doi:10.1176/appi.ajp.162.10.1805.

Comisión Regional del Medio Ambiente, 2006. Resolución de Calificación Ambiental N° 226/2006. Antofagasta, Chile.

Corenthal, L.G., Boutt, D.F., Hynek, S.A., Munk, L.A., 2016. Regional groundwater flow and accumulation of a massive evaporite deposit at the margin of the Chilean Altiplano. *Geophys. Res. Lett.* 43, 8017–8025. doi:10.1002/2016GL070076.

Cornellà, O., Salas, J., Aravena, R., Guzmán, E., Guimerà, J., Tore, C., Von Igel, W., Henríquez, A., Fock, A., 2009. Hidrogeologia de los sistemas lagunares del margen E del Salar de Atacama, in: *XII Congreso Geológico Chileno*. Santiago de Chile, 1–4.

Custodio, E., Llamas, M.R., 1976. Hidrología Subterránea (T.2), ed. Omega, 1224 pp.

Custodio, E., Bruggeman, G.A., 1987. Groundwater problems in coastal areas. *Studies and reports in hydrology*, UNESCO.

De Silva, S.L., 1989. Geochronology and stratigraphy of the ignimbrites from the 21o 30' S to 23o 30' S portion of the central Andes of northern Chile. *J. Volcanol. Geotherm. Res.* 37, 93–131. doi:10.1016/0377-0273(89)90065-6.

Dentz, M., Tartakovsky, D.M., Abarca, E., Guadagnini, a., Sanchez-Vila, X., Carrera, J., 2006. Variable-density flow in porous media. *J. Fluid Mech.* 561, 209-235. doi:10.1017/S0022112006000668.

Diersch, H.-J.G., 2014. FEFLOW: Finite Element Modeling of Flow, Mass and Heat Transport in Porous and Fractured Media. Springer-Verlag Berlin Heidelberg. 996 pp. doi:10.1007/978-3-642-38739-5.

Dirección General de Aguas, 1986. Balance Hidrologico Nacional II Region. Santiago, Chile.

Dirección General de Aguas, 2010. Actualización de la evaluación de la disponibilidad de recursos hídricos para constituir derechos de aprovechamientos en las subcuencas afluentes al Salar de Atacama. II Región Informe final. Santiago, Chile.

Dirección General de Aguas, 2013. Análisis de la oferta hídrica del Salar de Atacama. Santiago, Chile.

Dirección General de Aguas, 2014. Análisis de los mecanismos de evaporación y evaluación de los recursos hídricos del Salar de Atacama. Santiago, Chile.

Doherty, J., 2015. Calibration and Uncertainty Analysis for Complex Environmental Models. *Groundwater* 56, 673–674.

Doorenbos, J., Pruitt, W.O., 1975. Guidelines for predicting crop water requirements, in: *Irrigation and Drainage*, Paper 24. Food and Agriculture Organization of the United Nations, Rome.

Driesner, T., Heinrich, C.A., 2007. The system H_2O-NaCl. Part I: Correlation formulae for phase relations in temperature-pressure-composition space from 0 to 1000 °C, 0 to 5000 bar, and 0 to 1 XNaCl. *Geochim. Cosmochim. Acta* 71, 4880–4901. doi:10.1016/j.gca.2006.01.033.

Duffy, C.J., Al-Hassan, S., 1988. Groundwater circulation in a closed desert basin: Topographic scaling and climatic forcing. *Water Resour. Res.* 24, 1675–1688. doi:10.1029/WR024i010p01675.

Eccles, D.R., Berhane, H., 2011. Geological Introduction to Lithium-Rich Formation Water with Emphasis on the Fox Creek Area of West-Central Alberta, Report 2011-10. Energy Resources Conservation Board ERCB/AGS.

Eppelbaum, L., Kutasov, I., Arkady, P., 2014. Applied Geothermics. Springer-Verlag Berlin Heidelberg. doi:10.1007/978-3-642-34023-9.

Ericksen, G.E., Vine, J.D., Ballón, R., 1978. Chemical composition and distribution of lithium-rich brines in Salar de Uyuni and nearby salars in southwestern Bolivia). *Energy* 3, 355–363. doi:10.1016/0360-5442(78)90032-4.

Eugster, H.P., 1980. Geochemistry of evaporitic lacustrine deposits. *Annu. Rev. Earth Planet. Sci.* 8, 35–63.

Evans, R.K., 1978. Lithium reserves and resources. *Energy* 3, 379–385.

Fan, Y., Duffy, C.J., Oliver, D.S., 1997. Density-driven groundwater flow in closed desert basins: Field investigations and numerical experiments. *J. Hydrol.* 196, 139–184. doi:10.1016/S0022-1694(96)03292-1.

Ferguson, G., Gleeson, T., 2012. Vulnerability of coastal aquifers to groundwater use and climate change. *Nat. Clim. Chang.* 2, 342–345. doi:10.1038/nclimate1413.

Flexer, V., Baspineiro, C.F., Galli, C.I., 2018. Lithium recovery from brines: A vital raw material for green energies with a potential environmental impact in its mining and processing. *Sci. Total Environ.* 639, 1188–1204. doi:10.1016/j.scitotenv.2018.05.223.

Gajardo, G.M., Beardmore, J.A., 2012. The brine shrimp Artemia: Adapted to critical life conditions. *Front. Physiol.* 3, article 185. doi:10.3389/fphys.2012.00185.

García, M.G., Borda, L.G., Godfrey, L. V., López Steinmetz, R.L., Losada-Calderon, A., 2020. Characterization of lithium cycling in the Salar De Olaroz, Central Andes, using a geochemical and isotopic approach. *Chem. Geol.* 531, 119340. doi:10.1016/j.chemgeo.2019.119340.

Gardeweg, M., Ramírez, C.F., 1987. La Pacana caldera and the Atana Ignimbrite. A major ash-flow and resurgent caldera complex in the Andes of northern Chile. *Bull. Volcanol.* 49, 547–566. doi:10.1007/BF01080449.

Garreaud, R.D., Molina, A., Farias, M., 2010. Andean uplift, ocean cooling and Atacama hyperaridity: A climate modeling perspective. *Earth Planet. Sci. Lett. 292*, 39–50. doi:10.1016/j.epsl.2010.01.017.

Garrett, D.E., 2004. Handbook of Lithium and Natural Calcium Chloride. Academic Press. doi:10.1016/B978-0-12-276152-2.X5035-X.

Glover, R.E., 1959. The pattern of fresh-water flow in a coastal aquifer. *J. Geophys. Res.* 64, 4, 457-459. doi:10.1029/JZ064i004p00457.

Godfrey, L. V., Chan, L.H., Alonso, R.N., Lowenstein, T.K., McDonough, W.F., Houston, J., Li, J., Bobst, A., Jordan, T.E., 2013. The role of climate in the accumulation of lithium-rich brine in the central andes. *Appl. Geochemistry* 38, 92–102. doi:10.1016/j.apgeochem.2013.09.002.

Golder Associates, 2017a. Informe n°16 "Plan de Alerta Temprana para el acuífero Monturaqui-Negrillar-Tilopozo".

Golder Associates, 2017b. Modelo hidrogeológico conceptual y numérico para el acuífero de Monturaqui-Negrillar-Tilopozo.

González, G., Cembrano, J., Aron, F., Veloso, E.E., Shyu, J.B.H., 2009. Coeval compressional deformation and volcanism in the central Andes, case studies from northern Chile (23°S-24°S). *Tectonics* 28, 1–18. doi:10.1029/2009TC002538.

Grilli, A., 1985. Una aproximación al estudio de la evaporación desde salares, in: *VII Congreso de Ingeniería Hidráulica*. Concepción, Chile.

Grilli, A., Vidal, F., 1986. Evaporación desde salares: metodología para evaluar los recursos hídricos renovables. Aplicación a las regiones I y II. *Rev. la Soc. Chil. Ing. Hidráulica* 1, year 1, n° 2.

Hamann, E., Post, V., Kohfahl, C., Prommer, H., Simmons, C.T., 2015. Numerical investigation of coupled density-driven flow and hydrogeochemical processes below playas. *Water Resour. Res.* 51, 9338–9352. doi:10.1002/2015WR017833.

Hamza, V.M., Dias, F.J.S.S., Gomes, A.J.L., Terceros, Z.G.D., 2005. Numerical and functional representations of regional heat flow in South America. *Phys. Earth Planet. Inter.* 152, 223–256. doi:10.1016/j.pepi.2005.04.009.

Hardie, L.A., Smoot, J.P., Eugster, H.P., 1978. Saline lakes and their deposits: a sediment approach, in: Matter, A., Tucker, M.E. (Eds.), *Modern and Ancient Lake Sediments. International Association of Sedimentologists*. Wiley-Blackwell, pp. 7–42. doi:doi.org/10.1002/9781444303698.ch2.

Hardie, L.A., 1990. The roles of rifting and hydrothermal $CaCl_2$ brines in the origin of potash evaporites: An hypothesis. *Am. J. Sci.* 290, 43–106. doi:10.2475/ajs.290.1.43.

Hardie, L.A., 1991. On the significance of evaporites. *Annu. Rev. Earth Planet. Sci.* 19, 131–68. doi:10.1146/annurev.ea.19.050191.001023.

Hartley, A.J., Chong, G., 2002. Late Pliocene age for the Atacama Desert: Implications for the desertification of western South America. *Geology* 30, 43–46. doi:10.1130/0091-7613 (2002)030<0043:LPAFTA>2.0.CO;2.

HARZA, 1978. Desarrollo de los recursos de agua en el Norte Grande, Chile. Santiago, Chile.

Hayashi, M., 2004. Temperature-electrical conductivity relation of water for environmental monitoring and geophysical data inversion. *Environ. Monit. Assess.* 96, 119–128. doi:10.1023/B:EMAS.0000031719.83065.68.

Herrera, C., Custodio, E., Chong, G., Lambán, L.J., Riquelme, R., Wilke, H., Jódar, J., Urrutia, J., Urqueta, H., Sarmiento, A., Gamboa, C., Lictevout, E., 2016. Groundwater flow in a closed basin with a saline shallow lake in a volcanic area: Laguna Tuyajto, northern Chilean Altiplano of the Andes. *Sci. Total Environ.* 541, 303–318. doi:10.1016/j.scitotenv.2015.09.060.

Hofstra, A.H., Todorov, T.I., Mercer, C.N., Adams, D.T., Marsh, E.E., 2013. Silicate melt inclusion evidence for extreme pre-eruptive enrichment and post-eruptive depletion of lithium in silicic volcanic rocks of the Western United States: Implications for the origin of Lithium-Rich Brines. *Econ. Geol.* 108, 1691–1701. doi:10.2113/econgeo.108.7.1691.

Holzbecher, E., 2005. Groundwater flow pattern in the vicinity of a salt lake. *Hydrobiologia* 532, 233–242.

Houston, J., 2006a. Variability of precipitation in the Atacama Desert: Its causes and hydrological impact. *Int. J. Climatol.* 26, 2181–2198. doi:10.1002/joc.1359.

Houston, J., 2006b. Evaporation in the Atacama Desert: An empirical study of spatio-temporal variations and their causes. *J. Hydrol.* 330, 402–412. doi:10.1016/j.jhydrol.2006.03.036.

Houston, J., 2009. A recharge model for high altitude, arid, Andean aquifers. *Hydrol. Process.* 23, 2383–2393. doi:10.1002/hyp.7350.

Houston, J., Butcher, A., Ehren, P., Evans, K., Godfrey, L., 2011. The evaluation of brine prospects and the requirement for modifications to filing standards. *Econ. Geol.* 106, 1125–1239. doi:10.2113/econgeo.106.7.1225.

Hubbert, M.K., 1940. The theory of groundwater motion. *Eos, Trans. Am. Geophys. Union* 21, 648–648. doi:10.1029/TR021i002p00648-1.

Huerta-Vásquez, G., 2012. Evaluation of Chemical Patterns in Brines in the Salar de Atacama, Northern Chile : A Chemical and Isotopic approach. Master thesis. University of Waterloo.

IDAEA-CSIC, 2017. Cuarta actualización del modelo hidrogeológico del Salar de Atacama. Santiago, Chile. Accessed by permission.

Ide, F., 1978. Cubicación del yacimiento Salar de Atacama. Universidad de Chile.

Ide, F., Kunasz, I.A., 1990. Origin of lithium in Salar de Atacama, Northern Chile, in: Ericksen, G.E., Cañas-Pinochet, M.T., Reinemund, J.A. (Eds.), *Geology of the Andes and Its Relation to Hydrocarbon and Mineral Resources*. Houston, Texas, p. 452.

Iribar, V., Carrera, J., Custodio, E., Medina, A., 1997. Inverse modelling of seawater intrusion in the Llobregat delta deep aquifer. *J. Hydrol.* 198, 226–244. doi:10.1016/S0022-1694(96)03290-8.

Irvine, D.J., Sheldon, H.A., Simmons, C.T., Werner, A.D., Griffiths, C.M., 2014. Investigation de l'influence de l'hétérogénéité d'un aquifère sur le potentiel de convection libre thermique dans l'aquifère du Yarragadee en Australie occidentale. *Hydrogeol. J.* 23, 161–173. doi:10.1007/s10040-014-1194-1.

Jayne, R.S., Pollyea, R.M., Dodd, J.P., Olson, E.J., Swanson, S.K., 2016. Contraintes spatiales et temporelles sur l'écoulement régional des eaux souterraines dans la pampa du bassin du Tamarugal, désert d'Atacama, Chili. *Hydrogeol. J.* 24, 1921–1937. doi:10.1007/s10040-016-1454-3.

Jellison, R., Macintyre, S., Millero, F.J., 1999. Density and conductivity properties of Na-CO3-Cl-SO4 brine from Mono Lake, California, USA. *Int. J. Salt Lake Res.* 8, 41–53.

Johnson, E., Yáñez, J., Ortiz, C., Muñoz, J., 2009. Evaporation from shallow groundwater in closed basins in the Chilean Altiplano. *Hydrol. Sci. J.* 55, 624–635. doi:10.1080/02626661003780458.

Jordan, T.E., Mpodozis, C., Muñoz, N., Blanco, N., Pananont, P., Gardeweg, M., 2007. Cenozoic subsurface stratigraphy and structure of the Salar de Atacama Basin, northern Chile. *J. South Am. Earth Sci.* 23, 122–146. doi:10.1016/j.jsames.2006.09.024.

Kampf, S.K., Tyler, S.W., Ortiz, C.A., Muñoz, J.F., Adkins, P.L., 2005. Evaporation and land surface energy budget at the Salar de Atacama, Northern Chile. *J. Hydrol.* 310, 236–252. doi:10.1016/j.jhydrol.2005.01.005.

Kampf, S.K., Tyler, S.W., 2006. Spatial characterization of land surface energy fluxes and uncertainty estimation at the Salar de Atacama, Northern Chile. *Adv. Water Resour.* 29, 336–354. doi:10.1016/j.advwatres.2005.02.017.

Karl, T.R., Williams, C.N., 1987. An approach to adjusting Climatological Time Series for Discontinuous Inhomogeneities. *J. Clim. Appl. Meteorol.* 26, 1744–1762. doi:10.1175/1520-0450(1987)026<1744:AATACT>2.0.CO;2.

Karmanocky, F.J., Benison, K.C., 2016. A fluid inclusion record of magmatic/hydrothermal pulses in acid Salar Ignorado gypsum, northern Chile. *Geofluids* 16, 490–506. doi:10.1111/gfl.12171.

Kesler, S.E., Gruber, P.W., Medina, P.A., Keoleian, G.A., Everson, M.P., Wallington, T.J., 2012. Global lithium resources: Relative importance of pegmatite, brine and other deposits. *Ore Geol. Rev.* 48, 55–69. doi:10.1016/j.oregeorev.2012.05.006.

Klyukin, Y.I., Driesner, T., Steele-MacInnis, M., Lowell, R.P., Bodnar, R.J., 2016. Effect of salinity on mass and energy transport by hydrothermal fluids based on the physical and thermodynamic properties of H_2O-NaCl. *Geofluids* 16, 585–603. doi:10.1111/gfl.12181.

Kohfahl, C., Post, V.E.A., Hamann, E., Prommer, H., Simmons, C.T., 2015. Validity and slopes of the linear equation of state for natural brines in salt lake systems. *J. Hydrol.* 523, 190–195. doi:10.1016/j.jhydrol.2015.01.054.

Koltzer, N., Möller, P., Inbar, N., Siebert, C., Rosenthal, E., Magri, F., 2017. Thermal impacts of magmatic intrusions: A hypothesis of paleo-heating processes in the Tiberias Basin, Jordan-Dead Sea Transform. *Energy Procedia* 125, 80–87. doi:10.1016/j.egypro.2017.08.071.

Krupp, R.E., 2005. Formation and chemical evolution of magnesium chloride brines by evaporite dissolution processes - Implications for evaporite geochemistry. *Geochim. Cosmochim. Acta* 69, 4283–4299. doi:10.1016/j.gca.2004.11.018.

Lever, D.A., Jackson, C.P., 1985. On the equations for the flow of concentrated salt solution through a porous medium. Report N°. DOE/RW85.100.

Li, Z., Chi, G., Bethune, K.M., 2016. The effects of basement faults on thermal convection and implications for the formation of unconformity-related uranium deposits in the Athabasca Basin, Canada. *Geofluids* 16, 729–751. doi:10.1111/gfl.12180.

Li, R., Liu, C., Jiao, P., Wang, J., 2018. The tempo-spatial characteristics and forming mechanism of Lithium-rich brines in China. *China Geol.* 1, 72–83. doi:10.31035/cg2018009.

Lindsay, J.M., 2001. Magmatic Evolution of the La Pacana Caldera System, Central Andes, Chile: Compositional Variation of Two Cogenetic, Large-Volume Felsic Ignimbrites. *J. Petrol.* 42, 459–486. doi:10.1093/petrology/42.3.459.

Liu, W., Agusdinata, D.B., Myint, S.W., 2019. Spatiotemporal patterns of lithium mining and environmental degradation in the Atacama Salt Flat, Chile. *Int. J. Appl. Earth Obs. Geoinf.* 80, 145–156. doi:10.1016/j.jag.2019.04.016.

López Steinmetz, R.L., Salvi, S., García, M.G., Peralta Arnold, Y., Béziat, D., Franco, G., Constantini, O., Córdoba, F.E., Caffe, P.J., 2018. Northern Puna Plateau-scale survey of Li brine-type deposits in the Andes of NW Argentina. *J. Geochemical Explor.* 190, 26–38. doi:10.1016/j.gexplo.2018.02.013.

Lowenstein, T.K., Risacher, F., 2009. Closed basin brine evolution and the influence of Ca-Cl inflow waters: Death valley and Bristol dry lake California, Qaidam Basin, China, and Salar de Atacama, Chile. *Aquat. Geochemistry* 15, 71–94. doi:10.1007/s10498-008-9046-z.

Lowenstein, T.K., Dolginko, L.A.C., García-Veigas, J., 2016. Influence of magmatic-hydrothermal activity on brine evolution in closed basins: Searles Lake, California. *Bull. Geol. Soc. Am.* 128, 1555–1568. doi:10.1130/B31398.1.

Lu, C., Werner, A.D., Simmons, C.T., Luo, J., 2015. A Correction on Coastal Heads for Groundwater Flow Models. *Groundwater* 53, 164–170. doi:10.1111/gwat.12172.

Lusczynski, N.J., 1961. Head and Flow of Ground Water of Variable Density. *J. Geophys. Res.* 66, 4247–4256. doi:10.1029/JZ066i012p04247.

Maas, C., Emke, M.J., 1989. Solving varying density groundwater problems with a single density computer program, in: *10th SWIM*, Ghent.

Magaritz, M., Aravena, R., Peña, H., Suzuki, O., Grilli, A., 1990. Source of Ground Water in the Deserts of Northern Chile: Evidence of Deep Circulation of Ground Water from the Andes. *Ground Water* 28, 513–517.

Magri, F., 2009. Derivation of the coefficients of thermal expansion and compressibility for use in FEFLOW, in: *FEFLOW White Papers Vol III*. pp. 13–23.

Magri, F., Bayer, U., Maiwald, U., Otto, R., Thomsen, C., 2009. Impact of transition zones, variable fluid viscosity and anthropogenic activities on coupled fluid-transport

processes in a shallow salt-dome environment. *Geofluids* 9, 182–194. doi:10.1111/j.1468-8123.2009.00242.x.

Magri, F., Akar, T., Gemici, U., Pekdeger, A., 2010. Deep geothermal groundwater flow in the Seferihisar-Balçova area, Turkey: Results from transient numerical simulations of coupled fluid flow and heat transport processes. *Geofluids* 10, 388–405. doi:10.1111/j.1468-8123.2009.00267.x.

Magri, F., Akar, T., Gemici, U., Pekdeger, A., 2012. Numerical investigations of fault-induced seawater circulation in the Seferihisar-Balçova Geothermal system, western Turkey. *Hydrogeol. J.* 20, 103–118. doi:10.1007/s10040-011-0797-z.

Magri, F., Inbar, N., Siebert, C., Rosenthal, E., Guttman, J., Möller, P., 2015. Transient simulations of large-scale hydrogeological processes causing temperature and salinity anomalies in the Tiberias Basin. *J. Hydrol.* 520, 342–355. doi:10.1016/j.jhydrol.2014.11.055.

Magri, F., Möller, S., Inbar, N., Möller, P., Raggad, M., Rödiger, T., Rosenthal, E., Siebert, C., 2016. 2D and 3D coexisting modes of thermal convection in fractured hydrothermal systems - Implications for transboundary flow in the Lower Yarmouk Gorge. *Mar. Pet. Geol.* 78, 750–758. doi:10.1016/j.marpetgeo.2016.10.002.

Marazuela, M.A., Vázquez-Suñé, E., Custodio, E., Palma, T., García-Gil, A., Ayora, C., 2018. 3D mapping, hydrodynamics and modelling of the freshwater-brine mixing zone in salt flats similar to the Salar de Atacama (Chile). *J. Hydrol.* 561, 223–235. doi:10.1016/j.jhydrol.2018.04.010.

Marazuela, M.A., Vázquez-Suñé, E., Ayora, C., García-Gil, A., Palma, T., 2019a. Hydrodynamics of salt flat basins: The Salar de Atacama example. *Sci. Total Environ.* 651, 668–683. doi:10.1016/j.scitotenv.2018.09.190.

Marazuela, M.A., Vázquez-Suñé, E., Ayora, C., García-Gil, A., Palma, T., 2019b. The effect of brine pumping on the natural hydrodynamics of the Salar de Atacama: The damping capacity of salt flats. *Sci. Total Environ.* 654, 1118–1131. doi:10.1016/j.scitotenv.2018.11.196.

Marazuela, M.A., Vázquez-Suñé, E., Ayora, C., García-Gil, A., 2020. Towards more sustainable brine extraction in salt flats: Learning from the Salar de Atacama. *Sci. Total Environ.* 703, article 135605. doi:10.1016/j.scitotenv.2019.135605.

Mardones, L., 1986. Características geológicas e hidrogeológicas del Salar de Atacama, in: Lagos, G. (Ed.), *El Litio, Un Nuevo Recurso Para Chile*. pp. 181–216.

Mardones, L., 1998. Flux et évolution des solutions salines dans les systèmes hydrologiques des salars d'Ascotan et d'Atacama. PhD thesis. University of Paris.

Marion, G.M., Catling, D.C., Zahnle, K.J., Claire, M.W., 2010. Modeling aqueous perchlorate chemistries with applications to Mars. *Icarus* 207, 675–685. doi:10.1016/j.icarus.2009.12.003.

Marom, R., Amalraj, S.F., Leifer, N., Jacob, D., Aurbach, D., 2011. A review of advanced and practical lithium battery materials. *J. Mater. Chem*. 21, 9938–9954. doi:10.1039/c0jm04225k.

Mercer, J.W., Pinder, G.F., 1974. Finite element analysis of hydro-thermal systems, in: Oden, J.T., Zienkiewicz, O.C., Gallagher, R.H., Taylor, C. (Eds.), *Finite Element Analysis of Hydro-Thermal Systems*. University of Alabama Press, pp. 401–414.

Mishra, S.K., Singh, V., 2003. Soil Conservation Service Curve Number (SCS-CN) Methodology. Springer Netherlands. doi:10.1007/978-94-017-0147-1.

Mpodozis, C., Arriagada, C., Basso, M., Roperch, P., Cobbold, P., Reich, M., 2005. Late Mesozoic to Paleogene stratigraphy of the Salar de Atacama Basin, Antofagasta, Northern Chile: Implications for the tectonic evolution of the Central Andes. *Tectonophysics* 399, 125–154. doi:10.1016/j.tecto.2004.12.019.

Munk, L.A., Jochens, H., Jennings, M., Bradley, D.C., Hynek, S.A., Godfrey, L., 2011. Origin and evolution of Li-rich brines at Clayton Valley, Nevada, USA, in: *11th SGA Biennial Meeting*. Antofagasta, Chile, pp. 217–219.

Munk, L.A., Hynek, S.A., Bradley, D., Boutt, D.F., Labay, K., Jochens, H., 2016. Lithium brines: A global perspective. *Rev. Econ. Geol.* 18, 339–365.

Munk, L.A., Boutt, D.F., Hynek, S.A., Moran, B.J., 2018. Hydrogeochemical fluxes and processes contributing to the formation of lithium-enriched brines in a hyper-arid continental basin. *Chem. Geol.* 493, 37–57. doi:10.1016/j.chemgeo.2018.05.013.

Muñoz, N., Charrier, R., Jordan, T., 2002. Interactions between basement and cover during the evolution of the Salar de Atacama Basin, northern Chile. *Rev. geológica Chile* 29, 3–29. doi:10.4067/S0716-02082002000100004.

Muñoz-Pardo, J.F., Ortiz-Astete, C.A., 2004. Funcionamiento hidrogeológico del acuífero del núcleo del Salar de Atacama, Chile. *Ing. Hidráulica en Mex.* XIX, 69–81.

Nield, D.A., Simmons, C.T., Kuznetsov, A. V., Ward, J.D., 2008. On the evolution of salt lakes: Episodic convection beneath an evaporating salt lake. *Water Resour. Res.* 44, W02439. doi:10.1029/2007WR006161.

Obianyo, J.I., 2019. Effect of Salinity on Evaporation and the Water Cycle. *Emerg. Sci. J.* 3, 255–262. doi:10.28991/esj-2019-01188.

Ortiz, C., Aravena, R., Briones, E., Suárez, F., Tore, C., Muñoz, J.F., 2014. Sources of surface water for the Soncor ecosystem, Salar de Atacama basin, northern Chile. *Hydrol. Sci. J.* 59, 336–350. doi:10.1080/02626667.2013.829231.

Oude-Essink, G.H.P., Boekelman, R.H., 1996. Problems with large-scale modelling of salt water intrusion in 3D, in: *14th SWIM*, Malmö.

Oude-Essink, G.H.P., 2001. Improving fresh groundwater supply—problems and solutions. *Ocean Coast. Manag.* 44, 429–449. doi:10.1016/S0964-5691(01)00057-6.

Pananont, P., Mpodozis, C., Blanco, N., Jordan, T.E., Brown, L.D., 2004. Cenozoic evolution of the northwestern Salar de Atacama Basin, northern Chile. *Tectonics* 23, 1–19. doi: 10.1029/2003TC001595.

Parkhurst, D.L., Appelo, C.A.J., 2013. Description of Input and Examples for PHREEQC Version 3—A Computer Program for Speciation, Batch-Reaction, One-Dimensional Transport, and Inverse Geochemical Calculations, in: *Techniques and Methods* 6. p. 519.

Peterson, T.C., Easterling, D.R., 1994. Creation of homogeneous composite climatological reference series. *Int. J. Climatol.* 14, 671–679. doi:10.1002/joc.3370140606.

Philip, J.R., 1957. Evaporation, and moisture and heat fields in the soil. *J. Meteorol.* 14, 354–366. doi:10.1175/1520-0469(1957)014<0354:EAMAHF>2.0.CO;2.

Pool, M., Carrera, J., 2011. A correction factor to account for mixing in Ghyben-Herzberg and critical pumping rate approximations of seawater intrusion in coastal aquifers. *Water Resour. Res.* 47, W05506. doi:10.1029/2010WR010256.

Post, V.E.A., Kooi, H., Simmons, C., 2007. Using hydraulic head measurements in variable-density ground water flow analyses. *Ground Water* 45, 664–671. doi:10.1111/j.1745-6584. 2007.00339.x.

Post, V.E.A., Groen, J., Kooi, H., Person, M., Ge, S., Edmunds, W.M., 2013. Offshore fresh groundwater reserves as a global phenomenon. *Nature* 504, 71–78. doi:10.1038/nature 12858.

Post, V.E.A., Werner, A.D., 2017. Coastal aquifers: Scientific advances in the face of global environmental challenges. *J. Hydrol.* 551, 1–3. doi:10.1016/j.jhydrol.2017.04.046.

Pueyo, J.J., Chong, G., Ayora, C., 2017. Lithium saltworks of the Salar de Atacama: A model for MgSO4-free ancient potash deposits. *Chem. Geol.* 466, 173–186. doi:10.1016/ j.chemgeo.2017.06.005.

Rech, J.A., Currie, B.S., Michalski, G., Cowan, A.M., 2006. Neogene climate change and uplift in the Atacama Desert, Chile. *Geology*. doi:10.1130/G22444.1.

Reutter, K.J., Charrier, R., Gotze, H.J., Schurr, B., Wigger, P., Scheuber, E., Giese, P., Reuther, C.D., Schmidt, S., Rietbrock, A., Chong, G., Belmonte-Pool, A., 2006. The Salar de Atacama Basin: a Subsiding Block within the Western Edge of the Altiplano-Puna Plateau. *Andes Act. Subduction Orogeny* 303–325. doi:10.1007/978-3-540-48684-8_14.

Rio Chilex S.A, 1997. Evaluación hidrogeológica acuífero sector norte Salar de Atacama. URL http://sad.dga.cl/ipac20/ipac.jsp?session=15Y54918K1790.3317420&menu=search&asp ect=subtab39&npp=10&ipp=20&spp=20&profile=cirh&ri=&term=Evaluación+hidroge ológica+acuífero+sector+norte&index=.GW&x=0&y=0&aspect=subtab39. Last Access: 01-09-2017.

Risacher, F., Fritz, B., 1991. Geochemistry of Bolivian salars, Lipez, southern Altiplano: Origin of solutes and brine evolution. *Geochim. Cosmochim. Acta* 55, 687–705. doi:10.1016/0016-7037(91)90334-2.

Risacher, F., Alonso, H., 1996. Geoquímica del Salar de Atacama, parte 2: Evolución de las aguas. *Rev. Geol. Chile* 23, 123–134.

Risacher, F., Alonso, H., Salazar, C., 2003. The origin of brines and salts in Chilean salars: A hydrochemical review. *Earth-Science Rev.* 63, 249–293. doi:10.1016/S0012-8252(03)00037-0.

Risacher, F., Fritz, B., 2009. Origin of salts and brine evolution of Bolivian and Chilean salars. Aquat. *Geochemistry* 15, 123–157. doi:10.1007/s10498-008-9056-x.

Risacher, F., Fritz, B., Hauser, A., 2011. Origin of components in Chilean thermal waters. *J. South Am. Earth Sci*. 31, 153–170. doi:10.1016/j.jsames.2010.07.002.

Rissmann, C., Leybourne, M., Benn, C., Christenson, B., 2015. The origin of solutes within the groundwaters of a high Andean aquifer. *Chem. Geol.* 396, 164–181. doi:10.1016/j.chemgeo.2014.11.029.

Rockwood Lithium, 2015. Estudio de Impacto ambiental Proyecto modificaciones y mejoramiento del sistema de pozas de evaporación solar en el Salar de Atacama (Anexo 1). Para Estudio de impacto Ambiental Proyecto Modificaciones y Mejoramiento del Sistema de Pozas de Evaporación solar en el Salar de Atacama. Santiago, Chile. URL http://seia.sea.gob.cl/expediente/ficha/fichaPrincipal.php?modo=ficha&id_expediente=3788682. Last Access: 01-09-2017.

Rosen, M.R., 1994. The importance of groundwater in playas: A review of playa classifications and the sedimentology and hydrology of playas. *Geol. Soc. Am. Spec. Pap.* 289, 1–18. doi:10.1130/SPE289-p1.

Rushton, K.R., 1980. Differing positions of saline interfaces in aquifers and observation boreholes. *J. Hydrol.* 48, 185–189.

Salas, J., Guimerà, J., Cornellà, O., Aravena, R., Guzmán, E., Tore, C., Von Igel, W., Moreno, R., 2010. Hidrogeologia del sistema lagunar del margen este del Salar de Atacama (Chile). *Bol. Geol. y Min.* 121, 357–372.

Scanlon, B.R., Mace, R.E., Barrett, M.E., Smith, B., 2003. Can we simulate regional groundwater flow in a karst system using equivalent porous media models? Case study, Barton Springs Edwards aquifer, USA. *J. Hydrol.* 276, 137–158. doi:10.1016/S0022-1694(03)00064-7.

Scanlon, B.R., Keese, K.E., Flint, A.L., Flint, L.E., Gaye, C.B., Edmunds, W.M., Simmers, I., 2006. Global synthesis of groundwater recharge in semiarid and arid regions. *Hydrol. Process.* 20, 3335–3370. doi:10.1002/hyp.6335.

Scheihing, K., Tröger, U., 2018. Local climate change induced by groundwater overexploitation in a high Andean arid watershed, Laguna Lagunillas basin, northern Chile. *Hydrogeol. J.* 26, 705–719. doi:10.1007/s10040-017-1647-4.

Schmitt, A.K., 2001. Gas-saturated crystallization and degassing in large-volume, crystal-rich dacitic magmas from the Altiplano-Puna, northern Chile. *J. Geophys. Res. Solid Earth* 106, 30561–30578. doi:10.1029/2000jb000089.

Schurr, B., Rietbrock, A., 2004. Deep seismic structure of the Atacama basin, northern Chile. *Geophys. Res. Lett.* 31, 10–13. doi:10.1029/2004GL019796.

Shewchuk, J.R., 1996. Triangle: Engineering a 2D quality mesh generator and delaunay triangulator, in: Lin, M.C., Manocha, D. (Eds.), *Applied Computational Geometry Towards Geometric Engineering. WACG 1996. Lecture Notes in Computer Science*. Springer, Berlin, Heidelberg, pp. 203–222. doi:10.1007/BFb0014497.

Simmons, C.T., Narayan, K.A., Wooding, R.A., 1999. On a test case for density-dependent groundwater flow and solute transport models: The salt lake problem. *Water Resour. Res.* 35, 3607–3620. doi:10.1029/1999WR900254.

Simms, M.A., Garven, G., 2004. Thermal convection in faulted extensional sedimentary basins: Theoretical results from finite-element modeling. *Geofluids* 4, 109–130. doi:10.1111/j.1468-8115.2004.00069.x.

Skrzypek, G., Mydłowski, A., Dogramaci, S., Hedley, P., Gibson, J.J., Grierson, P.F., 2015. Estimation of evaporative loss based on the stable isotope composition of water using Hydrocalculator. *J. Hydrol.* 523, 781–789. doi:10.1016/j.jhydrol.2015.02.010.

Song, W., Gang, H., Ma, Y., Yang, S., Mu, B., 2017. Migration behavior of lithium during brine evaporation and KCl production plants in Qarhan Salt Lake. *Minerals* 7. doi:10.3390/min7040057.

Strack, O.D.L., 1976. A single-potential solution for regional interface problems in coastal aquifers. *Water Resour. Res.* 12, 1165–1174. doi:10.1029/WR012i006p01165.

Tarascon, J.-M., 2010. Is lithium the new gold? Nat. Chem. 2, 510–510. doi:10.1038/nchem.680.

Tejeda, I., Cienfuegos, R., Muñoz, J.F., Durán, M., 2003. Numerical Modeling of Saline Intrusion in Salar de Atacama. *J. Hydrol. Eng.* 8, 25–34. doi:10.1061/(ASCE)1084-0699 (2003)8:1(25).

Tyler, S.W., Muñoz, J.F., Wood, W.W., 2006. The response of playa and sabkha hydraulics and mineralogy to climate forcing. *Ground Water* 44, 3, 329–338. doi:10.1111/j.1745-6584. 2005.00096.x.

Universidad de Chile, 2016. Estudio estructural Zona Marginal, sector oriente del Salar de Atacama. Internal report of Sociedad Química y Minera de Chile S.A. (SQM).

USGS, 2017. Mineral commodities summary. URL https://minerals.usgs.gov/minerals/pubs/mcs/.

USGS, 2019. Mineral commodities summary. URL https://minerals.usgs.gov/minerals/pubs/mcs/.

Vásquez, C., Ortiz, C., Suárez, F., Muñoz, J.F., 2013. Modeling flow and reactive transport to explain mineral zoning in the Atacama salt flat aquifer, Chile. *J. Hydrol.* 490, 114–125. doi:10.1016/j.jhydrol.2013.03.028.

Vázquez-Suñé, E., Abarca, E., Carrera, J., Capino, B., Gámez, D., Pool, M., Simó, T., Batlle, F., Niñerola, J.M., Ibañez, X., 2006. Groundwater modelling as a tool for the European Water Framework Directive (WFD) application: The Llobregat case. *Phys. Chem. Earth* 31, 1015–1029. doi:10.1016/j.pce.2006.07.008.

Vigier, N., Decarreau, A., Millot, R., Carignan, J., Petit, S., France-Lanord, C., 2008. Quantifying Li isotope fractionation during smectite formation and implications for the Li cycle. *Geochim. Cosmochim. Acta* 72, 780–792. doi:10.1016/j.gca.2007.11.011.

Vikström, H., Davidsson, S., Höök, M., 2013. Lithium availability and future production outlooks. *Appl. Energy* 110, 252–266. doi:10.1016/j.apenergy.2013.04.005.

Vine, J.D., Dooley, J.R., 1980. Where on earth is all the lithium? doi:10.3133/ofr801234.

Warren, J.K., 2010. Evaporites through time: Tectonic, climatic and eustatic controls in marine and nonmarine deposits. *Earth-Science Rev.* 98, 217–268. doi:10.1016/j.earscirev.2009.11.004.

Warren, J.K., 2016. Evaporites. A geological compendium, Evaporites. Springer. doi:10.1007/978-3-319-13512-0.

Werner, A.D., Bakker, M., Post, V.E.A., Vandenbohede, A., Lu, C., Ataie-Ashtiani, B., Simmons, C.T., Barry, D.A., 2013. Seawater intrusion processes, investigation and management: Recent advances and future challenges. Adv. *Water Resour.* 51, 3–26. doi:10.1016/j.advwatres.2012.03.004.

Williams, T., Kelley, C., 1986. Gnuplot v5.2: An interactive plotting program.

Wood, W.W., Sanford, W.E., 1990. Ground-water control of evaporite deposition. *Econ. Geol.* 85, 1226–1235. doi:10.2113/gsecongeo.85.6.1226.

Wooding, R.A., Tyler, S.W., White, I., 1997. Convection in groundwater below an evaporating Salt Lake: 1. Onset of instability. *Water Resour. Res.* 33, 1199–1217. doi:10.1029/96WR03533.

XTERRAE, 2011. Modelo geológico del Salar de Atacama. Internal report of SQM.

Yechieli, Y., Wood, W.W., 2002. Hydrogeologic processes in saline systems: Playas, sabkhas, and saline lakes. *Earth-Science Rev.* 58, 343–365. doi:10.1016/S0012-8252(02)00067-3.

Yu, J.Q., Gao, C.L., Cheng, A.Y., Liu, Y., Zhang, L., He, X.H., 2013. Geomorphic, hydroclimatic and hydrothermal controls on the formation of lithium brine deposits in the Qaidam Basin, northern Tibetan Plateau, China. *Ore Geol. Rev.* 50, 171–183. doi:10.1016/j.oregeorev.2012.11.001.